Department of Civil and Environmental Engineering

Imperial College London

Efficient Modelling of RC Walls for Accurate Simulations under Earthquake Loading

Haochen Xie

A thesis submitted in fulfilment of the requirements for the degree of Doctor of Philosophy in the Department of Civil and Environmental Engineering of Imperial College London

June 2022

Declaration of Originality

I confirm that this thesis is my own work. Appropriate references are made whenever previously published or unpublished works of others are used.

Copyright Declaration

Abstract

Remarkable advances have been achieved in earthquake engineering in the past decades, given the growing awareness and concern regarding the global seismic risk. In the wake of the damage wrought by the recent earthquakes, reinforced concrete (RC) walls are commonly employed as effective seismic resisting components in new building structures or retrofitting solutions to enhance the seismic performance of existing sub-standard frame buildings. Current codes of practice recommend using nonlinear dynamic analysis as the most accurate technique for the seismic evaluation of RC buildings under earthquake loading. This necessitates the development of reliable numerical strategies for accurate simulation of RC walls under cyclic loading conditions representing seismic actions.

This research starts with a critical appraisal of currently available modelling strategies for RC walls associated with different levels of sophistication. They include: (i) the wide column approach with 1D beam elements, (ii) 2D FE models with nonlinear shell elements and (iii) detailed 3D FE descriptions with solid elements and embedded bar elements. Numerical simulations have been performed considering experimental slender and short wall specimens subjected to cyclic loading. Numerical-experimental comparisons highlight some drawbacks of existing modelling strategies as their inability to represent the actual degradation of strength and stiffness and the pinching characteristics of the cyclic behaviour, especially in the case of wall samples whose response is governed by flexure-shear interaction. In view of these limitations and to achieve more accurate response predictions, an efficient and practical 2D macro-element representation for RC walls is proposed in the second part of the research. It incorporates a biaxial concrete model based on the rotating crack approach to account for the nonlinear response under cyclic loading conditions. Accuracy and efficiency of the macro-element model have been demonstrated by validation studies, focusing on RC walls with different aspect ratios and an RC coupled wall system. The ability of the proposed model to predict the main cyclic response characteristics of RC walls, including stiffness and strength degradation, energy dissipation capacity, and pinched shapes of the hysteresis loops, has been confirmed by a favourable agreement between the numerical predictions and experimental findings.

The final part of this research proceeds with an application study on seismic analysis of a realistic four-storey RC frame-wall building. The developed macro-element model accounting for shear deformability and potential shear damage and failure provides a more realistic representation for RC walls than the wide column approach widely used in practice. Moreover, the macro-element modelling strategy requires a comparable computational cost to the wide column approach, which renders it suitable for nonlinear dynamic analysis of large scale structures and realistic seismic assessment of RC buildings with shear walls.

Acknowledgements

I have been very fortunate to have Prof. Bassam Izzuddin and Dr Lorenzo Macorini as my supervisors, who generously shared their immense knowledge and expertise. First and foremost, I would like to express my sincerest appreciation to Prof. Bassam Izzuddin for his guidance, patience, and unwavering support. His continued encouragement in my exploration of this research was a motivation throughout this work. I am also deeply indebted to Dr Lorenzo Macorini for his invaluable insights and helpful suggestions. I want to thank both of them for the constructive feedback that enhanced my knowledge and improved the quality of my research.

I want to take the opportunity to thank all the academic and administrative staff in the Department of Civil and Environmental Engineering at Imperial College London for their endless support that truly made my research journey a delightful one. Special thanks are extended to Ms Fionnuala Donovan and Miss Sarah Willis for their constant help and support.

Last, I would like to thank my colleagues and friends who supported me throughout my years of research. In particular, I wish to express my gratitude to (Dr) Moemen Hajjar and (Dr) Xi Chen, who started this journey with me. The vibrant interactions with them were always the highlights of my day. Thank you for making my years enjoyable. I also would like to thank: Dr Corrado Chisari, Dr Alejandro Barrero, Dr Andri Setiawan, Dr Stanyslav Grosman, Dr Alexandros Nordas, Dr Luis Santos, Dr Adrien Boyez, Dr Qili Fang, Dr Adeleke Soyemi, (Dr) Burak Sahin, (Dr) Matthew Chuo, (Dr) Joao Angelo Sio, (Dr) Junxu Lai for their kindness, encouragement and for being a good company throughout my spell at Imperial College. Last but not least, my deepest gratitude goes to my parents and to my sister for their emotional support and unconditional love, I am always grateful to have them standing by my side, and for that I will be indebted forever.

Table of Contents

Chapter 5 Validation of Macro-element for RC Walls 119

List of Tables

List of Figures

List of Symbols

Latin letters

A	Fictitious undamaged area
$\bar{A}$	Damaged area
A_c	Cross sectional area of concrete
A_{cv}	Gross area of the section resisting shear
A_{sl}	Tensile reinforcement area that extends $\geq (l_{bd} + d)$ beyond the section considered in Figure 2-5
A_{sw}	Cross sectional area of shear reinforcement
a_t	Tensile softening slope
b_c	Compressive interaction parameter
b_c	Factor for biaxial compressive interaction
b_w	Cross-sectional minimum width in the tensile area
b_{w}	Minimum width between compressive and tensile chords
d	Effective depth of a cross section
d	Scalar damage variable
E_{c1}	Secant compressive stiffness
E_{c2}	Compressive softening stiffness
E_s	Young's modulus of steel
E_{t1}	Initial tensile stiffness
E_{t2}	Tensile softening stiffness
$F(x)$	Yield function
$f_{b0r}, \tilde{f}_b$	Ratio between biaxial and uniaxial compressive strength
$\bar{f}_c(x), \bar{f}_t(x)$	Effective uniaxial compressive and tensile strength functions
f_c'	Compressive strength of concrete

f_{c1}	Compressive strength
f_{c2}	Residual compressive strength
f_{cd}	Design value of concrete compressive strength
f_{ck}	Characteristic cylinder strength of concrete
f_t	Tensile strength
f_{t0}	Initial uniaxial tensile strength
$\tilde{f}_y$	Ratio between uniaxial yielding stress and maximum strength in compression
f_{yh}	Yield strength of hoop reinforcement
f_{yt}	Yield strength of transverse reinforcement
f_{ywd}	Design yield strength of the shear reinforcement
$g(x)$	Plastic potential function
G_t	Fracture energy
h	Height of macro-element
$\boldsymbol{h}(x)$	Hardening function
h'	Width of the concrete core measured to the outside of the peripheral hoop
h_w	Wall height
I_1, J_2	Stress invariants for the biaxial case representing the interaction between normal and shear stresses
k	Coefficient; factor
K	Factor accounting for the confinement effect due to the transverse steel reinforcement in the boundary elements of a RC wall
$\boldsymbol{K}_0$	Initial stiffness
K_c	Ratio of the second stress invariant on the tensile meridian to that on the compressive meridian at initial yield
k_{c0}	Plastic strain corresponding to the compressive strength
K_s	Secant stiffness

l_w	Wall length
m_c	Normalised strain increment beyond ε_c
N	Applied axial load
N_{Ed}	Design value of the applied axial force (tension or compression)
n_{xc}	Numbers of monitoring points in confined boundary region
n_{xun}	Numbers of monitoring points in the unconfined web region
n_y	Numbers of monitoring points along the element height
r_c	Non-dimensional material parameter
r_c	Normalised residual compressive strength
r_s	Normalised shear softening relative to direct tensile softening
s	Spacing of the stirrups
s_c	Non-dimensional material parameter
s_c	Normalised initial compressive strength
s_h	Centre-to-centre spacing of hoop sets
T	Tensile force
t	thickness
v_1	Strength reduction factor for concrete cracked in shear
V_n	Shear resistance in ACI code
$V_{Rd,c}$	Design value of the concrete shear resistance
w	Width of macro-element
w_c, w_t	Material properties governing the stiffness recovery from tension to compression and vice versa
w_c	Width of confined region in macro-element
z	Inner lever arm of a member with constant depth

Greek letters

α_c	Aspect ratio of a RC wall
α_{cw}	Coefficient accounting for the stress state in the compressive chord
β	Compression softening effect due to the presence of transverse tensile strain
β_c	Elastic shear retention factor
γ_{12}	Shear strain in the 1-2 cooridnate system
γ_c	Partial factor for concrete
$\boldsymbol{\varepsilon}$	Strain tensor
ϵ	Flow potential eccentricity
$\varepsilon_{\perp}$	Transverse tensile strain
ε_1, ε_2	Principal strains in 1- and 2- direction respectively
ε_{cr}	Cracking strain
$\bar{\varepsilon}_{\mathrm{p}}$	Cumulative equivalent plastic strain
$\boldsymbol{\varepsilon_p}$	Plastic strain tensor
$\dot{\boldsymbol{\varepsilon}}_{\boldsymbol{p}}$	Plastic strain rate
ε_{pl}	Plastic strain
ε_x, ε_y	Normal strains in x- and y- direction respectively
γ_{xy}	Shear strain in x-y coordinate system
θ	Angle between the concrete compressive strut and the beam axis perpendicular to the shear force
$\boldsymbol{\kappa}$	Historical variables
κ_c, κ_t	Plastic strain-driven historical variables for compression and tension
λ	Modification factor to reduce expected performance of lightweight concrete relative to normal weight concrete
λ	Scaling factor (plastic multiplier)
μ	Parameter controlling unloading stiffness in tension

μ_s	Strain hardening factor of steel
ν	Poisson's ratio
ρ_{be}	Longitudinal steel reinforcement ratio
ρ_c	Ratio of k_{co} at onset of compressive damage
ρ_h	Horizontal web reinforcement ratio
ρ_l	Reinforcement ratio for longitudinal reinforcement
ϱ_s	Volumetric reinforcement ratio of the hoops in the concrete core measured to the outside of the hoops
ρ_{sx}, ρ_{sy}	Reinforcement ratios in x- and y- directions
ρ_t	Transverse reinforcement ratio
ρ_{trv}	Transverse steel reinforcement ratio
ρ_v	Vertical web reinforcement ratio
σ	Cauchy stress
$\bar{\sigma}$	Effective stress
$\boldsymbol{\sigma}$	Nominal Cauchy stress tensor
$\bar{\boldsymbol{\sigma}}$	Effective stress tensor corresponding to the physical stresses developed in the undamaged material
σ_c	Current compressive strength of concrete
σ_{cp}	Compressive stress in the concrete from axial load
σ_x, σ_y	Normal stresses in x- and y- direction respectively
σ_y	Yield strength
τ_{xy}	Shear stress in x-y coordinate system
Φ_c	Factor scaling direct tensile stresses for shear interaction
ψ	Dilation angle

Vectors and matrices

$\{d\}$	Element nodal displacement vector
$\{f\}$	Nodal resistance force vector
$\{f_c\}$	Nodal resistance force vector due to concrete contribution
$\{f_s\}$	Nodal resistance force vector due to steel contribution
$[k_t]$	Element tangent stiffness matrix
$[k_{tc}]$	Element tangent stiffness matrix due to concrete contribution
$[k_{ts}]$	Element tangent stiffness matrix due to steel contribution
$[K_T]$	Structural tangent stiffness matrix
$[N]$	Shape function matrix
$\{P\}$	Applied external load vector
$\{R\}$	Structural resistance force vector
$[T_\alpha]$	Transformation matrix
$\{u\}$	Element displacement field vector
$\{U\}$	Unknown incremental displacement vector
$\{\varepsilon\}_{12}$	Biaxial strain vector in the 1-2 coordinate system
$\{\varepsilon\}_{xy}$	Biaxial strain vector in the x-y coordinate system
$\{\sigma_c\}_{xy}$	Biaxial stress vector for concrete in the x-y coordinate system
$\{\sigma_s\}_{xy}$	Biaxial stress vector for steel in the x-y coordinate system

Abbreviations

1D, 2D, 3D	One-dimensional, two-dimensional and three-dimensional respectively
ACI	American Concrete Institute
AR	Aspect Ratio
BSI	British Standards Institution
CDPM	Concrete Damage Plasticity Model
CFT	Compression Field Theory
CSA	Canadian Concrete Code
CSMM	Cyclic Softened Membrane Model
CW	Coupled Wall
DBBC	Displacement-Based Beam-Column
DCH	Ductility Class High
DM	Damage Measure
DoF	Degree of Freedom
EC2, EC8	Eurocode 2, Eurocode 8
FA-STM	Fixed Angle-Softened Truss Model
FBBC	Forced-Based Beam-Column
FCM	Fixed Crack Model
FE	Finite Element
FEA	Finite Element Analysis
FSAM	Fixed-Strut-Angle-Model
FSAM	Fixed-Strut-Angle-Model
FW	Frame-wall
GP	Gauss Point
HHT	Hilber-Hughes-Taylor
IDA	Incremental Dynamic Analysis
IM	Intensity Measure

ITZ	Interfacial Transition Zone
MCFT	Modified Compression Field Theory
MVLEM	Multiple-Vertical-Line-Element model
NLTM	Nonlinear Truss Model
PARC	Physical Approach for Reinforced Concrete
RASTM	Rotating Angle Softened Truss Model
RC	Reinforced Concrete
RCM	Rotating Crack Model
SFI	Shear-Flexural-Interaction
SWM	Shear Wall Macro-element
TVLEM	Three-Vertical-Line-Element model
WC	Wide Column

Chapter 1

Introduction

1.1 Background and motivation

During the past decades, there has been a significant increase in the demand for using reinforced concrete (RC) in complex structural systems, such as high-rise buildings, bridges, dams, offshore oil and gas platforms, nuclear and liquefied gas containment vessels, and shell structures. Numerous RC structures have been built in earthquake-prone regions according to the codes of practice developed in periods when designers had limited knowledge in limiting structural damage induced by earthquakes and available strategies for disaster prevention were less advanced. In this respect, future earthquakes can cause significant social and economic disruptions to society. The performance objectives within the context of present codes include, among others, life safety, preservation of structural function, protection of building contents, minimum structural damage and reduced economic losses. Existing RC buildings need to be assessed and potentially retrofitted to achieve these goals.

In the current seismic engineering practice, the simplest and most commonly used approach for seismic analysis is based on linear analysis procedures with a single behaviour factor, which accounts for the ductility of the structure to reduce the force demand. Evidence from past seismic events suggests that this basis may result in conservative design. Furthermore, this method can be suitably applied to regular structures, where the expected inelastic deformations are uniformly distributed, but can be inaccurate for more complex structural forms, for example, a RC building featured in irregularities where the response is affected by the contribution of the higher modes.

There is a considerable amount of study investigating the structural response of RC buildings not designed to resist seismic loadings. Recent advancements in the nonlinear finite element (FE) method enable RC structures to be assessed in detail also under earthquake loading conditions. In addition, detailed FE models have been widely employed as reliable tools for numerical experiments that can readily simulate physical tests. In past years, modelling approaches have been progressively developed, shifting from elastic static analysis to dynamic elastic, nonlinear static and finally nonlinear dynamic analysis. This enables structural responses to be obtained by more reliable numerical predictions. However, nonlinear dynamic analysis is not commonly used in design practice and is limited to buildings of unusual importance or those with innovative earthquake protection techniques due to its considerable computational demands. Besides, nonlinear analysis methods pose challenges to engineers in accurately modelling the inelastic material behaviour and potential geometric nonlinearity.

The design of new buildings and retrofitting of existing sub-standard buildings often use RC shear walls, which play a crucial role in providing suitable lateral strength, stiffness and energy dissipation capacity to limit lateral displacements during a service-level earthquake and reduce damage on less ductile components during severe earthquakes. Nonetheless, concrete as a cohesive-frictional material exhibits complex nonlinear inelastic behaviour when subjected to various loading situations due to its heterogeneous and composite nature. Under severe seismic loading, the response of RC walls is affected by highly nonlinear phenomena, including cracking and crushing of concrete, spalling of concrete cover, yielding and pull-out of steel bars in tension, and buckling of reinforcement under compression.

The complex behaviour of RC walls under seismic loading has driven the development of advanced computational modelling strategies, which rely on adequate concrete constitutive models for representing the response under multiaxial stress states. Available modelling strategies for RC walls belong mainly to two groups: detailed FE models and beam or macro-element models. The former approach utilises computationally expensive 2D shell elements (Dashti, *et al*., 2017; Kolozvari *et al*., 2019; Lu *et al.,* 2015; Polak & Vecchio, 1993; Tripathi *et al*., 2020) or 3D solid elements (Spiliopoulos & Lykidis, 2006; Zienkiewicz *et al*., 2005) equipped with accurate material relationships to represent material nonlinearity in concrete and steel. In general, detailed 2D or 3D FE models can provide realistic response predictions, but the computational cost is prohibitive due to the high level of detail and sophistication involved.

In contrast, simplified models, for example, models with fibre beam-column elements (Spacone, *et al*., 1996; Zienkiewicz & Taylor, 2005) or macro-elements with multiple springs (Kabeyaswa *et al*., 1983; Massone, *et al*., 2006; Orakcal, *et al*., 2004; Vulcano*, et al*.,1988) or truss elements

(Kolozvari *et al*., 2018; Panagiotou *et al*., 2012) are much more efficient. They are commonly based on simplified assumptions for element kinematics, offering simplicity in numerical modelling. However, these methods involve crude approximations of the planar response, i.e., the internal stress distribution resulting from compatible axial, shear, torsional and flexural strains. Towards striking a balance between computational efficiency and modelling accuracy, it is necessary to develop an appropriate modelling strategy for RC walls.

1.2 Research aims and scope

This study enriches research efforts toward a more realistic seismic analysis of RC multi-storey buildings equipped with shear walls. The primary aim of the research is to develop an accurate and efficient modelling strategy for RC shear walls with rectangular cross sections under in-plane lateral cyclic loading conditions. The developed numerical description for RC walls is to be implemented into the advanced nonlinear finite element analysis program ADAPTIC (Izzuddin, 1991) developed at Imperial College for nonlinear static and dynamic analysis of structures subjected to extreme loading.

The main objectives of the research are defined as follows:

- Evaluation of the existing modelling strategies for RC walls. They include (i) simple 1D models with elasto-plastic beam-column elements, (ii) FE representations with nonlinear 2D shell elements and (iii) detailed nonlinear 3D FE models with solid elements with embedded bar elements. The accuracy, computational efficiency and robustness of these modelling approaches are to be assessed.
- Development of an accurate and efficient numerical 2D macro-element description. The developed macro-element should have flexible connectivity with framed building structures, for example, beams and columns and serves as a practical and efficient tool for RC wall representations.
- Development of an adequate biaxial concrete constitutive model to be incorporated into the macro-element. The material model should be simple and practical in formulation, computationally robust and accurate, and capable of representing the main behavioural characteristics of concrete under cyclic loading.
- Demonstration of model accuracy and numerical efficiency of the developed macro-element description. This is to be achieved by comparing the numerical predictions and

experimental results of RC walls with different aspect ratios and a RC coupled wall system subjected to cyclic loading.

- Investigation of seismic response of a realistic RC building with shear walls by employing the proposed numerical description. Focus is given to the investigation of the global structural response based on push-over analysis and dynamic time-history analysis following an incremental dynamic analysis (IDA) procedure.

1.3 Thesis outline

This thesis consists of seven chapters which are outlined as follows:

Chapter 1 introduces the background of this work and summarises the main research objectives.

Chapter 2 presents a literature review relevant to this research. The chapter starts with the previous research on RC walls, including their fundamental role in RC buildings, the cyclic response characteristics, the related failure modes and the shear strength calculation prescribed in current codes. This is then followed by summarising the recent developments in numerical modelling strategies and related cyclic constitutive models for RC walls, of which the advantages and limitations are commented on.

Chapter 3 gives a critical appraisal of the existing modelling strategies in ADAPTIC to analyse RC walls under monotonic and cyclic loading conditions. The ability of the different models to predict the structural response is investigated, focusing on numerical accuracy and computational efficiency. Subsequently, the merits and limitations of these modelling approaches are discussed, which paves the way to developing an accurate and efficient modelling strategy for RC walls.

Chapter 4 describes the development of a novel 2D macro-element formulation accounting for shear deformation for simulating RC walls under cyclic loading. A concrete biaxial material model based on the rotating crack approach is developed and incorporated into the macro-element formulation. The macro-element is verified firstly at the material point level and then at the element level. The influence of the input material parameters on the response predictions is investigated, providing a foundation for the subsequent validation studies.

Chapter 5 presents validation studies by employing the proposed macro-element and considering building components, including experimental RC wall specimens with different aspect ratios and a RC coupled wall system under cyclic loading. The impact of confinement imposed by transverse reinforcement and the number of loading cycles is analysed in the simulation of a slender wall sample. For the modelled RC walls, comparisons are made between the numerical predictions and experimental findings in terms of the global structural response, cumulative energy dissipation, and secant stiffness degradation. The RC coupled wall is analysed using macro-element and beam element representations.

Chapter 6 demonstrates the practical application of the proposed macro-element by analysing a realistic four-storey RC building with shear walls. The numerical results from push-over analysis predicted by the macro-element model and the wide column model are compared. Nonlinear dynamic time-history analysis is then performed to investigate the frame-wall building response to earthquakes. Finally, parametric assessment is conducted following an incremental dynamic analysis procedure to provide a more comprehensive picture of the global building response.

Chapter 7 summarises the main achievements providing final remarks. Recommendations are also made for future works on nonlinear modelling of RC walls.

Chapter 2

Literature Review

2.1 Introduction

During the past decades, there has been considerable research devoted to the investigation of the nonlinear response of RC walls. One of the primary aims was to develop efficient modelling approaches for RC walls subjected to earthquake loading. This chapter starts with a brief review of RC walls, including their critical role in RC buildings, the response characteristics under cyclic loading, the associated failure modes, and the current code provisions for shear. The following section outlines recent developments in the numerical modelling approach for RC walls under cyclic loading representing seismic actions. Existing modelling strategies available in the literature are grouped as: the wide column analogy, macro-element models and detailed FE descriptions. The merits and limitations of these modelling techniques are discussed in this chapter. Subsequently, constitutive models for concrete material subjected to cyclic loading are reviewed. They include advanced concrete damage plasticity and smeared crack-based models adopting the rotating and fixed crack approach. This chapter concludes by summarising previous research findings and pointing out the limitations of current numerical descriptions for RC walls. This provides the context for the numerical investigations and the novel developments carried out in this research, which will be presented and discussed in the subsequent chapters.

2.2 RC walls

2.2.1 Fundamental role in buildings

RC walls, also known as shear walls, are widely used in multi-storey buildings in areas of moderate-to-high seismic activity. Such components generally provide building structures with considerable stiffness, strength, and ductility, which are critical characteristics to achieve suitable seismic performance. Design codes (EC8, BSI, 2004) define a wall as a vertical element with an elongated cross section, for which the long-to-short dimension is greater than four to distinguish it from a column. The fundamental role of RC walls is transferring the seismic actions from roofs and floors to the ground foundation. In a building system, shear walls possess in-plane stiffness significantly greater than their connected beams. Walls are assumed as the main structural components to resist earthquake loads carrying a significant amount of the total base shear. They resist lateral forces primarily in the direction parallel to the long edge of the section. On the other hand, the framing beams and columns often act as secondary seismic resisting elements representing a second line of defence to the building in case of the development of significant damage in the walls.

In designing new building structures, RC buildings consisting exclusively of frames with a high degree of ductility pose primary design and construction challenges in most cases. EC8 (BSI, 2004b) puts forward capacity design provisions to avoid brittle shear failures in the frame components promoting the development of a global plastic mechanism, which guarantees an effective dissipation of the energy supplied by earthquake ground motions. A typical damage pattern observed in RC frame buildings subjected to earthquakes and not designed according to modern seismic codes is the soft-storey mechanism due to the inherent weakness of columns without proper detailing. This may result in the local failure of one storey due to the high ductility demand incurred or even total structural collapse.

To prevent the formation of a soft-storey, a recommended rule is following the weak-beam strong-column design, which ensures that the flexural capacity of the columns is greater than that of the connected beams at the beam-column joints. This requires the columns to have comparable dimensions against the major bending axis compared to beams, which are usually difficult to implement in the two orthogonal plan directions (Elghazouli, 2016). To this end, the use of walls in a new building is evidently one of the practically feasible and cost-effective solutions to prevent the formation of soft-storey mechanisms providing adequate earthquake resistance, especially for medium and high-rise constructions.

The seismic behaviour of buildings equipped with shear walls is usually more reliable than bare frame buildings. In seismic design, the critical region (plastic hinge region) at the wall base is generally detailed with adequate flexural ductility, and closely spaced transverse reinforcements to well confine the boundary elements. Moreover, the capacity design procedure proposed by EC8 (BSI, 2004b) requires adequate shear resistance throughout the wall height. Besides, flexural over-strength is also required above the wall base, allowing inelastic deformations to develop in the critical region and the full formation of the plastic hinge at the base of the wall. This underpins the objective of capacity design to attain a controlled ductile structural response in a building to prevent collapse for a given design-level earthquake. Another advantage of using RC walls is that they retain most vertical load resistance regardless of extensive cracking, as pointed out by Kappos (2014). This provides additional axial load capacity to the original building structure, which can be beneficial to the overall strength of the bottom storey and prevent building collapse.

The inclusion of new shear walls is also one of the most common retrofitting strategies to enhance the seismic performance of existing sub-standard building systems. EC8 (BSI, 2004b) also prescribes damage limitation requirements under earthquake loads with a larger probability of occurrence than the seismic design action. The retrofitting solution with RC walls effectively controls the overall and inter-storey drifts, hence limiting damage and protecting other structural and non-structural components in frequent or occasional earthquake events (Thermou and Elnashai, 2006). RC walls are typically positioned at the perimeter of the building or form a shear core at the building centre. A favourable seismic behaviour can be achieved by ensuring structural regularity in plan and elevation (Penelis and Penelis, 2014). Therefore, the preferable in-plan arrangement of RC walls in a building is the symmetrical arrangement, allowing the centres of mass and stiffness to coincide and reducing the torsional effects. Vertical uniformity and continuity are also required to avoid non-uniform ductility demand and discontinuity of stiffness. This can be accomplished by adding uniform walls from the foundation to the top of the buildings without interruptions, as recommended by EC8 (BSI, 2004b).

2.2.2 Cyclic behaviours and failure modes

Numerous experimental studies conducted in the past have shown that the global response of RC walls under horizontal in-plane cyclic loads depends on their slenderness, commonly expressed in terms of the aspect ratio (AR), where AR is the height to length ratio h_w/l_w. A slender wall with high AR ≥ 2.0 typically exhibits a flexural-dominated behaviour. In contrast, the response of a short wall with low AR is governed by shear. The behaviour of an intermediate wall with moderate AR is characterised by a combined deformation mode of flexure and shear. Nevertheless, the literature does not clearly define a specific AR value for a shear wall to be classified as short. Canadian concrete code A23.3 (CSA, 2004) and EC8 (BSI, 2004b) have noted that RC walls with AR less than 2.0 tend to fail in shear, whereas the limiting value of AR for shear dominated response is defined as 1.5 according to ACI 318-19 (2019); Kolozvari, *et al*. (2015); and Tran (2012). The shear-flexure interaction is affected by several aspects, including the wall geometry, detailing of the cross section, material properties and imposed axial load.

As mentioned before, the basic seismic design principle for RC walls is to inhibit brittle shear failure for a considered level of design earthquake motion. A wall element is desirably designed to provide adequate shear strength to facilitate flexural yielding of steel reinforcement according to the capacity design principle in modern seismic design codes, for example, EC8 (BSI, 2004b) and ACI 318-19 (2019). The flexural resistance is provided by the longitudinal reinforcement confined by stirrups at the two far ends of the section, acting as tension and compression chords alternatingly under cyclic loading. On the other hand, the concrete and the horizontal reinforcement provide shear resistance in the unconfined web region between the two chords.

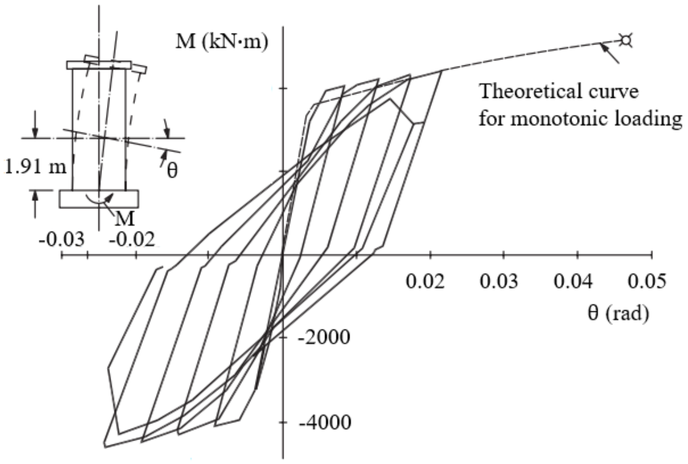

Figure 2-1: Hysteresis response of a structural wall dominated by flexure behaviour (Oesterle *et al*., 1980)

Figure 2-1 shows a representative cyclic response of a slender RC wall tested by Oesterle *et al*. (1980). The experimental moment-rotation relationship shows a stable form of hysteresis loops without pinching characteristics. The response is similar to that bending response of a beam, provided that the longitudinal reinforcement in the wall boundary elements is appropriately designed with sufficient confinements.

Whenever the shear reinforcement is adequate, a slender wall with flexural-dominated behaviour is likely to exhibit ductile failure, as illustrated in Figure 2-2(a), where the tensile steel reinforcement yields along with wide cracks forming in the tensile chord near the fixed base and large deflections develop at the top of the wall. If the tensile region is over-reinforced, the wall can also exhibit a brittle failure mode (Figure 2-2(c)), where concrete crushes at the compressive toe, accompanied by possible buckling of the longitudinal steel bars.

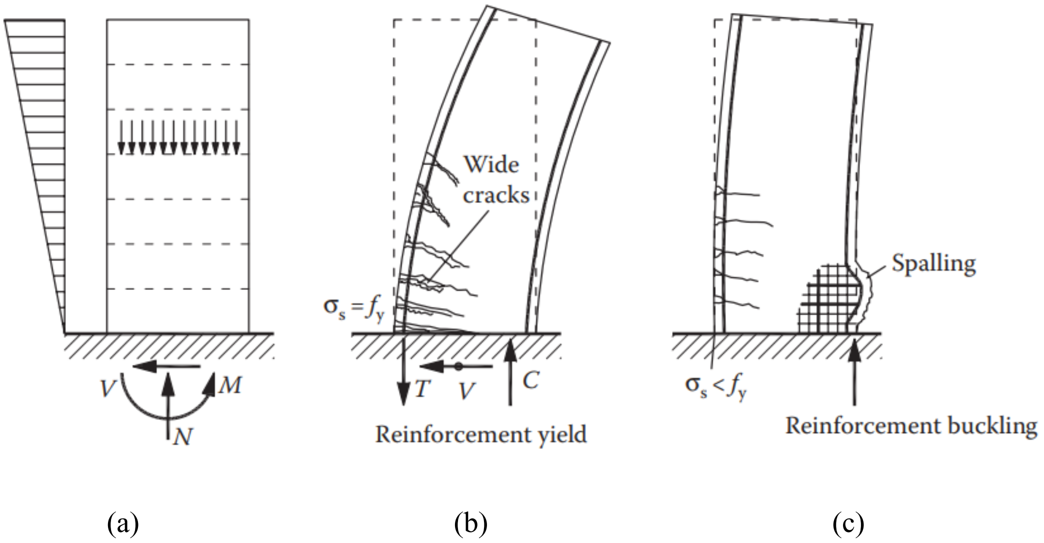

Figure 2-2: Flexural failure modes of slender walls: (a) loading patterns; (b) ductile failure; (c) brittle failure (Penelis & Penelis, 2014)

RC short walls are commonly used in low-rise constructions and at the lower levels of tall buildings. Figure 2-3 gives an example of the cyclic response of a RC wall under prevailing shear (Paulay & Priestley, 1992), where the hysteresis loops are characterised by highly pinched shapes. The response also exhibits rapid loss of strength and stiffness under reversed loading cycles. Therefore, the extent of pinching in the overall load-displacement cyclic curve indicates the contribution of shear deformation and degradation.

Paulay *et al.* (1982) reported typical shear failures observed in short walls, namely diagonal tension, diagonal compression and sliding shear failures. A diagonal tension failure occurs when the horizontal shear reinforcement is insufficient. The damage pattern of this failure mode is displayed in Figure 2-4(a). In the physical tests carried out by Hidalgo *et al.* (2002), the wall specimens failed in diagonal tension showing wide inclined cracks for each loading direction, which developed into corner-to-corner failure planes inclined at 45° to the horizontal direction. Diagonal tension failure can be suppressed by providing adequate shear reinforcement to carry a shear force larger than that associated with the developed plastic hinge at the base of the wall allowing also for flexural over-strength.

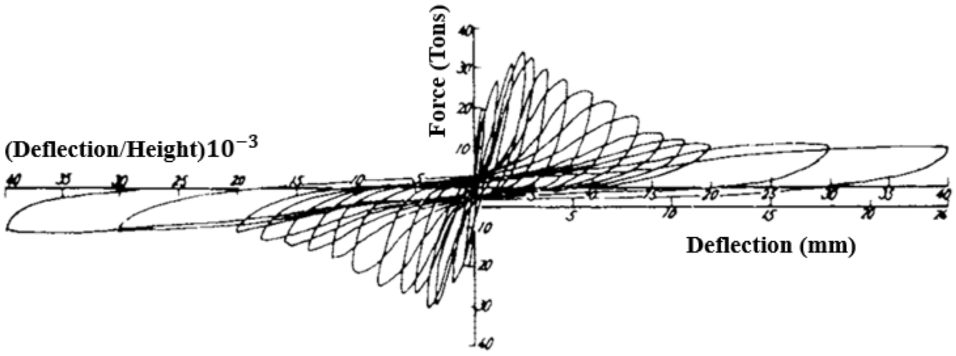

Figure 2-3: Hysteresis response of a structural wall dominated by shear behaviour (Paulay & Priestley, 1992)

In a short wall with sufficient web shear reinforcement, diagonal compression failure may be triggered by the crushing of the concrete compressive strut, as shown in Figure 2-4(b). Walls with barbells or flanges are more susceptible to diagonal compression failure than those with rectangular cross sections (Kappos, 2014). They can accommodate more longitudinal reinforcement in the boundary elements, which offers considerable flexural strength and, as a result, impose higher shear demands on the wall web. The concrete strength degradation induces this diagonal compression failure mode due to diagonal intersecting cracks opening and closing under reversed cyclic loading. The diagonal compression failure is essentially more brittle than the diagonal tension failure since it is related to concrete crushing instead of steel reinforcement yielding. Penelis & Penelis (2014) stated that diagonal compression strength may also deteriorate due to loading reversals in the plastic hinge region at the wall base. This is reflected in EC8 (CEN, 2004), where a reduction factor is applied to the design shear resistance against diagonal compression failure in the wall web.

Sliding shear failure may appear in heavily reinforced short walls under low levels of axial loading and high levels of shear stress. Walls failing in sliding shear initially experience inclined shear cracking followed by strength degradation of concrete between these cracks by increasing the number of loading cycles. Eventually, concrete crushing and spalling spread over the wall base and concentrate in a narrow band, as depicted in Figures 2-4(c) and (d). The upper portion of the wall slide on a weakened horizontal plane, leading to a drastic reduction of stiffness and energy dissipation capacity. Shear sliding can be resisted by dowel action of the vertical bars, shear friction across the horizontal cracks and shear resistance by the inclined steel bars arranged at the base of the wall.

In most cases, RC walls exhibit complex behaviour, especially under seismic loading conditions. They may feature mixed failure modes, such as the sliding shear-flexure failure shown in Figure 2-4(e). The wall behaviour is initially controlled by flexure since, by design, the shear resistance is typically higher than the shear force associated with the flexural strength. However, by increasing the amplitude of the horizontal cyclic displacements, the wall shear strength degrades below its flexural strength limit dominating the wall response up to collapse.

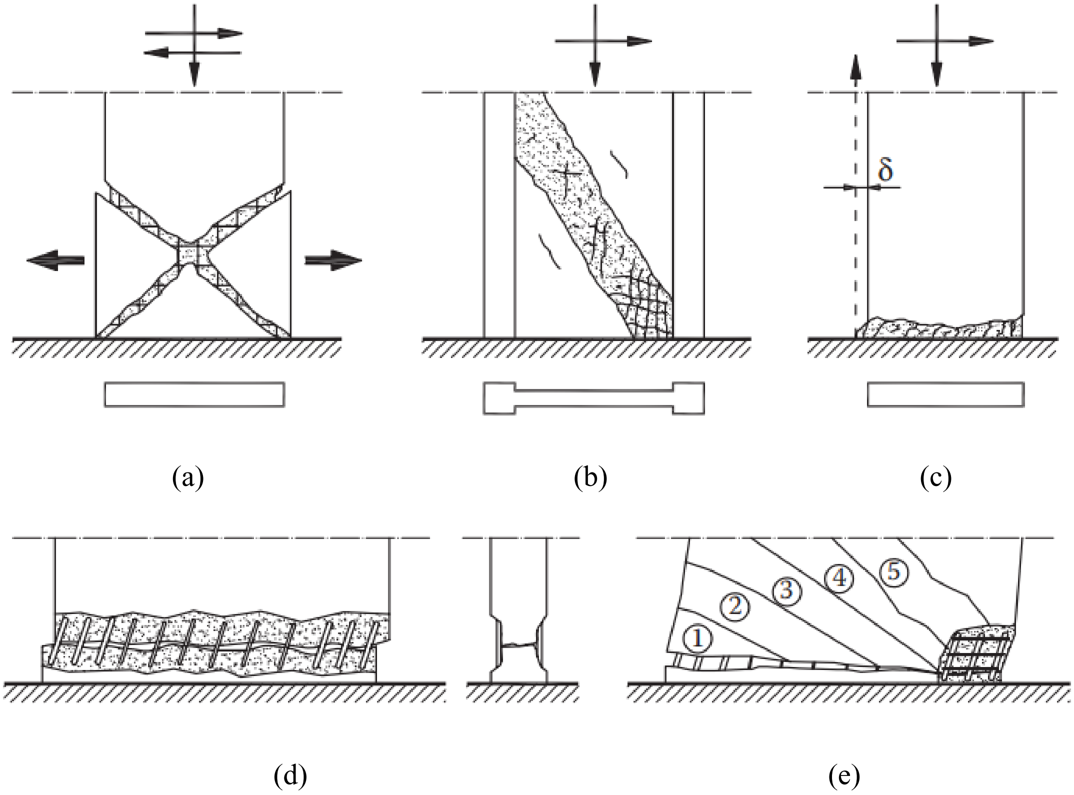

(a) (b) (c)

(d) (e)

Figure 2-4: Shear failure modes of walls: (a) diagonal tension; (b) diagonal compression; (c) sliding shear; (d) detail of sliding shear; (e) sliding shear-flexure failure (Penelis & Penelis, 2014; Salonikios, 2007)

2.2.3 Code provisions

2.2.3.1 EC2

EC2 (BSI, 2004a) prescribes that the design value of the shear resistance $V_{Rd,c}$ for RC walls should be calculated according to EC2 (BSI, 2004a), in which the $V_{Rd,c}$ can be determined for members with or without shear reinforcement. The design shear strength for members not requiring shear reinforcement prescribed by EC2 (BSI, 2004a) is given by:

$$V_{Rd,c} = \left[C_{Rd,c}k(100\rho_l f_{ck})^{1/3} + k_1\sigma_{cp}\right]b_w d \tag{2-1}$$

with a minimum of:

$$V_{Rd,c} = \left(v_{min} + k_1\sigma_{cp}\right)b_w d \tag{2-2}$$

where:

f_{ck} is the concrete characteristic cylindrical strength;

$k = 1 + \sqrt{\frac{200}{d}} \leq 2{,}0$;

$\rho_l = \frac{A_{sl}}{b_w d} \leq 0.02$;

$\sigma_{\mathrm{cp}} = N_{\mathrm{Ed}}/A_{\mathrm{c}} < 0.2 f_{\mathrm{cd}}$

A_{sl} is the tensile reinforcement area that extends ≥ $(l_{bd} + d)$ beyond the section considered as shown in Figure 2-5;

b_w is the cross-sectional minimum width in the tensile zone;

d is the effective depth of the cross section;

N_{Ed} is the axial force due to loading or prestressing ($N_{Ed} > 0$ for compression);

A_{c} is the gross cross-sectional area of concrete;

$C_{Rd,c}$, k_1 and v_{min} depend on National Annex. Recommended values are:

$C_{Rd,c} = 0.18/\gamma_c$;

$k_l = 0.15$;

$v_{min} = 0035 k^{3/2} \cdot f_{ck}^{1/2}$.

γ_c is the partial safety factor for concrete according to EC2 (BSI, 2004a), Clause 2.4.2.4, Table 2.1N, where $\gamma_c = 1.5$ for persistent and transient actions, and $\gamma_c = 1.2$ for accidental actions.

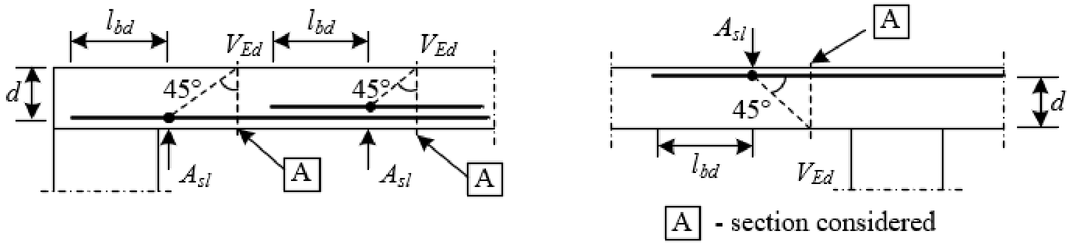

Figure 2-5: Definition of A_{sl} in calculating shear resistance of members without shear reinforcements in EC2 (BSI, 2004a)

For RC members with shear reinforcement, EC2 (BSI, 2004a) employs a variable inclination truss model (Figure 2-6) to calculate the design shear resistance as follows:

$$V_{Rd,s} = \frac{A_{sw}}{s} z f_{ywd} cot\ \theta \tag{2-3}$$

and

$$V_{\mathrm{Rd},max} = \frac{\alpha_{\mathrm{cw}} b_{\mathrm{w}} z v_1 f_{\mathrm{cd}}}{\cot\theta + \tan\ \theta} \tag{2-4}$$

where:

A_{sw} is the cross-sectional area of the shear reinforcement;

s is the spacing of the stirrups;

z is the inner lever arm of a member with a constant depth, corresponding to the considered bending moment in the element; $z = 0.9d$ is typically used in the shear analysis of RC member without axial force;

f_{ywd} is the design yield strength of the shear reinforcement;

θ is the angle between the concrete compressive strut and the beam axis perpendicular to the shear force. The recommended limiting values of $cot\ \theta$ are given by $1 \leq \cot\ \theta \leq 2.5$ according to National Annex.

α_{cw} is a coefficient accounting for the stress state in the compressive chord. National Annex recommends using the value of 1.0 for non-prestressed structures;

b_{w} is the minimum width between compressive and tensile chords;

v_1 is a strength reduction factor for concrete cracked in shear; For concrete with $f_{ck} \leq 60$ MPa, $v_1 = 0.6$.

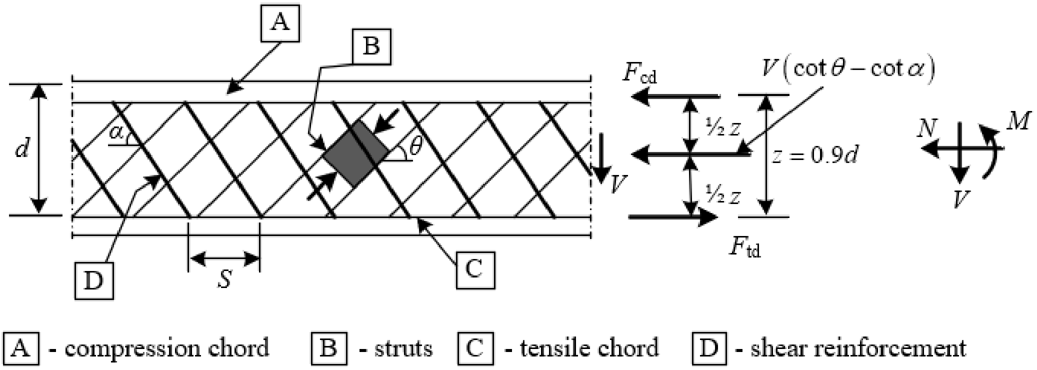

Figure 2-6: Truss model for shear reinforced members in EC2 (BSI, 2004a)

2.2.3.2 ACI 318

The U.S. design code ACI 318 (2019) provides a simpler equation to calculate the shear strength of RC walls. The shear resistance V_n accounts for the contributions of concrete and transverse shear reinforcements by the following:

$$V_n = \left(\alpha_c \lambda \sqrt{f_c'} + \rho_t f_{yt}\right) A_{cv} \tag{2-5}$$

where:

$\alpha_c = 3$ for $h_w/l_w \leq 1.5$;

$\alpha_c = 2$ for $h_w/l_w \geq 2.0$;

α_c varies linearly between 3 and 2 for $1.5 < h_w/l_w < 2.0$.

λ is the modification factor to reduce the expected performance of lightweight concrete relative to normal weight concrete;

f_c' is the specified compressive strength of concrete;

ρ_t is the transverse reinforcement ratio;

f_{yt} is the yield strength of transverse reinforcement;

A_{cv} is the gross area of the section resisting shear.

An upper limit $8\sqrt{f_c'}A_{cv}$ is imposed on the shear strength V_n to prevent potential diagonal compression failure. It is noted that ACI 318 (2019) considers increased shear resistance of short walls with AR$\leq$ 1.5 by specifying the concrete contribution $3\lambda\sqrt{f_c'}A_{cv}$. By contrast, the design for members with shear reinforcement according to EC2 (BSI, 2004a) only accounts for the shear resistance provided by horizontal reinforcement. Nevertheless, EC8 (BSI, 2004b) prescribes equations for designing ductile walls against diagonal tension and sliding shear failures for DCH buildings considering the contribution of horizontal web reinforcement and inclined bars.

2.3 Modelling strategies for RC walls

2.3.1 Wide column model

MacLeod (1973) proposed a simplified modelling strategy for RC walls utilising beam-column elements to represent RC walls in frame-wall structural systems. According to this strategy, often referred to as wide column analogy, the employed beam-column element called equivalent column is placed at the centreline of the physical wall and connected to the beams at each floor level by rigid links, as shown in Figure 2-7. The cross section of the 1D element can be assigned with specific properties to reflect the actual wall geometry. On the other hand, the horizontal rigid links have a length corresponding to the actual length of the wall.

Typically, the wide column approach for RC walls employs fibre-type beam-column force-based (Spacone *et al.*, 1996) or displacement-based elements (Zienkiewicz & Taylor, 2005). These elements incorporate multiple fibre sections at assigned locations within the element. In this respect, distributed plasticity is accounted for by determining the element response from numerical integrations of the fibre section responses. At each fibre section, material nonlinearity is considered by adopting specific uniaxial cyclic stress-strain relationships for concrete and steel reinforcement associated with the monitoring areas. Figure 2-8 shows a typical RC wall modelled by a forced-based beam-column (FBBC) element and a mesh of displacement-based beam-column (DBBC) elements. The FBBC element aggregates the response at the section level; therefore, it does not require mesh refinement at each storey for achieving accurate response predictions. By contrast, the DBBC element requires using a set of elements for each inter-storey height portion of the wall to reasonably capture the associated nonlinear curvature distribution.

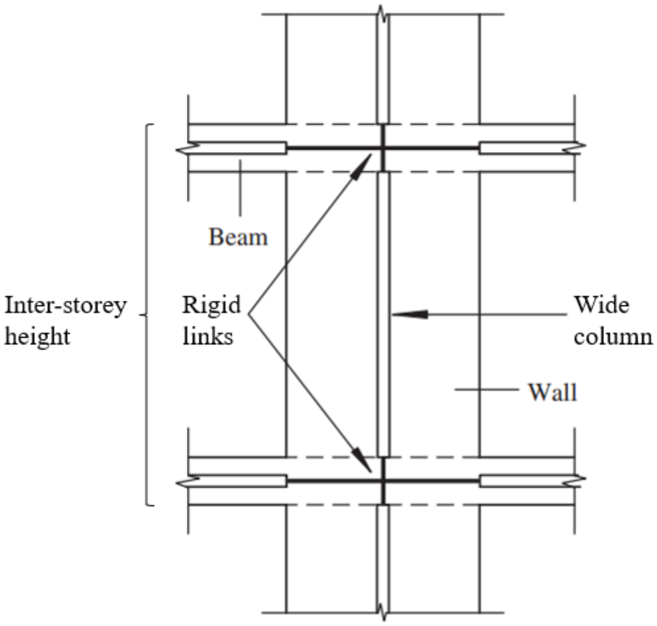

Figure 2-7: Wide column and rigid links for modelling a RC wall in frame-wall system

Martinelli & Filippou (2009) employed the FBBC element to simulate the nonlinear dynamic response of a full-scale seven-storey RC shear wall building under shaking table excitations representing earthquake ground motions. In this research, it was pointed out that the FBBC element is suitable for modelling RC walls with medium to high slenderness dominated by flexural behaviour with negligible shear effects. The fibre beam-column element is typically formulated based on the Euler–Bernoulli hypothesis, which assumes that plane sections remain plane and the influence of shear is neglected.

To overcome this limitation, attempts were made to account for shear deformation in the fibre beam-column element model. In a DBBC model, a shear spring (Figure 2-8) can be introduced in series with the beam elements at the wall bottom. Pugh (2012) utilised this strategy to simulate the wall response under cyclic loading, but the focus was placed on slender walls exhibiting predominantly flexural deformations. In the FBBC model (Figure 2-9), shear response models are commonly employed at the section level to represent the shear flexibility (Pugh *et al.*, 2015; Vásquez *et al.*, 2016). The FBBC formulation incorporates iterative procedures in the intra-element solution to obtain the element force associated with nodal displacements satisfying compatibility requirements between elements, as required by displacement-based FE analyses. In this respect, convergence issues may arise in the intra-element solution of FBBC models if strength degradation is rapid, as pointed out by Pugh *et al.* (2015). In addition, the uncoupled flexural and shear behaviour is a major limitation, although the fibre beam-column element achieves a good compromise between accuracy and computational efficiency.

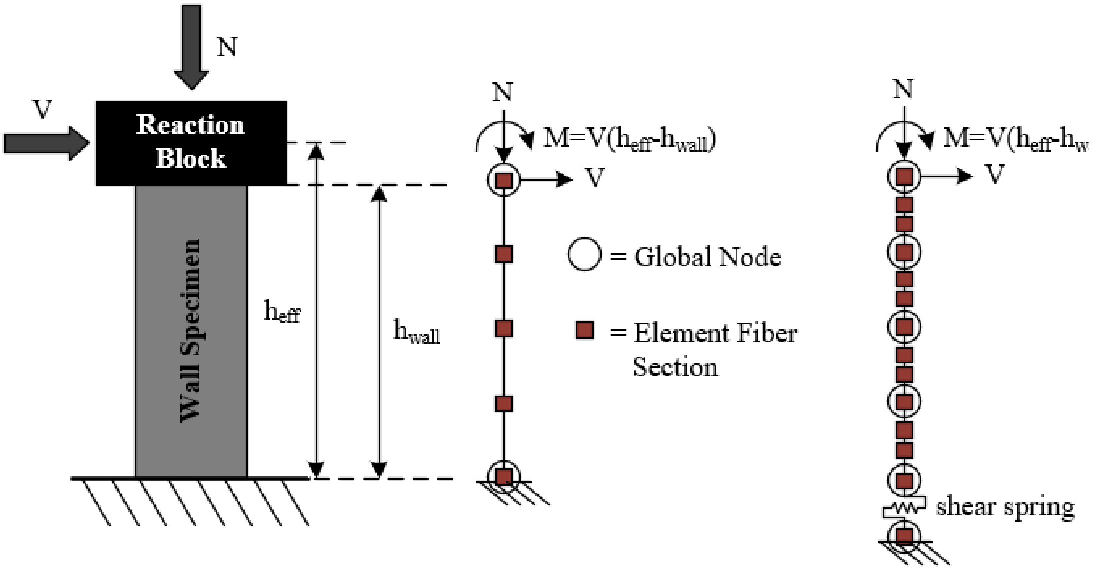

Figure 2-8: Typical RC wall (left) represented by fibre beam-column elements: forced based (centre) and displacement-based (right)

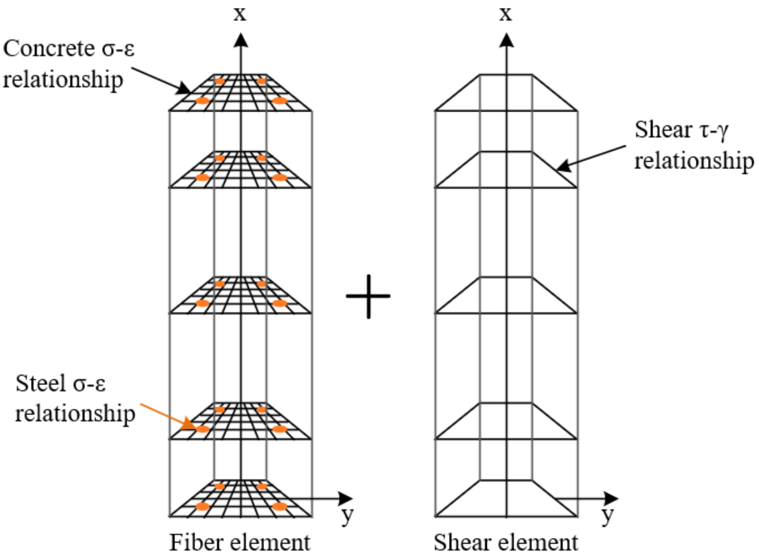

Figure 2-9: Schematic of a typical FBBC element

2.3.2 Macro-element models

Macro-elements with a reduced number of degrees of freedom represent computationally efficient tools to model RC wall components. In general, a series of nonlinear springs, multiple line or truss elements with specific constitutive models for concrete and reinforcing steel are adopted for describing the nonlinear response under generic loading conditions.

Kabeyaswa *et al.* (1983) proposed a Three-Vertical-Line-Element model (TVLEM) to effectively describe the shear walls of a full-scale seven-storey RC building in a shaking table test. As illustrated in Figure 2-10, the TVLEM idealises a RC wall portion as three vertical springs connected to an infinitely rigid beam at the floor level. In the TVLEM formulation, force-based hysteresis rules are adopted to account for axial, flexural and shear hysteretic behaviour. The two exterior vertical springs describe the axial stiffness of the confined boundary regions, whereas the interior vertical spring model the axial stiffness of the unconfined web region. The shear and flexural behaviour of the wall web is represented by shear and rotational springs. In this respect, the flexural and shear responses of the model are uncoupled. Besides, the model assumes that the moment distribution is uniform (thus constant curvature) over each inter-storey height in a frame-wall system. Kabeyaswa *et al.* (1983) demonstrated that the TVLEM well predicts the main features of the hysteresis behaviour of a RC wall except for the shear deformations. Nevertheless, this model was developed based on specific experimental data and required detailed calibration of the spring properties, which renders its general application difficult.

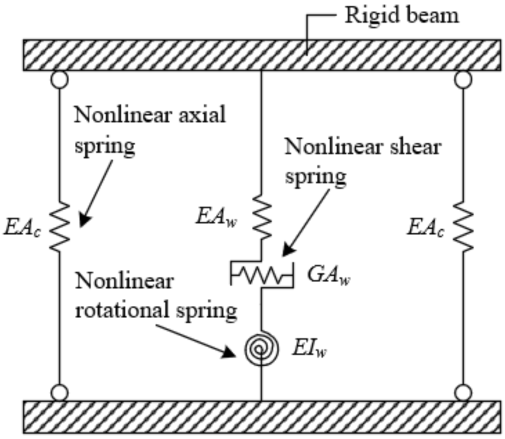

Figure 2-10: Three vertical line element model (TVLEM; Kabeyaswa *et al.* 1983)

Vulcano *et al.* (1988) developed the Multiple-Vertical Line Element model (MVLEM) based on a geometrical modification of the TVLEM incorporating refined hysteretic relationships for the nonlinear springs. Figure 2-11 shows the characteristics of the MVLEM, which is typically used to represent a vertical portion of a RC wall. This allows the use of a refined mesh consisting of a stack of springs placed on top of each other to define an RC wall at a single storey level. The two external springs represent the axial stiffness of the confined region. At least two longitudinal springs are employed to model the axial and flexural responses of the central panel. The rotational spring in the original TVLEM is replaced by multiple vertical springs in the MVLEM, which overcomes the inherent incompatibility of the TVLEM. On the other hand, the original horizontal spring located at the centre of rotation of the wall component is maintained to model the shear behaviour.

Although the MVLEM offers an improved representation of RC wall components, calibration is still required to select a suitable location for the centre of rotation and the position of the horizontal spring. Furthermore, a further shortcoming of the MVLEM, as stated by Wu *et al.* (2017), is that the adopted hysteresis laws are associated with somewhat arbitrary parameters depending on engineering judgement. To address this limitation, Orakcal *et al.* (2004) modified the MVLEM by adopting improved constitutive cyclic relationships for concrete and steel reinforcement to capture the flexural behaviour instead of the conventional force-based hysteresis rules for the vertical springs. The shear behaviour is modelled by linear elastic horizontal springs. The model showed good agreement between experimental and numerical results for slender wall specimens. However, such a model leads to approximate results when applied to the analysis of walls whose response is governed by shear flexural interaction in the concrete.

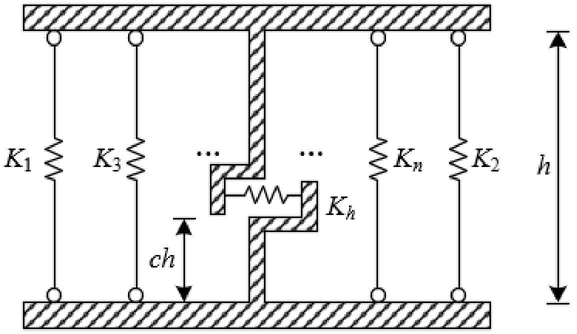

Figure 2-11: Multiple vertical line element model (MVLEM; Vulcano, Bertero and Colotti 1988)

In subsequent research, Massone *et al.* (2006) developed an improved model by adding horizontal shear springs to each vertical element (Figure 2-12) to represent the membrane behaviour for a portion of the wall. In this respect, the shear flexural interaction is incorporated by coupling flexural and shear response at each set of horizontal and vertical springs. The stress-strain concrete material law based on the Rotating Angle Softened Truss Model (RA-STM; Belarbi & Hsu, 1995; Pang & Hsu, 1995) is implemented in the element to model the nonlinear behaviour of the concrete. However, validation studies performed by Massone *et al.* (2006)

addressed only the monotonic response of wall specimens. Numerical results obtained from monotonic analysis of slender walls led to accurate predictions of the envelope curves from experimental tests on walls subjected to cyclic loading. However, the numerical results obtained in the simulation of short wall specimens under high shear stresses were not as accurate as for slender walls.

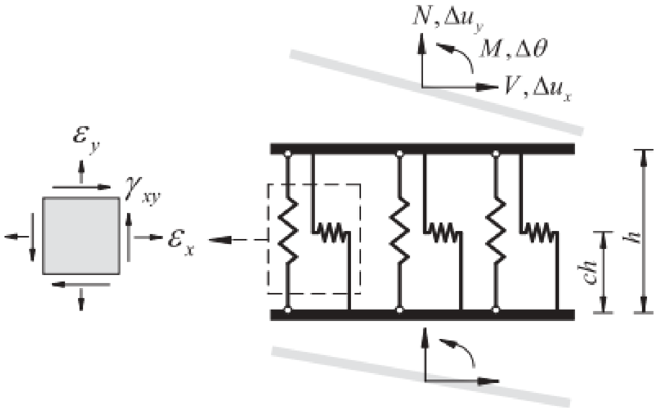

Figure 2-12: Modified MVLEM by Massone *et al.* (2006)

Kolozvari *et al.* (2015) further improved the MVLEM and developed a Shear-Flexural-Interaction Multiple-Vertical-Line-Element Model (SFI-MVLEM). This model replaces the uniaxial element in the original MVLEM with an RC panel element under membrane actions, including normal and shear stresses, as illustrated in Figure 2-13. The cyclic response of each RC panel is described using the Fixed-Strut-Angle-Model (FSAM) developed by Ulugtekin (2010) and extended by Orakcal *et al.* (2012), incorporating shear aggregate interlock effects. The SFI-MVLEM is conceptually similar to the original Massone's model and accounts for the shear flexural interaction at the RC panel level. It is also capable of simulating the cyclic response of RC wall specimens with slender and moderate aspect ratios.

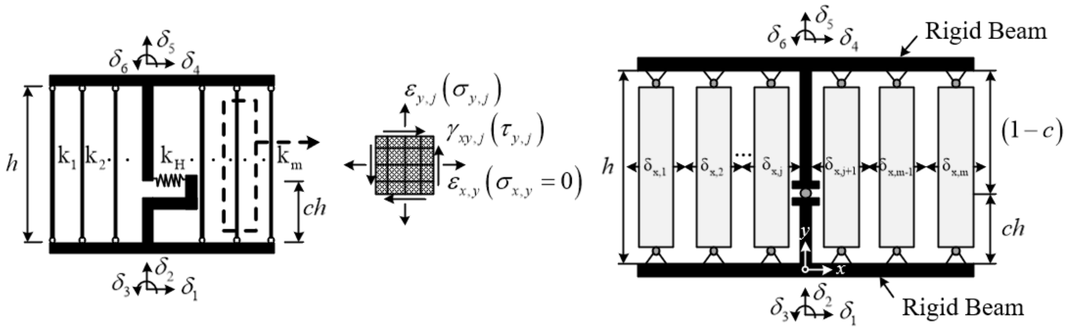

Figure 2-13: Shear-flexural interaction-multiple vertical line element model (SFI-MVLEM) (Kolozvari *et al.,* 2015)

The modelling of shear-flexural interaction was also addressed in the Nonlinear Truss Model (NLTM) proposed by Panagiotou *et al.* (2012). The model was developed based on the Strut-and-tie approach, where a RC wall is represented by horizontal, vertical, and diagonal truss elements. Figure 2-14 shows a typical NLTM describing a RC wall and the framing floor slabs. The parallel diagonal struts at a fixed inclination angle representing concrete follow only the principal compressive stress trajectories when reaching the ultimate load. The horizontal and vertical truss elements include the contributions of steel reinforcement and the surrounding concrete, where the exterior vertical elements correspond to the position of the longitudinal reinforcing steel at the far ends. Uniaxial cyclic uniaxial material models for concrete and steel are defined for the truss element, which allows for predicting the overall wall response with good accuracy.

Like most types of the shear wall macro-element, the NLTM can be generalised to the 3D analysis of non-planar RC walls. Lu *et al.* (2016) extended the 2D NLTM to 3D to simulate RC walls with complex cross-sectional geometry. The main modifications made to the 2D NLTM include the orientation of the diagonal truss elements and the concrete constitutive laws. In spite of its general applicability, some shortcomings of the NLTM are noted. Kolozvari *et al.* (2018) showed that the model typically overpredicts the initial stiffness and strength of wall specimens under cyclic loading, attributed to the overlapping areas introduced by the truss elements. Besides, shear strength and stiffness and the local element response depend on the inclination angle of the diagonal concrete strut and the mesh characteristics. This implies that the NLTM cannot be used for the simulation of RC walls under earthquake actions, where the principal compressive stress directions are expected to change under cyclic loading. Furthermore, this modelling approach has limited capability of predicting local failure modes, depending on appropriately determined truss element configuration.

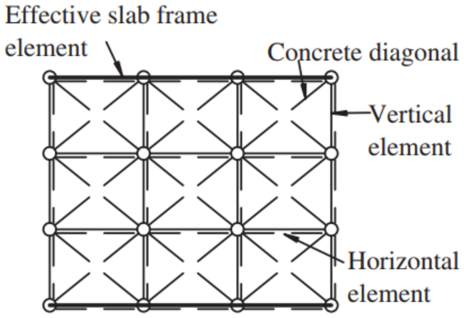

Figure 2-14: Nonlinear Truss Model (NLTM) representing an RC wall and framing slab (Panagiotou *et al.*, 2012)

2.3.3 Detailed FE models

In the past years, RC walls have also been investigated using detailed 2D or 3D finite element (FE) models using specific multidimensional constitutive relationships to represent concrete material. In this regard, this section aims to briefly present and critically discuss the results from some previous numerical studies where RC walls are modelled by meshes of 2D shell or 3D solid elements. A more detailed review of the available concrete constitutive models is given in Section 2.4.

Numerical simulations of RC walls using 3D solid elements are scarce in the literature. This is because of the significant computational efforts required in the analysis and the need of reliable and robust 3D constitutive models to simulate the complex triaxial stress state in the concrete. Spiliopoulos & Lykidis (2006) used 27-noded Lagrangian brick elements and 3-noded uniaxial truss elements to model concrete and steel reinforcement in a slender wall specimen under two reversed cycles. The numerical results exhibited poor predictions of energy dissipation. The authors pointed out that a model improvement allowing for bond-slip effects could potentially improve the response prediction.

Numerous 2D shell elements in the literature have been developed based on the layered approach (Hrynyk & Vecchio, 2015; Polak & Vecchio, 1993). The element thickness is discretised by several layers, each with a predefined number of Gauss points. The variations of material stress and stiffness over the shell element domain are considered at each layer. Steel reinforcements corresponding to specific layers arranged in the orthogonal directions are assumed as smeared. A single reinforcement layer acts as a uniaxial equivalent plate with uniform thickness. Typically, a perfect bond between concrete and steel reinforcement is assumed. Numerical integration of concrete and steel layer stresses is performed at the Gauss points over the element resulting in the element resistance force.

Polak & Vecchio (1993) adopted layered shell elements for analysing RC panels. Each shell element is characterised by nine nodes where eight side nodes have five degrees of freedom (DoF) each and the central node has two DoFs. Simple validations are conducted considering different imposed loads, including membrane, bending and out-of-plane shear loads. The numerical results under monotonic loading confirmed that the model can provide satisfactory accuracy.

More recently, multi-layered shell elements with specific bi-axial concrete cyclic constitutive models have been employed to simulate RC walls with different aspect ratios and complex cross-section shapes (Dashti *et al.*, 2017; Kolozvari *et al.*, 2019; Tripathi *et al.*, 2020). However, these previous numerical investigations focused on isolated wall specimens, as the large number of DoFs required and the associated high computational cost hinder their applications on large scale frame-wall systems.

2.4 Constitutive models for concrete under cyclic loading

2.4.1 Concrete damage plasticity models

2.4.1.1 Plasticity approach

The classical theory of plasticity, which was initially developed for modelling metals, was later employed also to represent the main nonlinear deformational characteristics of concrete. Although the typical behaviour of metals is different from the behaviour of concrete, some similarities can be observed mainly in the pre-failure macroscopy response, including the development of strain hardening under multi-axial compression and the irreversible strains upon unloading. In particular, some ductile behaviour is exhibited by concrete subjected to compression with confining pressure. The permanent deformations of concrete are attributed to the development of micro-cracks and slip, rendering the plasticity theory suitable.

The three essential assumptions involved in a plasticity model are: (i) a stress space-based initial yield surface that specifies the onset of plastic deformation under various loading conditions; (ii) a hardening rule that defines variations of the yield surface and work hardening of the material during the plastic flow; (iii) a flow rule associated with a plastic potential function, which relates the plastic deformations to the stress components (Chen, 1982). The hardening rule can be based on the kinematic hardening or isotropic hardening, depending on the evolution equations of the internal variables in the yield condition. Isotropic hardening involves a yield surface with changing size but the same shape upon plastic straining. In contrast, kinematic hardening considers a translation of the yield surface, which maintains the same size. Except for the assumptions mentioned above, it is necessary to introduce a failure criterion that serves as the upper limit of the current stress states in the plastic modelling of concrete.

In modelling concrete under cyclic loading conditions, the concept of bounding surface can be used (Abu-Lebdeh & Voyiadjis, 1993; Fardis & Chen, 1986; Voyiadjis & Abu-Lebdeh, 1994). The bounding surface, which remains unchanged under loading, encompasses all the changing loading surfaces. The initial yield surface with a closed shape expands and eventually develops into a failure surface. Chen & Buyukozturk (1985) proposed a rate-independent constitutive model for the behaviour of concrete under multiaxial cyclic compression. The model adopts a bounding surface depending upon the accumulated damage in the stress space, enabling the strength and deformation characteristics of the concrete material subjected to general loading conditions to be modelled. The nonlinear stress-strain response, stiffness degradation under cyclic loading, and the post-peak strain softening response are satisfactorily represented.

2.4.1.2 Damage approach

Damage-based concrete models formulated following continuum damage mechanics principles have been used in the past decades to model the nonlinear response of concrete. They represent the actual microstructural changes in concrete under different mechanical and environmental conditions, representing complex phenomena such as creep, fatigue, chemo-mechanical reactions and environmental degradation (Kachanov, 1986). The onset, propagation and coalescence of micro-cracks in the cement matrix around aggregates (Panoskaltsis *et al.*, 1994) result in internal damage within zones with weak mechanical resistance. Damage-based models can represent the formation and expansion of these micro-cracks, whose propagation and coalescence determine the reduced strength and deteriorated mechanical properties of concrete.

The underlying notion of continuum damage mechanics is to model the damaged material state with suitable mechanical variables. These internal state variables evolve during the loading process, which is described by mathematical equations representing the mechanical behaviour of the damaged materials. The principle of a uniaxial continuum damage model can be illustrated by considering a uniform bar subjected to uniaxial tensile stress, as shown in Figure 2-15. The size of this bar is deemed to be large enough to include voids and cracks. Based on the assumptions of isotropic damage and the concept of effective stress, the scalar damage factor, d, is defined as,

$$d = \frac{A - \bar{A}}{A} \tag{2-6}$$

where $\bar{A}$ is the effective stressed cross-sectional area corresponding to the damaged area and A represents the fictitious undamaged area. The effective area $\bar{A}$ is determined by eliminating the micro-cracks and cavities to produce an equivalent fictitious undamaged state in the bar. The damage state of the material is characterised by the value of the damage variable d, which ranges from 0 for the undamaged material to 1 for the fully damaged material.

The strain equivalence stated by Lemaitre (1985) assumes that the same constitutive relations are used for the damaged material and the virgin material, where the effective stress replaces the actual stress. The effective stress, $\bar{\sigma}$, can be determined by equating the force exerted on the damaged area, $\bar{A}$, with the force $T = \sigma A$ and the force applied on the fictitious undamaged area, A, with the force $T = \bar{\sigma}\,\bar{A}$, that is

$$T = \sigma A = \bar{\sigma}\,\bar{A} \tag{2-7}$$

where σ and $\bar{\sigma}$ = Cauchy stress and its effective counterpart, which gives,

$$\bar{\sigma} = \frac{\sigma}{(1-d)} \tag{2-8}$$

Therefore, the strain equivalence hypothesis states that the strain behaviour of the damaged material is modified only through the effective stress, an example of which is given by:

$$\varepsilon = \frac{\bar{\sigma}}{E} = \frac{\sigma}{(1-d)E} \tag{2-9}$$

where ε corresponds to the elastic strain and E is the Young's modulus.

Concrete material subjected to cyclic loading conditions experiences several damage responses, for example, cracking under tension, failure under compression, and stiffness degradation. To take into account different damage states, Mazars & Pijaudier-Cabot (1989) proposed different continuum damage models with multiple damage variables for concrete. These models also account for anisotropy, ductile behaviour, and crack closure.

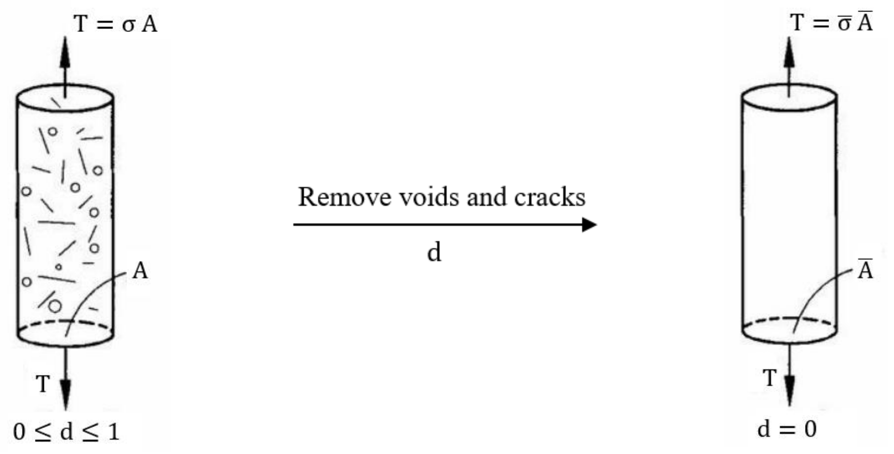

(a) (b)

Figure 2-15: A cylindrical bar subjected to uniaxial tension: (a) Damaged state; (b) Equivalent fictitious undamaged state (Voyiadjis, Voyiadjis and Kattan, 1999)

Indeed, the efficiency and performance of a concrete damage model rely mainly on the adopted damage variables, which are considered macroscopic approximations for representing the fundamental micro-cracking process. Based on the damage variables used, concrete damage models fall into two groups, including isotropic models with one or several damage variables (Faria *et al.*, 1998; Hatzigeorgiou *et al.*, 2001; Lee & Fenves, 1998; Simo & Ju, 1987), and anisotropic models with tensorial damage variables (Ortiz, 1985; Yazdani & Schreyer, 1990; Lemaitre & Chaboche, 1994). The isotropic damage models with one scalar damage variable, such as the model by (Simo & Ju, 1987a,b), are restricted to represent the unilateral effect of concrete. In addition, Poisson's ratio is assumed as a constant in such a model, which is not consistent with the actual Poisson's ratio decrease under tension and increase under compression due to micro-cracks. The complexities in the numerical algorithms of the anisotropic damage models hinder their practical applications. Nevertheless, using a higher-order damage tensor instead of one scalar damage variable could provide a more realistic representation of damage states in concrete materials.

2.4.1.3 Combined damage and plasticity

As discussed before, the nonlinear response of concrete under different loading conditions can be modelled based on plasticity or damage theories, which complement each other. The concrete behaviour is closer to plasticity than damage under compression, while the contribution of damage is greater under tension. Plasticity models formulated based on stress are convenient for modelling concrete under triaxial stress states. They can account for the yield surface corresponding to a particular hardening stage on the strength envelope. The unloading and path dependency can be well represented since the strain is split into elastic and plastic components. In addition, the ductile hardening behaviour can be described for concrete under high confined compression.

Nevertheless, experimental evidence revealed that plasticity models could not model the stiffness degradation upon unloading. In contrast, strain-based damage models rely on the continuous reduction in the elastic stiffness, which characterises the degradation phenomena for concrete under tensile loading and low confined compressive states. However, as pointed out by Lee & Fenves (1998), concrete damage models are not able to offer a proper dilatancy control, which is considered to be crucial for modelling concrete under multi-dimensional loading conditions.

In order to capture the observed phenomenological behaviour of concrete, coupled damage plasticity models can be used (Lee & Fenves, 1998; Lubliner *et al.*, 1989; Luccioni *et al.,* 1996; Simo & Ju, 1987; Yazdani & Schreyer, 1990). They are formulated by combining an effective (undamaged) stress-based plasticity model with a damage model considering plastic and elastic strain measures, such as the concrete damage-plasticity models (CDPM and CDPM2) developed by Grassl & Jirásek (2006) and Grassl *et al.* (2013). In the CDPM formulation, a single damage variable is used for both tension and compression to represent the monotonic response with unloading. However, this material description does not accurately represent the transition from tensile to compressive failure. CDPM2 extends the CDPM by incorporating separate damage variables for tension and compression.

Lee & Fenves (1998) proposed a damage-plasticity model allowing for stiffness degradation and using fracture-energy and multiple-hardening variables to model concrete subjected to cyclic loading. The description for the elastoplastic response is decoupled from the evaluation of damage, which is advantageous to the numerical implementation. Grassl & Rempling (2008) proposed a damage-plasticity interface model applied to the plane-stress analysis of an idealised heterogeneous material containing cylindrical inclusions and interfacial transition zones (ITZs) under cyclic loading. This interface model has the potential to represent the cyclic behaviour of concrete by using the mesoscale approach. Jalali & Dashti (2010) adopted the CDPM to predict the nonlinear behaviour of RC walls, but the numerical simulations are limited to monotonic loading conditions.

More recently, Chisari *et al.* (2020) proposed a concrete damage plasticity model (CDPM) based on the plastic-damage model developed by Lee & Fenves (1998), which enables a realistic representation of the quasi-brittle material response such as concrete or masonry under cyclic loading. Several critical behavioural aspects of concrete are considered in the CDPM, including the compressive and tensile softening behaviour as well as the strength and stiffness degradation under cyclic loading. This model has been implemented in ADAPTIC and will be employed to evaluate an existing modelling strategy for RC walls based on the use of 3D solid elements.

2.4.2 Smeared crack-based models

Modelling concrete cracking is crucial in finite element analysis of reinforced concrete structures to obtain accurate response predictions under different loading conditions. Two distinct methods are commonly used: the discrete crack approach and the smeared crack approach. The former approach, which was adopted in earlier studies conducted by Ngo & Scordelis (1967) and Nilson (1968), treats cracks as geometrical identities. It requires either automatic re-meshing to track the development of cracks or including pre-embedded crack trajectories in the finite element meshes. Cracks are modelled through displacement discontinuity in an interface element that separates two elements, corresponding to the physical separation introduced in a fracturing body. However, Lee & Fenves (1998) pointed out that the computational effort required by this strategy is prohibitive, especially when used in nonlinear dynamic simulations to investigate the seismic response of realistic RC structures.

The other alternative approach to simulate cracked concrete is based on the smeared crack concept proposed by Rashid (1968). It treats cracked solid as a continuum and allows a description in terms of stress-strain relations, which update the initial isotropic constitutive law to an orthotropic law upon the onset of cracking. The procedure is more computationally efficient and practical since the topology of the original finite element mesh is preserved. Moreover, the orientation of the crack planes, i.e., the axes of orthotropy, is determined by the condition of crack initiation without imposing other restrictions (Rots & Blaauwendraad, 1989). Although it seems that the basic assumption of displacement continuity is not consistent with the reality of physical discontinuity, the smeared crack approach is supported by the physical basis that the large scale of a representative continuum is comparable to the diffuse crack patterns, for example, in the realistic modelling of structural components like shear walls.

Within the scope of smeared crack approaches, it is assumed that the first crack forms along the direction perpendicular to the principal tensile stress direction when the maximum tensile stress exceeds the tensile strength of the concrete material. The orientation of a crack could be assumed as fixed, multi-directional or rotating. The difference lies in the hypothesis that the crack pattern is maintained constant, updated step-wisely or continuously. The following sections review the cyclic concrete constitutive models based on the rotating and fixed crack approaches.

2.4.2.1 Rotating crack models

In the smeared rotating crack approach, the principal stress and strain directions are assumed to coincide. The constitutive relations are applied in the principal direction, eliminating the necessity of modelling the hysteretic response of shear stresses. A well-known smeared rotating crack model was based on the Modified Compression Field Theory (MCFT) proposed by Vecchio & Collins (1986), which was developed to predict the load-deformation response of

RC elements subjected to in-plane shear and normal stresses. The MCFT stems from the Compression Field Theory (CFT) (Mitchell & Collins, 1974) for reinforced concrete under torsion and shear. The CFT ignores the contribution of concrete in tension by assuming zero tensile strength of concrete. Thus, it can only estimate the failure stress but not the deflections due to shear.

The constitutive laws in MCFT were derived from extensive experimental tests on reinforced concrete panels under pure shear or a combination of shear and axial stresses. The cracked concrete was considered as an orthotropic material with its stress-strain characteristics, including the compression softening effect. The Poisson effect was neglected after concrete cracking, considering that the axial deformations do not influence the transverse deformations for cracked concrete. Based on the assumption of the alignment of principal stress and principal strain directions, the formulations of equilibrium, compatibility, and constitutive relationships were associated with average stresses and average strains. Consideration was also given to tension stiffening to represent local stress conditions at crack locations, which were neglected in the CFT.

Palermo & Vecchio (2003) conducted the first analytical work to derive formulations for concrete subjected to reversed cyclic loading using the smeared rotating crack assumption. Formulations were proposed for RC membrane structures under cyclic loading in both compressive and tensile regimes, which were incorporated into a 2D nonlinear finite element analysis program. The algorithm employed was based on a secant stiffness procedure including compatibility, equilibrium, and constitutive relationships consistent with the MCFT. The main characteristics of this model were the nonlinear unloading adopting a Ramberg-Osgood relationship, linear reloading with stiffness degradation related to the elastic strain recovered in the unloading stage, and enhanced plastic strain offset calculations. The model was validated by Palermo & Vecchio (2004) based on experimental results on slender and squat walls, the structural responses of which were dominated by flexural and shear mechanisms, respectively. It was concluded that this simplified material description enables realistic representations of ultimate strength, ductility, energy dissipation and failure mechanism.

He *et al.* (2008) proposed a fracture energy-based smeared rotating crack approach for analysing RC structures under general loading conditions, particularly under reversed cyclic loading. The constitutive model simulated the most salient response characteristics of concrete subjected to quasi-statically reversed cyclic loading. It enables the representation of plastic strains, crack closing and reopening, nonlinear unloading and reloading with degraded reloading stiffness, allowing for energy dissipation and damage. Partial unloading and reloading rules for tension and compression loadings are also included in this formulation. The tensile and compressive fracture energies of concrete are considered as material properties and utilised to calibrate the softening branches of the tension and compression envelope curves. Furthermore, this constitutive model was employed with the four-node plane stress 2D element to analyse a slender wall subjected to cyclic loading, the numerical response of which agreed well with the experimental results. To this end, it can be established that the cyclic concrete constitutive models based on the smeared rotating crack approach have a good potential to be incorporated into a 2D finite element model.

2.4.2.2 Fixed crack models

A fixed crack model enables the principal strain direction to deviate from the principal stress direction after the first crack is formed. The Fixed Angle Softened Truss Model (FA-STM) was developed (Pang & Hsu, 1996) by assuming the crack direction is maintained fixed. Zhu *et al.* (2001) derived a rational expression for calculating shear modulus, which simplified the solution algorithm of the FA-STM. Since the Poisson effect of a cracked RC element was ignored, the FA-STM could only model the pre-peak curve of the shear stress against shear strain response but not the post-peak branch.

Later, Hsu & Zhu (2002) developed the softened membrane model (SMM) to describe the complete monotonic curve of the load-deformation response, representing the behaviour before and after cracking and the ascending and descending branches. The Poisson effect is incorporated into the model using the Hsu/Zhu ratios in the SMM formulation. Mansour & Hsu (2005b) proposed the cyclic softened membrane model (CSMM), an extension of the SMM to analyse RC membrane elements under reversed cyclic loading. Figure 2-16 shows an overview of the constitutive models used in CSMM. The stress-strain relationships were developed for concrete and embedded reinforcement steel bars in the unloading and reloading phases (Mansour *et al.*, 2001). A damage parameter, ξ, was introduced into the compressive envelope curve of concrete. The Hsu/Zhu ratios converting the biaxial strains to uniaxial strains were defined for application to cyclic loading.

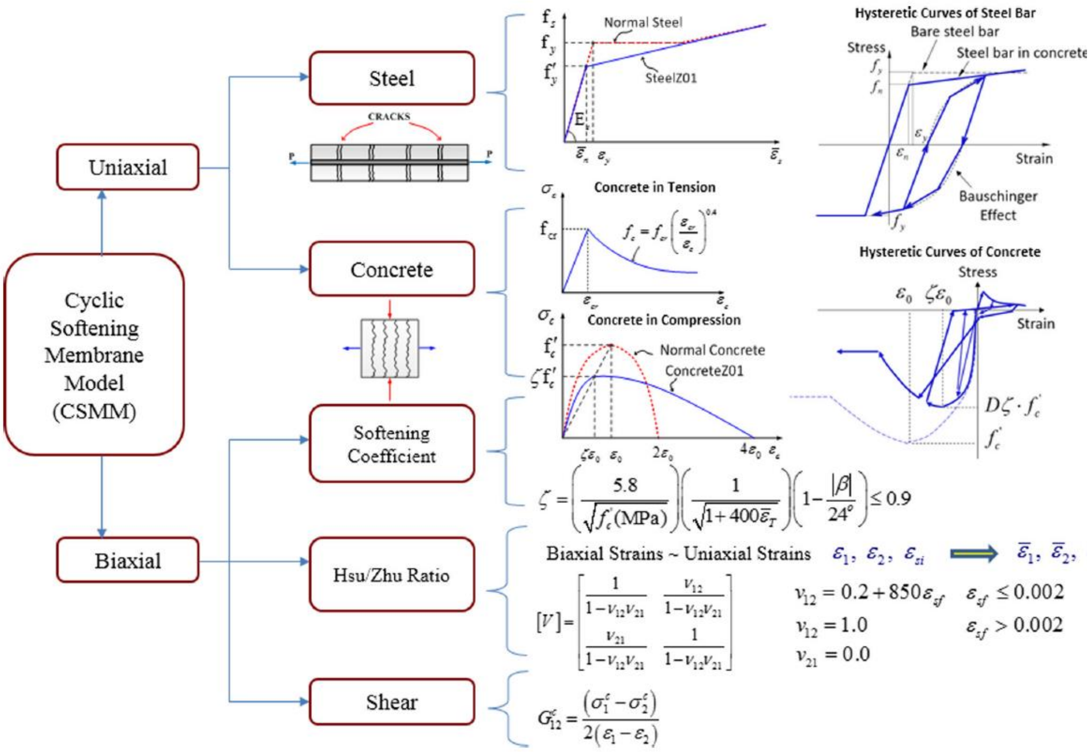

Figure 2-16: Overview of constitutive models used in the CSMM (Mansour & Hsu, 2005b)

The CSMM was validated against experimental tests on RC panels under cyclic shear stresses (Mansour & Hsu, 2005a). It was confirmed that CSMM could effectively model the hysteretic cycles of the shear stress and strain curves of RC membrane elements with steel reinforcement oriented at different angles regarding the applied principal stresses. The pinching characteristics can also be well represented. CSMM was proved as an efficient model to predict the response of structures characterised by a shear-dominant behaviour, including their shear stiffness, ductility and energy dissipation. In the CSMM, the equilibrium between external and internal forces requires an iterative procedure, as the Newton-Raphson solution scheme, based on a tangent stiffness matrix approach. An iterative procedure is also required to determine the assumed fixed crack angle, which may cause convergence problems in determining the wall response. A flow chart of this procedure is given in Figure 2-17.

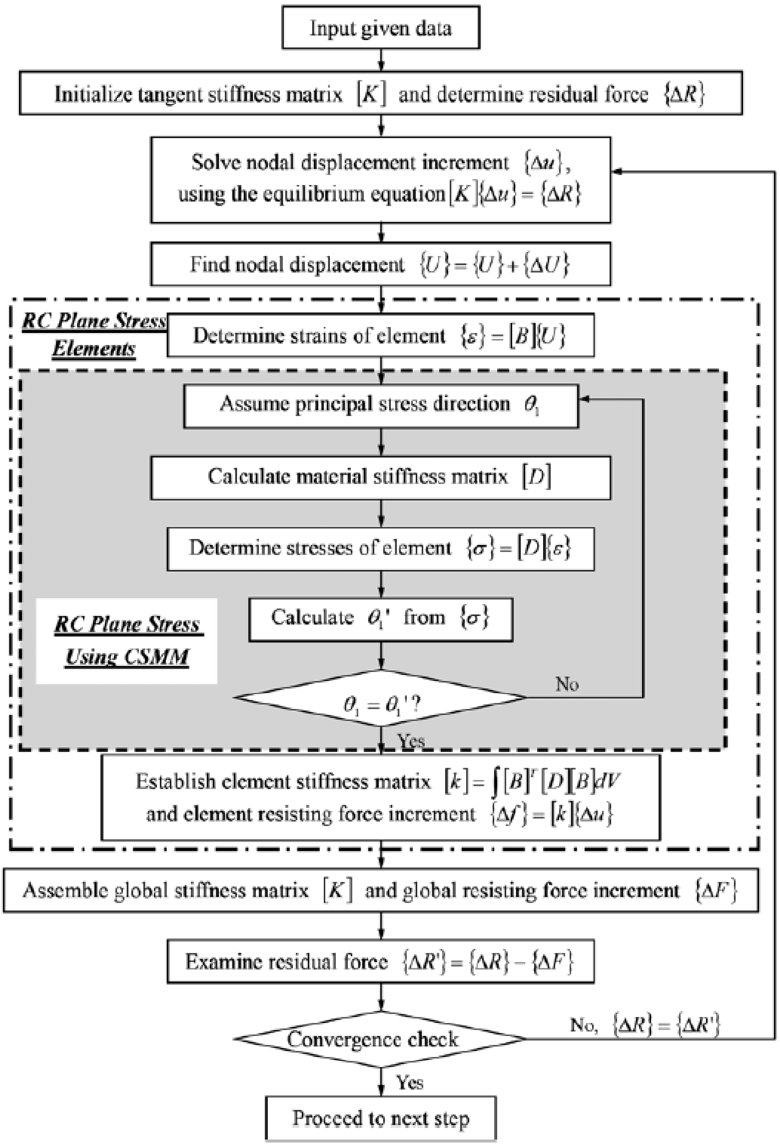

Figure 2-17: Nonlinear analysis algorithm using CSMM (Mo *et al.*, 2008)

More recently, Belletti *et al.* (2017) proposed a Physical Approach for Reinforced Concrete (PARC) for the response prediction of RC members under cyclic loadings. Numerical-experimental comparisons confirmed that the model could predict the nonlinear response of RC panels under cyclic loading, including cyclic shear response, stiffness degradation and energy dissipation, with reasonable accuracy.

2.5 Concluding remarks

RC shear walls are commonly used as the main lateral load resisting components in multi-storey buildings subjected to earthquake loading. Accurate numerical descriptions for RC walls are required for designing a new building or the seismic assessment of existing structures. This chapter has summarised the main response characteristics of RC walls and the potential failure modes under cyclic loadings. Subsequently, different modelling strategies for predicting the nonlinear response of RC walls, from the simplified 1D models to the refined 3D FE models, have been presented. This provides a background for the evaluations of current modelling approaches to simulate RC walls under cyclic loading in Chapter 3.

Simplified models based on the wide column analogy, multiple springs, or truss elements represent efficient computational tools to predict the cyclic response of RC walls. They commonly adopt strain-based or force-based hysteresis relationships at monitoring point or element levels. Nevertheless, the contribution of shear deformation and its interaction with the flexural behaviour have been mostly neglected in the model formulations.

By contrast, detailed FE models based using 2D shell or 3D solid elements can be employed to obtain more accurate response predictions and capture complex failure mechanisms. The limited attempts to simulate RC walls by employing detailed 3D FE modelling have been highlighted. Such models generally require a significant effort to develop the models and perform the simulations. For these reasons, they are not currently used for nonlinear seismic analysis of large multi-storey buildings with shear walls. This highlights the need to develop more efficient yet accurate descriptions for nonlinear simulations of RC walls under cyclic loading, as the novel macro-element model described in Chapter 4.

In the final part of the chapter, cyclic concrete constitutive models using concrete damage plasticity approaches and smeared crack-based models considering either fixed crack or rotating crack concepts have been reviewed. Previous studies have shown that smeared crack-based models are capable of predicting the cyclic response of RC walls. The fixed crack model requires defining specific hysteresis shear stress-strain relationships, whereas this need is eliminated in the rotating crack model. Besides, it should be pointed out that concrete cyclic material models rely on the use of several material input parameters and sophisticated calibration procedures. In this respect, Chapter 4 proposes a biaxial concrete constitutive model based on the rotating crack approach, which requires a basic set of input material parameters.

Chapter 3

Nonlinear FE Analysis of RC Walls

3.1 Introduction

RC shear walls are commonly employed in new building structures or adopted as retrofitting solutions for existing sub-standard frame buildings to resist in-plane lateral forces induced by earthquake ground accelerations. In general, the incorporation of RC walls into a frame building transforms its seismic behaviour, due to the high in-plane strength and stiffness of these structural components. Thus, a realistic description of RC walls is vital to achieve accurate response predictions of RC buildings with shear walls under earthquake loading.

This chapter analyses the monotonic and cyclic response of representative RC shear walls with rectangular cross sections under in-plane horizontal loads utilising existing modelling capabilities in ADAPTIC (Izzuddin, 1991). At first, the adopted numerical modelling strategies for RC walls are presented in Section 3.2. They include: (i) simple 1D models with elasto-plastic beam-column elements, (ii) finite element (FE) representations with nonlinear 2D shell elements and (iii) detailed nonlinear 3D FE models with solid elements. The ability of the different models to represent the response of RC walls is investigated in Section 3.3. More specifically, accuracy, computational efficiency and robustness of the available modelling approaches in ADAPTIC are assessed via comparisons against the results from physical experiments on RC walls subjected to in-plane cyclic loading. In the following Section 3.4, the merits and limitations of existing modelling strategies are discussed, highlighting the need to develop a novel accurate and efficient numerical description for nonlinear analysis of RC walls under cyclic loading conditions.

3.2 Current numerical modelling strategies

3.2.1 Simplified modelling with beam-column elements

As pointed out in Chapter 2, one of the simplest and most efficient numerical modelling strategies to represent RC walls is based on the wide column analogy, where a mesh of elasto-plastic beam-column elements with elongated cross section is used to describe a RC wall. In this research, the beam-column element 'cbp3' in ADAPTIC is employed. Such element was initially proposed by Izzuddin & Elnashai (1993) for large displacement nonlinear analysis of framed structures. The element is developed according to the fibre approach to account for the spread of plasticity within the cross section and along the member length. The assumptions made in the formulation are in accordance with the Euler-Bernoulli hypothesis, which assumes that plane sections remain plane and normal to the centroidal axis in the deformed configuration, thus neglecting transverse shear deformations.

A local reference system referred to as corotational system, which follows the element chord in the deformed configuration, is introduced to avoid the definition of complex strain-displacement relationships in the presence of large displacement. The introduction of such local system excludes rigid body contributions considering only strain-inducing states, which enables a convenient representation of geometric nonlinearity effects. Figure 3-1 shows the local freedoms and the nodal forces of the two-noded beam-column element. The six local degrees of freedom $\theta_{1y}, \theta_{1z}, \theta_{2y}, \theta_{2z}, \Delta, \theta_T$ are associated with the local element forces $M_{1y}, M_{1z}, M_{2y}, M_{2z}, F, M_T$. The formulation adopts cubic shape functions for the transverse displacements $v(x)$ and $w(x)$, whereas the centroidal axial strain is taken as constant.

Each element adopts two Gauss sections (Figure 3-2) for the numerical integration of the element stiffness matrix and the resistance nodal force vector. Each cross-section consists of several monitoring areas, where direct longitudinal stains are calculated based on the Euler-Bernoulli assumption and stresses are determined from strains using specific material stress-strain laws for the component materials.

Different uniaxial material models are incorporated for concrete and steel. In this research, a uniaxial trilinear concrete model (Figure 3-3) with an optional initial quadratic branch in compression is adopted. The compressive behaviour is defined by five input parameters, namely the secant compressive stiffness E_{c1}, the compressive strength f_{c1}, the compressive softening stiffness E_{c2}, the residual compressive strength f_{c2} and the parameter $\alpha = (E_{c1}^t - E_{c1})/E_{c1}$ defining the initial ascending compressive branch with α greater than zero implying a quadratic initial compressive response, where E_{c1}^t denotes the initial compressive tangent modulus. The model considers no residual tensile strength. Therefore, three parameters specify the tensile behaviour: the tensile strength f_t, the initial tensile stiffness E_{t1} and the tensile softening stiffness E_{t2}. Under cyclic loading conditions, the unloading/reloading stiffness is assumed to be the same as the initial stiffness or the initial compressive tangent modulus when the quadratic initial compressive response is defined. Steel reinforcement is modelled by a bilinear constitutive relationship with kinematic strain hardening, as shown in Figure 3-4, where the Young's modulus E, the yield strength σ_y and the strain hardening factor μ are specified.

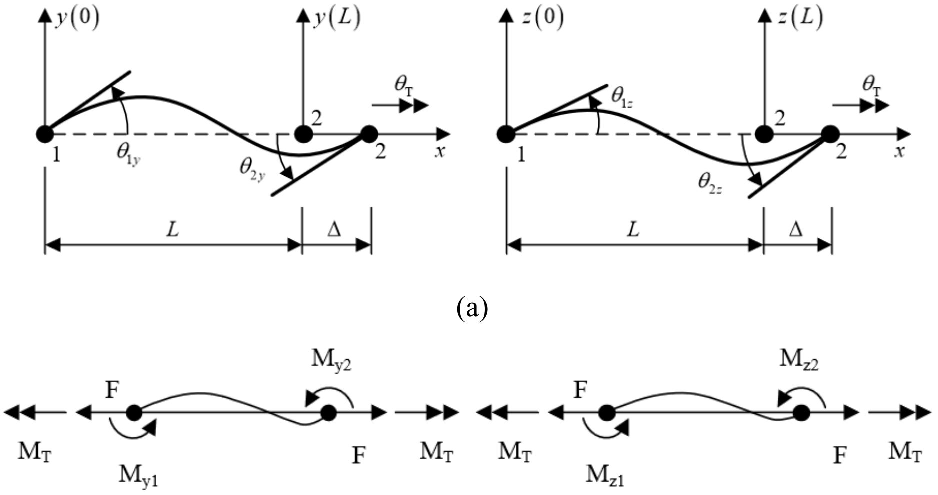

(a)

(b)

Figure 3-1: Cubic beam-column element 'cbp3': (a) local freedoms and (b) local forces in the x-y and x-z planes (Izzuddin & Elnashai, 1993)

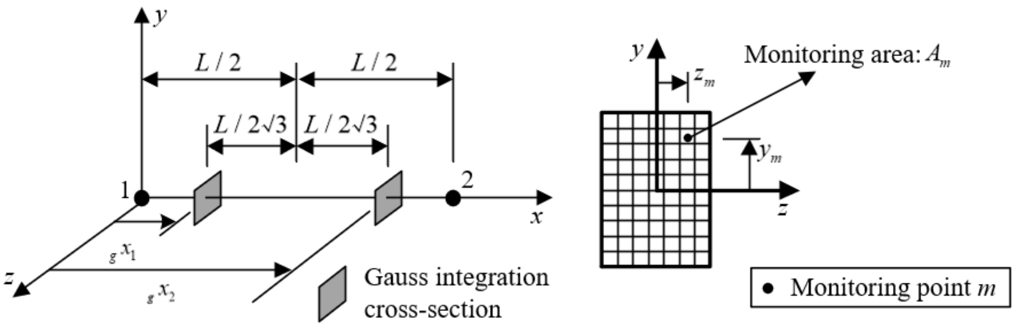

Figure 3-2: Gauss integration sections and monitoring areas distributed within the section (Izzuddin & Elnashai, 1993)

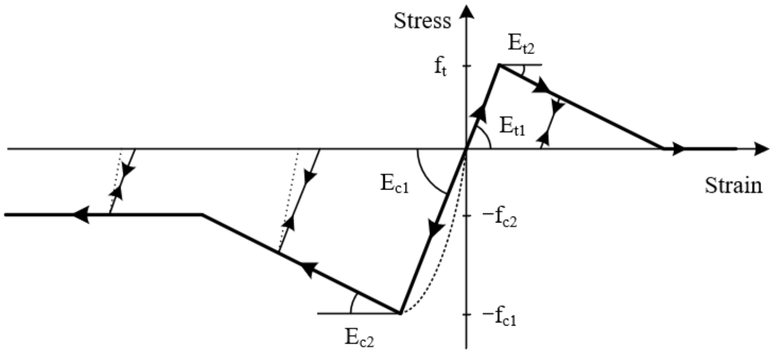

Figure 3-3: Trilinear concrete model ‘con1’

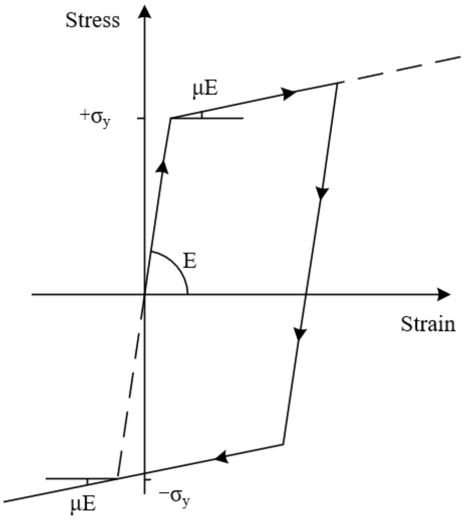

Figure 3-4: Bilinear elasto-plastic steel model ‘stl1’

3.2.2 Detailed 2D FE modelling

3.2.2.1 Nonlinear shell element description

In this research, RC walls are also modelled by a 2D modelling strategy utilising a mesh of 4-noded flat shell elements ‘csl4’ in ADAPTIC. The adopted shell element was developed by Izzuddin *et al.* (2004) to model composite-ribbed slabs with steel decks (Figure 3-5). According to this modelling approach, a RC flat slab can be represented as a special simplified composite slab. An important feature of this element is related to the treatment of geometric orthotropy underpinned by its kinematic description based on the modified Reissner–Mindlin hypothesis to reflect material discontinuity between the ribs of a composite slab. The element kinematics in the cover region with uniform depth retains the conventional Reissner–Mindlin assumptions, where plane sections remain plane after deformation but not necessarily perpendicular to the axial axis (Liu & Quek, 2013), thus allowing for shear deformation effects.

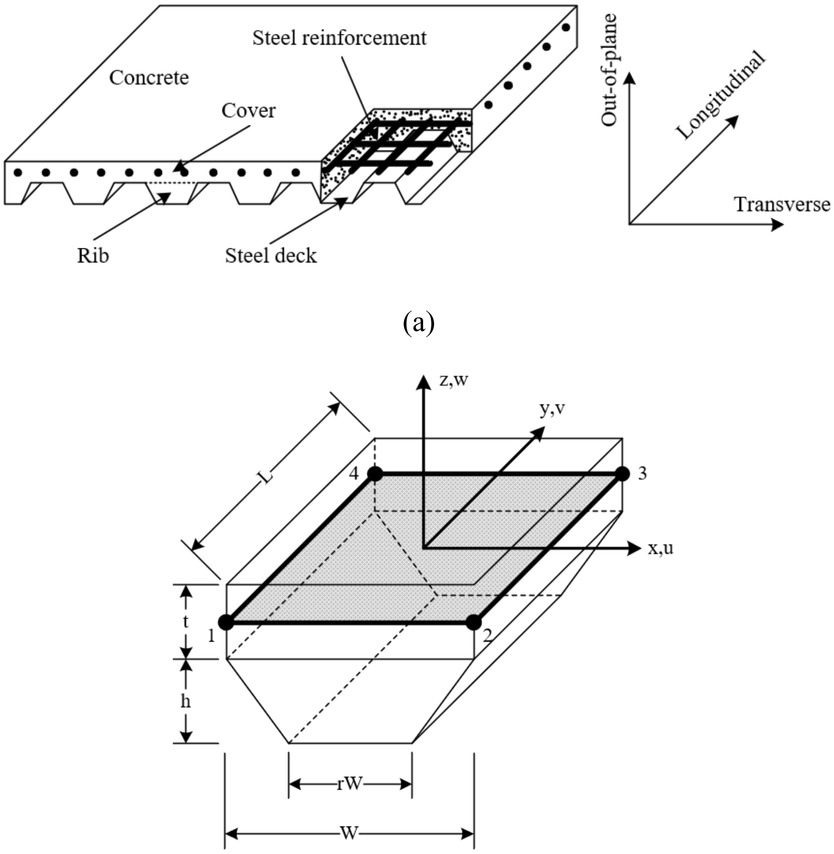

(b)

Figure 3-5: (a) Typical composite ribbed slab; (b) shell element ‘csl4’ (Izzuddin *et al.,* 2004)

In the shell element formulation, the variations of material stress and stiffness over the shell element domain are determined based on a layered approach. The element thickness is discretised by several layers, each with a predefined number of Gauss points. Steel reinforcements corresponding to specific layers arranged along two orthogonal directions are assumed as smeared. A single reinforcement layer acts as a uniaxial equivalent plate with uniform thickness. Besides, a perfect bond between concrete and steel reinforcement is assumed. The numerical integration of concrete and steel layer stresses is performed at the Gauss points over the element domain.

Both geometric and material nonlinearities are accounted for in the shell element formulation. Geometric nonlinearity due to large displacements and rotations is considered following the corotational strategy proposed by (Izzuddin, 2002). In this approach, geometrically nonlinear transformations between the local and global reference systems are performed, enabling the determination of the overall global response accounting for arbitrarily large rigid body rotations. The effects of material nonlinearity are allowed by establishing material stresses corresponding to material strains at each Gauss point based on the adopted biaxial concrete and uniaxial steel constitutive models, which will be discussed in detail in the following section.

3.2.2.2 Material constitutive models

In this research, the material model 'con11' in ADAPTIC developed by Izzuddin *et al.* (2004) is used for modelling the nonlinear response of concrete in 2D meshes with nonlinear shell elements. Material nonlinearity in steel reinforcement is described by employing the bilinear elasto-plastic model described in Section 3.2.1. The concrete material model accounts for the influences of compressive nonlinearity, tensile cracking, crack opening and closure, softening behaviour in tension and compression, and the effects due to elevated temperature. Material nonlinearity is treated allowing for biaxial planar stresses, while linear behaviour is assumed for the out-of-plane shear response.

The material behaviour in compression under a biaxial stress state $(\sigma_x, \sigma_y, \tau_{xy})$ is formulated based on the principles of plasticity with the use of an evolving plastic interaction surface (Figure 3-6(a)), according to the following criterion:

$$C(\sigma_x, \sigma_y, \tau_{xy}) = \sqrt{2\left[\left(\frac{1-b_c}{3}\right)I_1^2 + (2+b_c)J_2\right] + \sigma_c I_1} \leqslant \sigma_c \tag{3-1}$$

with

$$I_1 = \sigma_x + \sigma_y \tag{3-2}$$

$$J_2 = \frac{1}{3}\left(\sigma_x^2 - \sigma_x\sigma_y + \sigma_y^2\right) + \tau_{xy}^2 \tag{3-3}$$

where σ_c is the current compressive strength of concrete; b_c is a compressive interaction parameter which is usually taken as 0.6, but can be calibrated against experimental results (Kotsovos & Pavlovic, 1995); I_1 and J_2 denote the stress invariants for the biaxial case considering the contribution of normal and shear stresses, respectively. As shown in Figure 3-6(a), the current compressive strength of concrete, σ_c, is varying with the cumulative equivalent plastic strain, $\bar{\varepsilon}_p$, resulting in the evolution of the biaxial interaction surface. The compressive hardening and softening responses are activated for $(\bar{\varepsilon}_p < \varepsilon_c)$ and $(\bar{\varepsilon}_p > \varepsilon_c)$ respectively, as defined by:

$$\sigma_c = \left[\frac{s_c + (1 - s_c)\dfrac{\overline{\varepsilon_p}}{\varepsilon_c}\left(2 + \dfrac{r_c}{1 - r_c}\dfrac{\overline{\varepsilon_p}}{\varepsilon_c}\right)}{1 + \left(\dfrac{1 - s_c}{1 - r_c}\right)\left(\dfrac{\overline{\varepsilon_p}}{\varepsilon_c}\right)^2} \right] f_c \tag{3-4}$$

with:

$$\varepsilon_c = \frac{f_c}{E_c} \tag{3-5}$$

where s_c and r_c are the non-dimensional material parameters reflecting the onset of compressive nonlinearity and the residual post-crushing strength, as indicated in Figure 3-6(a). For a given stress state, when the compressive constraint set by the interaction surface is exceeded, additional plastic strains are introduced based on the associated flow rule. The single-step backward Euler method (Crisfield 1991) is used to correct the current stress state back to the interaction surface, which is potentially beneficial to generating a symmetric consistent tangent stiffness matrix (Izzuddin & Lloyd Smith, 1996).

The tensile behaviour of concrete is modelled following a smeared crack approach, which adopts a fixed crack orientation in the post-cracking stage. It is assumed that the first crack is perpendicular to the x-axis of the local reference system. In the most general form of a biaxial model, the orientation is perpendicular to the maximum principal stress direction that first exceeds the concrete tensile strength. In this case, constant geometric transformations need to be applied to transform the biaxial strains and stresses in the local element coordinate system to those in the cracked plane. The tensile nonlinearity is treated by using separate tensile strength envelopes for direct and shear stresses $(\sigma_{xt}, \sigma_{yt}, \tau_{xyt})$ associated with strains $(\varepsilon_{xc}, \varepsilon_{yc}, \gamma_{xyc})$, as shown in Figures 3-6(b) and (c). The irrecoverable strains induced by concrete cracking under tension are considered in the constitutive law. In Figure 3-6(b), $(\varepsilon_{xc}^0, \varepsilon_{yc}^0)$ the maximum crack strains accumulated up to the start of the current equilibrium step are indicated. A material softening parameter, a_t, is introduced in the envelope curve to represent the linear tensile softening response associated with the ultimate strain at zero tensile stress ε_t.

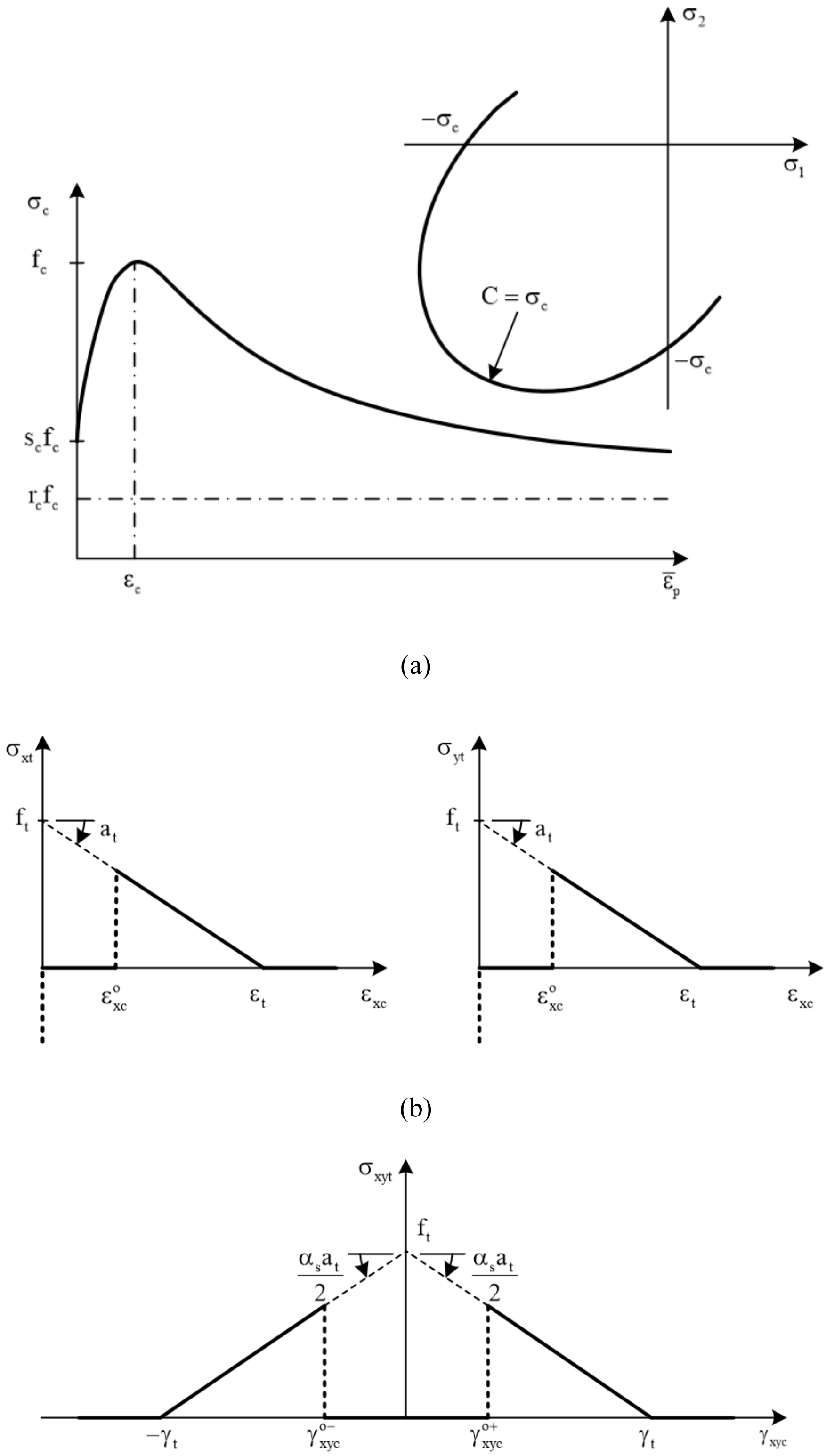

(a)

(b)

(c)

Figure 3-6: Biaxial concrete material model 'con11': (a) plasticity-based behaviour of concrete under compression; (b) tensile envelope for direct stresses; (c) tensile envelope for shear stresses (Izzuddin *et al.*, 2004)

It is worth noting that the model accounts for the crack opening and closure for the cases of ($\varepsilon_{xc} > 0, \varepsilon_{yc} > 0$) and ($\varepsilon_{xc} = 0, \varepsilon_{yc} = 0$), respectively. Besides, compressive stresses ($\sigma_x \leq 0, \sigma_y \leq 0$)) are allowed when a crack is closed. The planar shear response is modelled by applying a shear retention factor to the elastic constitutive matrix and using a shear strength envelope constraint (Figure 3-6(c)). The effective current shear strength is also introduced in the formulation of the shear response to account for the interaction between direct stresses and shear stresses. As pointed out by Izzuddin *et al.* (2004), negative and positive shear stresses are limited by two separate failure envelopes, allowing for the substantial resistance to be maintained for shearing in one direction even if the resistance is lost with significant damage in the other direction.

3.2.3 Detailed 3D FE modelling

3.2.3.1 Nonlinear solid element description

The adopted detailed 3D representation for RC walls relies on the use of a mesh of 3D solid elements. In preliminary simulations, two element types, namely the 8-noded 'bk08' element (Figure 3-7) and the 20-noded 'bk20' element available in ADAPTIC (Izzuddin, 1991) were used. The former element employs linear shape functions according to the standard formulation for 3D quadrilateral elements (Zienkiewicz *et al.*, 2005), while the 20-noded element utilises quadratic shape functions. It has been found that models with the basic 8-noded solid elements achieve response predictions for RC walls under in-plane loading very similar to those provided by higher-order elements requiring significantly less computational effort. For this reason, 8-noded solid elements have been adopted for detailed 3D simulations of RC walls in this research. The 'bk08' solid element allows for modelling 3D continuum large displacement problems treating geometric nonlinearity by using Green strains. Material nonlinearity in concrete is considered by a damage plasticity model (CDPM), which will be discussed in the next section.

Steel reinforcements in RC walls are explicitly modelled by the embedded bar element 'ebar' in ADAPTIC as proposed by Barrero Bilbao (2016). Such an embedded approach permits the individual representation of reinforcing bars (Figure 3-8) distributed within the concrete parent elements (i.e., the solid elements adopted for the 3D representation of the generic RC wall) with an arbitrary orientation. The uniaxial bilinear steel model 'stl1' introduced in Section 3.2.1 is utilised for the embedded bar element to model material nonlinearity of steel reinforcement assuming a perfect bond between the steel bars and the surrounding concrete.

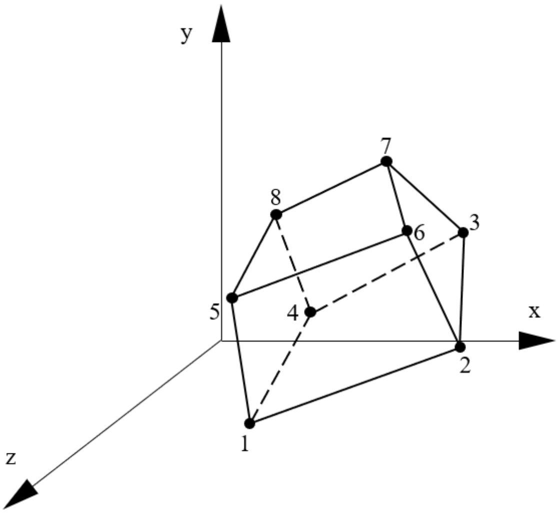

Figure 3-7: Geometry of solid element ‘bk08’

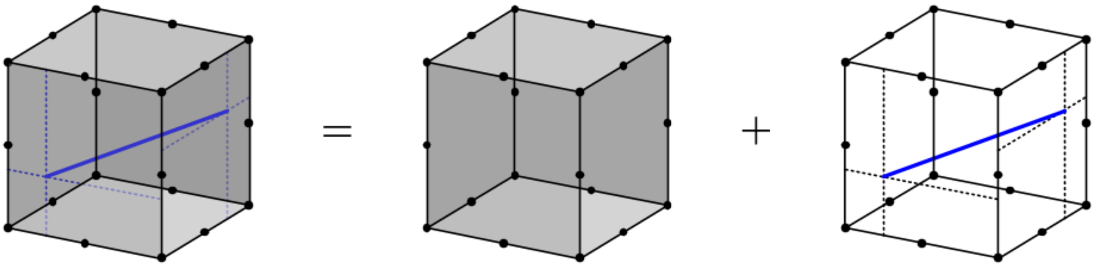

Figure 3-8: Illustration of an embedded bar element in a solid element (Barrero Bilbao, 2016)

3.2.3.2 Material constitutive models

In the constitutive models for the 3D detailed FE description, material nonlinearity in concrete is accounted for by utilising the advanced concrete damage plasticity model (CDPM) proposed by Chisari *et al.* (2020). The implementation of CDPM (‘cdpm2’ in ADAPTIC) is based on the plastic-damage model developed by Lee & Fenves (1998), which enables a realistic representation of the response of quasi-brittle materials such as concrete and masonry under cyclic loading conditions. Several critical behavioural aspects of concrete are considered in the CDPM, including the compressive and tensile softening behaviour as well as the strength and stiffness degradation under cyclic loading. In the CDPM formulation, the constitutive law allows for an elasto-plastic behaviour and damage degradation, which can be represented by the relationship:

$$\boldsymbol{\sigma} = (1-d)\bar{\boldsymbol{\sigma}} = (1-d)\boldsymbol{K}_0\left(\boldsymbol{\varepsilon} - \boldsymbol{\varepsilon_p}\right) \tag{3-6}$$

where $\boldsymbol{\sigma}$ is the nominal Cauchy stress tensor; $\bar{\boldsymbol{\sigma}}$ is the effective stress tensor corresponding to the physical stresses developed in the undamaged material; $\boldsymbol{K}_0$ is the initial stiffness. The isotropic damage is represented by using a scalar damage variable $d(\bar{\boldsymbol{\sigma}}, \boldsymbol{\kappa})$ as a function of the effective stress $\bar{\boldsymbol{\sigma}}$ and historical variables $\boldsymbol{\kappa}$.

The three main pillars in the context of classical plasticity theory, namely the flow rule, the yield function and the hardening rule are defined by Eqs. (3-7), (3-9) and (3-14). The plastic strain $\boldsymbol{\varepsilon_p}$ is evaluated in the effective stress space, which is in consistent with the framework proposed by Lee & Fenves (1998). The CDPM assumes a non-associated flow rule, and the plastic strain rate $\dot{\boldsymbol{\varepsilon}}_{\boldsymbol{p}}$ is given by:

$$\dot{\boldsymbol{\varepsilon}}_{\boldsymbol{p}} = \dot{\lambda}\frac{\partial g(\bar{\boldsymbol{\sigma}})}{\partial \bar{\boldsymbol{\sigma}}} \tag{3-7}$$

with λ as a scaling factor called the plastic multiplier. The utilised plastic potential function $g(\bar{\boldsymbol{\sigma}})$ has a Drucker-Prager form as follows:

$$g(\bar{\boldsymbol{\sigma}}) = \sqrt{(\epsilon f_{t0}\tan\psi)^2 + 3J_2} + \frac{\tan\psi}{3}I_1 \tag{3-8}$$

where ϵ is the flow potential eccentricity; f_{t0} designates the initial uniaxial tensile strength; ψ is the dilation angle; I_1 and J_2 are the first invariant of stress and the second invariant of deviatoric stress, respectively.

The yield function is based on the expression proposed by Lubliner *et al.* (1989); it considers the evolution of strength and is defined by:

$$F(\bar{\boldsymbol{\sigma}}, \boldsymbol{\kappa}) = \frac{1}{1-\alpha}\cdot\left(\alpha I_1 + \sqrt{3J_2} + \beta(\boldsymbol{\kappa})\langle\bar{\boldsymbol{\sigma}}_{max}\rangle - \gamma\langle-\bar{\boldsymbol{\sigma}}_{\boldsymbol{max}}\rangle\right) + \bar{f}_c(\kappa_c) \tag{3-9}$$

with:

$$\alpha = \frac{f_{b0r} - 1}{2f_{b0r} - 1} \tag{3-10}$$

$$\beta(\boldsymbol{\kappa}) = -\frac{\bar{f}_c(\kappa_c)}{\bar{f}_t(\kappa_t)}(1-\alpha) - (1+\alpha) \tag{3-11}$$

$$\gamma = \frac{3(1-K_c)}{2K_c - 1} \tag{3-12}$$

In the above, f_{b0r} is the ratio between biaxial and uniaxial compressive strength; K_c is the ratio of the second stress invariant on the tensile meridian to that on the compressive meridian at initial yield; $\bar{\sigma}_{max} = max(\bar{\sigma}_1, \bar{\sigma}_2, \bar{\sigma}_3)$ gives the maximum principal effective stress. $\bar{f}_c(\kappa_c)$ and $\bar{f}_t(\kappa_t)$ are the effective uniaxial strength functions associated with two plastic strain-driven historical variables κ_c and κ_t, where the subscripts c and t are used here to denote compression and tension, respectively. The effective uniaxial strength incorporates a hardening law, achieving improved robustness in the local problem, as previously pointed out by Minga *et al.* (2018). Figure 3-9(a) shows the yield surface in the deviatoric plane corresponding to different values of K_c, while the yield surface assuming a plane stress condition is shown in Figure 3-9(b). As the value of K_c tends to 1.0, the deviatoric cross-section of the yield surface approaches a circle from an approximate triangle. A typical value of K_c is $2/3$ for concrete, resulting in $\gamma = 3$.

The incremental plastic problem is solved by a set of nonlinear equations:

$$\begin{cases} d\bar{\boldsymbol{\sigma}} - \boldsymbol{K}_0\left(d\boldsymbol{\varepsilon} - d\lambda\dot{\hat{\boldsymbol{\varepsilon}}}^p\right) = 0 \\ F(\bar{\boldsymbol{\sigma}}, \boldsymbol{\kappa}) = 0 \\ d\boldsymbol{\kappa} - d\lambda h(\bar{\boldsymbol{\sigma}}, \boldsymbol{\kappa}) = 0 \end{cases} \tag{3-13}$$

The hardening function $\boldsymbol{h}(\bar{\boldsymbol{\sigma}}, \boldsymbol{\kappa})$ is defined by:

$$h(\bar{\boldsymbol{\sigma}}, \boldsymbol{\kappa}) = \begin{pmatrix} r(\bar{\boldsymbol{\sigma}})\langle\dot{\hat{\boldsymbol{\varepsilon}}}^p_{max}\rangle \\ (1 - r(\bar{\boldsymbol{\sigma}}))\langle -\dot{\hat{\boldsymbol{\varepsilon}}}^p_{min}\rangle \end{pmatrix} \tag{3-14}$$

where $r(\bar{\boldsymbol{\sigma}})$ is the stress weight factor; $\dot{\hat{\boldsymbol{\varepsilon}}}^p_{max}$ and $\dot{\hat{\boldsymbol{\varepsilon}}}^p_{min}$ are the maximum and minimum principal components of the tensor $\dot{\hat{\boldsymbol{\varepsilon}}}^p = \frac{\partial g}{\partial \bar{\sigma}}$.

The damage evolution is reflected by a scalar damage variable d as obtained by:

$$d(\bar{\sigma}, \boldsymbol{\kappa}) = 1 - [1 - s_t(\bar{\boldsymbol{\sigma}})d_c(\kappa_c)][1 - s_c(\bar{\boldsymbol{\sigma}})d_t(\kappa_t)] \tag{3-15}$$

with:

$$s_c(\boldsymbol{\bar{\sigma}}) = 1 - w_c(1 - r(\boldsymbol{\bar{\sigma}})) \tag{3-16}$$

$$s_t(\boldsymbol{\bar{\sigma}}) = 1 - w_t r(\boldsymbol{\bar{\sigma}}) \tag{3-17}$$

where the weight factors w_c and w_t, assumed as material properties govern the stiffness recovery from tension to compression and vice versa; $d_c(\kappa_c)$ and $d_t(\kappa_t)$ are two damage variables depending on the solution of the plastic problem and obtained at each load increment. Figure 3-10 illustrates a uniaxial loading cycle assuming $w_c = 1$ and $w_t = 0$ upon load reversal. In this case, the compressive stiffness is fully recovered as a crack closes from tension to compression, whereas the tensile stiffness is not recovered from compression to tension when crushing micro-cracks form.

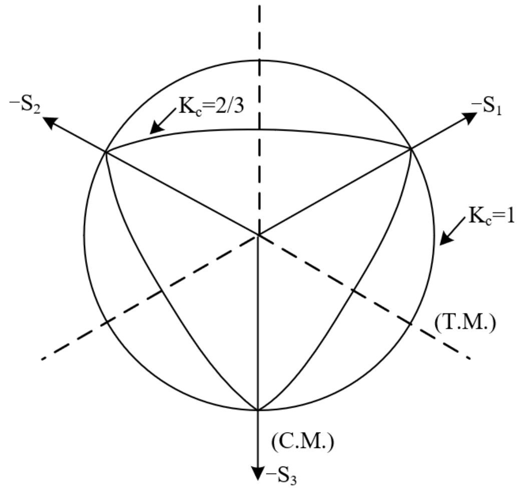

(a)

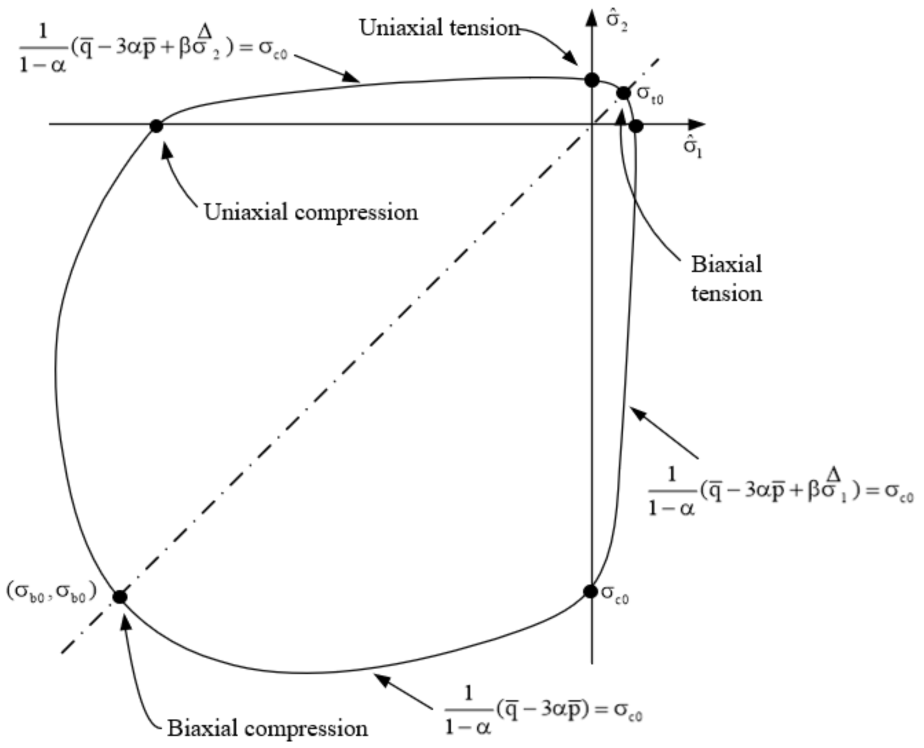

(b)

Figure 3-9: Yield surfaces in (a) the deviatoric plane and (b) under plane stress condition (Lee & Fenves, 1998; Smith, 2009)

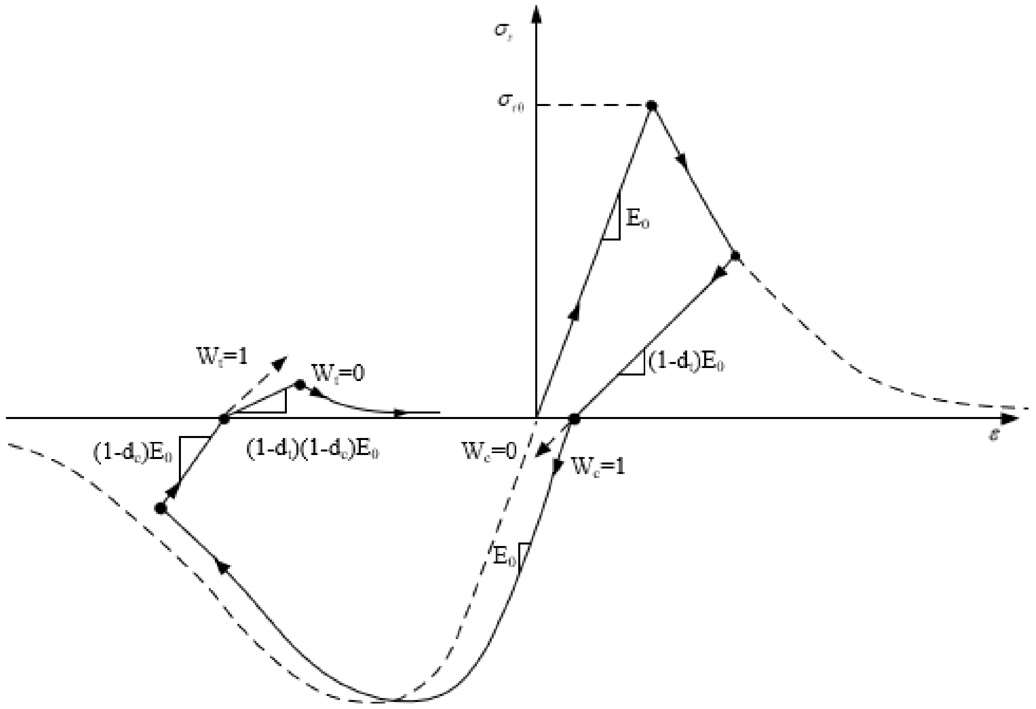

Figure 3-10: Illustration of stiffness recovery factors in a uniaxial loading cycle (Smith, 2009)

3.3 Numerical Simulations

In this section, numerical simulations of RC walls under in-plane horizontal loading are conducted by employing the existing modelling capabilities in ADAPTIC (Izzuddin, 1991) presented in Section 3.2. The selected wall specimens were tested in the laboratory in previous research which enables model validation by comparing the numerical predictions against experimental data. More specifically, two RC walls with rectangular cross sections have been analysed: a slender wall tested by Faraone *et al*. (2019) and a short wall tested by Salonikios *et al*. (1999). In the experiments, the wall specimens were subjected to in-plane cyclic loadings, representing typical seismic actions during an earthquake event. An overview of the experimental programmes is provided at first. It is followed by a presentation of the results of the nonlinear analyses performed in ADATPIC and an investigation of the ability of the existing modelling approaches to represent the main characteristics of the hysteresis response of RC walls under in-plane cyclic loading.

3.3.1 General

In the numerical simulations under in-plane horizontal loading, cracks develop in the RC wall specimens resulting in sudden release of energy and local softening, which may cause convergence problems in a displacement-controlled static analysis. In this respect, a dynamic analysis procedure is utilised to obtain both monotonic and cyclic responses. As pointed out by Macorini & Izzuddin (2011), such analysis technique has the merit of mitigating numerical issues due to the transformation of the suddenly released elastic energy at the crack formation into kinetic and viscous energy, facilitating the attainment of converged numerical solutions. The implicit Hilber-Hughes-Taylor (HHT) method (also known as the α-method), which is considered as one of the most effective time-integration schemes, is adopted to solve the dynamic equilibrium equations. This integration scheme enables the dissipation of the spurious contributions of the high-frequency modes (Hilber *et al*., 1977), leading to stable results with a relatively large time step compared to explicit methods. In this research, it is consistently assumed α = -1/3 to solve the nonlinear systems representing dynamic equilibrium.

In all the simulations performed in this chapter, the vertical load is imposed by either point load or UDL at the top of the wall specimens, and it is kept constant to mimic the experimental applied axial load. In the monotonic loading tests, the lateral loads are applied in the positive and negative directions, respectively, which gives rise to two push-over backbone curves. More specifically, a constant velocity and a zero-acceleration are assigned at the top nodes of the different FE meshes representing the wall specimens, thus leading to a linear variation of the top horizontal displacements with time. In the cyclic analyses, the lateral load is applied by simulating the experimental loading history, but assuming only one cycle per loading amplitude. A piecewise linear acceleration history is computed and applied at the node subjected to lateral loads achieving a piecewise cubic displacement history.

3.3.2 Slender wall test

3.3.2.1 Experimental program overview

Faraone *et al*. (2019) tested a full-scale slender RC shear wall under combined axial vertical compression and reversed horizontal cyclic loading. The primary purpose of the experiment was to study the response of post-installed anchors in walls experiencing shear-flexural cracks. Thus, special attentions were not only devoted to the global wall response, but also to the distribution of cracks and damage evolution during the application of lateral cyclic loading.

A schematic test set-up is depicted in Figure 3-11(a). The wall specimen, named AR2-8, represents a typical RC wall configuration in a multi-storey building. It is characterised by 2438mm length, 4877mm height (e.g. aspect ratio of 2.0) and 305mm thickness. Reinforcement details in the wall, as shown in Figures 3-11(a) and (b), were designed in accordance with the recent US codes of practice, ASCE 7-16 (2016) and ACI 318-14 (2014). The bottom of the wall was constrained by an RC footing built on the strong floor to prevent potential sliding and uplift of the wall when laterally loaded. In addition, out-of-plane supports were provided to hold the wall in its normal vertical position. An axial load of 2224 kN (8% of the cross-sectional capacity) was imposed on top of the wall by four post-tensioned threaded rods before the application of the lateral loading and kept constant during the cyclic test.

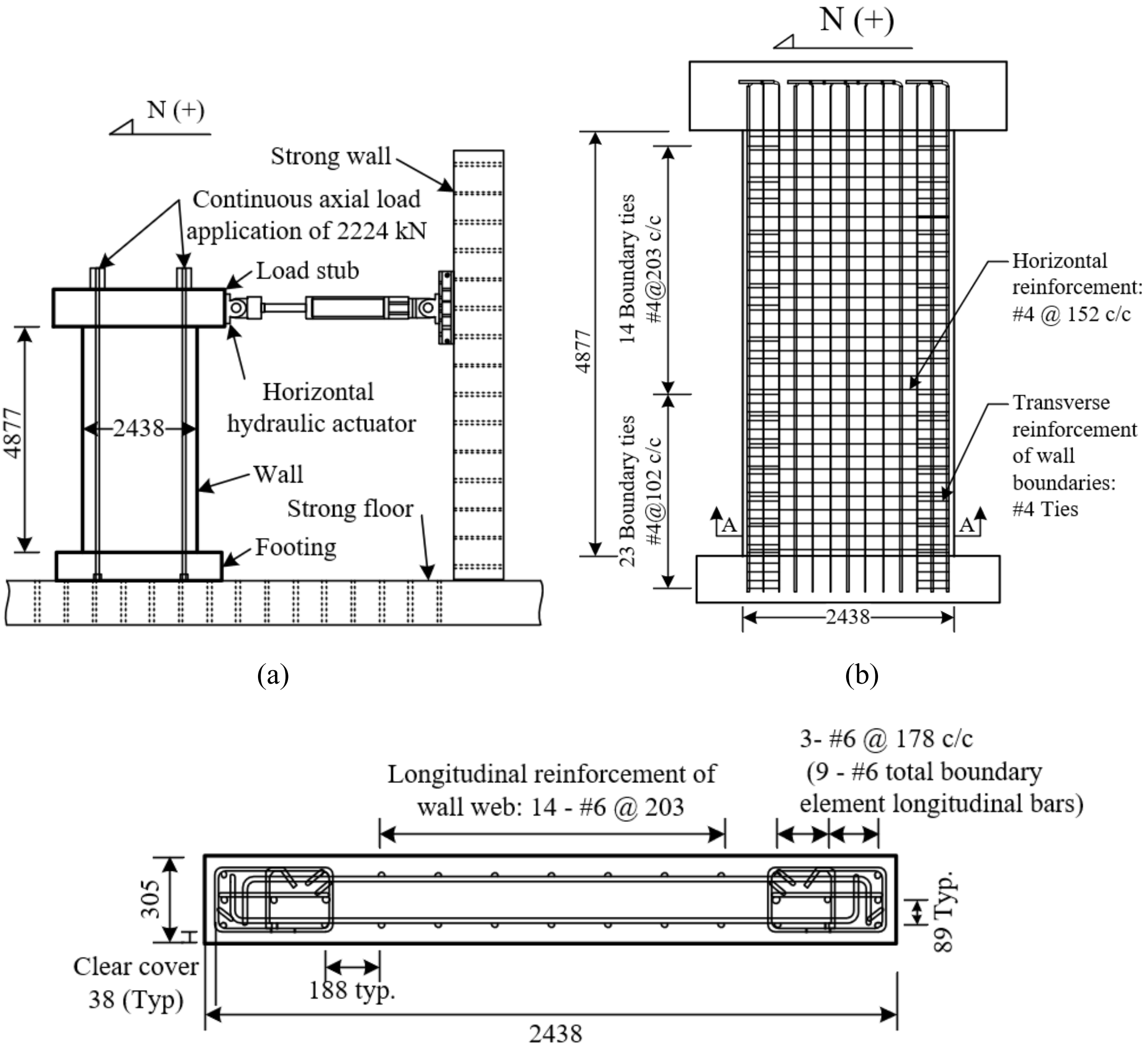

(a)

(b)

(c)

Figure 3-11: Experimental test on the slender wall by Faraone *et al*. (2019): (a) schematic test set-up; (b) reinforcement details in elevation; and (c) cross-sectional reinforcement details

The hydraulic actuator attached to the laboratory strong wall applied cyclic displacement history on the load stud, which further distributed the load at the top of the wall specimen. The experimental displacement loading protocol shown in Figure 3-12 is conformed to the ACI 374.2R-13 (2013) provisions. Three loading cycles were applied at each displacement amplitude, starting from 0.125% to 0.25% (expected yield), 0.50%, 0.70% and 1.0% drift ratios, whereafter extensive damage was expected to develop. Subsequently, two cycles were imposed at 1.50%, 2.0% and 2.5%, and a single cycle was finally incurred at 3% resulting in a significant reduction of wall resistance.

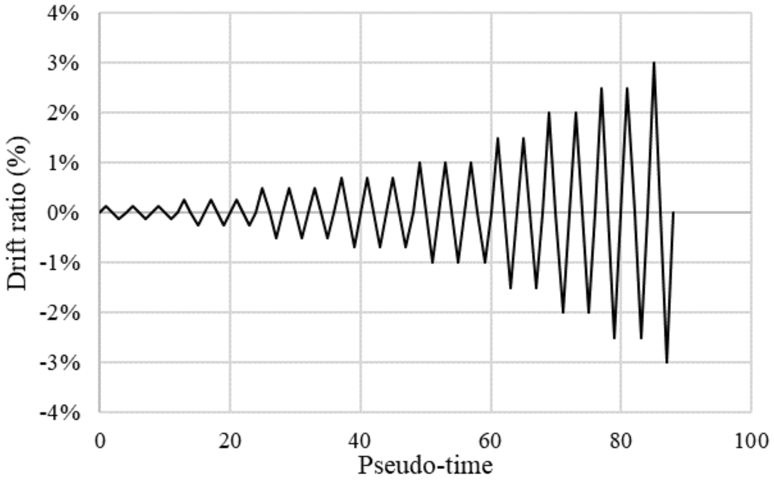

Figure 3-12: Displacement loading protocol (Faraone *et al*., 2019)

3.3.2.2 1D beam-column element modelling

The simplified 1D wide column approach described in Section 3.2.1 has been employed to simulate the response of the experimental slender wall. An initial mesh sensitivity study has indicated that a mesh of 10 elasto-plastic beam-column elements with a length of 487.7mm each, as shown in Figure 3-13(a), is suitable to provide convergent results with a reduced computational cost. In the beam element model, concentrated mass elements ('cnm3' in ADAPTIC) are lumped at nodes over the wall height, as required for performing dynamic analyses. The bottom node is fully restrained to represent the fixed base condition assumed in the experiment. In both monotonic and cyclic analysis, the lateral load is applied at the top node which is also subjected to a constant axial load of 2224kN.

The flexural wall section 'flxw' (Figure 3-13(b)) in ADAPTIC is utilised to represent the wall cross section allowing for the characteristics of the longitudinal steel reinforcement. This type of cross section is suitable for modelling symmetric walls taking into account the contributions of four materials, namely steel reinforcement, unconfined concrete, partially confined concrete in the wall web, and fully confined concrete in the boundary regions.

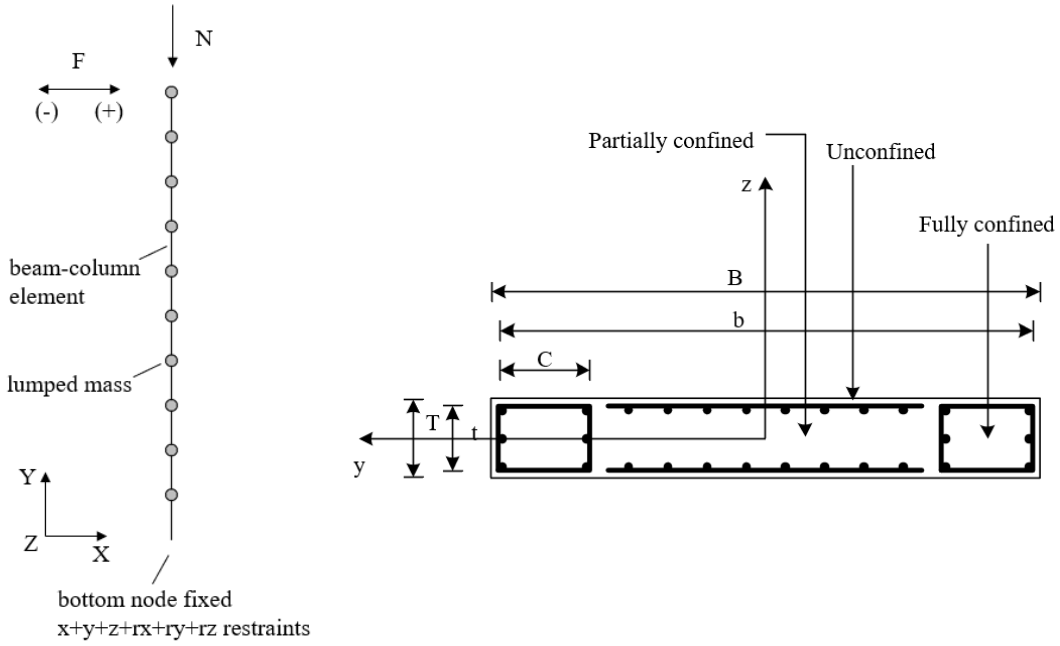

(a) (b)

Figure 3-13: 1D beam-column model for the slender wall: (a) numerical model (b) cross-section ‘flxw’ in ADAPTIC

Table 3-1 and Table 3-2 report the material parameters for steel reinforcement and concrete. The yield strength of steel reinforcement f_{ys} and the average concrete compressive strength f_{c1} determined from material tests (Faraone *et al.*, 2019) are equal to 503MPa and 41.37MPa, respectively. In the absence of test data, the Young’s modulus of steel is assumed as E_s = 200GPa and the strain hardening factor is taken as μ_s = 0.02. Moreover, it is assumed that the partial confinement effect in the web region is negligible. As a result, two groups of input material parameters are specified for concrete, as summarised in Table 3-2.

Table 3-1: Material parameters of steel model ‘stl1’

E_s $[GPa]$	f_{sy} $[MPa]$	μ_s $[-]$
200	503	0.02

Table 3-2: Material parameters of concrete model ‘con1’

Material	E_{c1} $[MPa]$	f_{c1} $[MPa]$	E_{c2} $[MPa]$	f_{c2} $[MPa]$	E_{t1} $[MPa]$	f_t $[MPa]$	E_{t2} $[MPa]$
Confined concrete	36415	48.59	-913	9.72	34514	3.59	-913
Unconfined concrete	34514	41.37	-20678	8.27	34514	3.59	-20678

In particular, the modified Kent and Park model proposed by Scott *et al.* (1982) is adopted to calibrate the material parameters f_{c1}, E_{c2} and f_{c2} for the compressive stress-strain envelope for both confined and unconfined concrete. For confined concrete, the compressive strength f_{c1} is enhanced by a factor K accounting for the confinement effect:

$$f_{c1} = Kf_c' \tag{3-18}$$

with:

$$K = 1 + \frac{\varrho_s f_{yh}}{f_c'} \tag{3-19}$$

where ϱ_s denotes the volumetric reinforcement ratio of the hoops in the concrete core measured to the outside of the hoops; f_{yh} refers to the yield strength of the hoop reinforcement, whereas f_c' is the compressive strength of unconfined concrete. According to the modified Kent and Park model, the compressive softening modulus is defined by:

$$E_{c2} = -KZ_m f_c' \tag{3-20}$$

with:

$$Z_m = \frac{0.5}{\dfrac{3 + 0.29f_c'}{145f_c' - 1000} + \dfrac{3}{4}\varrho_s\sqrt{\dfrac{h'}{s_h}} - 0.002K} \tag{3-21}$$

where h' is the width of the concrete core measured to the outside of the peripheral hoop; s_h corresponds to the centre-to-centre spacing of the hoop sets. The residual compressive strength of concrete is taken as 20% of the enhanced compressive strength:

$$f_{c2} = 0.2 \cdot Kf_{c1} \tag{3-22}$$

Finally, the concrete elastic modulus and tensile strength are estimated using Eq. (3-23) and (3-24) according to Model Code 2010 (fib, 2013) as:

$$E_{c1} = 21500 \cdot \left(\frac{f_{c1}}{10}\right)^{1/3} \tag{3-23}$$

$$f_t = 0.3 \cdot {f_{c1}}^{2/3} \tag{3-24}$$

Figure 3-14 compares the numerical monotonic response showing the variation of the lateral force against the top displacement to the backbone envelope obtained in the experimental test. The numerical results are in very good agreement with the experimental data, both in terms of initial stiffness and horizontal force capacity. However, the numerical prediction under the monotonic loading condition cannot capture the post-peak descending branch due to cyclic degradation that mainly occurred in the last cycle of the experiment. As discussed later, this is a common feature of all the numerical predictions also when using more detailed 2D or 3D models. The shear resistance of the considered slender wall specimen calculated according to the EC2 (BSI, 2004a) and ACI 318 (2009) formulations given in Section 2.2.3 are 2466kN and 2432kN, which are significantly higher than the experimental values.

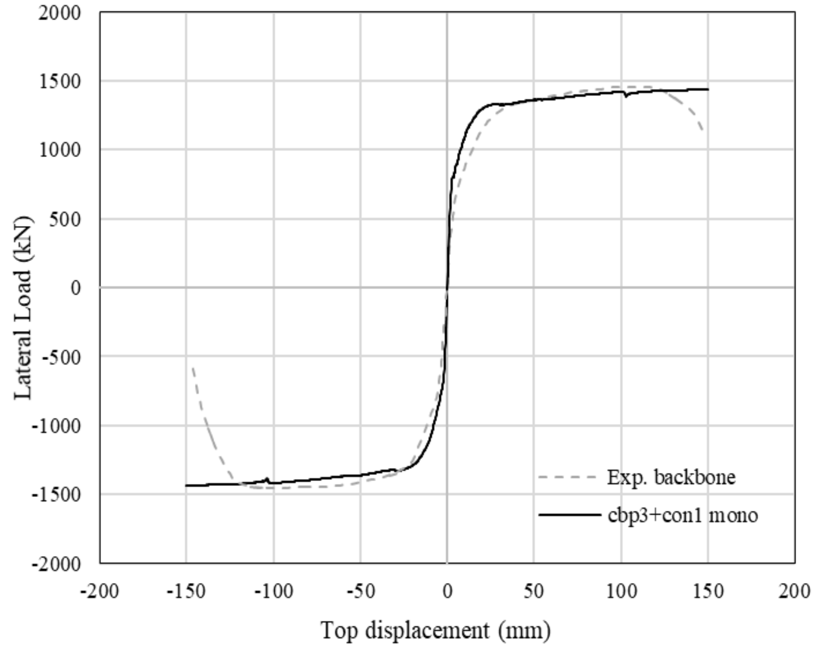

Figure 3-14: Validation of the 1D model with beam-column elements and ‘con1’ material model for the slender wall under monotonic loading

The numerical load-displacement curve under cyclic loading is compared against the results of the experimental test in Figure 3-15. It is observed that the 1D beam-column model successfully captures the main characteristics of the experimental cyclic response, including the progressive global stiffness degradation with the increasing drift level, the strength degradation in the last two cycles, and the pinching behaviour for each hysteresis loop. The lateral stiffness is well predicted during loading and reloading and by increasing the level of displacement. By contrast, the lateral stiffness during unloading is overestimated, resulting in a more considerable plastic deformation at zero horizontal loads which is attributed to the elastic unloading/reloading stiffness assumed in the uniaxial concrete material model.

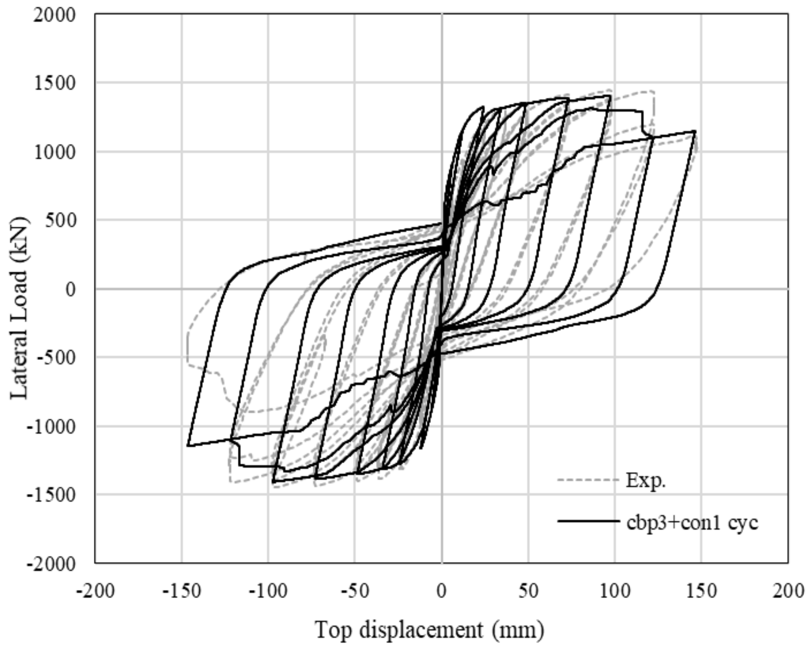

Figure 3-15: Validation of the 1D model with beam-column elements and ‘con1’ material model for the slender wall under cyclic loading

3.3.2.3 2D shell element modelling

The slender wall has also been modelled using the 2D FE representation with shell elements in ADAPTIC introduced in Section 3.2.2. Figure 3-16 shows the FE mesh with ‘csl4’ 4-noded elements for the wall specimen. A top stiff component representing a loading beam is introduced into the model to uniformly distribute the vertical axial load (9.12 N/mm^3) onto the top of the wall. The in-plane horizontal forces are applied utilising a spreader element available in ADAPTIC, which rigidly connects a master non-structural node located in the proximity of the wall (Figure 3-16) with a set of slave nodes along the stiff top part. The prescribed acceleration history representing the specific monotonic/cyclic loading condition is directly applied at the master node only, while the associated resistance forces are uniformly distributed onto the connected slave nodes. Uniform mesh sizes have been assumed for the wall and the loading beam, with element lengths of 244×244 mm^2 for the shell elements of the wall and 244×100 mm^2 for those of the loading beam, resulting in a total number of 210 shell elements. Each element features 4×4×2 Gauss points with 4×4 integration points in the plane of the wall and two integration layers in the out-of-plane direction. In addition, 232 concentrated mass elements are attached to all the nodes of the FE mesh except for the nodes at the bottom edge which are fully restrained. Table 3-3 lists the material parameters for the numerical simulations, where the concrete compressive and tensile strengths are the same as those employed in Section 3.3.2.2. The Poisson's ratio and tensile softening slope are assumed as 0.2 and 1000, respectively. The last seven parameters in Table 3-3 related to the concrete compressive and shear behaviours have been calibrated from experiments (Elghazouli & Izzuddin, 2004).

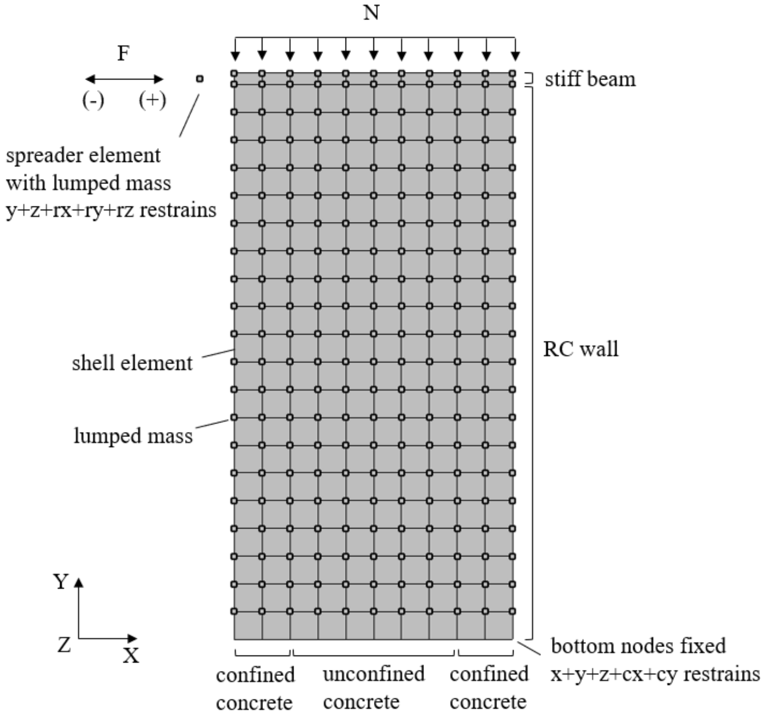

Figure 3-16: 2D shell element model for the slender wall specimen

As shown in Figure 3-17, the numerical results under monotonic loading condition show a reasonably good accuracy when compared to the experimental data with a 9% overestimation of the actual horizontal load capacity. Nevertheless, the numerical prediction implies a stiffer response since the predicted load capacity of 1590kN is reached at 21.2mm horizontal displacement compared to the experimental peak load of 1458kN at 99.3mm displacement. The initial stiffness of the wall is well simulated, whereas the post-elastic stiffness is overestimated before reaching the maximum load capacity. The numerical response features a relatively flat softening post-peak branch, where minor oscillations occur due to the development of cracks during loading.

Figure 3-18 shows an experimental-numerical comparison under cyclic loading condition. It can be seen that the employed shell element representation with the biaxial concrete model ‘con11’ provides a good prediction of the variation of the horizontal top displacement against the applied horizontal force. The main features of the experimental cyclic response are well represented, including the pinching behaviour developing in the first few cycles of the experiment, but the analysis terminates at 50 mm displacement due to numerical problems.

Table 3-3: Material parameters of concrete model ‘con11’

No.	Parameter	Definition	Values for	
			Unconfined concrete	Confined concrete
1	E_{c1}	Young’s modulus	34514 MPa	
2	ν	Poisson’s ratio	0.2	
3	f_t	Tensile strength	3.59 MPa	
4	a_t	Tensile softening slope	1000	
5	f_c	Compressive strength	41.37 MPa	48.59 MPa
6	s_c	Normalised initial compressive strength	0.4	
7	r_c	Normalised residual compressive strength	0.4	
8	m_c	Normalised strain increment beyond ε_c	1.0	
9	b_c	Factor for biaxial compressive interaction	0.6	
10	β_c	Elastic shear retention factor	0.4	
11	Φ_c	Factor scaling direct tensile stresses for shear interaction	0.4	
12	r_s	Normalised shear softening relative to direct tensile softening	0.4	

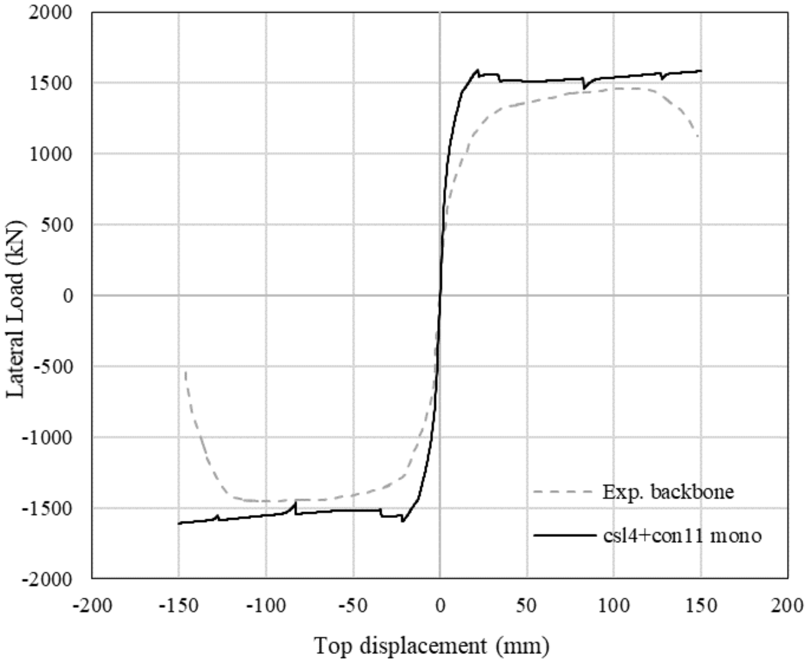

Figure 3-17: Validation of the 2D FE description with 2D shell elements and ‘con11’ material model for the slender wall under monotonic loading

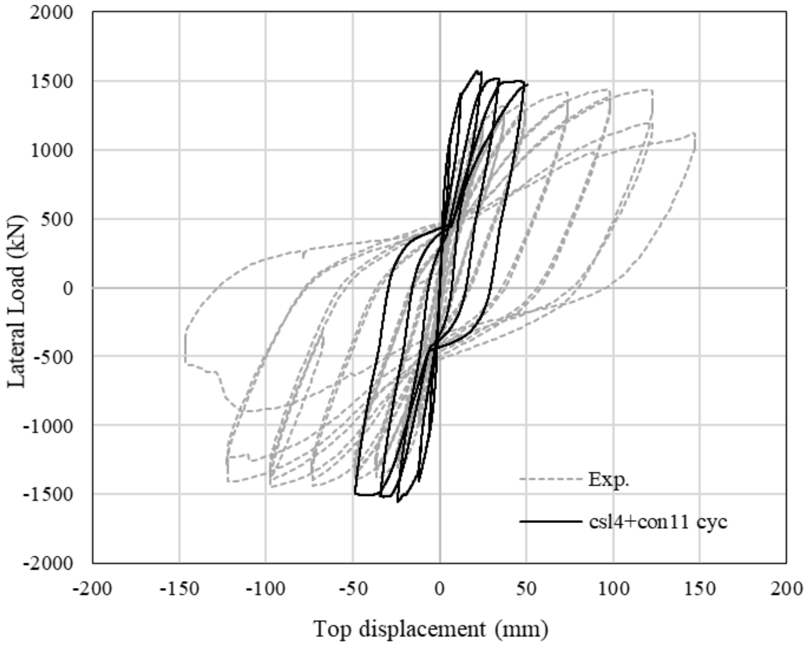

Figure 3-18: Validation of the 2D FE description with 2D shell elements and ‘con11’ material model for the slender wall under cyclic loading

3.3.2.4 3D solid element modelling

Finally, the slender RC wall has been analysed by employing the detailed 3D modelling approach with solid elements described in Section 3.2.3. The wall is discretised by two layers of solid elements over its thickness; the steel reinforcement bars are individually represented by embedded bar elements and modelled by macro-segments across the solid elements. The FE mesh consists of 420 8-noded solid elements, 504 steel macro-segments and 694 lumped masses, as shown in Figure 3-19. The out-of-plane displacements at the middle nodes at the boundary of the two layers are restrained, and the bottom nodes are modelled as fully restrained against all translations. Similar loading conditions as considered in the 2D shell model are applied here. The vertical uniformly distributed load of 0.0299 N/mm^3 is imposed on the stiff beam at the top of the wall and kept constant during analysis. In addition, a spreader element distributes the imposed horizontal loads at six nodes on the left face of the stiff beam, which further transfers the loads to the wall.

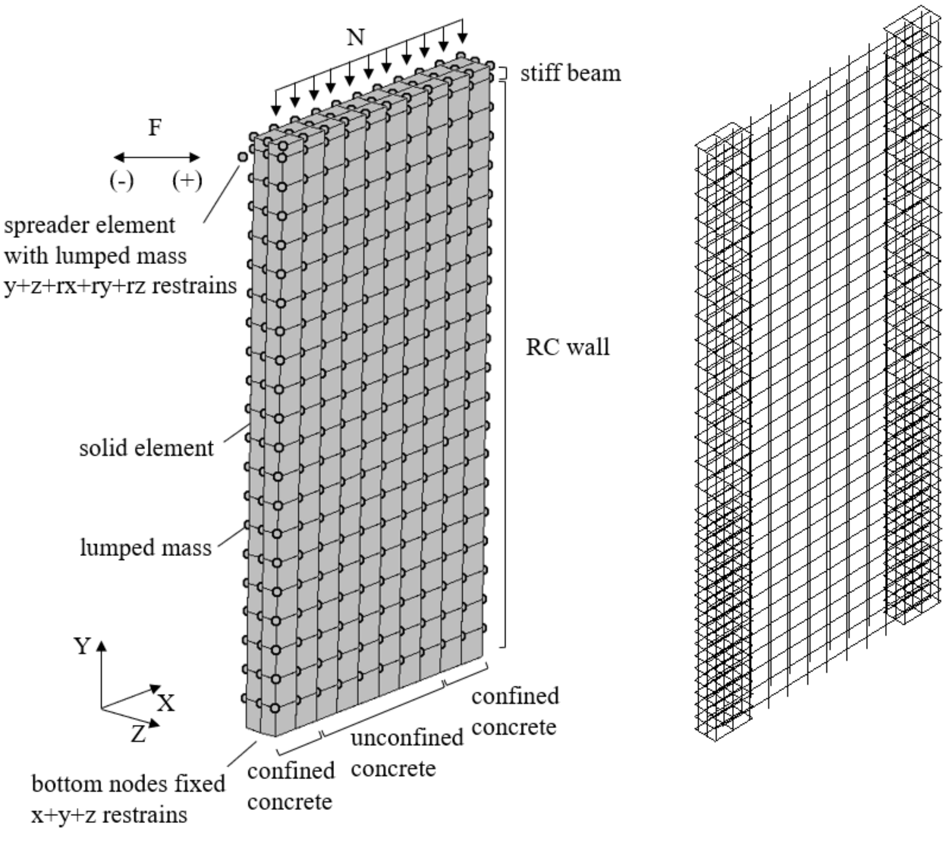

(a) (b)

Figure 3-19: 3D solid model for the slender wall specimen: (a) 3D FE mesh; (b) reinforcement mesh

The concrete material parameters employed for the numerical analysis are given in Table 3-4. The elastic properties, compressive strength and tensile strengths are the same as those used in Section 3.3.2.3. The remaining parameters define the concrete behaviour under multiaxial stress states. In particular, the ratio of the biaxial to the uniaxial compressive strength equal to 1.16 is defined based on the experimental findings by Kupfer & Gerstle (1973). Typical values of the dilation angle $\psi = 35°$ and the flow eccentricity $\epsilon = 0.1$ are adopted. The stiffness recovery factors define a fully recovered compressive stiffness from tension to compression and a zero recovery of tensile stiffness from compression to tension in the case of uniaxial cyclic loading. Moreover, the fracture energy, referring to the energy required to propagate a tensile crack of unit area, is calculated according to Model Code 2010 (Fib, 2013) by:

$$G_t = 73 \cdot {f_c}^{0.18} \tag{3-25}$$

The remaining parameters μ, $\tilde{f}_y$, k_{co} and ρ_c are calibrated to achieve a good agreement with the experimental response.

The experimental backbone curve is represented by the detailed 3D FE model with reasonable accuracy, as shown in Figure 3-20. The predicted initial stiffness and maximum load are close to the experimental values. The discrepancies in the post-peak response are due to the degradation of strength, which characterises the actual behaviour under cyclic loading but not the numerical prediction under monotonic loading condition. On the other hand, the numerical curve under cyclic loading in Figure 3-21 shows an excessive degradation of strength, which is associated to a rapid accumulation of damage in the concrete material. Furthermore, it can be seen that the detailed 3D FE discretisation with the CDPM for concrete does not offer an accurate representation of the actual pinching characteristics displayed by the experimental cyclic load-displacement curve.

Table 3-4: Material parameters of concrete model 'cdpm2'

No.	Parameter	Definition	Values for Unconfined concrete	Values for Confined concrete
		Elastic properties		
1	E_{c1}	Young's modulus	34514 MPa	
2	ν	Poisson's ratio	0.2	
		Multiaxial behaviour		
3	$\tilde{f}_b$	Ratio between biaxial and uniaxial compressive strength	1.16	
4	ψ	Dilation angle	35°	
5	ϵ	Flow potential eccentricity	0.1	
6	K_c	Defined in Eq. (3-12)	0.66	
7	w_t	Tensile stiffness recovery factor	0	
8	w_c	Compressive stiffness recovery factor	1	
		Tensile behaviour		
9	f_t	Tensile strength	3.59 MPa	
10	G_t	Fracture energy	0.143 N/mm	
11	μ	Parameter controlling unloading stiffness in tension	0.8	
		Compressive behaviour		
12	f_c	Compressive strength	41.37 MPa	48.59 MPa
13	$\tilde{f}_y$	Ratio between uniaxial yielding stress and maximum strength in compression	0.3	
14	k_{c0}	Plastic strain corresponding to f_c	0.002	
15	ρ_c	Ratio of k_{co} at onset of compressive damage	1.0	

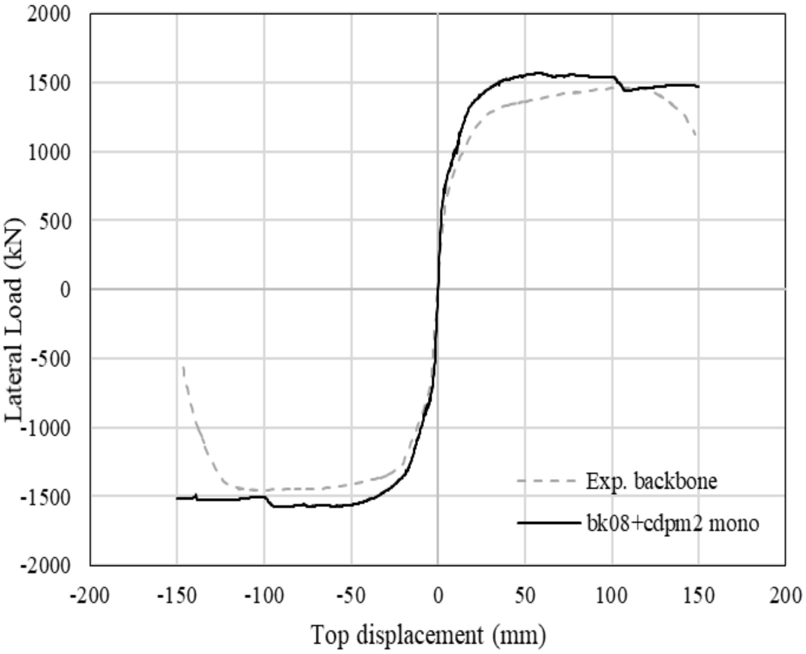

Figure 3-20: Validation of the model with 3D solid elements and concrete material model 'cdpm2' for the slender wall under monotonic loading

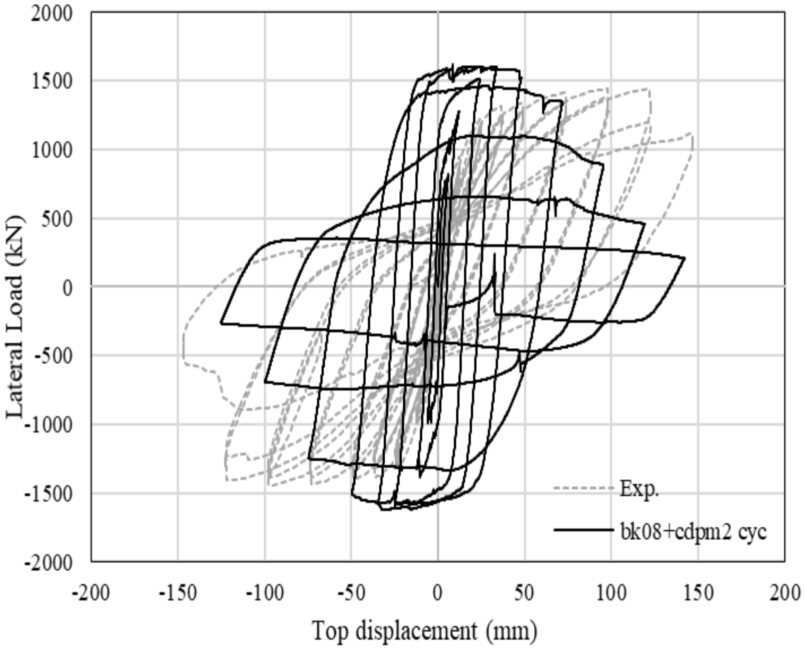

Figure 3-21: Validation of the model with 3D solid elements and concrete material model 'cdpm2' for the slender wall under cyclic loading

3.3.3 Short wall test

3.3.3.1 Experimental program overview

The specimen LSW3 tested by Salonikios *et al.* (1999) has been considered in subsequent numerical-experimental comparisons. The short RC wall sample has 1200mm length, 1200mm height and 100mm thickness. It is subjected to a constant axial force and cyclic in-plane horizontal loads as the slender wall analysed before. Figure 3-22 shows the reinforcement details of the wall specimen LSW3. The web reinforcement utilises two orthogonal grids with 4.2mm diameter bars spaced at 100mm, leading to a reinforcement ratio 0.277% that meets the minimum requirements 0.2% and 0.25% as prescribed in EC2 (BSI, 2004a) and ACI 318-14 (2014). Six 8mm diameter bars are used for longitudinal bars in the confined boundary elements. This results in a reinforcement ratio of 1.3 %, which fulfils the 0.5% requirement in EC8 (BSI, 2004b). The 4.2mm transverse reinforcements spaced at 27mm are used to confine the longitudinal bars, giving a reinforcement ratio 1.7%.

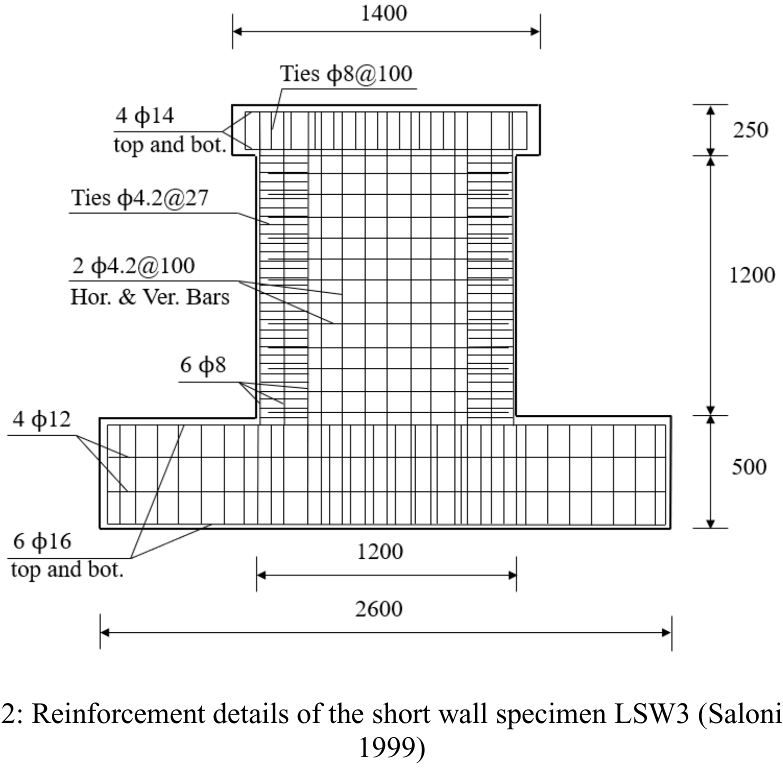

Figure 3-22: Reinforcement details of the short wall specimen LSW3 (Salonikios *et al.*, 1999)

The experimental set-up is schematically shown in Figure 3-23. In the experiment, the constant axial load was imposed by a vertical hydraulic actuator, which was attached to a large steel beam sitting on two columns. The wall and the columns were fixed to the strong floor of the laboratory by footings. The lateral load was applied cyclically on the stiff beam at the top of the wall. It is important to note that although some researchers argue that using a stiff top beam would lead to overestimating the shear capacity of a RC wall, Salonikios *et al*. (1999) stated that this loading arrangement resembles the actual condition of a typical RC wall within a building structure, where it is usually connected to stiff RC beams and at the different floor levels. The experimental loading protocol adopted the typical procedure of applying three constant displacement amplitude cycles per ductility level up to failure. In the experiment, a displacement control procedure was used except for the first cycle in the elastic range. The loading was applied with 2mm increments up to reaching 16mm. It was followed by 4mm increments up to failure, which was assumed after reaching a 75% force reduction after peak load.

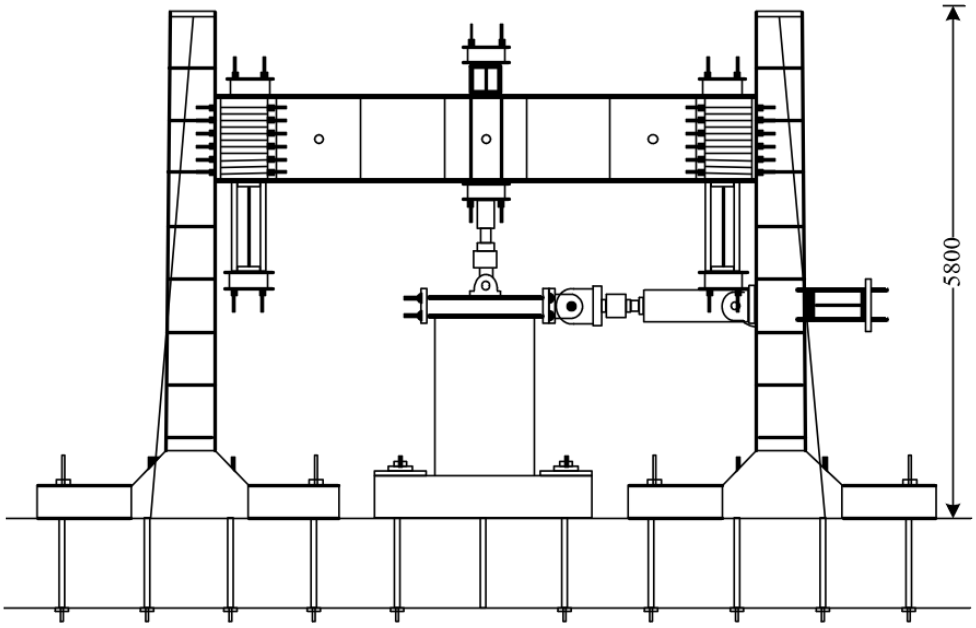

Figure 3-23: Schematic test set-up for the experimental test on the short wall specimen LSW3 (Salonikios *et al*., 1999)

3.3.3.2 1D beam-column element modelling

The wall specimen is firstly simulated using the 1D modelling approach with elasto-plastic beam-column elements. A model with 10 beam-column elements, similar to the discretisation introduced in Section 3.3.2.2, is used in the numerical simulations. Table 3-5 and Table 3-6 summarise the employed material parameters for steel reinforcement and concrete. The only material properties available from the experiment are the yield strength of steel f_{sy} and the compressive strength for unconfined concrete f_{c1}, whereas the remaining parameters are specified consistently the material properties set out in Table 3-1 and Table 3-2. For steel reinforcement, a strain hardening parameter $\mu_s = 0.01$ is considered.

Table 3-5: Material parameters of steel model ‘stl1’

E_s [GPa]	f_{sy} [MPa]	μ_s [−]
200	585	0.01

Table 3-6: Concrete material parameters for the wide column model of the short wall sample

	$\mathrm{E_{c1}}$ [MPa]	$\mathrm{f_{c1}}$ [MPa]	$\mathrm{E_{c2}}$ [MPa]	$\mathrm{f_{c2}}$ [MPa]	$\mathrm{E_{t1}}$ [MPa]	$\mathrm{f_t}$ [MPa]	$\mathrm{E_{t2}}$ [MPa]
Confined concrete	32280	33.85	-449	6.77	28746	2.49	-449
Unconfined concrete	28746	23.90	-5893	4.78	28746	2.49	-5893

Figure 3-24 and Figure 3-25 display experimental-numerical comparisons for the considered wall under monotonic and cyclic loading conditions. The shear resistances of this short wall specimen calculated based on the EC2 (BSI, 2004a) and ACI 318 (2009) are 249kN and 235kN, which are very close to the experimental values. It is noted that a significant stiffer response of the wall is predicted compared to the experimental backbone curve. The numerical cyclic curve for the first sixth cycles is plotted in Figure 3-25. The comparison against the experimental curve confirms that the adopted 1D representation cannot capture the actual strength degradation under cyclic loading. Furthermore, the numerical curve features a stiffness increase in the loading branch at the sixth cycle, which is more pronounced in the positive quadrant and not observed in the experimental response.

Figure 3-26 shows the numerical response at the sixth cycle in the positive quadrant, where AB and BC represent the loading and unloading paths, respectively. The change in stiffness in the loading branch is deemed to be due to the closure of cracks when the wall is loaded. This is shown in Figures 3-27 and 3-28, where the stress-strain curves of steel reinforcement and concrete at the extreme fibres of the wall cross section are plotted. These figures illustrate that: (i) steel reinforcement at the extreme compressive and tensile fibres experiences strain hardening; (ii) concrete crack is closed developing compressive resistance at the extreme compressive fibres and then re-opened to experiencing softening behaviour; and (iii) the concrete at the extreme tensile fibre is within the fully cracked zone with zero resistance.

Considering the results above, it can be confirmed that the simplified model with 1D beam-column elements is not suitable for modelling RC short walls. This is expected, since shear deformation and potential shear damage are neglected according to the Euler-Bernoulli hypothesis assumed in the beam-column element formulation.

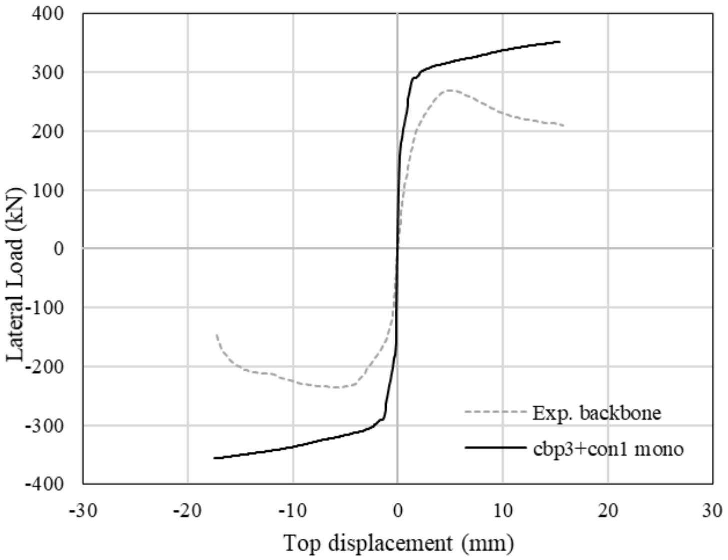

Figure 3-24: Validation of the 1D model with beam-column elements and concrete material model 'con1'for short wall under monotonic loading

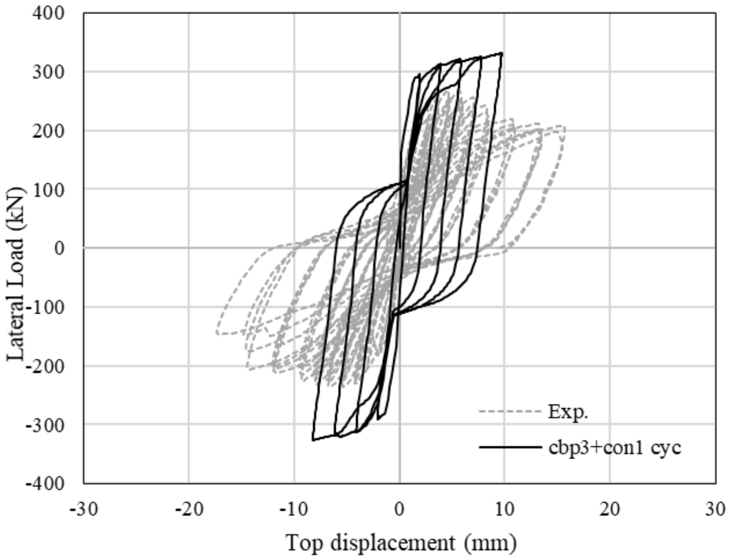

Figure 3-25: Validation of the 1D model with beam-column elements and concrete material model 'con1'for short wall under cyclic loading

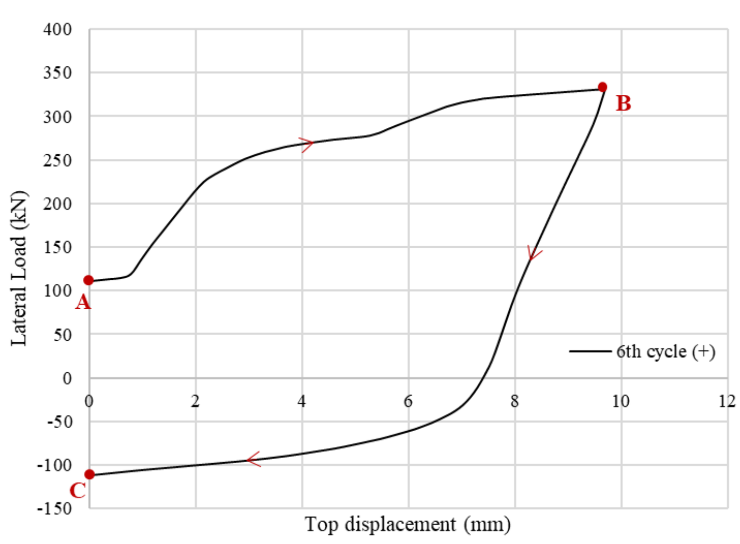

Figure 3-26: Force-displacement curve at the 6th loading/unloading cycle (+ve)

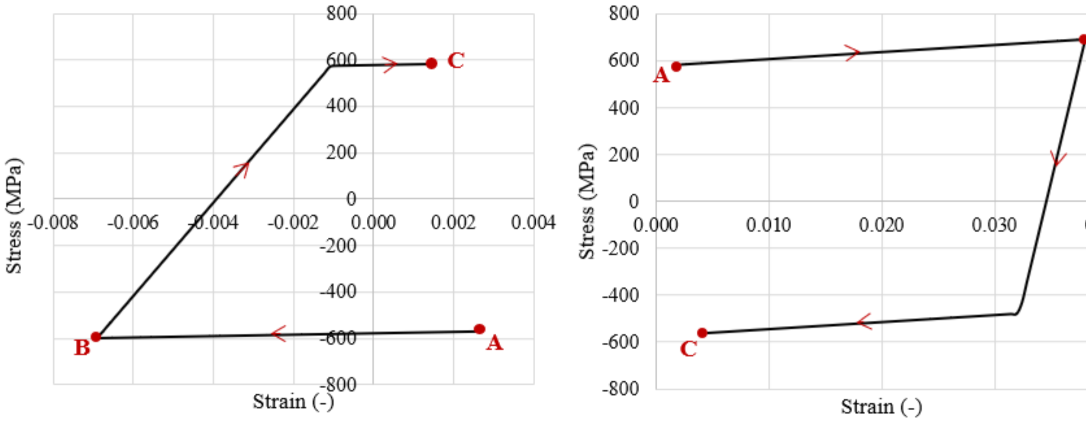

(a)

(b)

Figure 3-27: Stress-strain curves of steel reinforcements at extreme (a) compressive and (b) tensile fibres

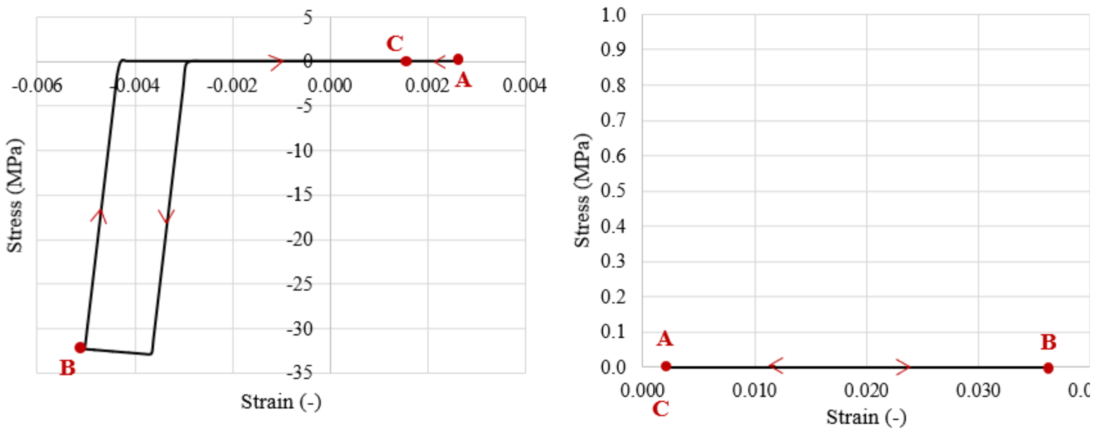

(a)

(b)

Figure 3-28: Stress-strain curves of concrete at extreme (a) compressive and (b) tensile fibres

3.3.3.3 2D shell element modelling

In this section, the analysed short wall specimen is modelled using 2D shell elements with a biaxial CDPM for concrete, which is a condensed version of the material model 'cdpm2' allowing for plane stress condition. The FE mesh generated for the numerical simulations consists of 110 shell elements and 133 lumped masses attached to the nodes. Moreover, the boundary conditions and applied loads are similar to those employed in the 2D representation for the slender wall in Section 3.3.2.3. The material parameters for steel reinforcement and concrete are reported in Table 3-5 and Table 3-7.

Table 3-7: Material parameters of concrete model 'cdpm2'

No.	Parameter	Definition	Values for	
			Unconfined concrete	Confined concrete
		Elastic properties		
1	E_{c1}	Young's modulus	32282 MPa	
2	ν	Poisson's ratio	0.2	
		Tensile behaviour		
3	f_t	Tensile strength	2.49 MPa	
4	G_t	Fracture energy	0.129 N/mm	
5	μ	Parameter controlling unloading stiffness in tension	0.2	
		Compressive behaviour		
6	f_c	Compressive strength	23.90 MPa	33.85 MPa
7	$\tilde{f}_y$	Ratio between uniaxial yielding stress and maximum strength in compression	0.3	
8	k_{c0}	Plastic strain corresponding to f_c	0.0015	
9	ρ_c	Ratio of k_{co} at onset of compressive damage	1.0	

Figure 3-29 and Figure 3-30 compare the predicted monotonic and cyclic responses with the experimental results. As shown in Figure 3-29, the monotonic numerical response in the negative quadrant achieves a better agreement with the experimental backbone curve than in the positive quadrant. The initial stiffness and the displacements at peak load are well simulated. Moreover, the numerical model predicts a softening post-peak response, which has not been predicted by the 1D modelling approach. Regarding the numerical cyclic curve shown in Figure 3-30, higher energy dissipation generated within the first few cycles is observed as compared to the experimental response. Once again, the results obtained confirm that the employed CDPM for concrete does not enable capturing the pinching characterising of the actual cyclic response. Besides, the predicted cyclic curves feature a significant reduction in strength when the wall is unloaded at the fourth cycle for a displacement of around -3mm. This is due to the predicted shear sliding failure developing at the bottom part of the wall model, as shown by the deformed shape in Figure 3-31(a) with the concrete shear stress contour. Figure 3-31(b) provides a schematic representation of the actual cracking patterns observed at the end of the experimental test, where flexural cracks initiated from one edge are crossed by inclined shear cracks developed from the other edge. The concrete shear stress obtained from the numerical models gives an indication of the shear critical regions. Apart from the sliding shear at the wall base, the numerical model suggests the development of the characteristic criss-cross cracks similar to the experimental cracking pattern.

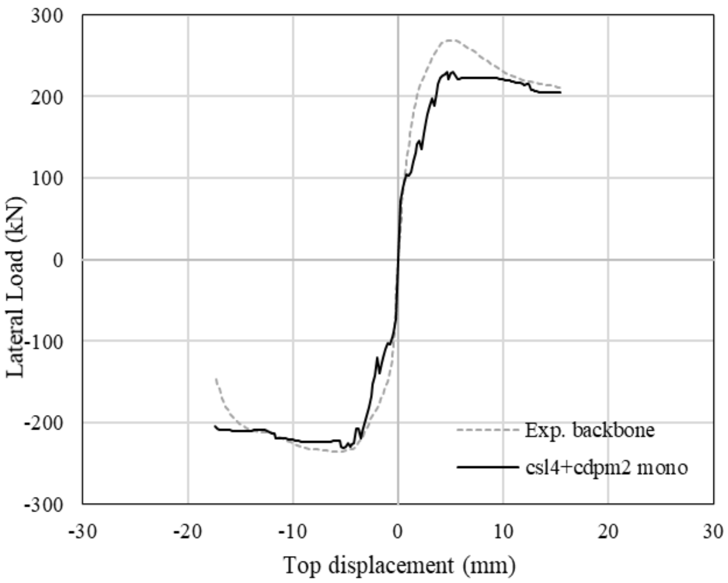

Figure 3-29: Validation of 2D FE model with 2D shell elements and concrete material model ‘cdpm2’ for the short wall under monotonic loading

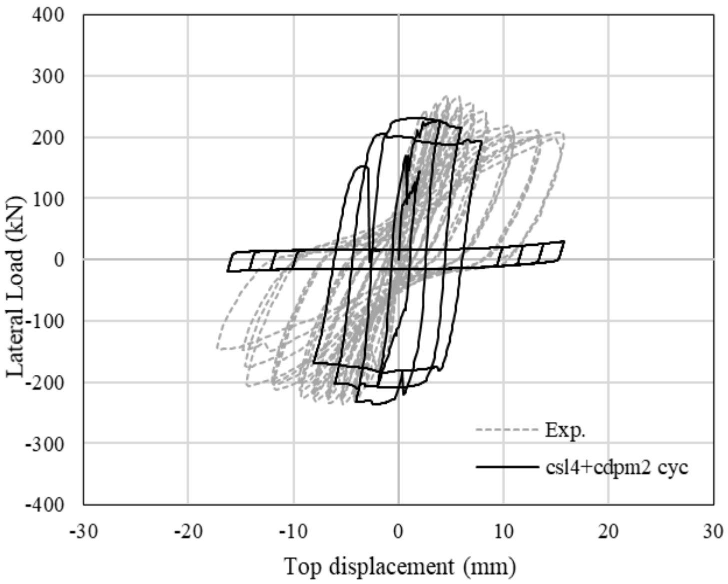

Figure 3-30: Validation of 2D FE model with 2D shell elements and concrete material model 'cdpm2' for the short wall under cyclic loading

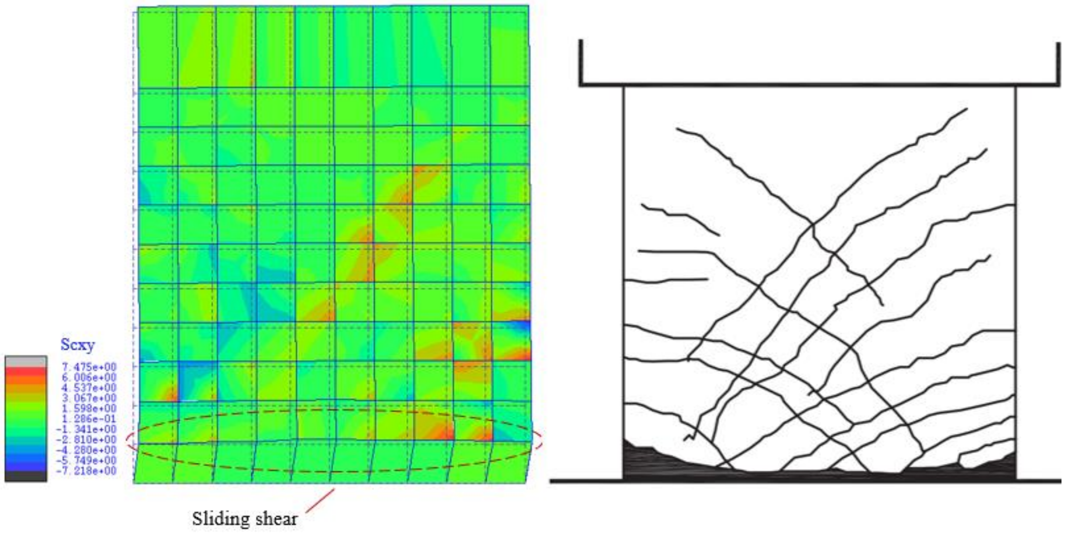

(a) (b)

Figure 3-31: Short wall under cyclic loading: (a) predicted deformed shape and concrete shear stress contours at -3mm (4th cycle) and (b) experimental cracking patterns at the end of test (Salonikios *et al*., 1999)

3.3.3.4 3D solid element modelling

The detailed 3D modelling approach described in Section 3.2.3 is employed here for the numerical simulation of the experimental short wall. The FE mesh consists of 420 solid elements, 504 embedded bar elements and 694 lumped masses. The wall specimen is discretised by a mesh of 120×120×50mm^3 solid elements, where 10×10×2 elements are arranged along the height, the length and the thickness of the wall. The same sets of material parameters given in Table 3-5 and Table 3-7 are used for the numerical simulations, expect for $\tilde{f}_y$ which is taken as 0.8.

Figure 3-32 and Figure 3-33 compare the numerical results against the experimental curves for the monotonic and cyclic analyses. It can be observed that the predicted monotonic response is closer to the experimental backbone curve in the negative quadrant, which is consistent with the finding from the 2D FE model. Despite the initial stiffness and the initial post-elastic response are well predicted, the numerical model does not reproduce the softening branch of the experimental backbone curve. This has been found also in the previous numerical investigations, and it is due to the actual strength degradation under cyclic loading, which affects the experimental backbone curve, but it is not allowed for in the numerical simulation under monotonic loading. On the other hand, the numerical response under cyclic loading is characterised by realistic strength and stiffness degradation, as shown in Figure 3-33.

The predicted deformed shape and tensile damage in the wall model at 10mm top displacement are displayed in Figure 3-34(a). The damage distribution representing the cracks developed in the wall tends to reproduce the experimental cracking patterns shown in Figure 3-31. The bottom part of the wall exhibits a sliding shear deformation, leading to strength degradation at 10mm, as shown in Figure 3-33. In addition, out-of-plane deformations are observed in the confined concrete region at the two bottom edges of the wall, which represent the spalling of the concrete cover also observed in the physical test.

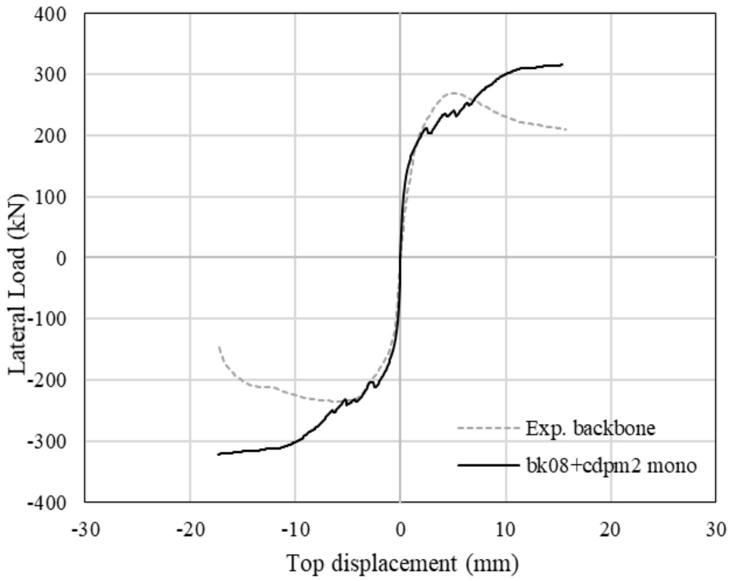

Figure 3-32: Validation of the 3D FE model with solid elements and concrete material model ‘cdpm2’ for the short wall under monotonic loading

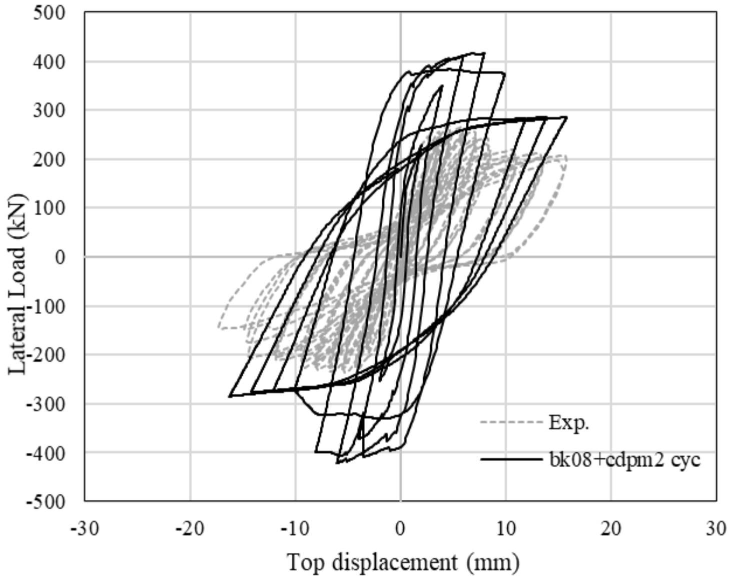

Figure 3-33: Validation of the 3D FE model with solid elements and concrete material model ‘cdpm2’ for the short wall under cyclic loading

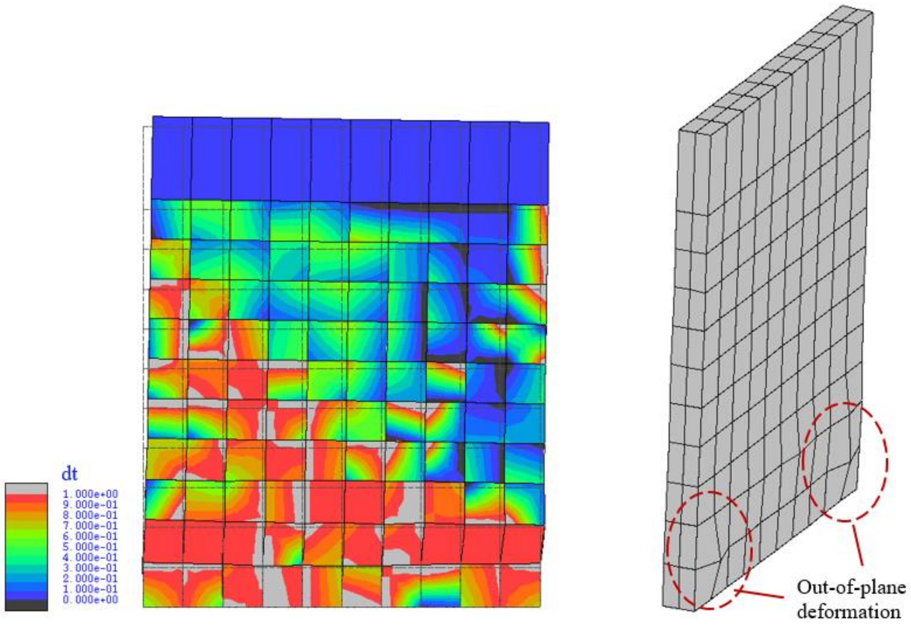

(a) (b)

Figure 3-34: 3D short wall model under cyclic loading: (a) predicted deformed shape and damage at 10mm (5th cycle); and (b) out-of-plane deformation at the end of the analysis

Additional numerical analyses are performed to investigate the influence of different material parameters on the monotonic response. As mentioned previously, a long duration dynamic analysis procedure is utilised to obtain the monotonic response. Initial numerical investigations showed that the numerical results may exhibit significant fluctuations due to potential dynamic effects. To minimise dynamic oscillations, a sensitivity study has been performed assuming different initial velocities of 0.01mm/s, 0.1mm/s, 0.5mm/s and 1mm/s. It has been found that the numerical results based on 0.01mm/s or 0.1mm/s offer good numerical stability, whereas fluctuations manifest when larger velocities are assumed. Thus, in subsequent numerical simulations on the short wall specimen the initial velocity has been set to 0.01mm/s.

The material parameters considered in the parametric studies are the dilation angle ψ, fracture energy G_t, tensile strength f_t, plastic strain k_{c0} and steel strain hardening parameter μ. The dilation angle ψ accounts for the volume change in a concrete specimen when it experiences large inelastic strains. Typical values of the dilation angle adopted in the CDPM from literature are in the range of 10-50° (Malm, 2006; Moharram *et al.*, 2017; Sümer & Aktaş, 2015). Figure 3-35 shows the numerical results considering ψ=15°, 25°, 35°, and 45°. Sudden strength drops are found for dilatancy values smaller than 35°, which might be due to the release of the elastic energy upon the formation of major cracks and the stress redistribution within the wall. In general, the use of smaller ψ values produces a more brittle behaviour of concrete. Because of dilatancy, the confinement pressure increases, leading to enhanced concrete ductility.

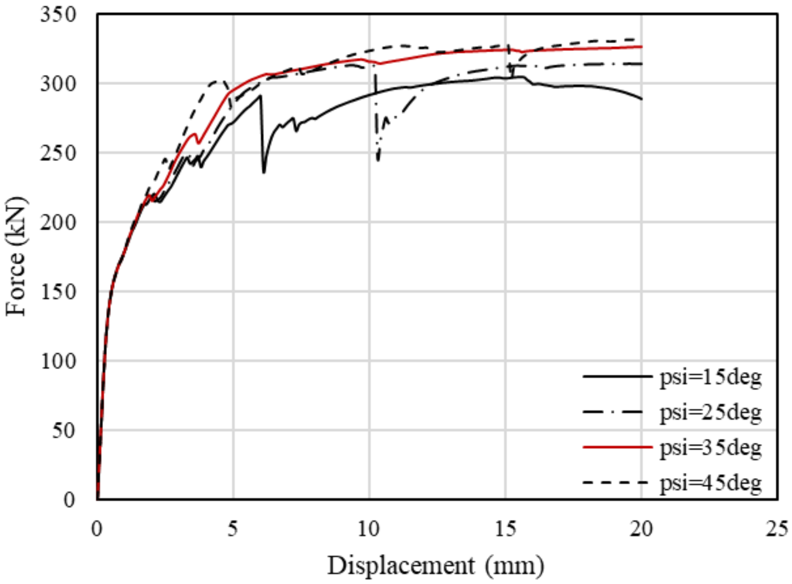

Figure 3-35: Influence of ‘cdpm2’ parameter ψ on the response

The fracture energy refers to the energy required to obtain a stress-free crack within a unit area. It defines the area under the stress-strain curve after attaining peak load under tension. According to Bangash (2001), the fracture energy of normal concrete typically range from 0.05N/mm to 0.2N/mm. Figure 3-36 plots the force-displacement curves with fracture energy varying from $0.5G_t$ to $10G_t$, where G_t=0.129N/mm has been calculated according to Model Code 2010 (Fib, 2013). A very high fracture energy value (e.g. $10G_t$) implies an elastic perfectly plastic tensile behaviour, thus resulting in a significant increase in the wall capacity. On the other hand, a reduction of the wall resistance is observed for $0.5G_t$.

It is recalled that the concrete tensile strength is assumed using Eq. (3-24) according to Model Code 2010 (Fib, 2013). Model Code 2010 (Fib, 2013) also recommends that the lower and upper bound values of the characteristic tensile strength can be estimated by $0.7f_t$ and $1.3f_t$ when experimental data is not available. In this respect, Figure 3-37 presents the monotonic responses considering: $0.01f_t$=0.025MPa, $0.25f_t$=0.62MPa, $0.5f_t$=1.25MPa, f_t=2.49MPa and $1.5\ f_t$=3.74MPa, where f_t is the tensile strength reported in Table 3-7. As expected, the tensile strength plays an important role in the response prediction, particularly before reaching the peak load. The numerical curve based on an unrealistic value of $0.01f_t$ produce results with oscillations owing to the significant cracks developed. It is also noted that the numerical simulation using a large value of $1.5f_t$ causes convergence problems.

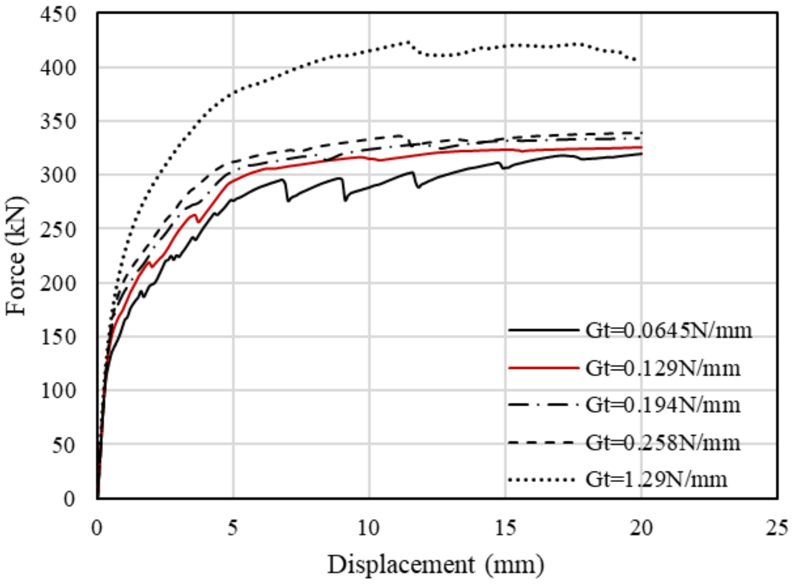

Figure 3-36: Influence of ‘cdpm2’ parameter G_t on the response

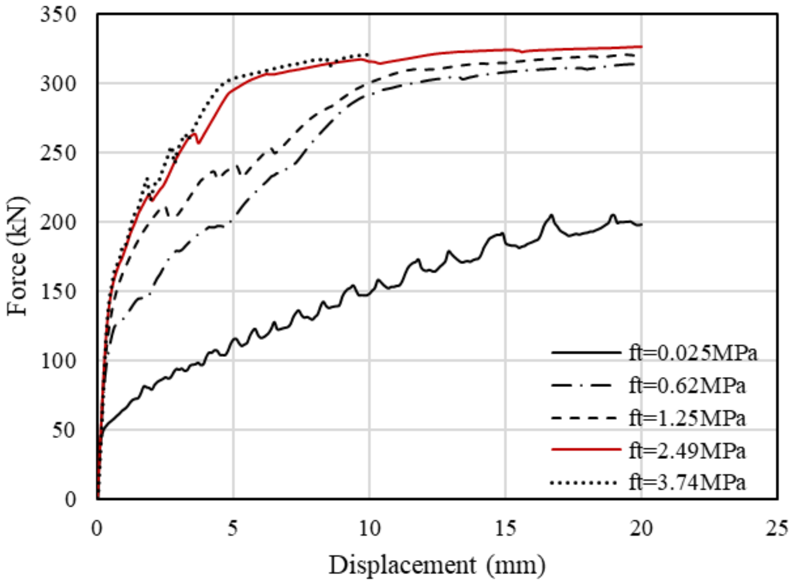

Figure 3-37: Influence of ‘cdpm2’ parameter f_t on the response

Figure 3-38 shows the impacts of different plastic strains k_{c0} on the monotonic response. The considered value varies from 0.005 up to 0.0025 with an increment of 0.005. It can be observed that the use of the smallest plastic strain, 0.005, predicts softening regime accompanied by jumps due to potential compressive damage. The higher plastic strain values imply that the response tends to be elastic perfectly plastic under compression. With increasing plastic strains, the divergence of the post-peak response is remarkably reduced, and minor hardening is observed for larger values of plastic strains. Lastly, Figure 3-39 investigates the influences of steel strain hardening on the response, which indicates that its impact on the post-peak branch is less pronounced than the concrete material parameters.

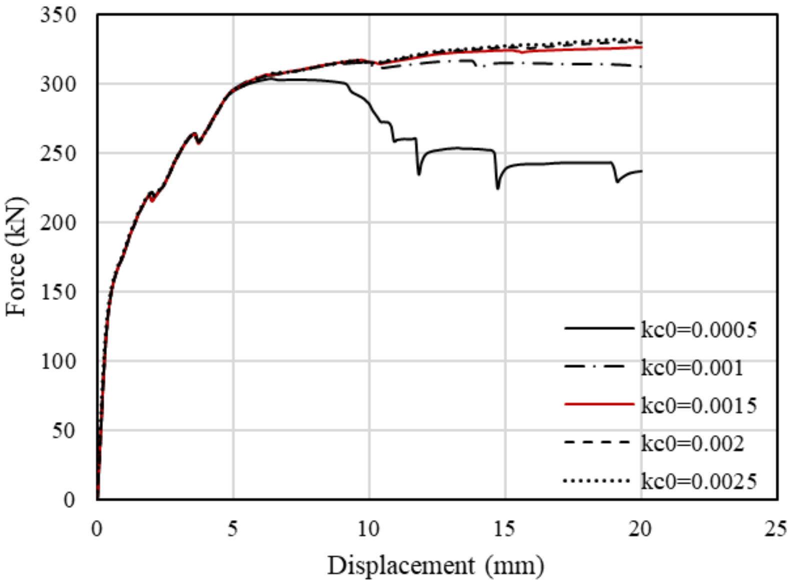

Figure 3-38: Influence of ‘cdpm2’ parameter k_{c0} on the response

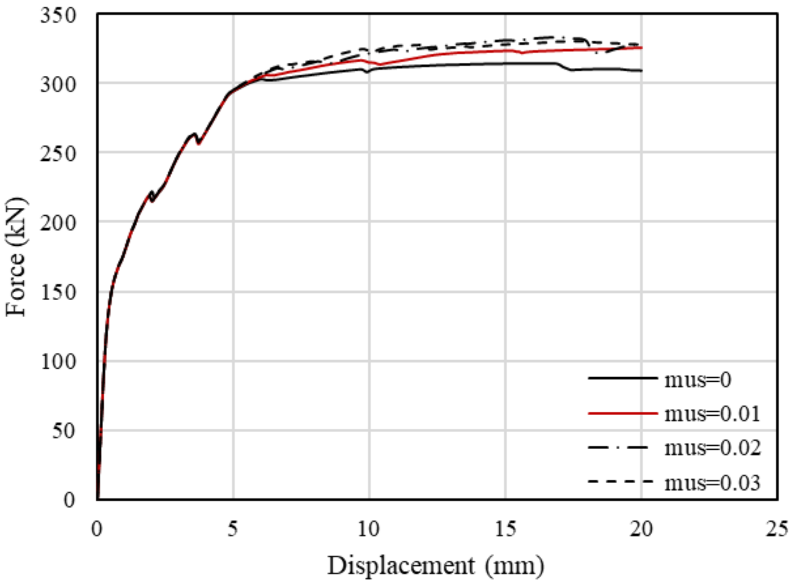

Figure 3-39: Influence of steel strain hardening on the response

3.4 Discussion

This section discusses the numerical results obtained by using the three alternative existing modelling strategies for the simulation of slender and short RC walls under monotonic and cyclic loading. Focus is placed on accuracy, computational efficiency, and robustness of the alternative wall models. It has been found that the 1D wide column representation is the most efficient and accurate in reproducing the monotonic and cyclic response of the analysed slender wall. By contrast, current 2D and 3D FE models show reduced potential. The 2D shell model incorporating the biaxial concrete model 'con11' suffers from convergence issues, especially under cyclic loading conditions. On the other hand, the primary limitation of the concrete material model 'cdpm2' is that the model cannot capture the pinching features of the actual wall response. However, the concrete damage plasticity model is capable of predicting strength and stiffness degradations which are other key characteristics of the actual wall behaviour under cyclic loading conditions.

The numerical predictions of the short wall response based on the current three modelling strategies are less accurate than the results obtained for the slender wall specimen. The 1D beam modelling approach assuming the Euler-Bernoulli hypothesis is not suitable for modelling short walls dominated by shear deformation. The use of the 'cdpm2' concrete model in 2D and 3D FE descriptions requires further calibration of the input material parameters to achieve a close agreement with the experimental response. Moreover, the CDPM does not lead to a realistic representation of the actual pinching features of the hysteretic response under cyclic loading.

Table 3-8 compares the computational cost of the different numerical modelling approaches for the considered wall specimens. As expected, the 3D FE models with a large number of DOFs require significant running time, especially under cyclic loading conditions. Moreover, additional time is required for creating the 3D mesh for both concrete and the embedded steel macro-segments and for the calibration of the input material parameters. This indicates a practical limitation of the adopted detailed 3D modelling strategy to simulate the nonlinear seismic response of a large scale RC structure as realistic building structures with RC shear walls. It is worth noting that the 2D shell model requires comparable time for the cyclic analyses as the 3D solid model, which is related to the iterative biaxial condensation procedure in the 2D concrete material model. Regarding the robustness of the different models, the slender wall simulations generally achieve a good convergence. However, the 2D shell and 3D solid models may suffer from convergence issues, particularly under cyclic loading conditions.

Table 3-8: Summary of numerical models and computational times

Wall type	Model	Concrete model	Steel idealisation	No. of nodes	No. of elements	Wall-clock time (hr:min:sec)	
						Mono.	Cyc.
Slender	1D beam	con1	fibre	11	20	0:0:4	0:1:33
	2D shell	con11	smeared	243	443	0:21:35	1:10:55
	3D solid	cdpm2	embedded	727	1618	3:1:24	**14:25:43**
Short	1D beam	con1	fibre	11	20	0:0:0.4	0:0:2
	2D shell	cdpm2 (condensed)	smeared	133	233	0:35:4	1:0:28
	3D solid	cdpm2	embedded	398	1251	2:22:46	1:19:24

3.5 Concluding remarks

Nonlinear analysis of RC walls under seismic loading requires accurate and realistic numerical descriptions. The chapter gives a critical appraisal of existing modelling strategies in ADAPTIC to analyse RC walls under monotonic and cyclic loading conditions. The conclusions drew in this chapter are related to the material models implemented in ADAPTIC. The available modelling approaches involve different levels of sophistication: simple 1D models based on the wide column analogy, 2D FE models with nonlinear shell elements, and the most sophisticated 3D FE description with solid elements and embedded bar elements. The 1D wide column approach utilises elasto-plastic beam-column elements with uniaxial trilinear concrete model, which offers simplicity in modelling. However, its over-simplification does not provide information on the stress and strain distributions in modelling 2D components as RC walls. On the other hand, the detailed 2D or 3D FE models incorporating the advanced concrete damage plasticity model (CDPM) allow for a more realistic representation of the specific geometrical and reinforcement characteristics of typical RC walls.

In this chapter, the main features and the detailed implementation of the three alternative modelling approaches in ADAPTIC are presented first. Subsequently, they are employed for the numerical simulations of two experimental RC walls: a slender wall with an aspect ratio of 2.0 and a short wall with an aspect ratio of 1.0. Numerical results are compared with the experimental curves for each case. The experimental cyclic responses of the slender wall with flexural dominated behaviour are well reproduced by the numerical simulations based on the 1D beam-column model. However, this modelling strategy is less accurate for the short wall dominated by shear deformation. It is also established that the CDPM incorporated in detailed 2D and 3D FE descriptions does not represent the actual pinching characteristics exhibited by the experimental cyclic response of slender and short walls. To this end, it is established that there is a crucial need for developing a novel accurate but efficient modelling strategy for analysing RC shear walls under cyclic loading, particularly for walls with shear dominated behaviour. The next chapter describes the development of a novel 2D macro-element formulation incorporating an efficient biaxial concrete material model.

Chapter 4

Novel Marco-element Formulation for RC walls

4.1 Introduction

Existing modelling capabilities for nonlinear analysis of RC walls available in ADAPTIC (Izzuddin, 1991) have been assessed in the previous chapter. Focus was placed on the response up to collapse of slender and short walls, which were previously studied experimentally under in-plane cyclic loading. The investigated modelling strategies include the wide column approach with beam elements allowing for material and geometric nonlinearity, 2D FE descriptions with nonlinear shell elements, and detailed nonlinear models employing 3D solid elements. The 2D and 3D FE representations have shown good potential enabling accurate simulations of RC walls under monotonic loading conditions. However, the cyclic response predictions with these models have been found to be less robust and accurate mainly due to the inability of current concrete material models to represent the main features of the complex response under cyclic loading conditions. Importantly, the calibration of the input material parameters is relatively complex, and it often requires an iterative calibration process. Furthermore, the prohibitive computational cost hinders the practical use of detailed FE models for the seismic analyses of large scale structural systems, such as realistic RC buildings with multiple shear walls. The wide column approach based on elasto-plastic beam elements generally leads to accurate predictions when compared against experimental data for slender walls. Nevertheless, the Euler-Bernoulli hypothesis assumed in the beam element formulation renders it unsuitable for analysing short and moderate height walls, where shear deformations may have a significant influence on the actual response.

In view of the above, this chapter proposes a novel 2D reinforced concrete plane stress macro-element, which accounts for the contribution of shear deformations. The proposed macro-element aims to provide an efficient and accurate numerical tool for modelling RC shear walls with rectangular cross-sections under monotonic and cyclic loading conditions. Firstly, the main features of the proposed shear wall macro-element are presented. Then, Section 4.2 provides a detailed description of the macro-element formulation. A computer code for the proposed formulation has been developed in FORTRAN and implemented into the nonlinear structural analysis program ADAPTIC (Izzuddin, 1991). In the following, Section 4.3 illustrates the solution procedure of the proposed macro-element model implemented in ADAPTIC. Afterwards, Section 4.4 presents the material constitutive models incorporated within the macro-element, including (1) a biaxially condensed version of the CDPM that has been employed in the detailed 2D and 3D FE descriptions and (2) a newly developed biaxial rotating crack concrete model. In Section 4.5, the implemented macro-element is verified against existing models in ADAPTIC, followed by the investigation of the effects on the response predictions of variations of input material parameters in Section 0. Finally, the main achievements are highlighted in Section 4.7, which concludes this chapter.

4.2 Development of 2D macro-element representation

4.2.1 Characteristics of the macro-element

A 2D 4-noded shear wall macro-element, 'swm4', is proposed here for modelling RC walls with rectangular cross-sections subjected to in-plane loading. Figure 4-1 schematically depicts the macro-element modelling strategy, where a single macro-element describes an inter-storey height portion of a RC shear wall. The macro-element features a grid of monitoring points, where the contributions of both concrete and orthogonal steel reinforcement are considered. Each monitoring point with an assigned portion of the modelled RC wall component represents a RC membrane allowing for the interaction between flexure and shear response. The developed macro-element enables user-defined numbers of monitoring points n_{xun} in the unconfined web region, n_{xc} in the confined boundary region, and n_y along the element height. Compared to the wide column approach, a more realistic distribution of stresses/strains can be achieved at the macro-element level using a sufficient number of monitoring points. As shown in Figure 4-2, a typical two-storey wall can be represented by a refined discretisation with more than one macro-element per storey height. Such modelling strategy leads to an efficient representation of RC structural walls.

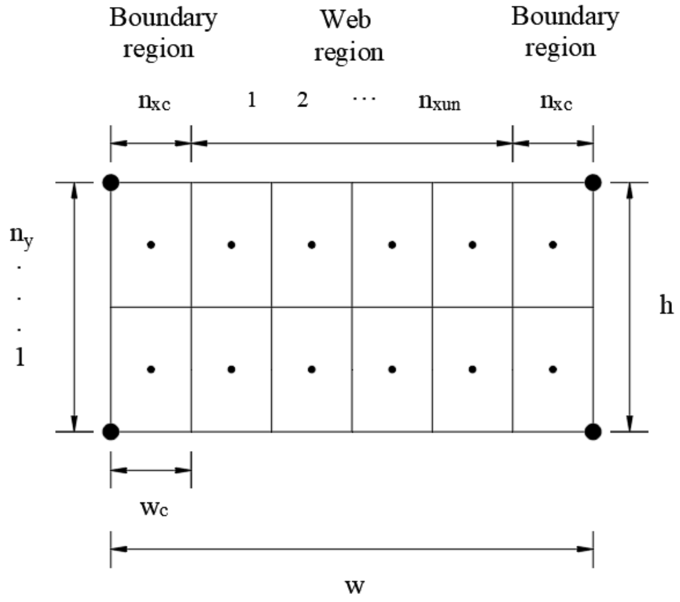

Figure 4-1: Shear wall macro-element representation for a portion of a RC wall

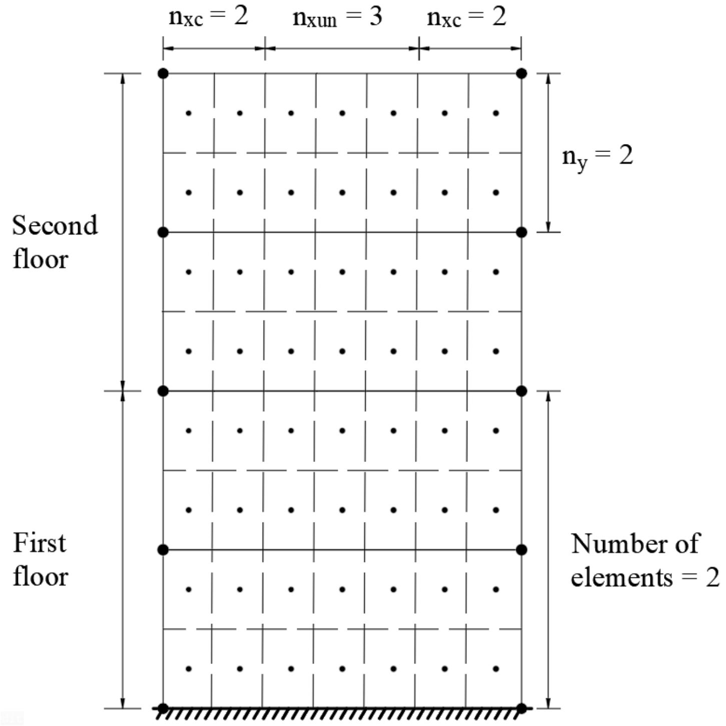

Figure 4-2 Macro-element description for a typical RC wall

4.2.2 Element kinematics

For a generic monitoring point within the developed macro-element model, the corresponding strain state can be determined through element kinematics based on the local element nodal displacements. Figure 4-3 shows the proposed shear wall macro-element, 'swm4', representing a RC wall portion in the local element x-y coordinate system. Each macro-element possesses a total of 8 degrees of freedom (DOFs): 1 horizontal and 1 vertical displacement per node, which gives the local element nodal displacement vector:

$$\{d\} = \langle u_1, v_1, u_2, v_2, u_3, v_3, u_4, v_4 \rangle^T \tag{4-1}$$

The origin of the x-y axes is taken at the macro-element centre, where the natural coordinate system (ξ, η) is established to map the real coordinates (x,y):

$$\xi = \frac{2x}{w}, \qquad \eta = \frac{2y}{h} \tag{4-2}$$

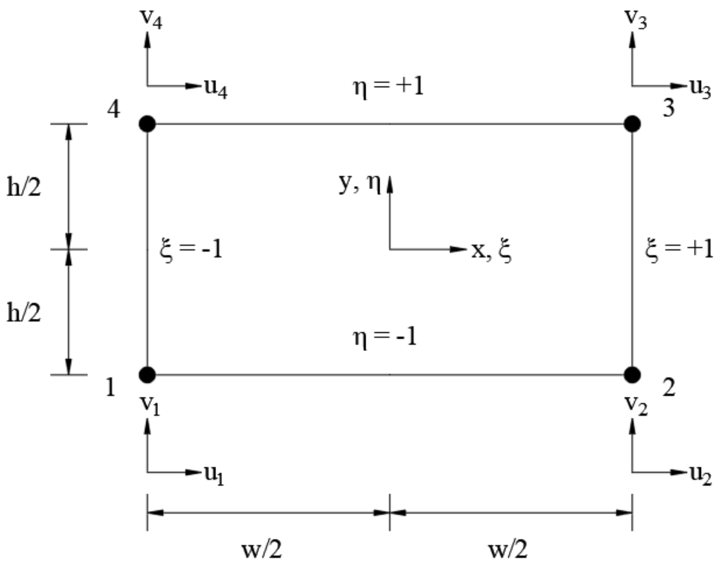

Figure 4-3: 'swm4' local coordinate system and degrees of freedom

The shape functions employed to relate the nodal displacement, $\{d\}$ to the displacement field within the element, $\{u\}$, correspond to the standard shape functions of a 4-noded quadrilateral element as reported in Zienkiewicz *et al*. (2005):

$$\{u\} = [N]\{d\} \tag{4-3}$$

with:

$$[N] = \begin{bmatrix} N_1(\xi,\eta) & 0 & N_2(\xi,\eta) & 0 & N_3(\xi,\eta) & 0 & N_4(\xi,\eta) & 0 \\ 0 & N_1(\xi,\eta) & 0 & N_2(\xi,\eta) & 0 & N_3(\xi,\eta) & 0 & N_4(\xi,\eta) \end{bmatrix} \tag{4-4}$$

$$\begin{aligned} N_1(\xi,\eta) &= \frac{1}{4}(1-\xi)(1-\eta), \qquad & N_2(\xi,\eta) &= \frac{1}{4}(1+\xi)(1-\eta) \\ N_3(\xi,\eta) &= \frac{1}{4}(1+\xi)(1+\eta), \qquad & N_4(\xi,\eta) &= \frac{1}{4}(1-\xi)(1+\eta) \end{aligned} \tag{4-5}$$

where $N_{i=1,4}$ are the shape functions for node (i) of the macro-element.

Given the displacement field approximation by Eq. (4-3) to (4-5), the material strains, including two direct strains and one shear strain in the local x-y coordinate system, can be obtained using compatibility relations based on first-derivatives of displacement with respect to the natural coordinates ξ and η:

$$\{\varepsilon\}_{xy} = \begin{Bmatrix} \varepsilon_x \\ \varepsilon_y \\ \gamma_{xy} \end{Bmatrix} = \begin{Bmatrix} \dfrac{\partial u}{\partial x} \\ \dfrac{\partial v}{\partial y} \\ \dfrac{\partial u}{\partial y} + \dfrac{\partial v}{\partial x} \end{Bmatrix} = \begin{Bmatrix} \dfrac{2}{w}\dfrac{\partial u}{\partial \xi} \\ \dfrac{2}{h}\dfrac{\partial v}{\partial \eta} \\ \dfrac{2}{h}\dfrac{\partial u}{\partial \eta} + \dfrac{2}{w}\dfrac{\partial v}{\partial \xi} \end{Bmatrix} \tag{4-6}$$

or:

$$\{\varepsilon\}_{xy} = [B]\{d\} \tag{4-7}$$

where $[B]$ matrix is determined by differentiating $[N]$ relative to ξ and η:

$$[B] = \frac{1}{2}\begin{bmatrix} B_1(\eta) & 0 & B_3(\eta) & 0 & B_5(\eta) & 0 & B_7(\eta) & 0 \\ 0 & B_2(\xi) & 0 & B_4(\xi) & 0 & B_6(\xi) & 0 & B_8(\xi) \\ B_2(\xi) & B_1(\eta) & B_4(\xi) & B_3(\eta) & B_6(\xi) & B_5(\eta) & B_8(\xi) & B_7(\eta) \end{bmatrix} \tag{4-8}$$

$$\begin{aligned} B_1(\eta) &= \frac{-1+\eta}{w}, \quad & B_2(\xi) &= \frac{-1+\xi}{h}, \quad & B_3(\eta) &= \frac{1-\eta}{w}, \quad & B_4(\xi) &= \frac{-1-\xi}{h} \\ B_5(\eta) &= \frac{1+\eta}{w}, \quad & B_6(\xi) &= \frac{1+\xi}{h}, \quad & B_7(\eta) &= \frac{-1-\eta}{w}, \quad & B_8(\xi) &= \frac{1-\xi}{h} \end{aligned} \tag{4-9}$$

As implied by the components of the $[B]$ matrix, the direct strain ε_x remains constant in the local element x-direction but varies linearly in the y-direction. By contrast, ε_y is constant in the y-direction, whereas it varies linearly in the x-direction. The shear strain γ_{xy} varies linearly in both x- and y-directions. The natural coordinates of a generic monitoring point are determined from the following expressions:

$$\xi(i_\xi) = \begin{cases} \dfrac{w_c(2i_\xi-1)}{n_{xc}w} - 1, \ i_\xi \le n_{xc} \\ \dfrac{2w_c}{w} + \dfrac{(w-2w_c)(2i_\xi - 2n_{xc}-1)}{wn_{xun}} - 1, \ n_{xc} < i_\xi \le n_{xc} + n_{xun} \\ \dfrac{2(w-w_c)}{w} + \dfrac{w_c(2(i_\xi - n_{xc}-n_{xun})-1)}{wn_{xc}} - 1, \ n_{xc} + n_{xun} < i_\xi \le 2n_{xc} + n_{xun} \end{cases} \tag{4-10}$$

$$\eta(i_\eta) = \frac{2i_\eta - 1}{n_y} - 1 \tag{4-11}$$

where i_ξ and i_η are the counters corresponding to the monitoring point location, i.e., for the most bottom and left monitoring point $i_\xi = 1$ and $i_\eta = 1$.

4.2.3 Element resistance forces and tangent stiffness matrix

Assuming plane stress condition for the represented RC membrane, the concrete stresses $\{\sigma_c\}_{xy}$ and the steel stresses $\{\sigma_s\}_{xy}$ in the local element x-y coordinate system at the monitoring points can be determined based on the adopted material constitutive models, which will be discussed in more detail in Section 4.3. The concrete stresses consist of the two direct stresses σ_{cx} and σ_{cy}, and the shear stress τ_{cxy}, whereas the steel stresses $\{\sigma_s\}_{xy}$ include the contributions of the uniaxial stress component along the local element horizontal and vertical directions without considering the dowl action, thus:

$$\{\sigma_c\}_{xy} = \langle \sigma_{cx}, \sigma_{cy}, \tau_{cxy} \rangle^T \tag{4-12}$$

$$\{\sigma_s\}_{xy} = \langle \sigma_{sx}, \sigma_{sy} \rangle^T \tag{4-13}$$

The nodal resistance forces $\{f\}$ and tangent stiffness matrix $[k_t]$ of the macro-element with the contributions of concrete and steel reinforcement are defined as:

$$\{f\} = \{f_c\} + \{f_s\} \tag{4-14}$$

$$[k_t] = [k_{tc}] + [k_{ts}] \tag{4-15}$$

in which the subscripts 'c' and 's' represent concrete and steel, respectively.

The expressions for the element resistance force vector and the tangent stiffness matrix can be obtained by employing the virtual work principle, as in standard finite element techniques (Zienkiewicz & Taylor, 2005), which gives:

$$\{f_c\} = \sum_{i=1}^{ng} [B]_i^T \cdot \{\sigma_c\}_{xy} \cdot A_c \cdot t \tag{4-16}$$

$$\{f_s\} = \sum_{i=1}^{ng} [B]_{i\ 1:8,1:2}^T \cdot \{\sigma_s V_s\} \tag{4-17}$$

$$\{\sigma_s V_s\} = \langle \sigma_{sx} \cdot \rho_x, \sigma_{sy} \cdot \rho_y \rangle^T \cdot A_c \cdot t \tag{4-18}$$

$$[k_{tc}] = \sum_{i=1}^{ng} [B]_i^T \cdot [D_{tc}] \cdot [B]_i \cdot A_c \cdot t \tag{4-19}$$

$$\begin{aligned}[k_{ts}] = (&\sum_{i=1}^{ng} [B]_{i\ 1:8,1:1}^T \cdot [B]_{i_{1:1,1:8}} \cdot E_{sx} \cdot \rho_x \\ &+ \sum_{i=1}^{ng} [B]_{i\ 1:8,2:2}^T \cdot [B]_{i_{2:2,1:8}} \cdot E_{sy} \cdot \rho_y) \cdot A_c \cdot t\end{aligned} \tag{4-20}$$

where $ng = (\ 2n_{xun} + n_{xc})\ n_y$ corresponds to the total number of monitoring points within a macro-element; $[B]_i$ is the $[B]$ matrix at a specific monitoring point calculated using Eq. (4-8), whereas the $[B]_{i_{m:n,j:k}}$ denotes the submatrix of $[B]_i$ with row 'm' to 'n' and columns 'j' to 'k'; A_c is the tributary area for an RC membrane and t is the macro-element thickness; $\{\sigma_s V_s\}$ is the vector of steel stresses multiplied by the volume of steel. ρ_x and $\rho_y$are the reinforcement ratios in x- and y- directions. $[D_{tc}]$ is the concrete material tangent stiffness matrix depending on the adopted constitutive models; E_{sx} and E_{sy} are the Young's moduli of the two orthogonal steel reinforcement layers in the local element x-y coordinate system.

4.3 Solution procedure

The proposed macro-element formulation is implemented in the nonlinear structural analysis program ADAPTIC, where an iterative procedure is adopted. At the global structural level, the equilibrium conditions are established by a set of nonlinear equations:

$$[K_T]\Delta\{U\} = \{P\} - \{R\} \tag{4-21}$$

where $\{U\}$ is the unknown incremental displacement; $\{P\}$ is the applied external load; $[K_T]$ and $\{R\}$ are the structural tangent stiffness matrix and resistance forces. The solution of these nonlinear equations representing the global structural response is solved for each incremental displacement/load step and global iteration. The difference between $\{P\}$ and $\{R\}$ defines the out-of-balance force, which is checked to achieve an equilibrium state until the convergence criteria are satisfied.

A hierarchical diagram is depicted in Figure 4-4, showing the solution procedure for the proposed macro-element model. At first, the global element nodal displacements $\{U^e\}$ as a subset of the global displacements $\{U\}$ are transformed into the local element nodal displacements $\{d\}$ through kinematics relationships. Then, the local deformations $\{\varepsilon\}$ at the monitoring point level are obtained by compatibility relations via the $\{B\}$ matrix collecting first derivatives of the shape functions. Subsequently, the stresses $\{\sigma\}$ and corresponding material tangent stiffness matrix $[D_t]$ are determined using the specific material models for concrete and steel reinforcement and then they are integrated to obtain the local nodal resistance forces $\{f\}$ and the element tangent stiffness matrix $[k_t]$. They are then transformed into the global element entities $\{R^e\}$ and $[{K_T}^e]$, which are eventually assembled to the global structural resistance forces $\{R\}$ and tangent stiffness matrix $[K_T]$. An iterative correction for the displacement $\{U\}$ is performed if the equilibrium condition is not satisfied at the current load step and global iteration.

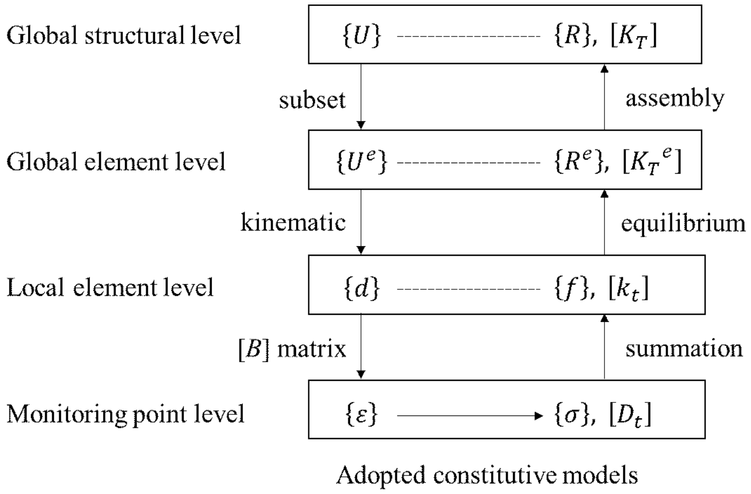

Figure 4-4: Solution procedure for the macro-element approach

4.4 Adopted material constitutive models

Concrete material nonlinearity is accounted for in the implemented shear wall macro-element by incorporating two material constitutive models, a biaxial concrete damage plasticity model (CDPM) and a rotating crack model (RCM). The biaxial CDPM has been incorporated into the macro-element for the purpose of verifying the element algorithm by numerical comparisons against 2D and 3D FE discretisations adopting the same concrete material model. Detailed verification examples will be presented in Section 4.5. However, as the numerical investigations in Chapter 3 have confirmed that the use of CDPM many lead to inaccurate predictions, mainly due to its inability to describe the actual pinching feature of the hysteretic response, a new RCM for RC membranes has been developed and used within the proposed macro-element to achieve improved predictions under cyclic loading conditions. For steel reinforcement, the bilinear elasto-plastic model with kinematic hardening is employed for calculating the steel stresses $\{\sigma_s\}_{xy}$ in the local element horizontal and vertical directions.

4.4.1 Proposed biaxial concrete model

The proposed biaxial concrete material model is based on the smeared rotating crack angle approach, in which the crack orientation rotates during the numerical simulation also after the first crack formation. In the RCM, it is assumed that the directions of the principal stresses coincide with the directions of the principal strains. The axes of orthotropy are defined as normal and parallel to the principal strain axes and continuously aligned with the changing crack orientation. Consequently, only two normal stresses corresponding to the principal stresses are determined in the principal system. This eliminates the need to define the hysteresis shear stress-strain relationship.

By contrast, in the fixed crack model (FCM), the directions of material orthotropy are fixed after the formation of the first crack, when the first principal stress exceeds the cracking stress of concrete. As a result, separate constitutive models are required to define the hysteresis normal and shear stress-strain relationships. The assumption of fixed crack is not consistent with experimental observations, as pointed out by Palermo and Vecchio (2003). Cracks experience minor rotation when the concrete is equally reinforced in the longitudinal and transverse directions. However, in engineering practice, different amounts of reinforcement will be provided. Thus, FCM may not realistically represent the actual response.

To this end, the rotating crack assumption is adopted here for obtaining the stress states at each monitoring point within the macro-element. The strains in the principal 1-2 coordinate system, $\{\varepsilon\}_{12}$, calculated at each monitoring point are as follows:

$$\{\varepsilon\}_{12} = [T_\alpha] \cdot \{\varepsilon\}_{xy} \tag{4-22}$$

$$[T_\alpha] = \begin{bmatrix} c^2 & s^2 & c \cdot s \\ s^2 & c^2 & -c \cdot s \\ -2c \cdot s & 2c \cdot s & c^2 - s^2 \end{bmatrix} \tag{4-23}$$

$$c = cos(\alpha), \qquad s = sin(\alpha)$$

where $[T_\alpha]$ is the transformation matrix; α is the orientation of the principal strain direction, which defines the angle between the x-y coordinate system and 1-2 coordinate system. As no shear strain occurs on the crack plane, the angle α can be obtained by imposing:

$$\gamma_{12} = -2c \cdot s \cdot \varepsilon_x + 2c \cdot s \cdot \varepsilon_y + (c^2 - s^2)\, \gamma_{xy} = 0 \tag{4-24}$$

which gives:

$$\alpha = \frac{1}{2} acrtan(\frac{\gamma_{xy}}{\varepsilon_x - \varepsilon_y}) \tag{4-25}$$

The uniaxial stress-strain relationship discussed in Section 4.4.2 is used to determine the concrete stresses, $\{\sigma_c\}_{12}$ in the 1-2 coordinate system, which is then transformed back to the concrete stresses, $\{\sigma_c\}_{xy}$ in the local element x-y coordinate system as follows:

$$\{\sigma_c\}_{xy} = [T_\alpha]^T \cdot \{\sigma_c\}_{12} \tag{4-26}$$

where $[T_\alpha]^T$ is the transpose of the transformation matrix $[T_\alpha]$.

The concrete tangent stiffness matrix is determined by:

$$[D_{tc}]_{xy} = \frac{\partial\{\sigma_c\}_{xy}}{\partial\langle\varepsilon\rangle_{xy}} \tag{4-27}$$

$$\frac{\partial\{\sigma_c\}_{xy}}{\partial\langle\varepsilon\rangle_{xy}} = \begin{bmatrix} \frac{\partial\sigma_{cx}}{\partial\varepsilon_x} & \frac{\partial\sigma_{cx}}{\partial\varepsilon_y} & \frac{\partial\sigma_{cx}}{\partial\gamma_{xy}} \\ \frac{\partial\sigma_{cy}}{\partial\varepsilon_x} & \frac{\partial\sigma_{cy}}{\partial\varepsilon_y} & \frac{\partial\sigma_{cy}}{\partial\gamma_{xy}} \\ \frac{\partial\tau_{cxy}}{\partial\varepsilon_x} & \frac{\partial\tau_{cxy}}{\partial\varepsilon_y} & \frac{\partial\tau_{cxy}}{\partial\gamma_{xy}} \end{bmatrix} \tag{4-28}$$

The components of $[\mathrm{D_{tc}}]_{\mathrm{xy}}$ are determined by the chain rule of differentiation:

$$\frac{\partial\sigma_{cx}}{\partial\varepsilon_x}=\frac{\partial\sigma_{cx}}{\partial\sigma_{c1}}\frac{\partial\sigma_{c1}}{\partial\varepsilon_1}\frac{\partial\varepsilon_1}{\partial\varepsilon_x}+\frac{\partial\sigma_{cx}}{\partial\sigma_{c2}}\frac{\partial\sigma_{c2}}{\partial\varepsilon_2}\frac{\partial\varepsilon_2}{\partial\varepsilon_x}+\frac{\partial\sigma_{cx}}{\partial\alpha}\frac{\partial\alpha}{\partial\varepsilon_x} \tag{4-29}$$

$$\frac{\partial\sigma_{cx}}{\partial\varepsilon_y}=\frac{\partial\sigma_{cx}}{\partial\sigma_{c1}}\frac{\partial\sigma_{c1}}{\partial\varepsilon_1}\frac{\partial\varepsilon_1}{\partial\varepsilon_y}+\frac{\partial\sigma_{cx}}{\partial\sigma_{c2}}\frac{\partial\sigma_{c2}}{\partial\varepsilon_2}\frac{\partial\varepsilon_2}{\partial\varepsilon_y}+\frac{\partial\sigma_{cx}}{\partial\alpha}\frac{\partial\alpha}{\partial\varepsilon_y} \tag{4-30}$$

$$\frac{\partial\sigma_{cx}}{\partial\gamma_{xy}}=\frac{\partial\sigma_{cx}}{\partial\sigma_{c1}}\frac{\partial\sigma_{c1}}{\partial\varepsilon_1}\frac{\partial\varepsilon_1}{\partial\gamma_{xy}}+\frac{\partial\sigma_{x}}{\partial\sigma_{c2}}\frac{\partial\sigma_{c2}}{\partial\varepsilon_2}\frac{\partial\varepsilon_2}{\partial\gamma_{xy}}+\frac{\partial\sigma_{cx}}{\partial\alpha}\frac{\partial\alpha}{\partial\gamma_{xy}} \tag{4-31}$$

$$\frac{\partial\sigma_{cy}}{\partial\varepsilon_x}=\frac{\partial\sigma_{y}}{\partial\sigma_{c1}}\frac{\partial\sigma_{c1}}{\partial\varepsilon_1}\frac{\partial\varepsilon_1}{\partial\varepsilon_x}+\frac{\partial\sigma_{y}}{\partial\sigma_{c2}}\frac{\partial\sigma_{c2}}{\partial\varepsilon_2}\frac{\partial\varepsilon_2}{\partial\varepsilon_x}+\frac{\partial\sigma_{cy}}{\partial\alpha}\frac{\partial\alpha}{\partial\varepsilon_x} \tag{4-32}$$

$$\frac{\partial\sigma_{cy}}{\partial\varepsilon_y}=\frac{\partial\sigma_{y}}{\partial\sigma_{c1}}\frac{\partial\sigma_{c1}}{\partial\varepsilon_1}\frac{\partial\varepsilon_1}{\partial\varepsilon_y}+\frac{\partial\sigma_{y}}{\partial\sigma_{c2}}\frac{\partial\sigma_{c2}}{\partial\varepsilon_2}\frac{\partial\varepsilon_2}{\partial\varepsilon_y}+\frac{\partial\sigma_{cy}}{\partial\alpha}\frac{\partial\alpha}{\partial\varepsilon_y} \tag{4-33}$$

$$\frac{\partial\sigma_{cy}}{\partial\gamma_{xy}}=\frac{\partial\sigma_{y}}{\partial\sigma_{c1}}\frac{\partial\sigma_{c1}}{\partial\varepsilon_1}\frac{\partial\varepsilon_1}{\partial\gamma_{xy}}+\frac{\partial\sigma_{y}}{\partial\sigma_{c2}}\frac{\partial\sigma_{c2}}{\partial\varepsilon_2}\frac{\partial\varepsilon_2}{\partial\gamma_{xy}}+\frac{\partial\sigma_{cy}}{\partial\alpha}\frac{\partial\alpha}{\partial\gamma_{xy}} \tag{4-34}$$

$$\frac{\partial\tau_{cxy}}{\partial\varepsilon_x}=\frac{\partial\tau_{cxy}}{\partial\sigma_{c1}}\frac{\partial\sigma_{c1}}{\partial\varepsilon_1}\frac{\partial\varepsilon_1}{\partial\varepsilon_x}+\frac{\partial\tau_{cxy}}{\partial\sigma_{c2}}\frac{\partial\sigma_{c2}}{\partial\varepsilon_2}\frac{\partial\varepsilon_2}{\partial\varepsilon_x}+\frac{\partial\tau_{cxy}}{\partial\alpha}\frac{\partial\alpha}{\partial\varepsilon_x} \tag{4-35}$$

$$\frac{\partial\tau_{cxy}}{\partial\varepsilon_y}=\frac{\partial\tau_{cxy}}{\partial\sigma_{c1}}\frac{\partial\sigma_{c1}}{\partial\varepsilon_1}\frac{\partial\varepsilon_1}{\partial\varepsilon_y}+\frac{\partial\tau_{cxy}}{\partial\sigma_{c2}}\frac{\partial\sigma_{c2}}{\partial\varepsilon_2}\frac{\partial\varepsilon_2}{\partial\varepsilon_y}+\frac{\partial\tau_{cxy}}{\partial\alpha}\frac{\partial\alpha}{\partial\varepsilon_y} \tag{4-36}$$

$$\frac{\partial\tau_{cxy}}{\partial\gamma_{xy}}=\frac{\partial\tau_{cxy}}{\partial\sigma_{c1}}\frac{\partial\sigma_{c1}}{\partial\varepsilon_1}\frac{\partial\varepsilon_1}{\partial\gamma_{xy}}+\frac{\partial\tau_{cxy}}{\partial\sigma_{c2}}\frac{\partial\sigma_{c2}}{\partial\varepsilon_2}\frac{\partial\varepsilon_2}{\partial\gamma_{xy}}+\frac{\partial\tau_{cxy}}{\partial\alpha}\frac{\partial\alpha}{\partial\gamma_{xy}} \tag{4-37}$$

where the partial derivatives are obtained from Eq. (4-22), (4-25) and (4-26) as follows:

$$\begin{gathered}
\frac{\partial\sigma_{cx}}{\partial\sigma_{c1}}=c^2, \quad \frac{\partial\sigma_{cx}}{\partial\sigma_{c2}}=s^2, \quad \frac{\partial\sigma_{cy}}{\partial\sigma_{c1}}=s^2, \quad \frac{\partial\sigma_{cy}}{\partial\sigma_{c2}}=c^2 \\
\frac{\partial\tau_{cxy}}{\partial\sigma_{c1}}=c\cdot s, \quad \frac{\partial\tau_{cxy}}{\partial\sigma_{c2}}=-c\cdot s, \quad \frac{\partial\varepsilon_1}{\partial\varepsilon_x}=c^2, \quad \frac{\partial\varepsilon_2}{\partial\varepsilon_x}=s^2 \\
\frac{\partial\varepsilon_1}{\partial\varepsilon_y}=s^2, \quad \frac{\partial\varepsilon_2}{\partial\varepsilon_y}=c^2, \quad \frac{\partial\varepsilon_1}{\partial\gamma_{xy}}=c\cdot s, \quad \frac{\partial\varepsilon_2}{\partial\gamma_{xy}}=-c\cdot s \\
\frac{\partial\sigma_{cx}}{\partial\alpha}=2c\cdot s\cdot(\sigma_2-\sigma_1), \qquad \frac{\partial\sigma_{cy}}{\partial\alpha}=2c\cdot s\cdot(\sigma_1-\sigma_2) \\
\frac{\partial\tau_{cxy}}{\partial\alpha}=(c^2-s^2)(\sigma_1-\sigma_2) \\
\frac{\partial\alpha}{\partial\varepsilon_x}=\frac{-\gamma_{xy}}{2\cdot\left(\varepsilon_x-\varepsilon_y\right)^2\cdot\left[\left(\frac{\gamma_{xy}}{\varepsilon_x-\varepsilon_y}\right)^2+1\right]}=\frac{-\gamma_{xy}}{2\cdot\left[{\gamma_{xy}}^2+\left(\varepsilon_x-\varepsilon_y\right)^2\right]},
\end{gathered} \tag{4-38}$$

$$\frac{\partial \alpha}{\partial \varepsilon_y} = \frac{\gamma_{xy}}{2 \cdot \left(\varepsilon_x - \varepsilon_y\right)^2 \cdot \left[\left(\frac{\gamma_{xy}}{\varepsilon_x - \varepsilon_y}\right)^2 + 1\right]} = \frac{\gamma_{xy}}{2 \cdot \left[{\gamma_{xy}}^2 + \left(\varepsilon_x - \varepsilon_y\right)^2\right]}$$

$$\frac{\partial \alpha}{\partial \gamma_{xy}} = \frac{1}{2 \cdot (\varepsilon_x - \varepsilon_y) \cdot \left[\left(\frac{\gamma_{xy}}{\varepsilon_x - \varepsilon_y}\right)^2 + 1\right]} = \frac{1}{2 \cdot (\frac{{\gamma_{xy}}^2}{\varepsilon_x - \varepsilon_y} + \varepsilon_x - \varepsilon_y)}$$

In addition, from the uniaxial stress-strain relationships:

$$\frac{\partial \sigma_{c1}}{\partial \varepsilon_1} = E_{tc1}, \qquad \frac{\partial \sigma_{c2}}{\partial \varepsilon_2} = E_{tc2} \tag{4-39}$$

where E_{tc1} and E_{tc2} are the concrete tangent stiffness in the 1- and 2-directions, respectively.

4.4.2 Adopted uniaxial material models

As mentioned before, the concrete stresses $\{\sigma_c\}_{12}$ are calculated in the principal 1-2 directions. The proposed RCM incorporates a modified version of the trilinear concrete model used in Chapter 3. Vecchio & Collins (1986) observed that the cracked concrete membrane in compression exhibited reduced strength and stiffness than uniaxially compressed concrete. This compression softening effect due to the presence of transverse tensile strain is accounted for by introducing the softening coefficient β, which is determined internally in the rotating crack model formulation based on the following expression proposed by Vecchio and Collins (1986):

$$\beta = \frac{1}{0.80 + 0.34 \frac{\varepsilon_\perp}{\varepsilon_c}} \tag{4-40}$$

where ε_c is the compressive strain and $\varepsilon_\perp$ is the transverse tensile strain.

This compression softening effect is applied by modifying the compressive envelope of the stress-strain curve using β, as shown in Figure 4-5, where the dotted line refers to the unsoftened compressive envelope. The adopted limiting value for β is $0.6 \leq \beta \leq 1.0$, according to the recommendation provided by (Miyahara *et al.*, 1987). The compressive softening effect is applied only on the envelope curve. At each load step, the value of β is calculated based on the values of ε_c and $\varepsilon_\perp$. More specifically, Eq. (4-40) only applies when at least one of the principal strains is less than zero. In the case that both ε_c and $\varepsilon_\perp$ are positive, there will be no compressive softening. During unloading/reloading, the value of β is maintained fixed until the concrete compressive strain reaches the minimum compressive strain in the previous loading cycle.

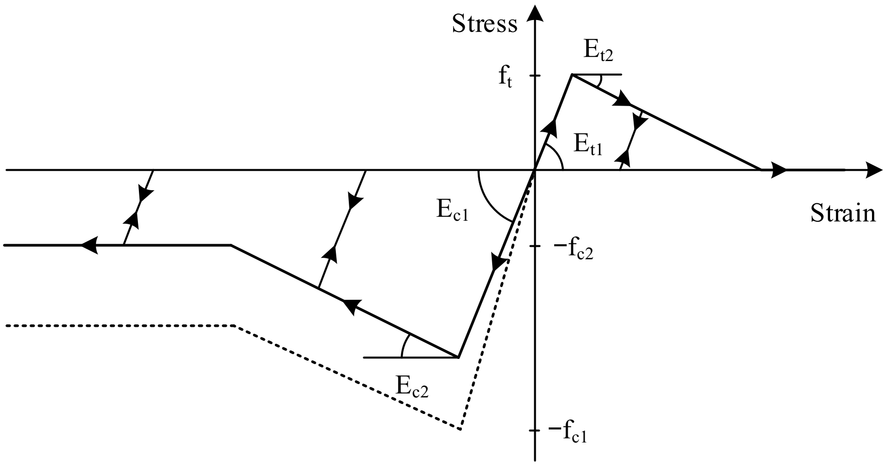

Figure 4-5: Uniaxial concrete material constitutive laws in RCM

4.4.3 Cyclic loading considerations

Under cyclic loading conditions, the full loading path of the adopted uniaxial concrete material model in the implemented RCM formulation is shown in Figure 4-6. In a specific principal direction, the concrete is unloaded from tension to compression and reloaded to the tensile regime again. Upon unloading from either the tensile or compressive envelope, the cracking strain ε_{cr} and plastic strain ε_{pl} are established and stored as state variables. When unloading from the tensile envelope, the cracking strain is fully recovered to the origin, representing the closure of a crack. Then, as unloading from the compressive envelope, the origin is shifted by the plastic strain offset, followed by a reloading path passing through the previously stored cracking strain component. In this respect, the principal stress is determined depending on the input principal strain relative to the summation of the plastic strain offset and cracking strain. Subsequently, the reloading curve is characterised by a tensile stiffness targeting the tensile softening envelope with reduced tensile strength.

As illustrated in the preceding sections, the implemented RCM establishes the local element x-y coordinate system and the principal 1-2 coordinate system. Figure 4-7 schematically shows the determination of the concrete stresses $\{\sigma_c\}_{xy}$ in the local element x-y coordinate system. At each incremental displacement/load step, the concrete stresses $\{\sigma_c\}_{xy}$ are obtained by: (1) transforming the given material point strains $\{\varepsilon\}_{xy}$ into $\{\varepsilon\}_{12}$; (2) determining the concrete stresses $\{\sigma_c\}_{12}$ based on the incorporated uniaxial material laws; and (3) transforming back the concrete stresses $\{\sigma_c\}_{12}$ into $\{\sigma_c\}_{xy}$.

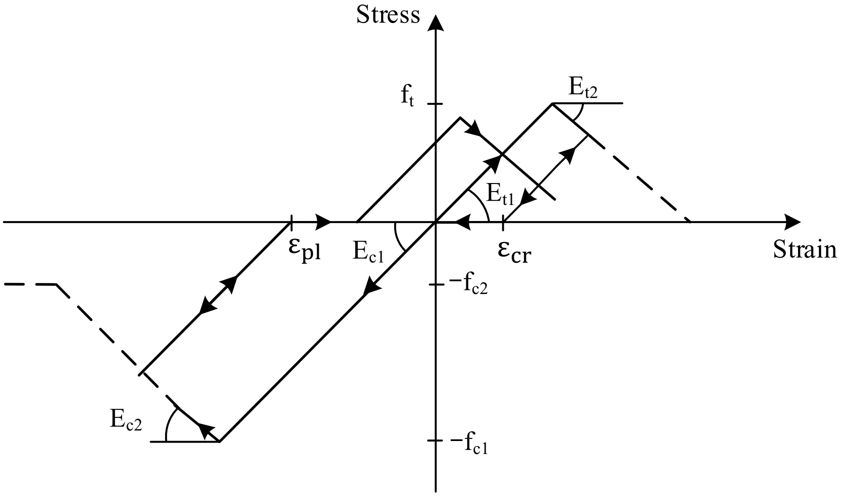

Figure 4-6: Full loading path and state variables

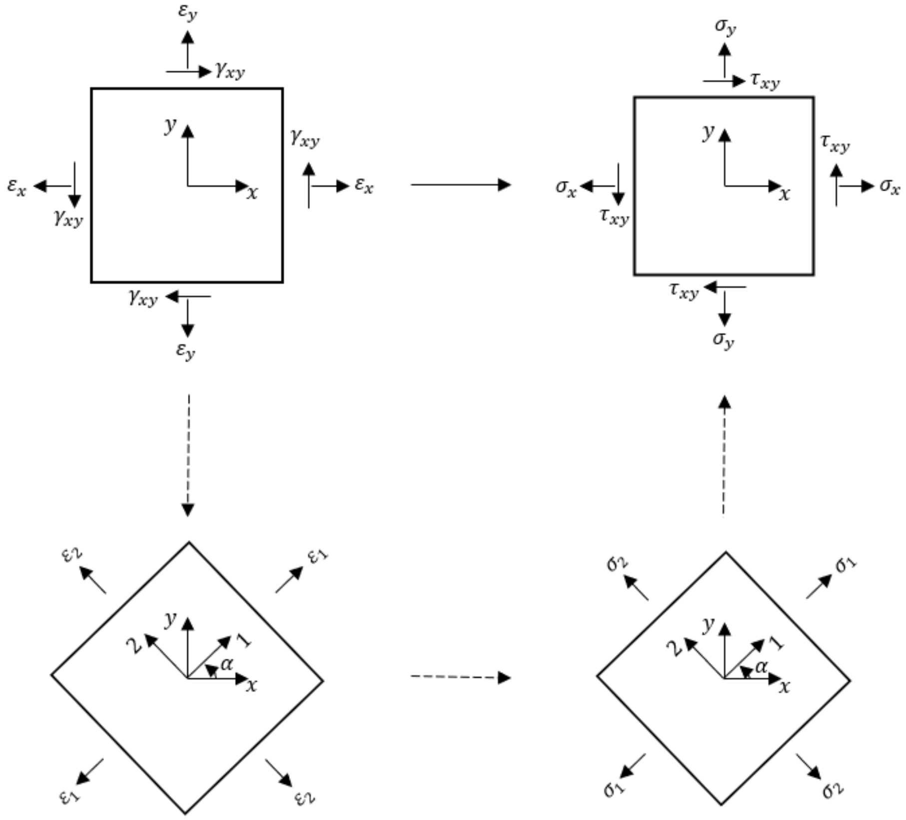

Figure 4-7: Determination of stress states in RCM

In the implementation of the RCM formulation, the orientation of the principal tensile strain direction α is calculated first, given a biaxial strain state at the material point of the macro-element. This angle ranges from -45° to 45° relative to the horizontal local element x-axis, as implied from Eq. (4-25). The rotating crack varies between 45° and 135° since the principal tensile direction is normal to the crack. Two sets of plastic strains $(\varepsilon_{cr}, \varepsilon_{pl})$ are established in the principal 1-2 axes at each incremental load step. Considering the previous load step $i-1$ and the current load step i, the stress in each principal direction is determined based on the given input material properties and the plastic strains $(\varepsilon_{cr}, \varepsilon_{pl})_{1,i-1}$ at the previous load step, $i-1$. Besides, it is assumed that:

(I) if both α_{i-1} and α_i are in the range of [-45°,0) or [0, 45°], then:

- the plastic strains $(\varepsilon_{cr}, \varepsilon_{pl})_{1,i-1}$ stored in the previous principal tensile direction are used to update the plastic strains $(\varepsilon_{cr}, \varepsilon_{pl})_{1,i}$ in the current principal tensile direction;
- similarly, the plastic strains $(\varepsilon_{cr}, \varepsilon_{pl})_{2,i-1}$ stored in the previous principal compressive direction are used to update the plastic strains $(\varepsilon_{cr}, \varepsilon_{pl})_{2,i}$ in the current principal tensile direction.

(II) if α_{i-1} is in the range [-45°,0) and α_i is in the range [0, 45°], or, α_{i-1} is in the range [0, 45°] and α_i is in the range [-45°,0), then:

- the plastic strains $(\varepsilon_{cr}, \varepsilon_{pl})_{1,i-1}$ stored in the previous principal tensile direction is used to update the plastic strains $(\varepsilon_{cr}, \varepsilon_{pl})_{2,i}$ in the current principal compressive direction;
- similarly, the plastic strains $(\varepsilon_{cr}, \varepsilon_{pl})_{2,i-1}$ stored in the previous principal compressive direction are used to update the plastic strains $(\varepsilon_{cr}, \varepsilon_{pl})_{1,i}$ in the current principal tensile direction.

To this end, the concrete stresses $\{\sigma_c\}_{12}$ and the associated tangent stiffness E_{tc1} and E_{tc2} are determined, which are then used to calculate the concrete stress $\{\sigma_c\}_{xy}$ and the consistent tangent stiffness matrix $[D_{tc}]_{xy}$.

At the monitoring point level, when the CDPM is adopted, the stresses are updated, and the concrete tangent stiffness matrix is determined by solving the plasticity problem using an incremental iterative strategy. By contrast, the RCM does not require an iterative procedure to solve the local problem, implying that the RCM possesses inherent computational efficiency.

4.5 Verification of 2D macro-element

To verify the developed macro-element model with the concrete RCM, numerical examples are presented in this section by comparing the concrete material response of a single element using macro-element ‘swm4’ against those obtained by using solid element ‘bk08’ and shell element ‘csl4’. Various loading conditions are applied monotonically and cyclically in the tests, including uniaxial compression, uniaxial tension, and pure shear. This is then followed by modelling a RC wall utilising more than one macro-element, from which the accuracy of the ‘swm4’ numerical response at the element level is investigated.

4.5.1 Verification at material point level

4.5.1.1 Uniaxial loading test

A 100×100×100mm^3 concrete cube is modelled by a solid element ‘bk08’ (Figure 4-8(a)) and a shell element ‘csl4’ (Figure 4-8(b)) with the CDPM, and the results of nonlinear simulations under compressive and tensile loading are compared against the experimental stress-strain curves obtained by Karsan & Jirsa (1969) and Gopalaratnam & Shah (1985). The geometrical characteristics of the modelled concrete specimen are chosen so that the 3D and 2D elements have the same characteristic element length, which affects the tensile softening slope. A macro-element ‘swm4’ model for the same concrete element (Figure 4-8(c)) with the CDPM and the RCM are generated and tested under the same loading regimes to verify the use of the two concrete material models within the developed macro-element description. The boundary conditions applied on these numerical models are depicted in Figure 4-8(d).

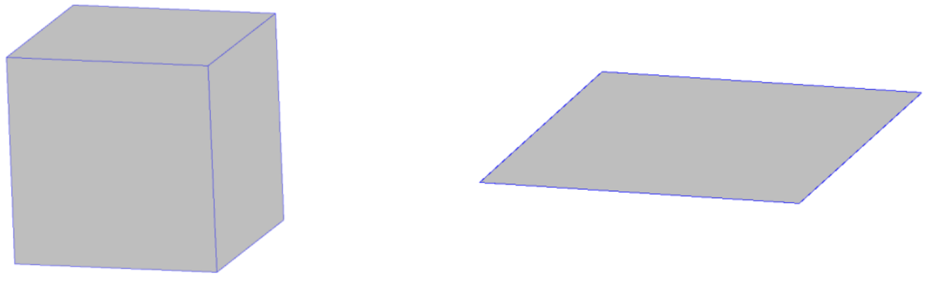
(a) (b)

Figure 4-8: Concrete cube models: (a) solid element; (b) shell element; (c) macro-element; (d) boundary conditions assumed in the numerical test (Con’d)

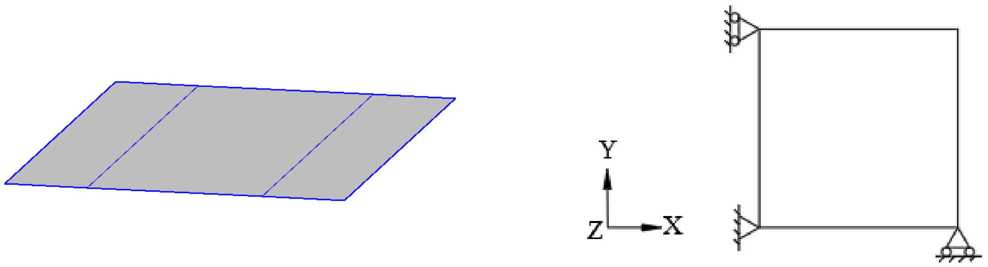

(c)

(d)

Figure 4-8: Concrete cube models: (a) solid element; (b) shell element; (c) macro-element; (d) boundary conditions assumed in the numerical test

- *Monotonic loading*

The material parameters related to the monotonic loading tests are summarised in Table 4-1. The stress-strain curves obtained by the ‘bk08’ model are calibrated against experimental results, which gives a set of CDPM material parameters for the ‘csl4’ and ‘swm4’ models. The material parameters for RCM are calibrated and used for ‘swm4’ to verify the accuracy of the implemented material model.

Table 4-1: Material parameters for monotonic loading tests

Material model	Elastic properties	Compressive behaviour	Tensile behaviour
CDPM	$E_c = 31700\text{MPa}$ $E_t = 33400\text{MPa}$ $\nu = 0.18$	$f_c = 27.6\text{MPa}$ $\tilde{f}_y = 0.6$ $k_{co} = 0.00125$ $\rho_c = 1.0$ $f_{res} = 0.276\text{MPa}$	$f_t = 3.48\text{MPa}$ $G_t = 0.04\text{N/mm}$
RCM		$E_{c1} = 13142\text{MPa}$ $f_{c1} = 27.6\text{MPa}$ $E_{c2} = -5000\text{MPa}$ $f_{c2} = 0.276\text{MPa}$	$E_{t1} = 33400\text{MPa}$ $f_t = 3.48\text{MPa}$ $E_{t2} = -6816\text{MPa}$

The prescribed compressive or tensile displacements are applied at the nodes at the right edge in the global X-direction, inducing a uniform stress/strain field within the elements. The deformed shapes of the concrete cube using different elements under uniaxial compression and uniaxial tension are shown in Figure 4-9. The stress-strain curves from monotonic compression tests (Figure 4-10) and monotonic tension tests (Figure 4-11) show good agreements when the CDPM is used with different elements, demonstrating the accuracy of the implemented macro-element formulation. The softening branches of the RCM response are approximate due to the linear softening stiffness of the adopted uniaxial concrete constitutive laws.

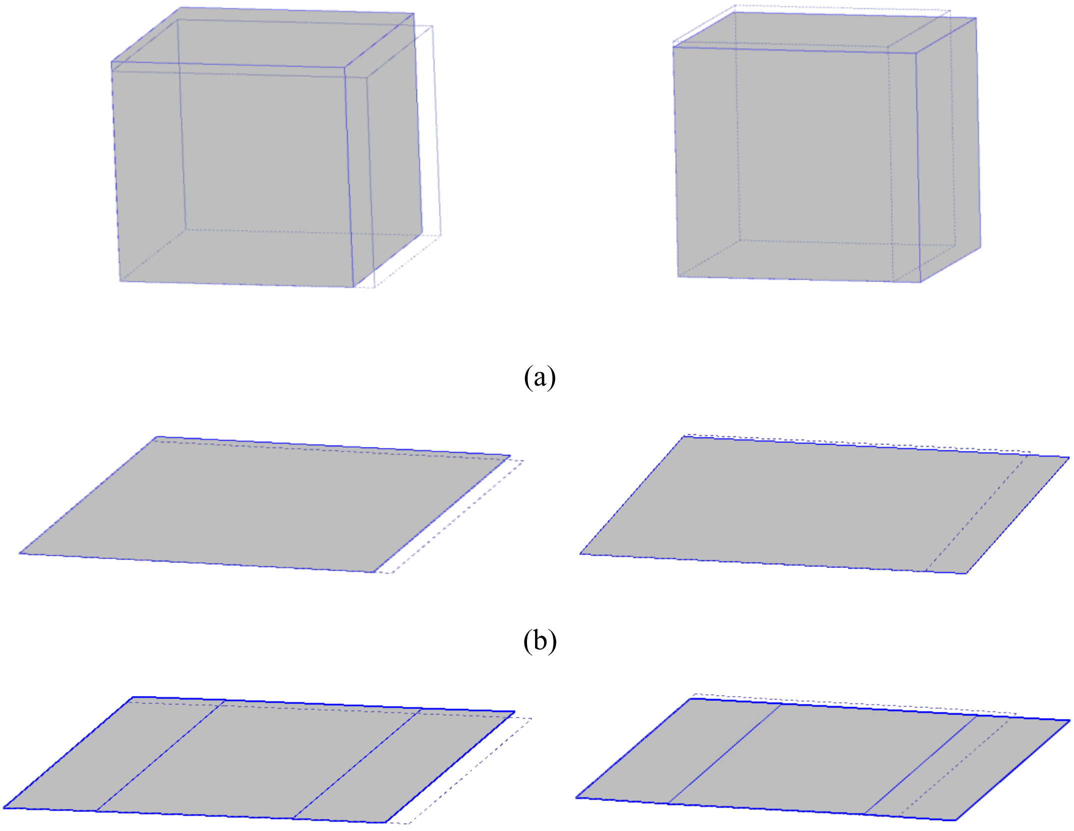

(a)

(b)

(c)

Figure 4-9: Deformed shapes of (a) solid element, (b) shell element and (c) macro-element under uniaxial compression (left) and uniaxial tension (right)

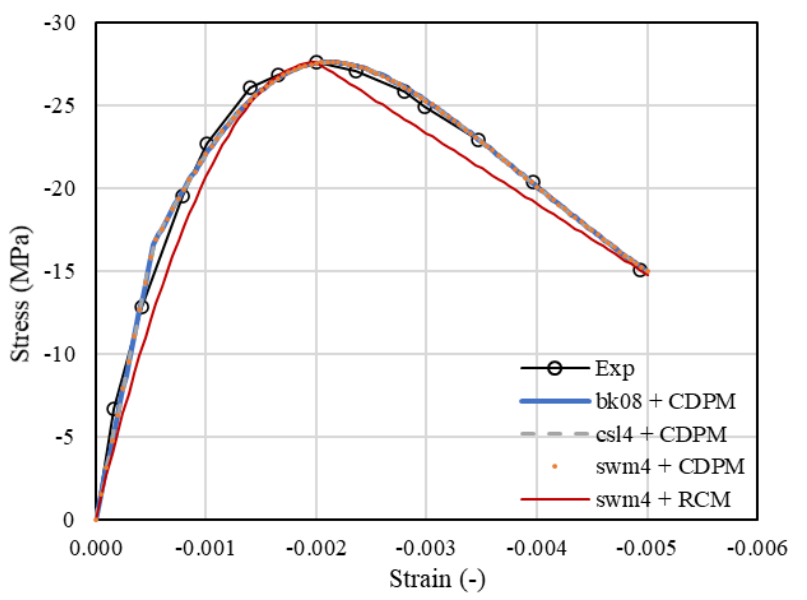

Figure 4-10: Stress-strain curves of elements under uniaxial monotonic compression

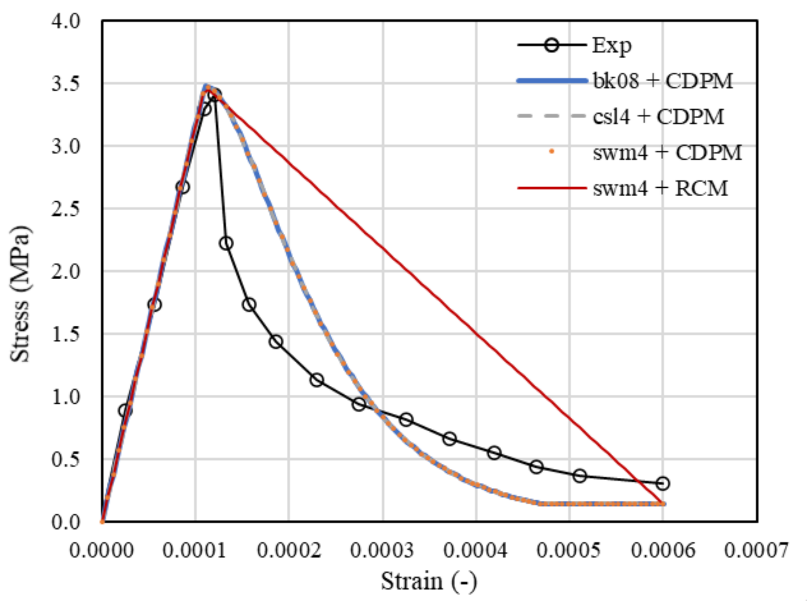

Figure 4-11: Stress-strain curves of elements under uniaxial monotonic tension

- *Cyclic loading*

Similarly, in the cyclic loading tests, the CDPM material parameters presented in Table 4-2 are calibrated for ‘bk08’ models and subsequently employed also for ‘csl4’ and ‘swm4’ models. It is noted that, in the CDPM, the parameters $\tilde{f}_y$, k_{co}, and ρ_c not only define the compressive stress-strain envelope, but also determine the unloading branches. The ratio between the yielding stress and maximum strength in compression $\tilde{f}_y$ defines the extend of nonlinearity of the initial ascending branch of the stress-strain curve before reaching the compressive strength. The plastic strain k_{co} at f_c controls the area under the stress-plastic strain curve, which also governs the unloading branch. The parameter ρ_c defines where the compressive damage starts. The damage in tension is governed by μ, smaller value of which gives strong stiffness degradation. The use of low values of ρ_c and μ can cause convergence problems. By contrast, the calibration of the RCM material parameters (Table 4-2) requires less effort, since the characteristics of the unloading branches are determined only by the softening moduli E_{c2} and E_{t2}.

Table 4-2: Material parameters for cycliс tests

Material model	Elastic properties	Compressive behaviour	Tensile behaviour
CDPM	$E_c = 31700\text{MPa}$ $E_t = 31700\text{MPa}$ $\nu = 0.18$	$f_c = 27.6\text{MPa}$ $\tilde{f}_y = 0.31$ $k_{co} = 0.00075$ $\rho_c = 0.4$ $f_{res} = 0.276\text{MPa}$	$f_t = 3.48\text{MPa}$ $G_t = 0.04\text{N/mm}$ $\mu = 0.9$
RCM		$E_{c1} = 15166\text{MPa}$ $f_{c1} = 27.6\text{MPa}$ $E_{c2} = -5000\text{MPa}$ $f_{c2} = 0.276\text{MPa}$	$E_{t1} = 31700\text{MPa}$ $f_t = 3.48\text{MPa}$ $E_{t2} = -7937\text{MPa}$

As in the monotonic loading tests, uniform strains and stresses are introduced, where the cyclic displacement history is applied. Figure 4-12 and Figure 4-13 show the stress-strain curves obtained from the numerical cyclic tests, which are compared against the experimental results achieved by Karsan & Jirsa (1969) and Gopalaratnam & Shah (1985). As evident from the material model formulations, neither CDPM nor RCM can capture the local hysteresis loops shown in the experimental response. This is because both models adopt linear unloading/reloading branch. The numerical results obtained from CDPM models with different elements are the same. As for the macro-element model with RCM, the unloading branches are approximately represented as the unloading stiffness follows the initial stiffness. In contrast, the CDPM provides an improved representation of the stiffness degradation, as shown by the experimental curves.

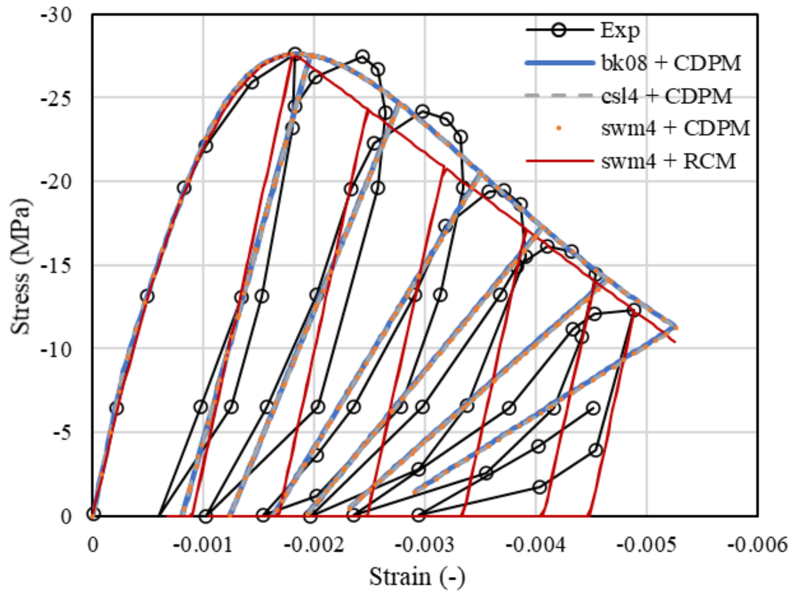

Figure 4-12: Stress-strain curves under uniaxial cyclic compression

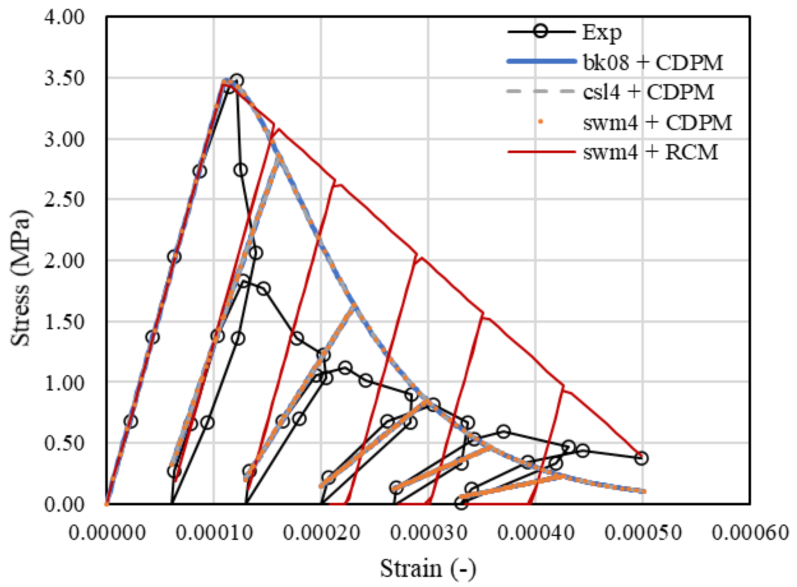

Figure 4-13: Stress-strain curves under uniaxial cyclic tension

4.5.1.2 Shear loading test

The 100×100×100mm^3 concrete cube is modelled here for testing the single element response under pure shear cyclic loading. The boundary conditions applied in this case are shown in Figure 4-14(a). In the 'csl4' and 'swm4' models, only the two nodes on the right edge are free to move in the global Y-direction, while the other nodes are restrained. For the 'bk08' model, nodes on the right face are free to move in the global Y-direction and the nodes on the top surface are free to move in the global Z-direction, whereas the remaining degrees of freedom are restrained. Prescribed translational displacements in the global Z-direction are applied for these models, inducing a uniform shear strain/stress field. In order to have comparable numerical models, the same set of material parameters presented in Table 4-2 is used. The exception is that the parameter μ for the CDPM is modified to 0.1, thus reducing the incurred tensile damage during unloading. The deformed shapes of the three tested elements are shown in Figures 4-14(b), (c) and (d).

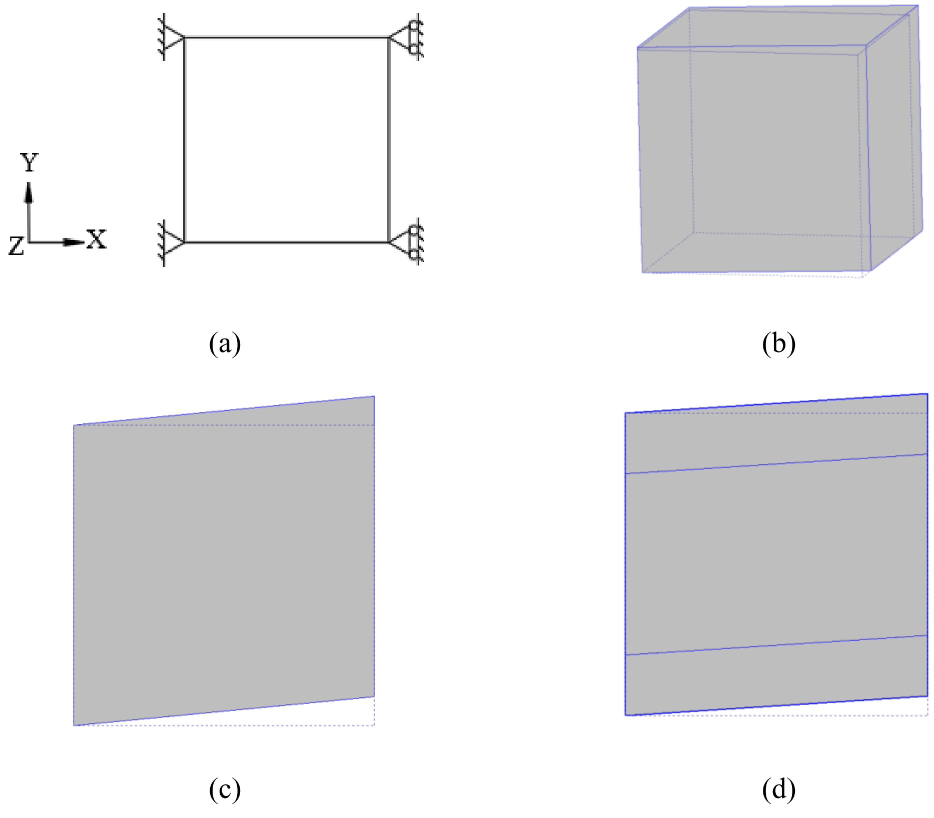

(a) (b)

(c) (d)

Figure 4-14: Concrete cube models under shear: (a) boundary conditions (b) solid element; (c) shell element; (d) macro-element

Figure 4-15 plots the resulting shear stresses against the shear strains from the numerical tests. Both CDPM and RCM employed for the different elements predict a similar level of maximum shear stress. When CDPM is used, the macro-element model predicts the same results as the solid element and shell element models. The numerical response achieved from 'swm4' model with RCM predicts a pinching characteristic of the cyclic loops, which cannot be obtained from the model with CDPM.

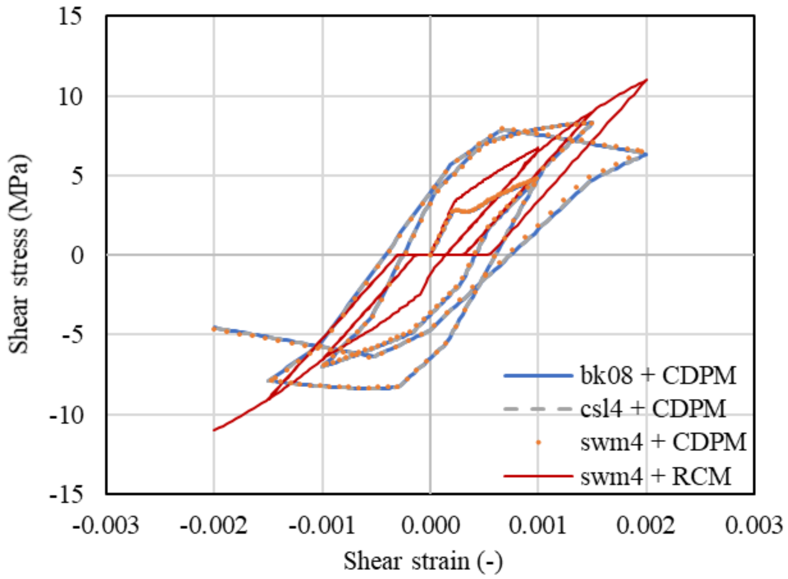

Figure 4-15: Stress-strain curves under cyclic shearing

4.5.2 Verification at element level

In subsequent numerical studies, the developed macro-element 'swm4' is used to simulate the slender RC wall specimen tested by Faraone *et al*. (2019) and analysed with existing numerical descriptions in ADAPTIC in Chapter 3. The macro-element model employs the concrete material model CDPM using the input material parameters reported in Table 3-4. A mesh sensitivity study is conducted first to investigate the influence of the mesh characteristics on the macro-element model response. As the transverse reinforcement details vary along the height of the wall specimen with reduced spacing at the bottom part (Figure 3-11(b)), at least 2 macro-elements are required to provide a realistic description of the RC wall. It is recalled from Figure 3-11(b) that the considered wall specimen is characterised by different reinforcement ratios in the top (height = 1956mm to 4877mm) and bottom (height = 0 to 1956mm) parts. As summarised in Table 4-3, in the preliminary mesh sensitivity study the wall is discretised using a different number of elements along the wall height with different macro-element sizes for the top and bottom parts.

Vertical and horizontal in-plane loads are applied at the two top two nodes of the wall model. The vertical forces are kept constant during the analysis, while the horizontal loading is monotonically increased up to failure. As discussed previously, long-duration dynamic analysis with prescribed initial velocity and zero acceleration at the loaded nodes is carried out to obtain the push-over response of the wall. The numerical load-top displacement curves shown in Figure 4-16 indicate that the numerical results converge upon mesh refinement. When the bottom portion of the wall is modelled with the same number of macro-elements, the refined mesh for the top portion does not significantly affect the response. This implies that as expected the plastic deformations are localised at the wall base, which can also be observed from the deformed shape of the numerical models using 3, 5 and 7 macro-elements as displayed in Figure 4-17.

Table 4-3: Considered wall discretisation

Model	Element No. (total)	Element No. (bottom)	Element No. (top)
MS1	2	1	1
MS2	3	1	2
MS3	4	2	2
MS4	5	2	3
MS5	6	3	3
MS6	7	3	4

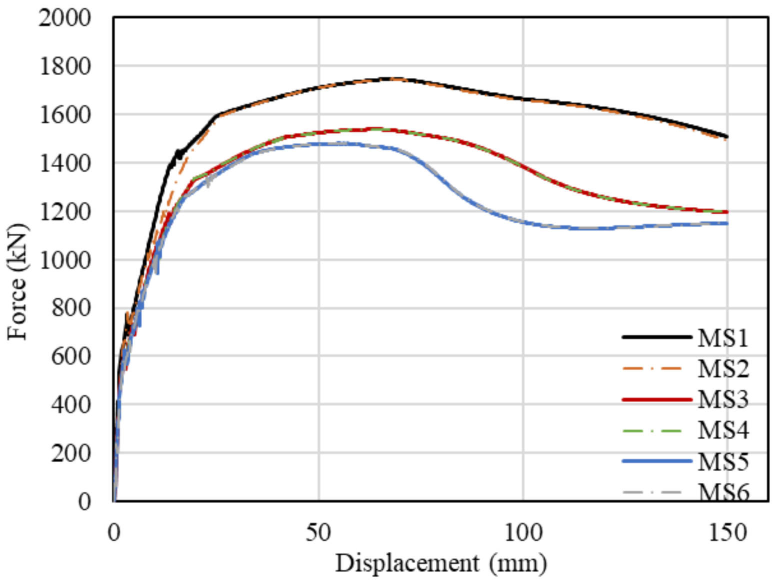

Figure 4-16: Macro-element mesh sensitivity study

To assess the accuracy of the implemented macro-element, Figure 4-18 compares the numerical response obtained from the macro-element model with 4 elements (MS3) against that provided by the detailed 3D FE model with solid elements 'bk08'. The two numerical curves are almost identical before reaching the maximum load. The macro-element model predicts a more pronounced softening behaviour after peak load, especially when using a reduced number of (n_{xc}, n_{xun}, n_y = 2×2×2). Importantly, the computational time required by the macro-element model with reduced degrees of freedom is around 1 second, which is significantly reduced compared to the detailed solid element model taking 115 minutes and 57 seconds to complete the numerical simulation.

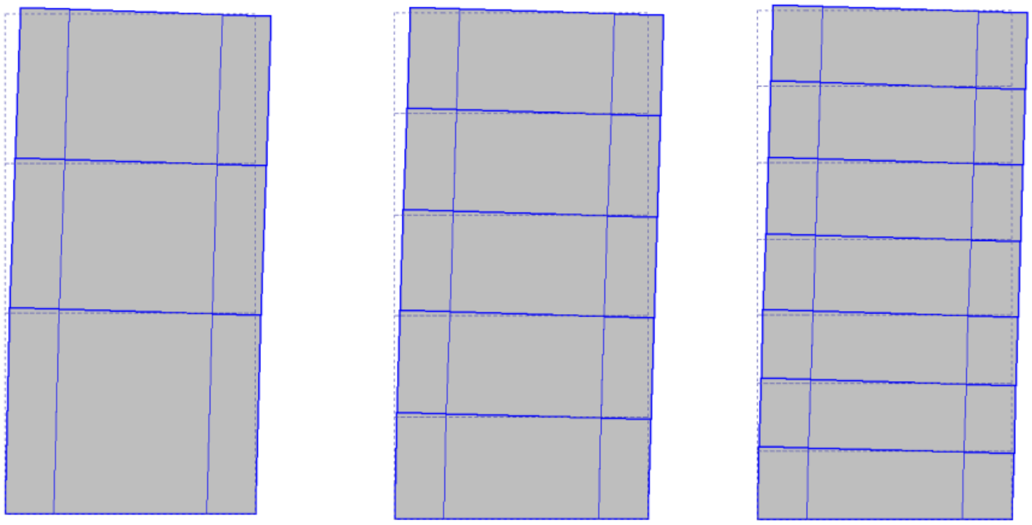

(a) (b) (c)

Figure 4-17: Deformed shapes of macro-element models with different mesh configurations: (a)MS2; (b)MS4; (c)MS6

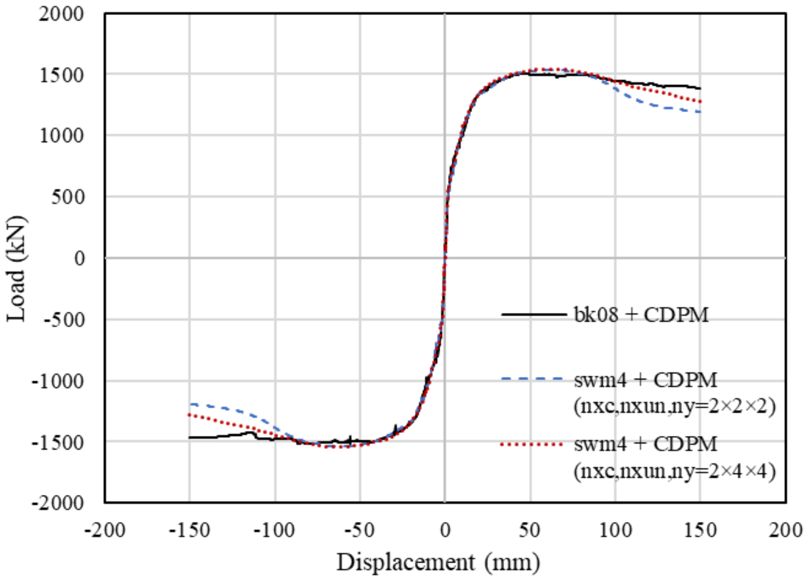

Figure 4-18: Numerical comparisons on the slender wall response using macro-elements and a 3D FE mesh with solid elements

4.6 Material parametric studies

4.6.1 Monotonic loading tests

In a subsequent study, parametric simulations are conducted to investigate the influence of different material parameters of RCM on the prediction of the monotonic response of a representative RC wall. A wall sample similar to the wall tested by Faraone *et al.* (2019) is represented by one macro-element. The analysed wall with 4877mm height, 2438mm length and 305mm thickness has the same steel reinforcement characteristics as the bottom portion of the experimental specimen. Realistic values of concrete material properties (Table 4-4) are considered for the baseline model. The steel reinforcement with a yield strength of 503 MPa is modelled as an elastic perfectly plastic material with no strain hardening. As assumed in the mesh sensitivity study, the top two nodes of the wall are subjected to lateral loads and constant axial forces. Figure 4-19 shows the push-over curve and the deformed shape at maximum displacement of the baseline model. A sudden drop before reaching the peak resistance can be observed in the predicted response due to the formation of cracks leading to energy release and stress redistribution within the wall. Then, the response curve is followed by further load increment up to the peak load.

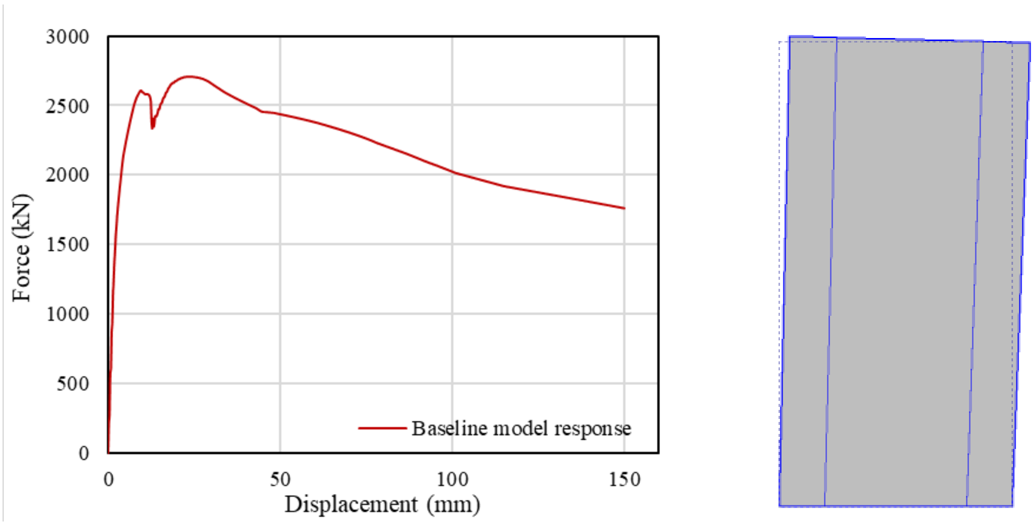

(a) (b)

Figure 4-19: Baseline model: (a) push-over response; (b) deformed shape

The influence of an individual material parameter on the response curve is investigated by assuming a range of values for that parameter, while the other parameters are kept the same as in the baseline model. Figure 4-20 to Figure 4-26 show a series of numerical responses obtained from the parametric investigation. It can be seen that the secant compressive stiffness E_{c1} affects the response before reaching the peak strength, as it defines the strain corresponding to the concrete compressive strength and controls the compressive cracks during loading. By increasing the secant compressive stiffness, the model predicts a stiffer initial response and a shift of the force drop to smaller displacement levels is noted. As expected, the compressive strength f_{c1} and the compressive softening modulus E_{c2} strongly affect the maximum load prediction and the softening branch as indicated in Figures 4-21 and 4-22. On the other hand, the initial response before the sudden force drop due to cracking are barely affected by these two parameters. As revealed in Figure 4-23, the influence of the residual strength f_{c2} stands out only for larger displacement levels, where an increased residual resistance is obtained using large f_{c2} values.

Table 4-4: Baseline model RCM material parameters [MPa] for the numerical test under monotonic loading

E_{c1}	f_{c1}	E_{c2}	f_{c2}	E_{t1}	f_t	E_{t2}
30000	30	-3000	6	30000	3	-3000

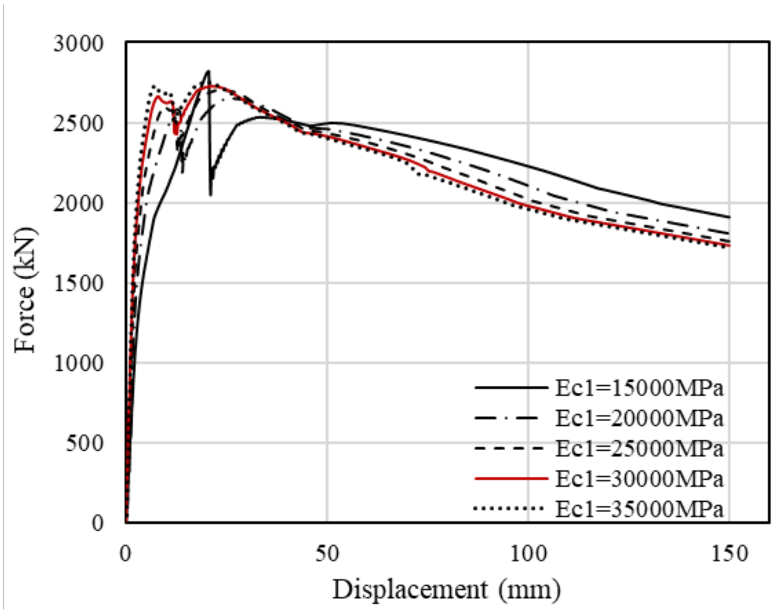

Figure 4-20: Influence of RCM parameter E_{c1} on the monotonic response of the RC wall sample

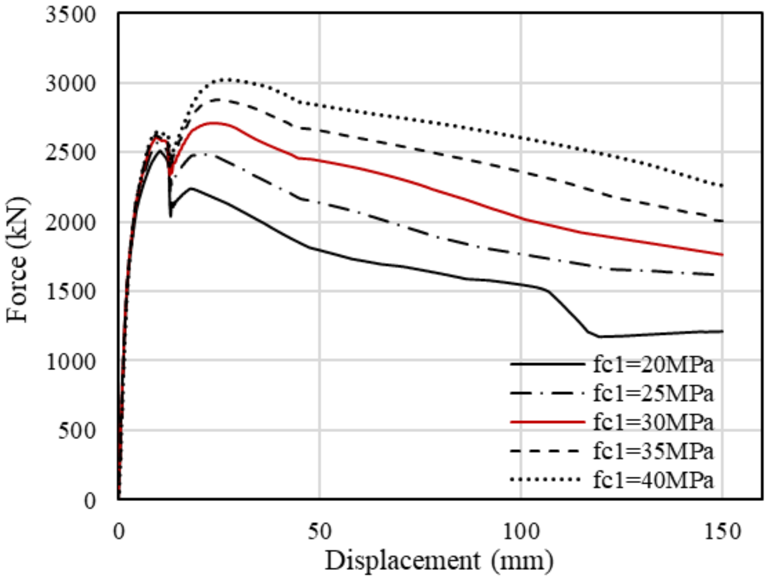

Figure 4-21: Influence of RCM parameter f_{c1} on the monotonic response of the RC wall sample

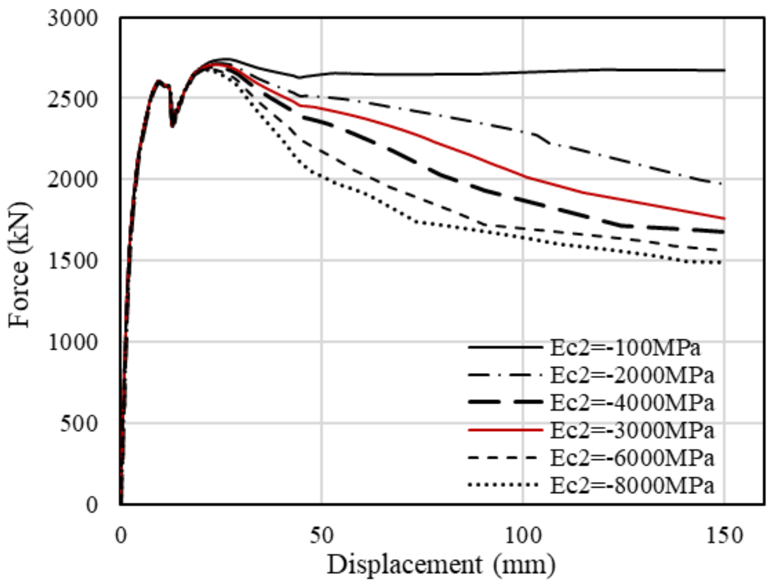

Figure 4-22: Influence of RCM parameter E_{c2} on the monotonic response of the RC wall sample

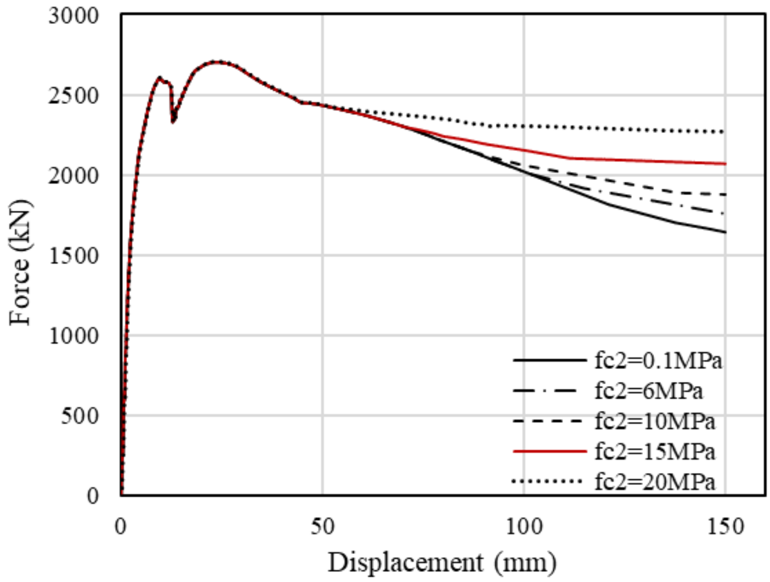

Figure 4-23: Influence of RCM parameter f_{c2} on the monotonic response of the RC wall sample

In terms of parameters related to the tensile behaviour, it is noted from Figure 4-25 that the concrete tensile strength f_t has an important role in the response prediction of the wall, where the use of high f_t values leads to an increased initial stiffness and maximum load. By contrast, changes in the initial tensile stiffness E_{t1} barely affect the numerical predictions. The influence of the tensile softening stiffness E_{t2} is studied in Figure 4-26. When the value of E_{t2} is taken as an unrealistic value -100 MPa, the concrete tensile behaviour is elasto-plastic, causing a drastic increase in the wall resistance. As expected, it can be observed from Figure 4-25 and Figure 4-26 that the global post-peak responses are typically independent from the variations of the concrete tensile strength f_t and tensile softening stiffness E_{t2}.

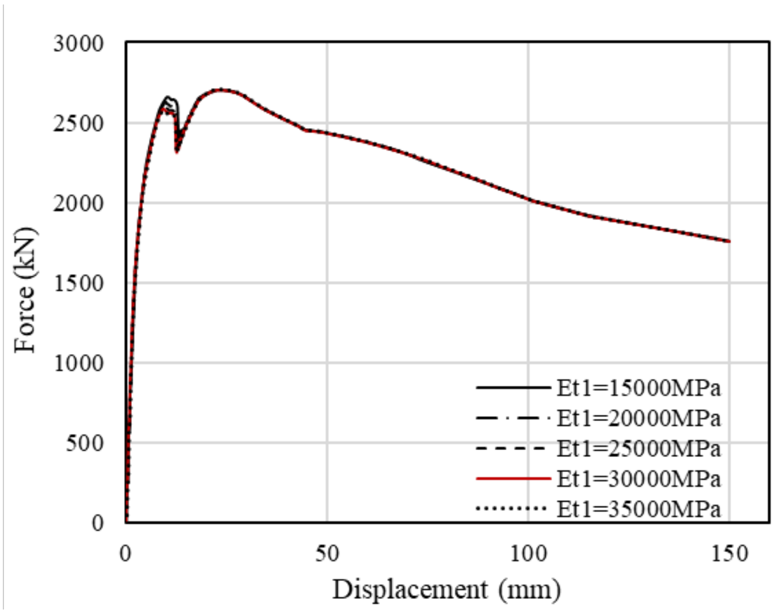

Figure 4-24: Influence of RCM parameter E_{t1} on the monotonic response of the RC wall sample

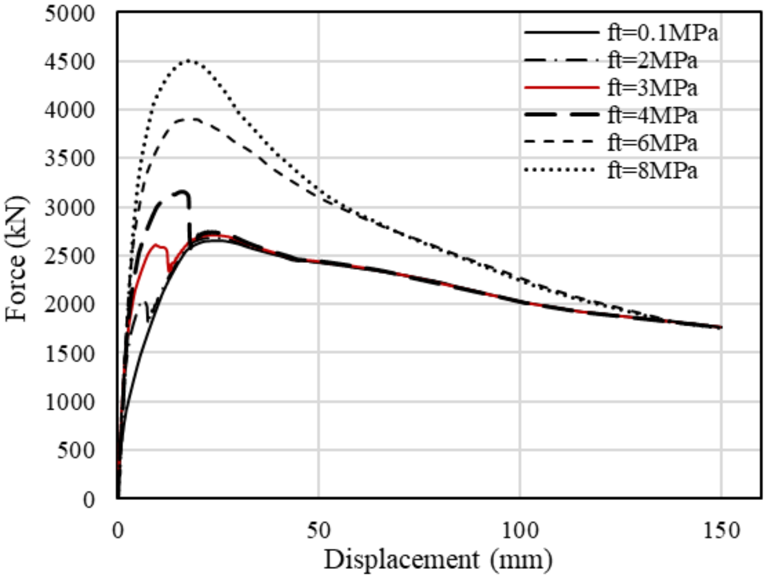

Figure 4-25: Influence of RCM parameter f_t on the monotonic response of the RC wall sample

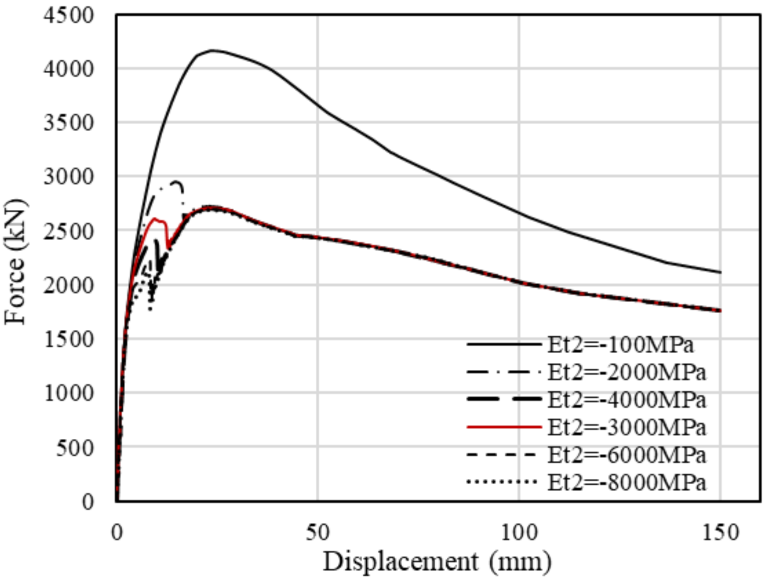

Figure 4-26: Influence of RCM parameter E_{t2} on the monotonic response of the RC wall sample

4.6.2 Cyclic loading tests

A short RC wall specimen is considered here to study the influences of RCM concrete material parameters on the cyclic response predictions. The analysed wall sample has 900mm height, 900mm length and 80mm thickness. It is reinforced with two orthogonal grids of steel reinforcement with 8mm diameter bars at 122mm and 219mm spacings in the horizontal and vertical directions, respectively. For the baseline model, the concrete material properties employed in the simulation are reported in Table 4-5. The Young's modulus, the yield strength, and the strain hardening parameter for steel reinforcements are defined as 200GPa, 500MPa and 0.01. The initial simulation used a single macro-element to represent the wall. Nevertheless, the resulting cyclic response exhibit a minor degree of pinching of the hysteresis loops since the strain approximations based on the element kinematics are less accurate. To obtain a more representative cyclic response curve, three macro-elements are employed to generate the baseline model. Besides, the boundary conditions and lateral loads are applied similarly to the monotonic loading tests. The cyclic lateral loads imposed at the top of the wall are prescribed to a single cycle with target drift ratios 0.1%, 0.16%, 0.33%, 0.57%, 0.82%, 1.15%, 1.64%, 2.13% and 2.62% in both the positive and negative directions.

Table 4-5: Baseline model RCM material parameters [MPa] in cyclic tests

E_{c1}	f_{c1}	E_{c2}	f_{c2}	E_{t1}	f_t	E_{t2}
27133	20	-1000	4	27133	2	-1000

Material parametric analyses are conducted by varying the concrete material properties listed in Table 4-5. Numerical results are obtained by changing a specific input material parameter in the baseline model while keeping the remaining material properties unchanged. The aim is to find the critical parameters that influence the primary characteristics of the cyclic response, including the varying envelope curve, the stiffness and strength degradations, and the pinched shapes of the hysteresis loops. It has been found that parameters f_{c1}, E_{c2}, f_t and E_{t2} have the most pronounced effects, as shown in Figure 4-27 to Figure 4-30, where the baseline model responses are displayed in red colour throughout. The response predicted by the baseline model exhibits the main features of cyclic wall behaviour displayed in physical tests on similar wall specimens, including the envelope curve with post-peak softening, secant stiffness degradation in successive loops, degradations of unloading/reloading stiffness, and plastic deformation at zero force followed by pinching behaviour upon unloading to zero displacements.

The influences of varying concrete compressive strength are shown in Figure 4-27, where the values of f_{c1} are set as 15MPa, 20MPa, 25MPa and 30MPa. As expected, this parameter directly determines the overall wall capacity. The wall exhibits a more ductile behaviour, with the cyclic envelope tending to the elasto-plastic response without softening when the value of f_{c1} increases. As a result, the reloading curves in the cyclic response predictions change due to the target envelopes having different degrees of softening. In addition, with the same compressive softening modulus, the variation of f_{c1} controls the plastic strains as the wall is unloaded to zero loads, which affects the rate of degradations of the unloading/reloading stiffness. This can also alter the pinching behaviour controlled by the transition from compressive to tensile behaviour at the material point level.

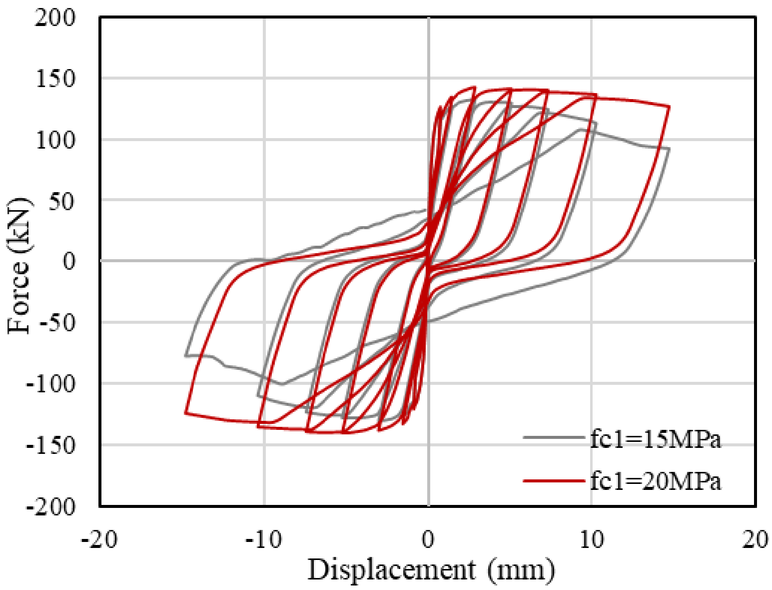

(a)

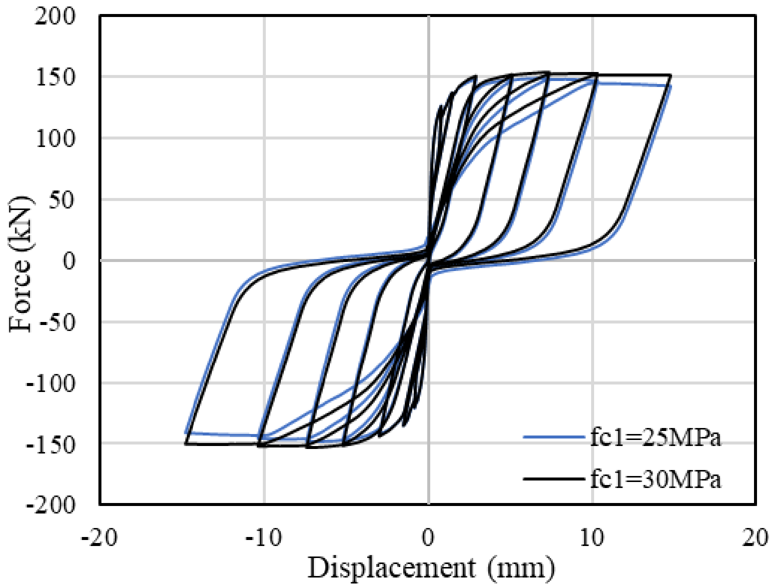

(b)

Figure 4-27: Influence of RCM parameter f_{c1} on the cyclic response of a short wall specimen

In Figure 4-28, the effects of compressive softening modulus E_{c2} are studied considering a relatively small value -100MPa resembling the elasto-plastic compressive behaviour and three realistic values -1000MPa, -2000MPa and -3000MPa. Predicted cyclic responses can be distinguished by the post-peak softening behaviour and the pinching characteristics. It can be found that the peak lateral load capacity of the wall is barely affected by E_{c2}, unlike in the previous monotonic loading tests on the slender wall. By contrast, the increasing level of softening is caused by a larger absolute value of E_{c2}, which is consistent with the conclusion drawn from Figure 4-22. Consequently, the unloading and reloading branches in the cyclic response predictions are affected by the global post-peak behaviour, similar to the findings from the parametric studies on f_{c1}.

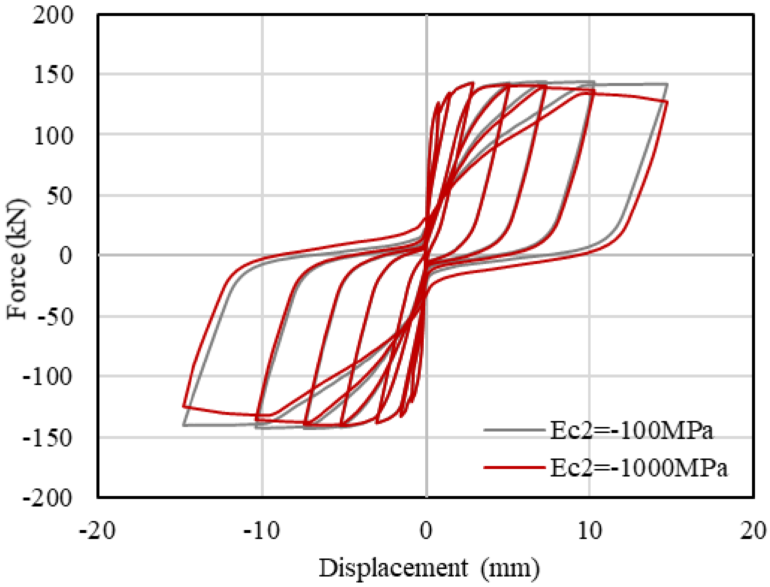

(a)

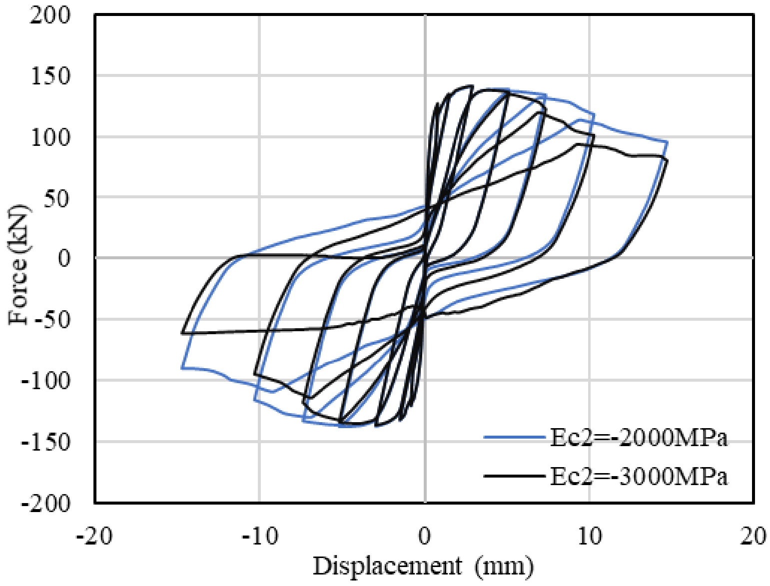

(b)

Figure 4-28: Influence of RCM parameter E_{c2} on the cyclic response of a short wall specimen

Regarding the concrete tensile material properties, Figure 4-29 displayed the cyclic response curves obtained using different tensile strengths, where f_t = 1MPa to f_t = 4MPa are considered. It can be observed that f_t has significant influence on the initial stiffness of the wall. The use of the unrealistic high value of f_t, for example 3MPa and 4MPa result in the increasing peak load corresponding to the smaller displacement level. In addition, the greater value of f_t notably decrease the rate of unloading stiffness degradation and the degree of pinching. In the following, the influences of E_{t2} on the cyclic response are investigated in Figure 4-30. The numerical results are marginally affected except for the case of E_{t2} = -100MPa. It can be seen that the overall wall capacity is substantially increased considering the elasto-plastic tensile behaviour. Moreover, the influence of E_{t2} on the unloading stiffness is more pronounced when E_{t2} is changed from -1000MPa to -2000MPa.

From the material parametric studies it can be concluded that f_{c1} and E_{c2} play crucial roles in determining the main characteristics of the cyclic response prediction, particularly the stiffness and strength degradation and the pinching behaviour of the global cyclic hysteresis loops. Special attention should be paid to the use of realistic values of f_t and E_{t2} as they can strongly affect the unloading stiffness. The conclusions drawn here have been utilised to calibrate the macro-element models used in the numerical-experimental comparisons for model validation presented in Chapter 5.

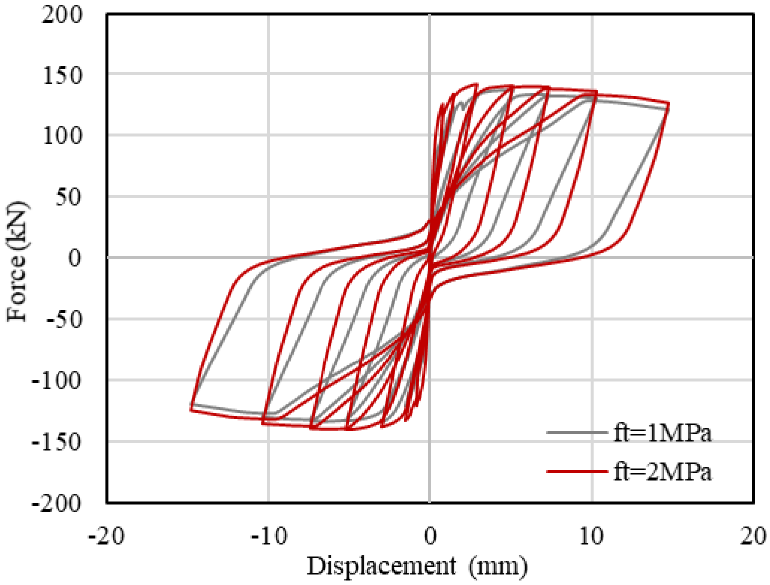

(a)

Figure 4-29: Influence of RCM parameter f_t on the cyclic response of a short wall specimen (Con’d)

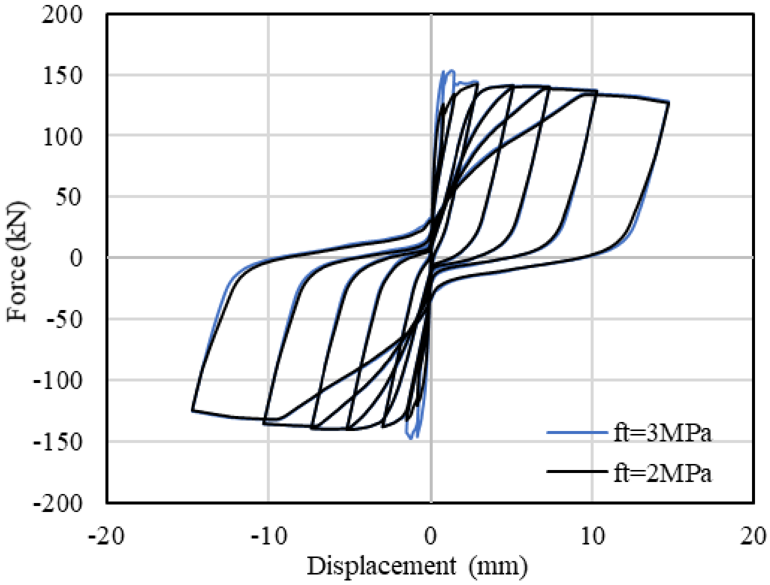

(b)

Figure 4-29: Influence of RCM parameter f_t on the cyclic response of a short wall specimen

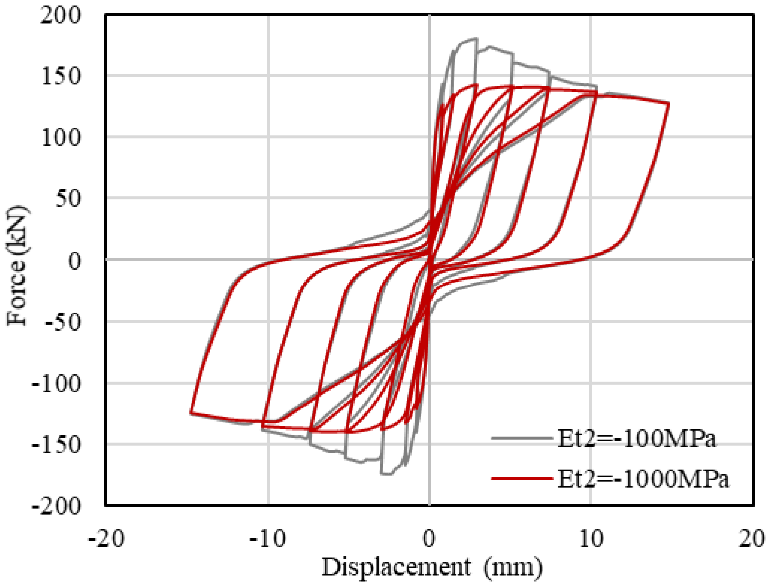

(a)

Figure 4-30: Influence of RCM parameter E_{t2} on the cyclic response of a short wall specimen (Con'd)

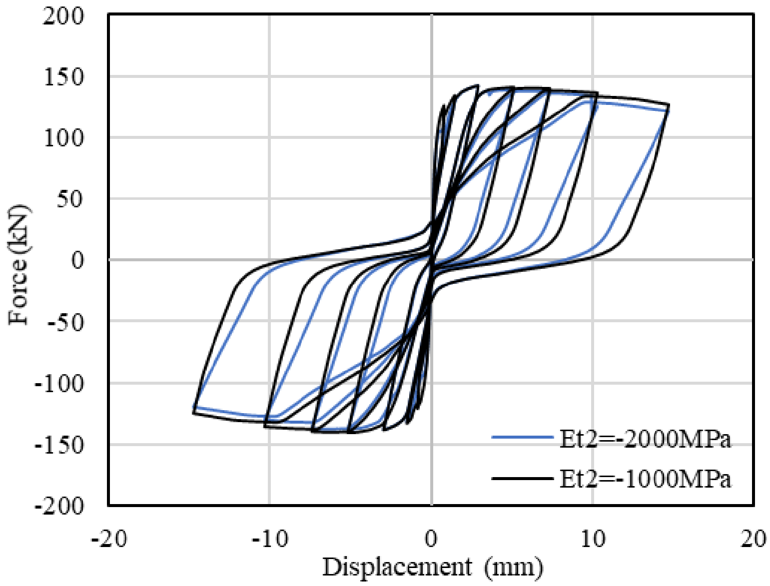

(b)

Figure 4-30: Influence of RCM parameter E_{t2} on the cyclic response of a short wall specimen

4.7 Concluding remarks

This chapter has developed a novel modelling strategy for accurate an efficient analysis of RC shear walls under in-plane lateral loading conditions. A 2D specialised macro-element has been proposed and implemented into the finite element program ADAPTIC. The macro-element incorporates two concrete material models: (i) a condensed version of the sophisticated concrete damage plasticity model (CDPM) used in the detailed 2D and 3D FE models in ADAPTIC and (ii) a newly developed biaxial concrete model (RCM) based on the rotating crack approach.

The accuracy of the implemented macro-element is verified first at the monitoring point level by single element numerical tests and then at the element level by modelling a RC wall specimen. Numerical analyses based on comparable models using 3D solid elements and 2D shell elements have been conducted and obtained results have been compared against the macro-element model predictions. It has been found that the proposed macro-element is capable of accurately modelling RC walls subjected to in-plane loading. The mesh sensitivity study of the macro-element models suggests that the use of at least four macro-elements leads to an accurate prediction of the response of typical slender walls. Afterwards, material parametric investigations have been conducted to investigate the influence of the input material parameters of the RCM on the wall response. As opposed to the more sophisticated CDPM model, the implemented RCM relies on fewer input material parameters that can be obtained from simple experimental material tests or calibrated based on analytical concrete material models. It has been found that the computational effort required to model a RC wall using the proposed macro-element description is significantly reduced compared to the detailed 3D solid element or 2D shell element models. This makes it suitable for modelling large structures as realistic building systems equipped with RC shear walls.

It is worth noting that the developed macro-element approach, despite offering numerical accuracy and computational efficiency, is not capable of modelling struct actions, localised concrete spalling and reinforcement buckling that may be exhibited by typical RC walls at collapse. Furthermore, steel reinforcement anchorage failure due to poor detailing is not taken into account, since the proposed macro-element formulation assumes a perfect bond between concrete and steel reinforcement.

Chapter 5

Validation of Macro-element for RC Walls

5.1 Introduction

This chapter employs the shear wall macro-element proposed in Chapter 4 for analysing a range of RC wall components. The primary aim is to demonstrate that the developed macro-element guarantees considerable efficiency in achieving accurate and reliable response predictions. Numerical simulations under in-plane cyclic loading condition have been performed on selected experimental RC shear wall specimens with rectangular cross section and different aspect ratios and a RC coupled wall. The numerical results are compared against experimental data to examine the accuracy of the macro-element model. The main cyclic response characteristics of RC walls are investigated, including stiffness deterioration, strength degradation, and the pinching of the hysteresis loops. Besides, the accuracy of the developed macro-element in predicting the actual dissipated energy and stiffness degradation of RC walls under cyclic loading is investigated and discussed.

In the following, Section 5.2 presents validation studies considering the slender wall tested by Faraone *et al*. (2019) and investigated in Chapter 3 using existing modelling strategies in ADAPTIC. The influence of concrete confinement due to transverse reinforcement and the number of loading cycles on the response prediction is also analysed to better understand the potential of the developed macro-element model. Subsequently, Section 5.3 and Section 5.4 consider the physical tests conducted by Salonikios *et al*. (1999), analysing a series of walls with short and moderate aspect ratios and varying reinforcement details. Section 5.5

investigates a five-storey RC coupled wall system tested by Lu and Chen (2005), and finally Section 5.6 provides conclusions based on the results of the validation studies.

5.2 Slender wall

5.2.1 Numerical models

This section performs numerical simulations using the developed macro-element representation considering the experimental RC slender wall AR2-8, previously analysed using existing modelling strategies in Section 3.3.2. A description of the experimental programme and the test set-up is provided in Section 3.3.2.1, where details of the wall specimen are also given. Table 5-1 summarises the reinforcement details for wall AR2-8, for which the detailed design procedure can be found in Faraone *et al*. (2019).

Table 5-1: Reinforcement details for wall AR2-8

Wall	Horizontal web	Vertical web	Longitudinal	Transverse
	ρ_v (%)	ρ_h (%)	ρ_{be} (%)	ρ_{trv} (%)
AR2-8	0.6 2 #4@152.4mm	1.0 2 #6@203.2mm	2.2 9 #6@177.8mm	1.25 #4@101.6mm (bottom part) #4@203.2mm (top part)

Based on the mesh sensitivity analysis performed in Section 4.5.2, the use of five macro-elements along the wall height is deemed appropriate. Moreover, it is found that adding a stiff steel beam onto the top of the wall model enables a convenient application of the vertical and in-plane horizontal forces. Thus, in the numerical simulations for model validation, the axial load (8% of the cross-sectional capacity) is applied to the top two nodes of the steel beam element. Figure 5-1 shows the resulting mesh with loading and boundary conditions. Each macro-element features a relatively dense distribution of monitoring points (n_{xc}, n_{xun}, n_y = 4×10×10), as illustrated in Figure 5-1, in comparison to those previously defined in Section 4.5.2. The cyclic horizontal load is applied by a spreader element through a piecewise linear acceleration history to achieve a piecewise cubic displacement history. All the bottom nodes are fixed, whereas the remaining nodes are restrained in the out-of-plane direction.

The material parameters reported in Table 3-1 and Table 3-2 for steel reinforcement and concrete are used for the nonlinear simulation with the macro-element model. It is recalled that in the previous numerical investigation with beam-column elements in Chapter 3, the modified Kent and Park model (Scott *et al.*, 1982) has been adopted, taking into account the confinement effects due to the transverse reinforcement in the boundary elements. The material properties for the uniaxial constitutive concrete model, including the compressive strength f_{c1}, the compressive softening stiffness E_{c2} and the residual compressive strength f_{c2} have been determined using Eqs (3-18) - (3-22). An additional model is generated by setting the concrete material parameters in the confined regions the same as those used for the unconfined web region to investigate the impact of the confinement effects on the response.

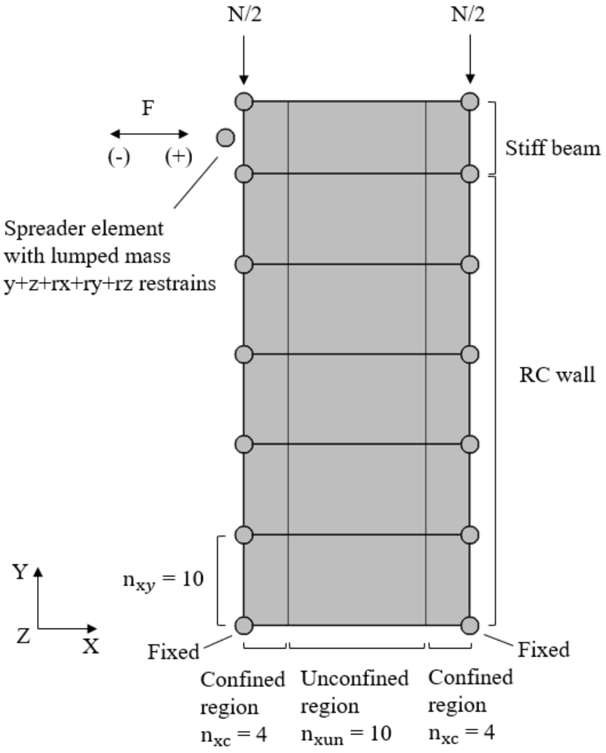

Figure 5-1: Macro-element representation for wall AR2-8

5.2.2 Influence of confinement effects

Figure 5-2 compares the experimental data with the numerical results obtained from the models with and without accounting for the confinement effects due to transverse reinforcements in the boundary elements. It can be observed that the unconfined model (without the confinement effect) provides a better response prediction than the confined model (with the confinement effect). As shown in Figure 5-2(b), typical cyclic response characteristics are reproduced well, including the stiffness and strength degradation, the load capacity, and the stiffness of the unloading branches. The pinching behaviour is marginally overestimated especially in the last two cycles by the unconfined model. On the contrary, the confined model (Figure 5-2(a)) shows a close agreement regarding pinching behaviour and the displacement at the initiation of cracks closure. However, the latter model overpredicts the wall strength without showing strength degradation. Considering the results presented in Section 3.3.2, it is noted that the developed macro-element guarantees a significantly improved accuracy compared to existing modelling strategies. It is also found that the implemented macro-element formulation requires substantially less computing time (30secs) than the detailed 2D (70mins) or 3D FE modelling strategies (865mins). The experimental cyclic response is validated following further material parametric studies in the next section.

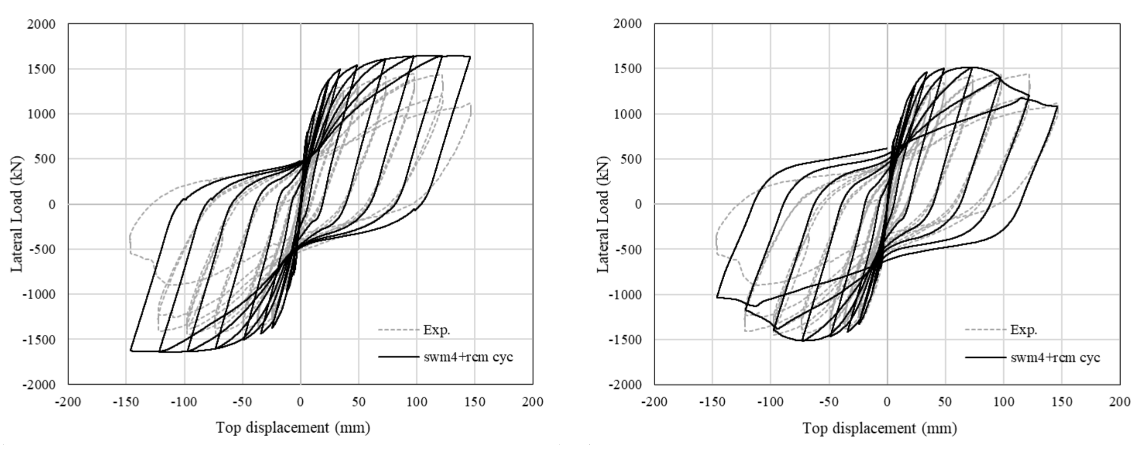

(a) (b)

Figure 5-2: Numerical-experimental comparisons of slender wall AR2-8 under cyclic loading: (a) with (confined model) and (b) without confinement effects (unconfined model)

5.2.3 Calibration of material parameters

A major advantage of the developed macro-element description is that the response prediction can be calibrated in a relatively simple manner since the employed concrete material model requires only a few parameters. In a parametric study has been found that the compressive softening stiffness E_{c2} has the most pronounced impact on the wall cyclic behaviour.

Figure 5-3 presents further investigations on the influences of the concrete material parameter E_{c2} in the confined region. The considered range of values for E_{c2} are specified as -2000MPa, -2500MPa, -3000MPa and -4000MPa, noting that the value of -913MPa is used for the previous confined model (Figure 5-2(a)). The decreasing values of E_{c2} alter the reloading branches in the first quadrant, which in turn affects the rate of strength degradation, as displayed in Figure 5-3. The simulation using E_{c2}=-2500MPa achieves the best agreement with the experimental results. The numerical prediction accurately captures the main cyclic response characteristics, although the reloading branches slightly overestimate the test results. With decreased values of E_{c2}, as displayed in Figure 5-3(c) and (d), the predicted response in the final cycle shows a loss of resistance when the displacements unload to 100mm and then reload in the opposite direction. This corresponds to the development of sliding shear failure in the bottom part of the wall.

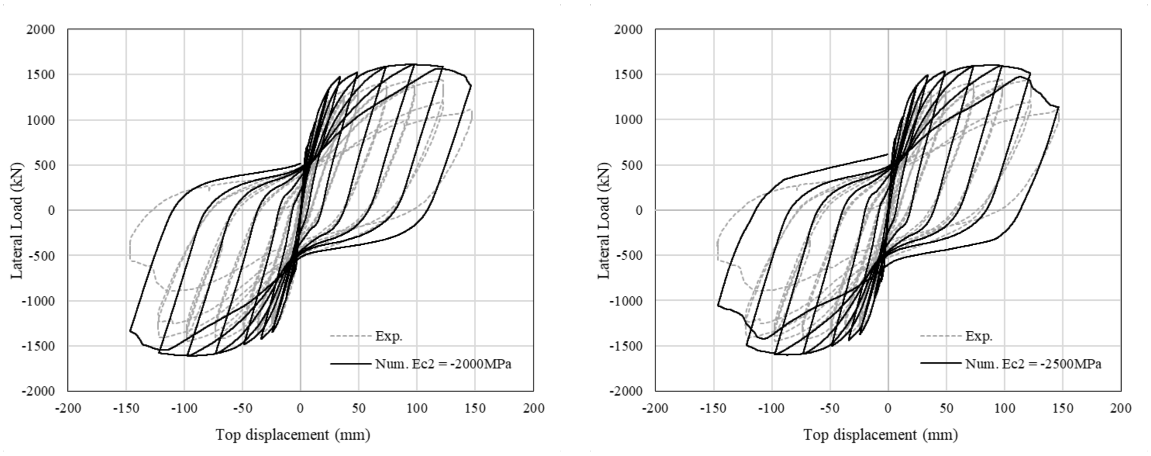

(a)

(b)

Figure 5-3: Numerical simulations with varying E_{c2} for the confined concrete of wall AR2-8 model: (a) E_{c2}=-2000MPa; (b) E_{c2}=-2500MPa; (a) E_{c2}=-3000MPa; (b) E_{c2}=-4000MPa (Con'd)

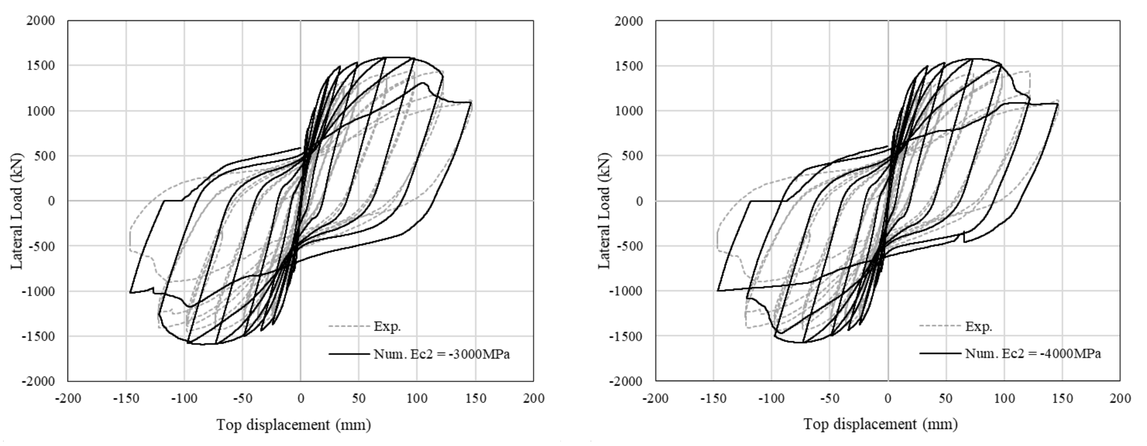

(c) (d)

Figure 5-3: Numerical simulations with varying E_{c2} for the confined concrete of wall AR2-8 model: (a) E_{c2}=-2000MPa; (b) E_{c2}=-2500MPa; (a) E_{c2}=-3000MPa; (b) E_{c2}=-4000MPa

5.2.4 Influence of loading cycles

Upon model validation under cyclic loading, further analyses have been carried out to investigate the effects of the number of loading cycles on the response. As described in Section 3.3.2.1, the original experimental loading protocol assumes at least two loading cycles per drift level. Two additional numerical analyses have been performed based on two and three loading cycles at each displacement level to investigate the influence of applying multiple cycles for the same displacement amplitude. Figure 5-4 reveals that the numerical curves associated with the application of multiple cycles are in good agreement with the experimental data. The numerical results exhibit cyclic degradations after consecutive cycles at a specific drift level. However, it is noted that such predicted cyclic degradation is more pronounced than that observed in the tests. More specifically, when subjected to two loading cycles (Figure 5-4(a)) and three loading cycles (Figure 5-4(b), the wall model experiences early shear sliding failure at the bottom of the wall, which is not observed in the test. Thus, accurate calibration of the model material parameters should also consider the effects of repeated loading cycles, as they may affect the predicted failure mode for the analysed wall.

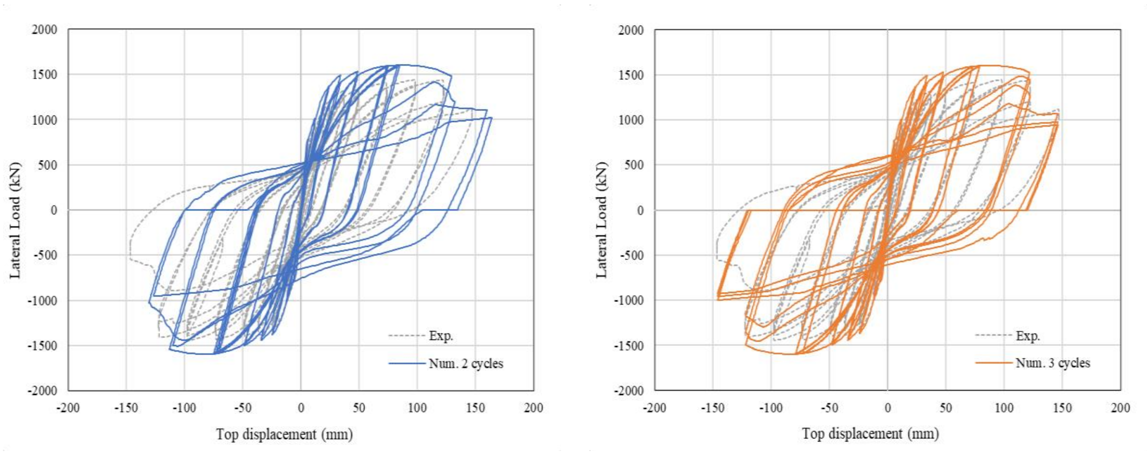

(c) (d)

Figure 5-4: Influence of the number of loading cycles for the same horizontal displacement level: (a) two cycles; (b) three cycles

5.3 Short wall

5.3.1 Experimental specimens

Further numerical investigations have been conducted analysing the wall specimens tested in the comprehensive experimental program carried out by Salonikios *et al*. (1999). It involved a series of RC wall tests, including six specimens with a moderate aspect ratio of 1.5 (MSW series) and five specimens with a low aspect ratio of 1.0 (LSW series). The walls were tested under in-plane cyclic loading, where the influence of the level of axial load, the web reinforcement ratio, and the reinforcement ratio in the boundary region was investigated. An earlier version of EC8 (CEN, 1995) was utilised to design the wall specimens against shear using either orthogonal web reinforcement or bidiagonal reinforcements. The latter provides effective control of sliding and the pinching characteristics in the subsequent cyclic loops. The detailed descriptions of the experimental program and the test set-up have been given in Section 3.3.3.1.

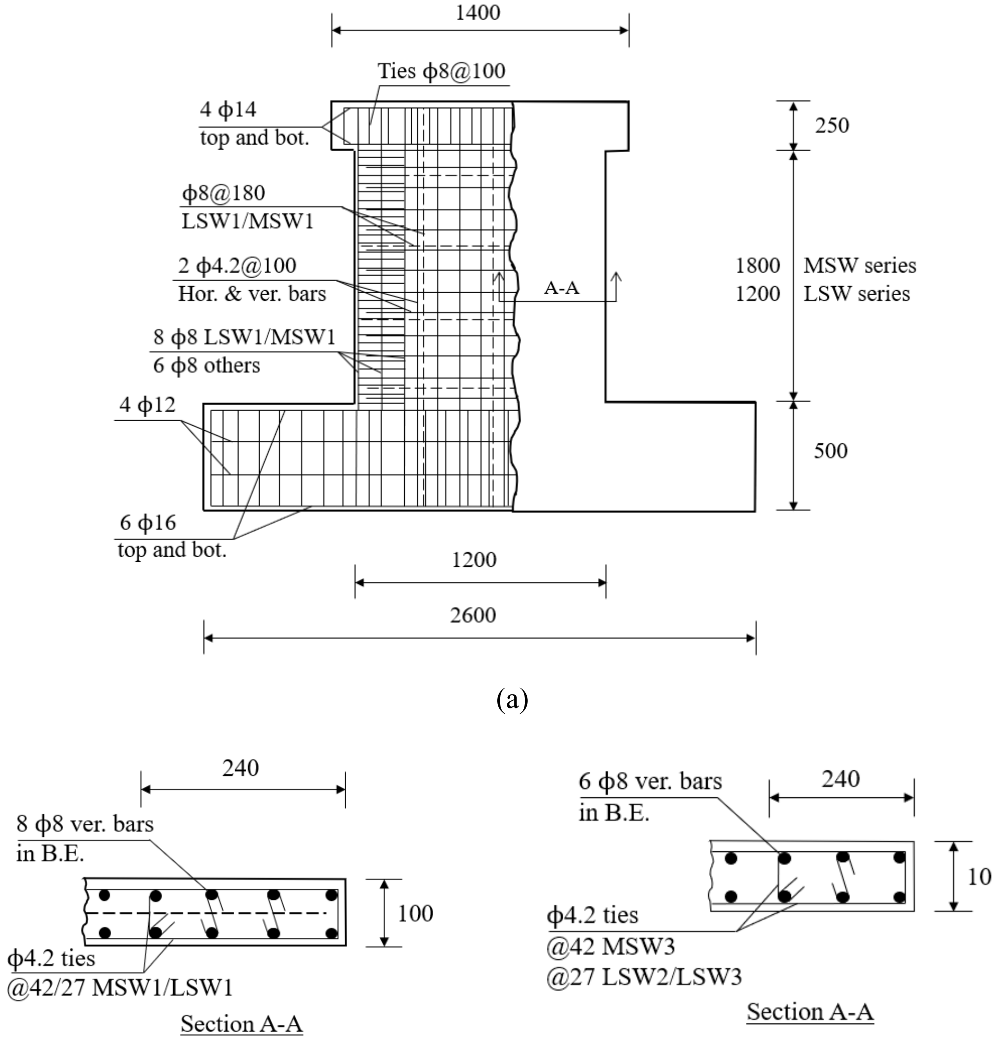

(a)

(b) (c)

Figure 5-5: Schematic reinforcement details of the selected RC wall specimens tested by Salonikios *et al*. (1999): (a) elevation views; (b) section A-A for LSW1 and MSW1 specimens; (c) section A-A for MSW3, LSW2 and LSW3 specimens

In the present and following sections, only the walls with orthogonal web reinforcement are analysed. More specifically, the specimens LSW1, LSW2, LSW3, MSW1, and MSW3 have been selected for numerical-experimental comparisons. All the wall specimens have the same cross-sectional area of 1200×100mm^2, corresponding to 1:2.5 scaled wall samples based on a typical wall configuration. The wall heights are1800mm and 1200mm for the samples with moderate and low aspect ratios, respectively. Figure 5-5 schematically depicts the geometry and the reinforcement details for the selected five wall specimens.

In the low aspect ratio wall series, LSW2 and LSW3 have the same web reinforcement ratio of 0.277 %, resulting from two curtains with 4.2 mm diameter bars at 100 mm spacing. This meets the minimum requirements for the web reinforcement of 0.2% and 0.25% as prescribed in EC2 (BSI, 2004a) and ACI 318-14 (2014). The boundary regions with 100×240mm^2 cross-sections are provided with six 8mm diameter longitudinal bars, leading to a reinforcement ratio of 1.3 %, which fulfils the 0.5% requirement in EC8 (BSI, 2004b). Two more longitudinal 8 mm steel bars are provided in the boundary elements of wall LSW1. All the longitudinal bars in the LSW wall series are confined by the 4.2 mm stirrups spaced at a close spacing of 27 mm. As indicated by the dashed lines in Figure 5-5, the specimen LSW1 is equipped with an additional orthogonal steel grid with 8 mm diameter bars spaced at 180 mm, which effectively doubles the web reinforcement ratio of the specimen LSW2 and LSW3. Moreover, the specimen LSW3 is subjected to a constant axial load corresponding to 7% of the cross-sectional capacity, whereas no axial loads are applied on the specimens LSW1 and LSW2.

Table 5-2: Reinforcement details for walls LSW1/LSW2/LSW3

Wall	ρ_h (%)	ρ_v (%)	ρ_{be} (%)	ρ_{trv} (%)	N
LSW1	0.565 2 ϕ4.2@100mm 1 ϕ8@180mm	0.565 2 ϕ4.2@100mm 1 ϕ8@180mm	1.7 8 ϕ8	1.7 ϕ4.2 @27mm	-
LSW2	0.277 2 ϕ4.2@100mm	0.277 2 ϕ4.2@100mm	1.3 6 ϕ8	1.7 ϕ4.2 @27mm	-
LSW3	0.277 2 ϕ4.2@100mm	0.277 2 ϕ4.2@100mm	1.3 6 ϕ8	1.7 ϕ4.2 @27mm	$0.07A_cf_c$

Table 5-2 summarises the reinforcement details for the LSW series. It is inferred from the reinforcement details that LSW1 is a representative example of a wall designed to resist more severe seismic forces than the LSW2/LSW3. The set of concrete material properties in Table 5-3, which were calculated according to the modified Kent and Park model (Scott *et al.*, 1982), are used in the initial numerical simulations. The steel reinforcement properties have been previously given in Table 3-5. The modelling assumptions made for the slender wall in Section 5.2.1 are also applied to the LSW1, LSW2 and LSW3 models, whereas 6 macro-elements are employed to represent the RC wall samples.

Table 5-3: Material parameters for analysing walls LSW1/LSW2/LSW3

Wall	Material	E_{c1} $[MPa]$	f_{c1} $[MPa]$	E_{c2} $[MPa]$	f_{c2} $[MPa]$	E_{t1} $[MPa]$	f_t $[MPa]$	E_{t2} $[MPa]$
LSW1	Confined	31730	32.15	-425	6.43	28047	2.30	-425
	Unconfined	28047	22.20	-4926	4.44	28047	2.30	-4926
LSW2	Confined	31532	31.55	-416	6.31	27792	2.30	-416
	Unconfined	27792	21.60	-4605	4.32	27792	2.30	-4605
LSW3	Confined	32280	33.85	-449	6.77	28746	2.49	-449
	Unconfined	28746	23.90	-5893	4.78	28746	2.49	-5893

5.3.2 Numerical-experimental comparisons

Figure 5-6 presents preliminary numerical-experimental comparisons for the considered low aspect ratio walls LSW1, LSW2 and LSW3. It is recalled that the walls LSW1 and LSW2 are identical except for reinforcement ratios, whereas LSW2 and LSW3 differ only in the applied compressive axial forces.

In general, the macro-element models for all three wall specimens simulate the overall shapes of the experimental cyclic loops with a reasonable level of accuracy. The models give good predictions of the initial stiffnesses and the global stiffness degradations in the consecutive cyclic excursions. The pinched hysteretic behaviour shown by the experimental curves is effectively represented by the numerical simulations. Minor underestimations of pinching are found in the wall LSW1 and LSW2 predictions, whereas more notable differences are revealed in the numerical results for wall LSW3. In contrast to walls LSW1 and LSW2, wall LSW3 exhibits less pinched hysteresis loops implying a more ductile behaviour attributed to the confinement effects due to the imposed compressive axial load. As a result, wall LSW3 dissipate substantially higher hysteretic energy than walls LSW1 and LSW2, as shown in Figure 5-6.

The experimentally measured peak horizontal loads are typically well predicted within the 2% range. As expected, the force capacity of wall LSW1 is greater than that of wall LSW2 since wall LSW1 has a double amount of web steel reinforcements compared to wall LSW2. Compared to the wall LSW2 response, wall LSW3 achieves increased overall resistance due to higher axial force, effectively limiting the sliding deformation at the wall bottom portion. After reaching the peak load, the experimental responses of the three specimens show progressive strength degradation, which is not predicted by the numerical models with macro-elements. Conversely, the numerical load-displacement curves show a marginal increase in strength by increasing the top displacement, especially the numerical response predicted by the wall LSW3 model. This, in turn, affects the unloading and reloading stiffness reductions with the increasing cyclic displacement amplitude, since the envelope curve controls the unloading and reloading branches.

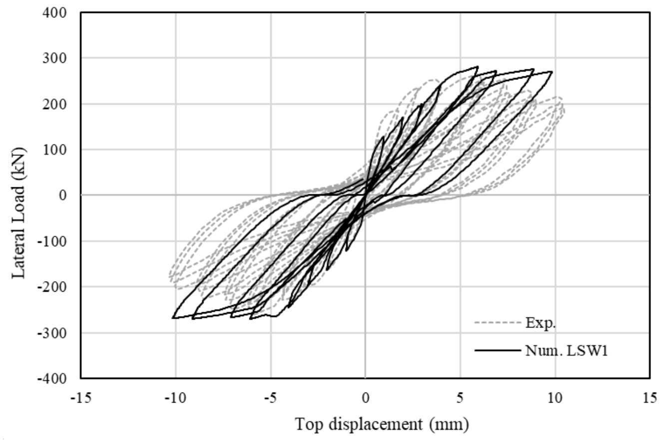

(a)

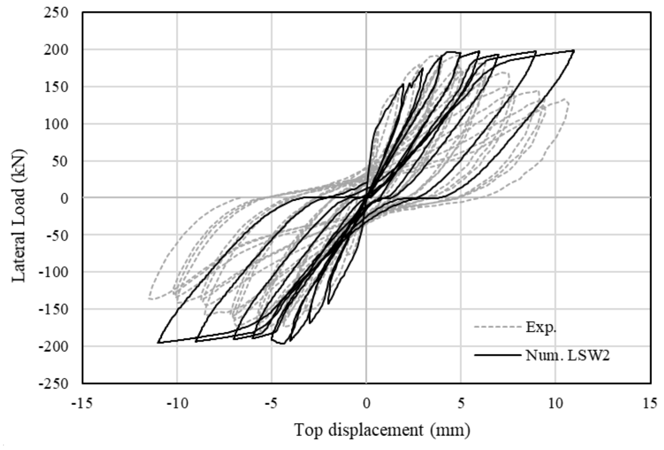

(b)

Figure 5-6: Numerical-experimental comparisons for the short wall specimens (a) LSW1, (b) LSW2 and (c) LSW3 under cyclic loading allowing for concrete confinement (Con’d)

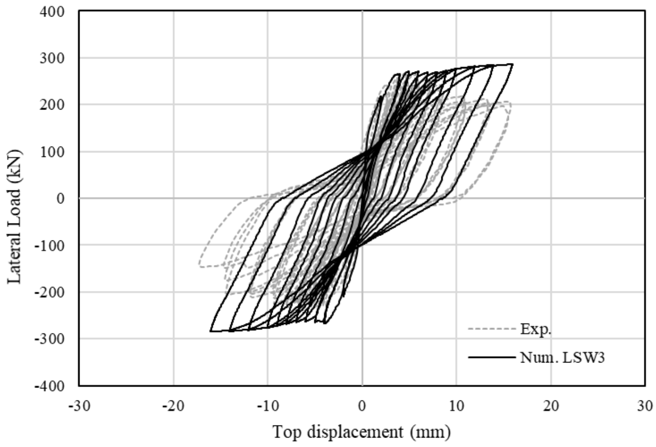

(c)

Figure 5-6: Numerical-experimental comparisons for the short wall specimens (a) LSW1, (b) LSW2 and (c) LSW3 under cyclic loading allowing for concrete confinement

As discussed before, a similar strength increase characterises the numerical prediction of the slender wall model under cyclic loading, when allowing for the confinement effects in the concrete material (Figure 5-2(a)). Further simulations on the slender wall specimen disregarding the confinement contribution by using unconfined concrete material parameters led to improved predictions. Similar simulations have been carried out also for the short wall samples adopting the unconfined concrete material properties given in Table 5-3 also in the confined boundary regions.

Figure 5-7 displays the experimental curves compared against the predicted cyclic responses obtained from the unconfined model for the analysed short wall specimens. As seen in Figure 5-7(b), in the simulation of the cyclic response for specimen LSW2, the unconfined model shows no significant difference from that produced by the confined model (Figure 5-6(b)). This suggests that the confinement effect of transverse reinforcement in the boundary elements is less critical than other geometrical or mechanical properties. On the contrary, the confinement effect plays an essential role in the cyclic response prediction for walls LSW1 and LSW3 leading to a reduction of about 10% of the peak load and a softening post-peak behaviour, indicating that the local material behaviour in the confined regions strongly affects the response of the two wall specimens. The predicted cyclic loops shown in Figure 5-7(a) and (c) exhibit typical brittle shear behaviour, particularly in the final cyclic loading excursions at large displacement amplitudes. By inspecting the deformed shapes (Figure 5-8) in the simulations, walls LSW1 and LSW3 fail in sliding shear at the bottom of the wall. The sliding shear failure mode is consistent with the simulation based on the 2D FE modelling strategy with shell elements in Section 3.3.3.3.

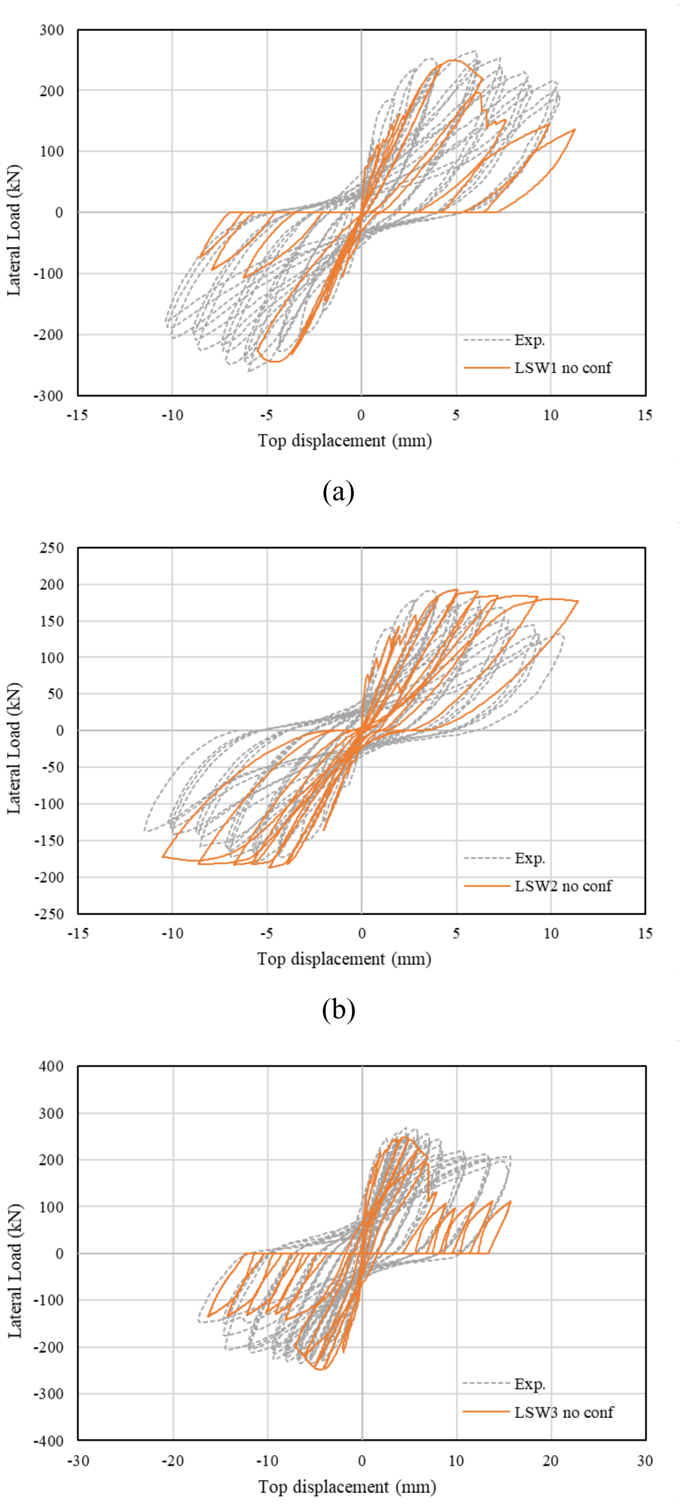

(a)

(b)

(c)

Figure 5-7: Numerical-experimental comparisons of the short wall specimens: (a) LSW1; (b) LSW2; and (c) LSW3 under cyclic loading without confinement effects (unconfined models)

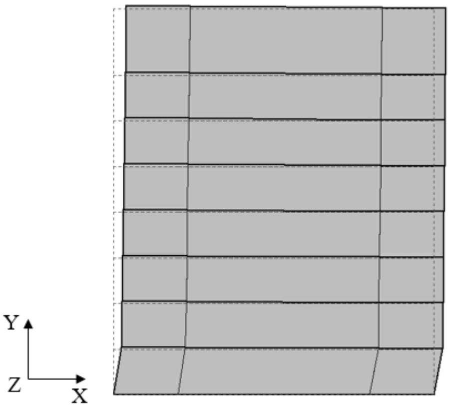

Figure 5-8: Deformed shape of wall specimen LSW1 at displacement = 7mm

Further material calibration studies have been conducted using the confined concrete model for the boundary regions of the wall specimens to obtain a closer agreement with the experimental curves. Figure 5-9 presents the final numerical curves obtained by the calibrated set of material model parameters. For wall LSW2, the strain hardening factor for steel reinforcement is modified to 0.001 from the initially assumed value of 0.01 to increase the amount of strength degradation shown by the predicted wall response. In Figure 5-9(b), an improved force-displacement prediction for the final two loading excursions showing a minor degree of global softening, which is in accordance with the experimental findings, can be seen.

Contrary to wall LSW2, in preliminary numerical simulations it has been established that the concrete material parameters in the confined regions have major effects on the predicted response for wall LSW1 and LSW3. Hereafter, the calibration of the concrete material parameters f_{c1} and E_{c2} is conducted based on numerical-experimental comparisons at structural scale. A good agreement with the experimental curve for wall LSW1, as shown in Figure 5-9(a), has been found by reducing the assumed concrete compressive strength f_{c1} from 32.5 MPa to 28 MPa and the compressive softening stiffness E_{c2} from -425 MPa to -4000 MPa to represent a reduced degree of confinement due to transverse steel reinforcements. The final cyclic loop in the positive quadrant shows a strength reduction as it approaches the unloading point. In the negative quadrant, the response curve reveals a sudden resistance drop due to shear sliding failure developing in the bottom part of the wall model. As a result, the wall resistance at the unloading point of the final loop well simulates the experimentally measured values of about 200kN. Similarly, for wall LSW3, the concrete compressive strength and compressive softening stiffness are modified from 33.85MPa and -449MPa to 30MPa and -1000MPa, respectively.

As displayed in Figure 5-9(c), the numerical cyclic response features a post-peak softening branch in the final three loading excursions, which are not appropriately modelled in the previous confined model (Figure 5-6(c)). Moreover, the calibrated cyclic response for wall LSW3 shows a very accurate representation of the unloading branches up to 12mm displacement providing a good prediction of the global stiffness degradation and residual plastic deformations upon load reversal. Nevertheless, the calibrated model again overestimates the experimental pinching characteristics. This is the case only for LSW3 but not for other walls.

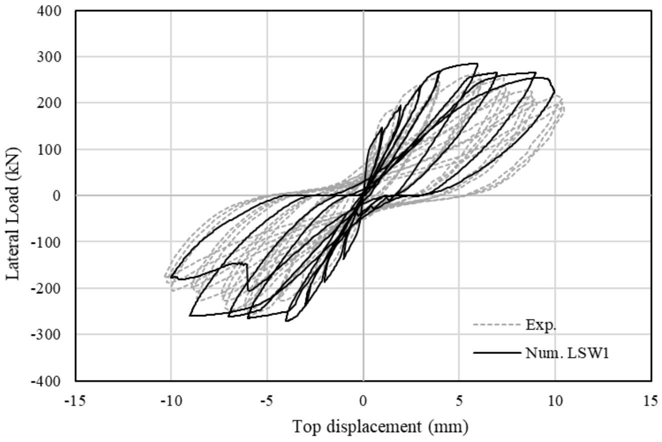

(a)

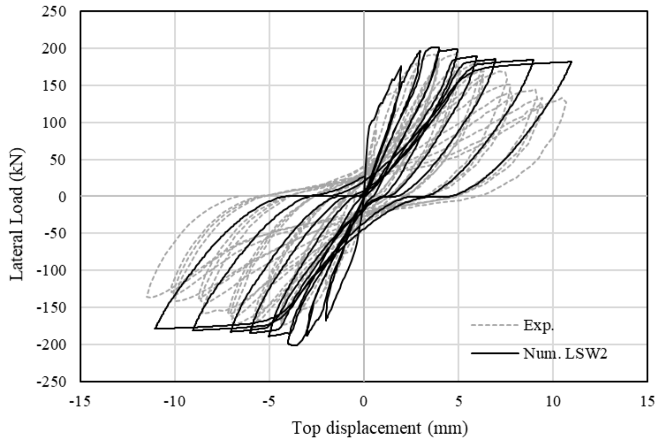

(b)

Figure 5-9: Numerical-experimental comparisons under cyclic loading using calibrated material parameters for the short wall specimens: (a) LSW1; (b) LSW2 and (c) LSW3 (Con’d)

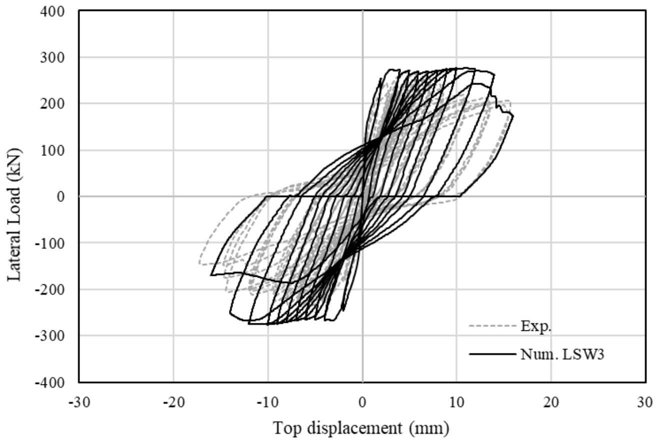

(c)

Figure 5-9: Numerical-experimental comparisons under cyclic loading using calibrated material parameters for the short wall specimens: (a) LSW1; (b) LSW2 and (c) LSW3

5.3.3 Cumulative energy dissipation

This section investigates the ability of the proposed macro-element model to represent the energy dissipated in the hysteresis loops of the three RC short wall specimens under cyclic loading. It complements the previous model validation based on direct comparisons between the experimental and numerical cyclic load-displacement curves. Figure 5-10 plots the variation of the cumulative dissipated energy with the cyclic excursion number. The cumulative dissipated energy is calculated as the area enclosed by a load-displacement hysteretic loop. The excursion number corresponds to a specific level of displacement amplitude. The experimental cumulative energy at each excursion number is taken as the average value of energy dissipated in the loops per displacement amplitude. In contrast, the numerical cumulative energy dissipation is associated with a single cyclic loop due to the adopted simplified loading history.

The results of the investigation show a very good agreement between the numerical and experimental energy dissipation capacity especially for wall LSW1. Figure 5-10(a) confirms that the macro-element model successfully predicts the energy dissipation in the first three cycles, with only minor differences with the experimental results in the following excursions. By contrast, the numerical model with macro-elements underpredicts the cumulative dissipated energy for wall LSW2 (Figure 5-10(b)). Finally, the model for wall LSW3 leads to an overestimation of the actual cumulative dissipated energy mainly due to the reduced pinching of the numerical hysteresis loops.

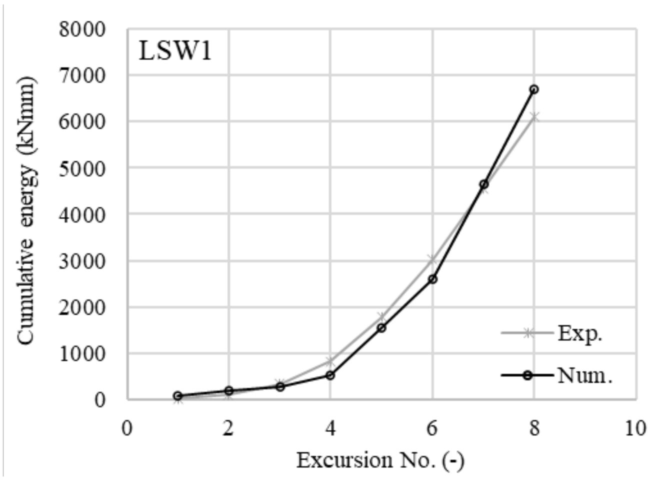

(a)

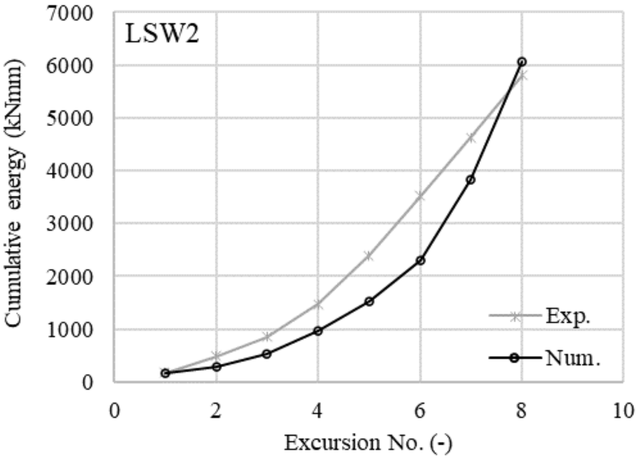

(b)

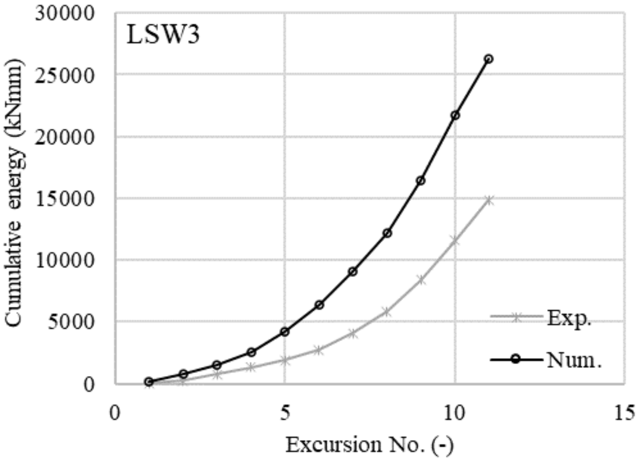

(c)

Figure 5-10: Numerical-experimental comparisons of the cumulative energy dissipation against excursion No. for specimens: (a) LSW1; (b) LSW2 and (c) LSW3

5.3.4 Secant stiffness degradation

A further investigation considers the prediction of the stiffness degradation by increasing the number of cycles. In the tests under cyclic loading, the stiffness to horizontal loading of the RC wall samples degrades nonlinearly due to concrete cracking and yielding of steel reinforcements. Figure 5-11 provides an illustration for the determination of the secant stiffness for loos at two consecutive drift levels in the positive quadrant. The secant stiffness corresponds to the slope of the line at the peak load per displacement amplitude. Figure 5-12 compares the degraded secant stiffness values against the top displacement based on the load-displacement curves plotted in Figure 5-9. The results in the positive and negative quadrants lead to two sets of individual numerical and experimental curves, representing the secant stiffness degradations in the two opposite directions. For the experimental secant stiffness, the average value of the slopes for multiple cycles at the same displacement amplitude is used.

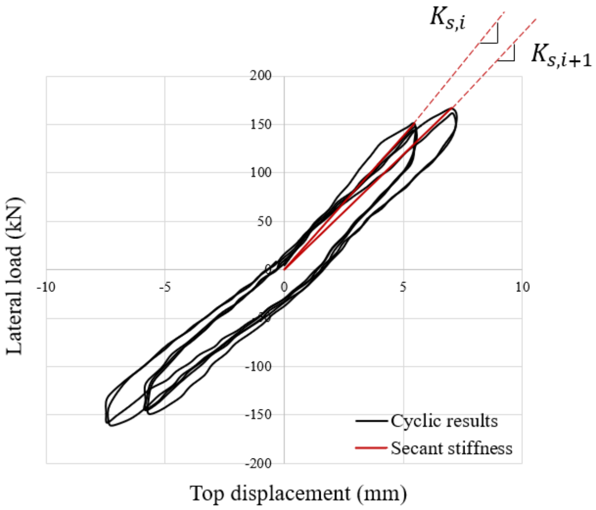

Figure 5-11: Secant stiffness definition

As shown in Figure 5-12, the predicted secant stiffness values reduce, which is consistent with the experimental results and it is particularly evident for the initial two drift levels as the loading direction changes from the positive to the negative direction. In general, the macro-element models for the three wall specimens provide a good approximation of the stiffness degradation with minor overestimations of the actual experimental results. The rate of secant stiffness degradation agrees well with the experimental degradation rate especially for wall LSW2, although the numerical model slightly overestimates the secant stiffness for drift ratios in the range of 0.5 to 1.0%. In contrast, the LSW3 model typically overpredicts the secant stiffnesses by around 10 to 30%, owing to the reduced post-peak softening response shown in Figure 5-9.

Overall, the investigation performed here corroborates that the macro-element representation gives a good representation of the secant stiffness degradation for short walls.

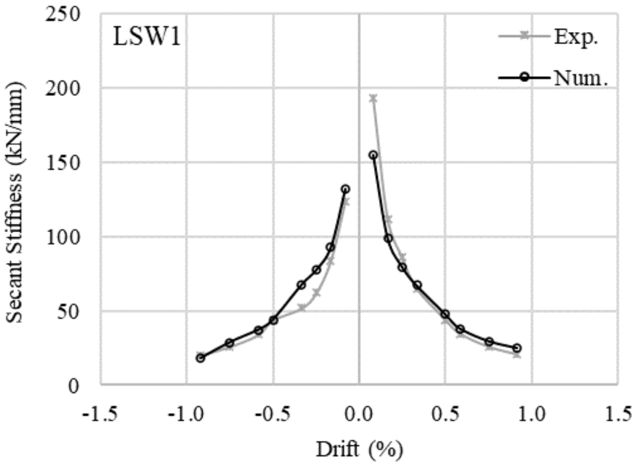

(a)

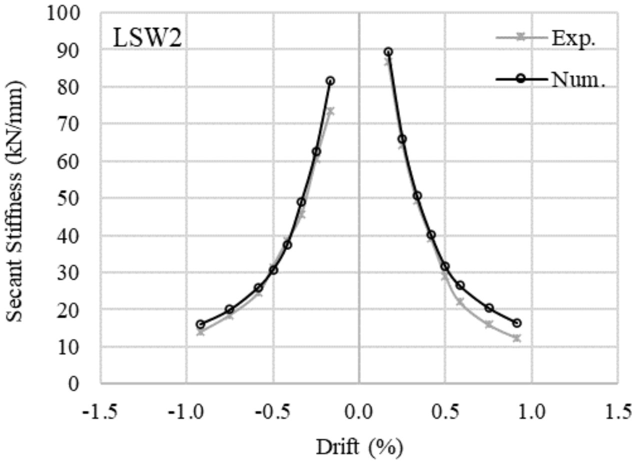

(b)

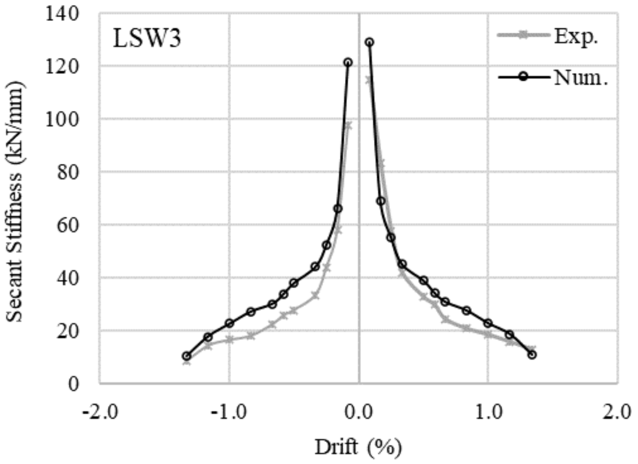

(c)

Figure 5-12: Numerical-experimental comparisons of secant stiffness degradation for specimens: (a) LSW1; (b) LSW2 and (c) LSW3

5.4 Moderate wall

5.4.1 Experimental specimens

Subsequent numerical investigations have been performed on the wall specimens MSW1 and MSW3 with an aspect ratio of 1.5. The wall samples with moderate aspect ratio are characterised by similar amount of main longitudinal and web steel reinforcements to that used in the wall LSW1, LSW2 and LSW3, as reported in Table 5-4 and illustrated in Figure 5-5. The only difference between the MSW and LSW wall series is the amount of transverse reinforcement in the boundary regions, which features 4.2 mm bars spaced at 42mm leading to a reinforcement ratio of 1.1% in the MSW specimens. Furthermore, wall MSW1 is characterised by a double amount of web reinforcement than wall MSW3 representing a typical RC wall component designed to resist higher shear forces.

Table 5-4: Reinforcement details for walls MSW1/MSW3

Wall	ρ_h (%)	ρ_v (%)	ρ_{be} (%)	ρ_{trv} (%)	N
MSW1	0.565 2 ϕ4.2@100mm + 1 ϕ8@180mm	0.565 2 ϕ4.2@100mm + 1 ϕ8@180mm	1.7 8 ϕ8	1.1 ϕ4.2 @42mm	-
MSW3	0.277 2 ϕ4.2@100mm	0.277 (2 ϕ4.2@100mm)	1.3 6 ϕ8	1.1 ϕ4.2 @42mm	$0.07A_cf_c$

Table 5-5: Material parameters for walls MSW1/MSW3

Wall	Material	E_{c1} $[MPa]$	f_{c1} $[MPa]$	E_{c2} $[MPa]$	f_{c2} $[MPa]$	E_{t1} $[MPa]$	f_t $[MPa]$	E_{t2} $[MPa]$
MSW1	Confined	31858	32.54	-653	6.51	29602	2.30	-653
	Unconfined	29602	26.10	-7268	5.22	29602	2.30	-7268
MSW3	Confined	31192	30.54	-609	6.11	28826	2.30	-609
	Unconfined	28826	24.10	-6012	4.82	28826	2.30	-6012

Based on the results from the preliminary mesh sensitivity study, the numerical models employed here utilise 6 macro-elements for representing the analysed RC wall specimens with similar boundary and loading conditions to the macro-element models developed for the numerical investigation of the short wall samples. The concrete material parameters of the macro-element models for the moderate wall specimens MSW1 and MSW3 are reported in Table 5-5.

5.4.2 Numerical-experimental comparisons

Figure 5-13 shows the load-displacement curves obtained by modelling the MSW walls with macro-elements considering the confinement effects due to transverse reinforcement. In terms of the pinching features exhibited by the experimental curves, the wall MSW3 model provides an improved prediction compared to the MSW1 model, which only shows a minor degree of pinched shape. The peak strength of wall MSW1 is accurately estimated by the numerical model within 5% accuracy. However, both models again overpredict the post-peak strength suggesting that the confined concrete material parameters play crucial roles also in the response predictions of walls with intermediate height.

As in the previous numerical investigation on the short walls, additional numerical simulations have been carried out employing unconfined concrete material properties also in the confined boundary elements, leading to the curves shown in Figure 5-14. The results confirm the importance of employing a realistic set of concrete input material parameters in the confined regions for the wall specimens MSW1 and MSW3.

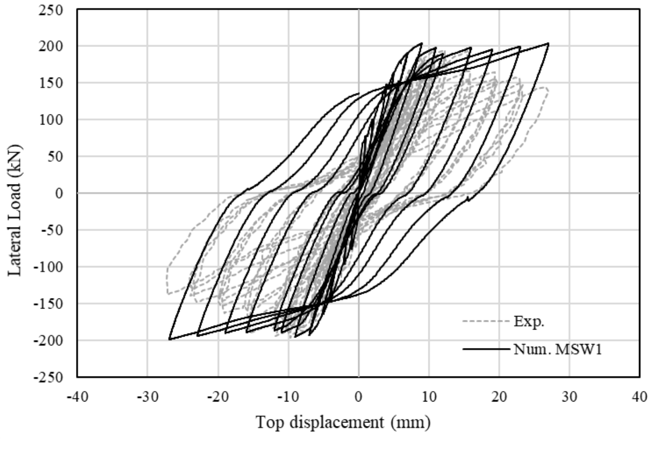

(a)

Figure 5-13: Numerical-experimental comparisons on the wall specimens: (a) MSW1 and (b) MSW3 under cyclic loading considering concrete confinement effects (confined models) (Con’d)

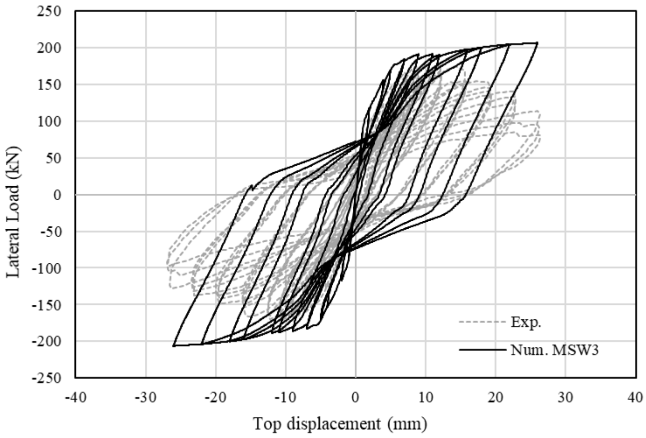

(b)

Figure 5-13: Numerical-experimental comparisons on the wall specimens: (a) MSW1 and (b) MSW3 under cyclic loading considering concrete confinement effects (confined models)

It is noted that the numerical results produced by the unconfined models achieve a good agreement with the experimental curves. However, the confinement effects of transverse reinforcement need to be duly accounted for. In light of this consideration, further calibration of the concrete material properties has been performed. Thus, to improve the accuracy of the numerical predictions for MSW1 wall, the original compressive softening stiffness of -653MPa is modified to -4000MPa and the compressive strength is kept as 26.10MPa for the confined region.

As shown in Figure 5-15(a), the material calibration leads to a post-peak softening prediction, which is not achieved by the original confined model, and an improved representation of the pinched loops. Besides, the accuracy of the predicted peak load is maintained. For the MSW3 model, the compressive strength and the compressive softening stiffness in the confined region are modified from 30.54MPa and -609MPa to 27MPa and -3000MPa, leading to the results in Figure 5-15(b). It can be observed that the accuracy of the numerical cyclic response improves significantly as compared to the confined model results shown in Figure 5-13(b). An abrupt change of the wall strength at 4.5mm displacement in the last cycle is found due to the shear sliding failure.

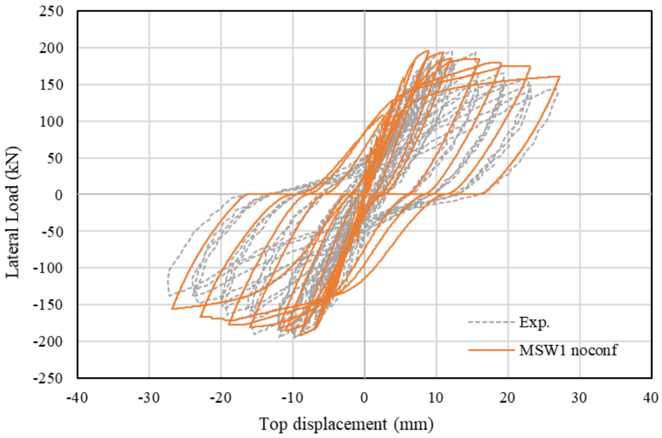

(a)

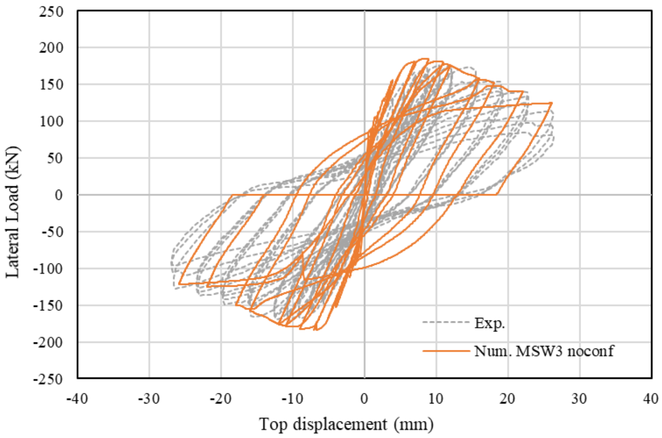

(b)

Figure 5-14: Numerical-experimental comparisons on the wall specimens: (a) MSW1 and (b) MSW3 under cyclic loading without confinement effects (unconfined models)

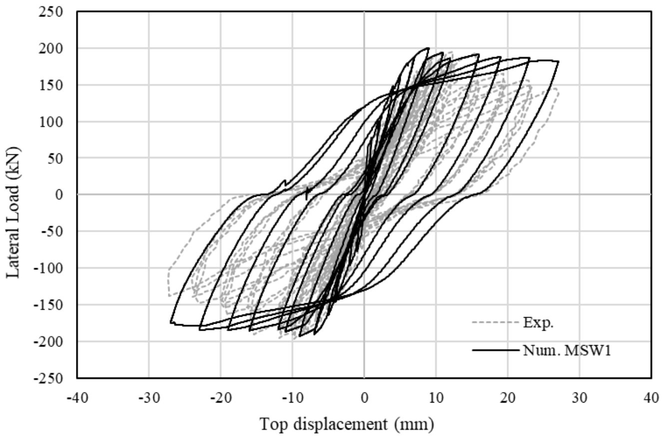

(a)

Figure 5-15: Numerical-experimental comparisons on the wall specimens: (a) MSW1 and (b) MSW3 under cyclic loading (calibrated models) (Con’d)

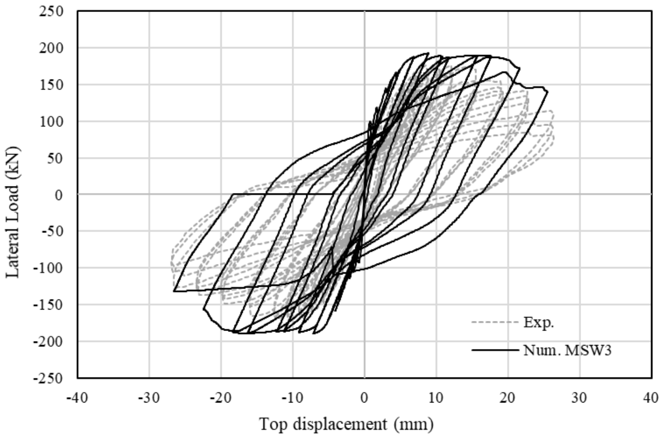

(b)

Figure 5-15: Numerical-experimental comparisons on the wall specimens: (a) MSW1 and (b) MSW3 under cyclic loading (calibrated models)

5.4.3 Cumulative energy dissipation

As shown in Figure 5-16, the energy dissipation capacity of the moderate wall models is evaluated based on the cyclic load-displacement curves with calibrated concrete material parameters presented in Figure 5-15. The figure shows that the macro-element models for both moderate walls guarantee an accurate estimation of the dissipated energy up to excursion No.9, corresponding to 18mm displacement amplitude.

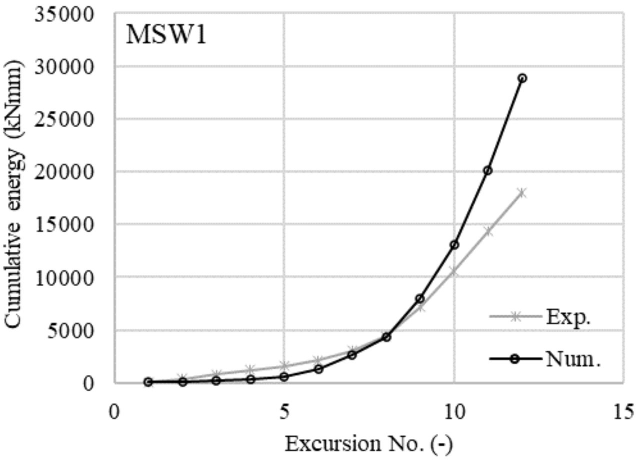

(a)

Figure 5-16: Numerical-experimental comparisons of cumulative energy dissipation against excursion no. for specimens: (a) MSW1 and (b) MSW3 (Con'd)

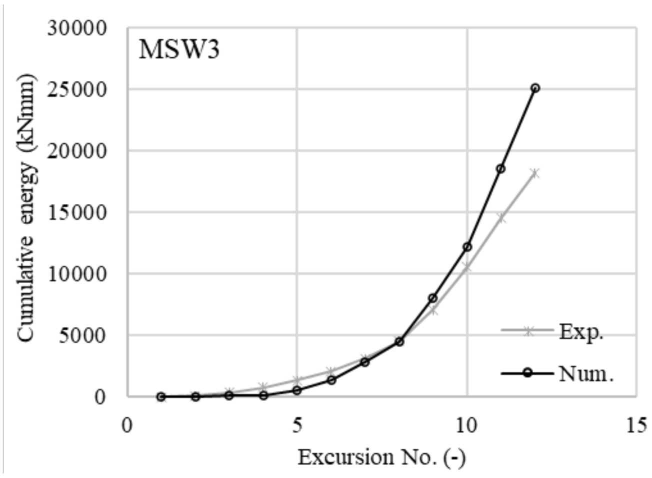

(b)

Figure 5-16: Numerical-experimental comparisons of cumulative energy dissipation against excursion no. for specimens: (a) MSW1 and (b) MSW3

Unlike the short wall LSW3 subjected also to axial load, the macro-element model for moderate wall MSW3 well predicts the energy dissipation capacity except for the last three cycles. The experimental dissipated energies are slightly overestimated for the remaining three loading cycles. It is also noted that the dissipated energies in the first few cycles predicted by the MSW models are generally more accurate than those predicted by the LSW models.

5.4.4 Secant stiffness degradation

Following the same procedure detailed in Section 5.3.4, the stiffness degradation of the global cyclic loops is assessed using the results reported in Figure 5-15 in the two loading directions. As shown in Figure 5-17, the two numerical models provide reasonably accurate results of the secant stiffnesses and the rate of stiffness degradation compared to the experimental values. The MSW1 model well simulates the secant stiffnesses in the negative quadrant, whereas the MSW3 model offers a better prediction in the positive quadrant. These are also confirmed by the results shown in Figure 5-15, when comparing the unloading points in the lateral load-displacement curves. It is also noted that the secant stiffness of the wall MSW1 increases when it is unloaded from the positive to the negative drift in the first cycle, which might be related to the experimental error incurred. However, the numerical model successfully captures the expected reduction of secant stiffness.

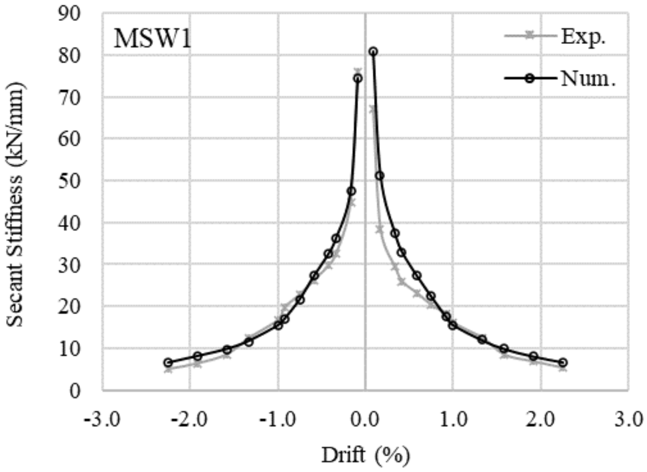

(a)

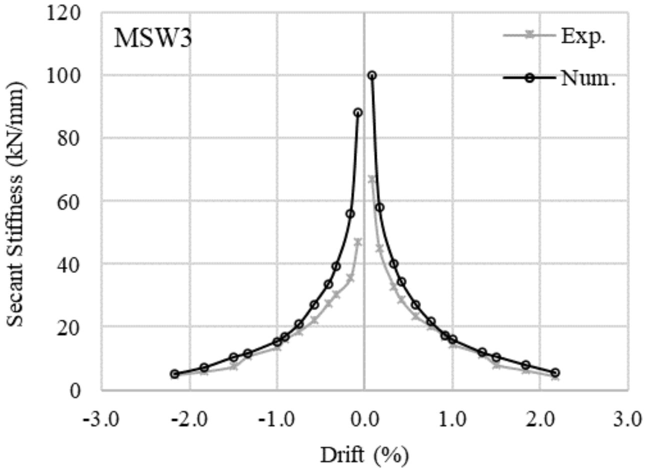

(b)

Figure 5-17: Numerical-experimental comparisons of secant stiffness degradation for specimens: (a) MSW1 and (b) MSW3

5.5 RC coupled wall

5.5.1 Experimental program overview

The simulations conducted in this section consider the five-storey RC coupled wall system tested by Lu and Chen (2005). The specimen named CW2 is a 1/4 scale prototype of a structural component in a typical high-rise RC building. Figure 5-18 gives the reinforcement details of the wall piers and the coupling beams, which were designed and constructed according to the Chinese high-rise building code JGJ 3-91 (Ministry of Construction, 1991). The two wall piers were connected by coupling beams with the same depth at each storey. The top beam was used for loading, anchorage, and support providing out-of-plane stability, while the middle beam was merely for loading and supporting specimens CW1 and CW3 in the same test series. The specimens CW1 and CW3 were not considered in this section since the experiment did not follow the prescribed loading protocols. The axial load of 200kN, corresponding to 10% of the gross sectional capacity, was vertically imposed on the top and continuously applied during the test. For specimen CW2, the top beam was subjected to 3 loading cycles per displacement amplitude up to 1.25% drift level. Concrete material properties tested in the laboratory are summarised in Table 5-6.

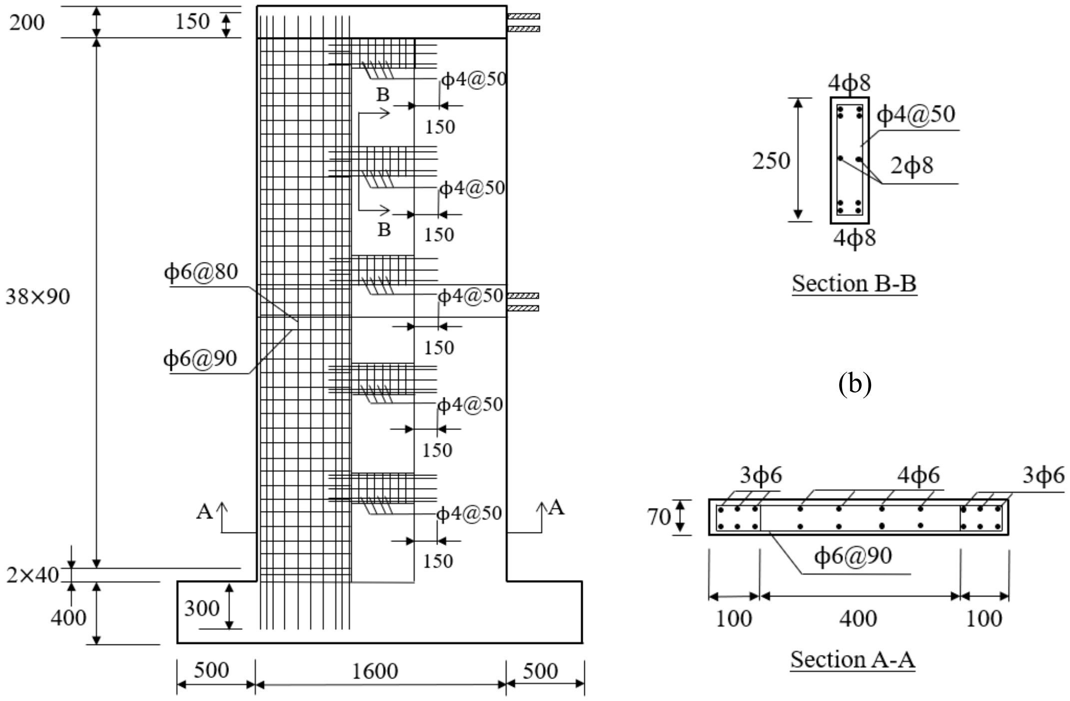

(a) (b) (c)

Figure 5-18: Schematic reinforcement details of the coupled wall specimen CW2: (a) elevation view; (b) wall piers; (c) coupling beam

Table 5-6: Concrete material properties tested for specimen CW2

Floor	E_c (GPa)	f_c (MPa)	f_t (MPa)
1	31.2	38.6	2.63
2	33.8	38.7	2.63
3	27.6	40.1	2.69
4,5	30.7	47.4	3.01

5.5.2 Numerical models

Two different models are generated to represent the coupled wall system, for which the coupling beams are modelled by either beam elements ‘cbp3’ or the implemented macro-element ‘swm4’. Each storey uses 3 macro-elements to represent the wall. The coupled beam is represented by 5 beam-column elements. Figure 5-19 presents the FE mesh of the model with ‘cbp3’ elements. The wall pier at each floor utilises three macro-elements, in which the top two elements are connected to the coupling beam. The link elements (‘lnk3’), assuming fully rigid rotational degrees of freedom, connect the macro-elements to the beam elements, thus adding the contribution of rotational stiffness at the connections. Hereafter, the model with the ‘swm4’, ‘cbp3’ and ‘lnk3’ elements is called the *link model*, while the model using only macro-elements is called the *macro model* (Figure 5-20). The two numerical models are subjected to one loading cycle per drift level to facilitate the analysis, as for the previously investigated RC wall specimens. A constant axial load is applied as nodal forces at the top four nodes, whereas the spreader element is employed for imposing the cyclic lateral forces using the displacement control.

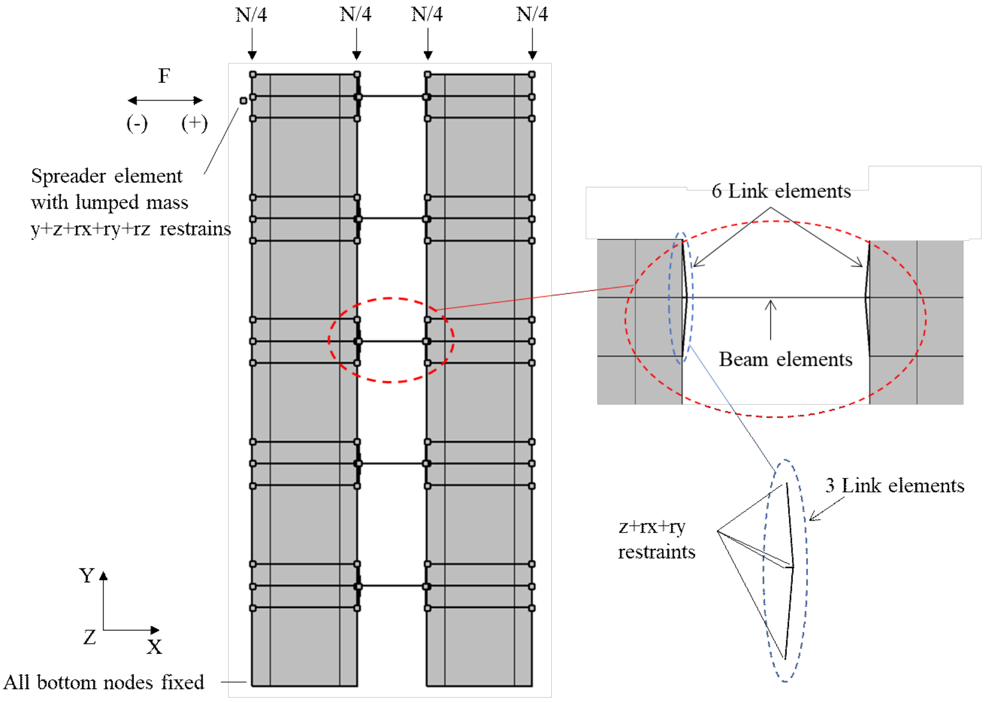

Figure 5-19: Macro-element representation of coupled wall specimen CW2 with coupling beams modelled by beam elements ‘cbp3’

The wide column approach has been previously recognised as an accurate and efficient modelling strategy for modelling the RC slender wall in Section 3.3.2.2. For comparison purposes, the coupled wall specimen CW2 is modelled also by a mesh of 1D elasto-plastic beam-column elements based on the wide column concept, as shown in Figure 5-21. The wall portion at a single floor height and each coupling beam are represented by seven and five beam elements, respectively, to capture the spread of plasticity. As in the previous link model, the rigid links are employed to connect the wall piers and coupling beams, thus providing rotational stiffness. Furthermore, the wide column model applies comparable loading and boundary conditions as in the models with macro-elements.

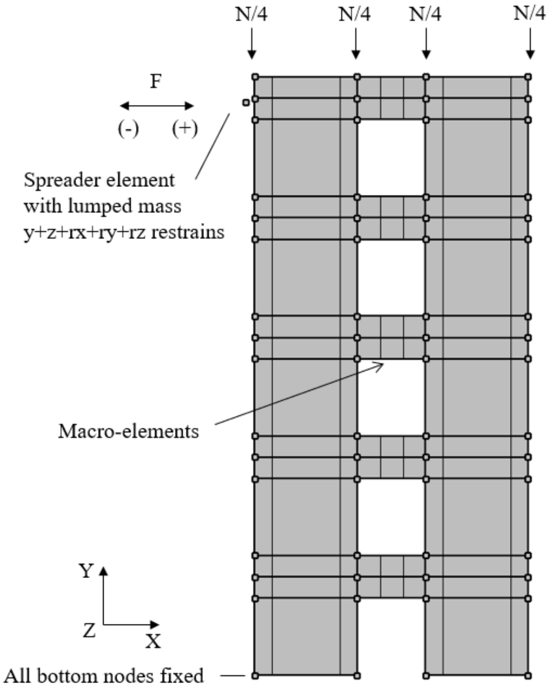

Figure 5-20: Macro-element representation of coupled wall specimen CW2 with coupling beams modelled by macro-elements 'swm4'

5.5.3 Numerical-experimental comparisons

Figure 5-22 and Figure 5-23 present the numerical-experimental comparisons for specimen CW2 subjected to cyclic loadings, where the numerical curves have been obtained using the *link model* and the *macro model*. Both numerical descriptions replicate the experimental load-displacement curves with a reasonable level of accuracy and successfully capture the overall shape of the hysteretic loops. Most importantly, the degree of pinching and the displacements at zero forces are well described, as shown in the figure. The experimental unloading branches are well simulated, although the degraded unloading stiffnesses are not captured in the final few cycles. This may be due to the characteristics of the assumed concrete material relationships which do not allow for stiffness degradation under cyclic loading (Figure 4-6). Furthermore, the coupled wall capacity of 137 kN is accurately predicted. However, this value is attained at 45mm displacement rather than at 25 mm in the experiment, which suggests that the numerical model exhibits a more ductile behaviour.

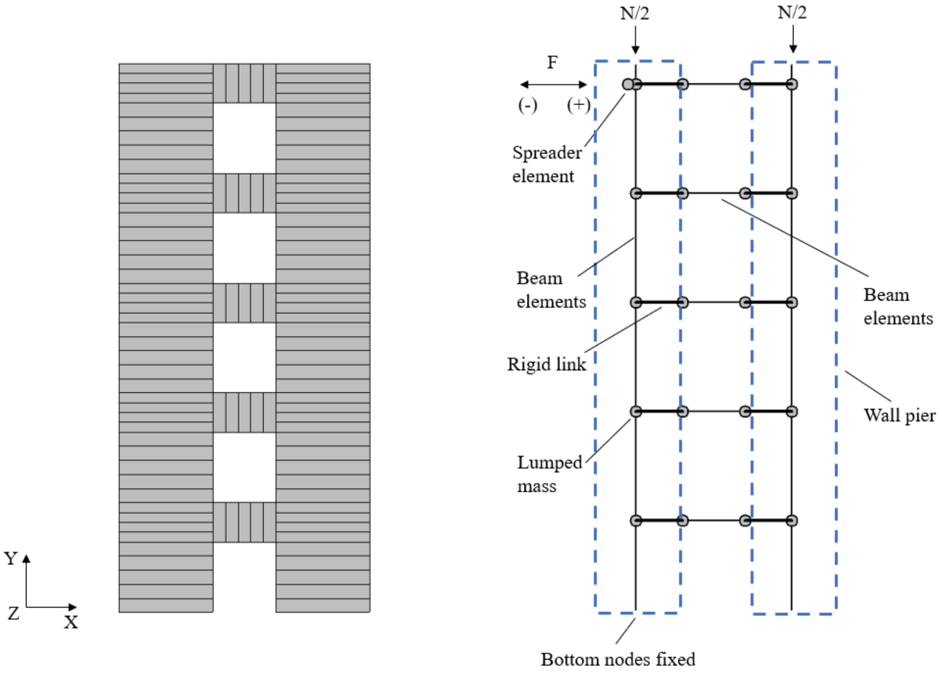

Figure 5-21: Wide column representation of coupled wall specimen CW2

The most significant divergence between the numerical and test results is that the post-peak strength degradation is not observed in the numerical response, particularly at the last two drift levels, i.e., at displacements 42 mm and 45 mm. The experimental data are overestimated at each reloading branch in the positive and negative quadrants. This feature has been previously found also in the wall simulations, when accounting for the confined concrete effects in the boundary elements. The predicted responses plotted in the two figures are comparable with marginal differences, which suggests that the wall pier contribution dominates the coupled wall system behaviours. This is consistent with the experimental findings by Lu & Chen (2005), who reported that the coupling beams mainly behaved within the elastic range.

Figure 5-24 presents the results obtained using the *link model* without considering the confinement effects provided by the transverse reinforcement. The numerical model predicts a more brittle wall behaviour and estimates a peak strength of 122kN at 19mm displacement, which underpredicts the experimental value of 137kN at 25mm. The resulting 11% difference is related to the contribution of the confinement effects on the wall response. Furthermore, it can be observed that the pinching of the hysteresis loops has not significantly changed, while the reloading curves tend to be closer to the experimental curves due to reduced compressive strength and softening stiffness.

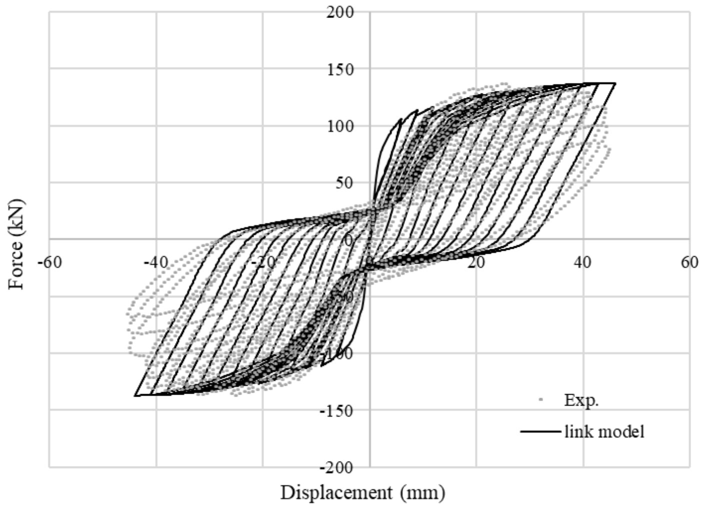

Figure 5-22: Numerical-experimental comparisons on the coupled wall CW2 under cyclic loading with the *link model*

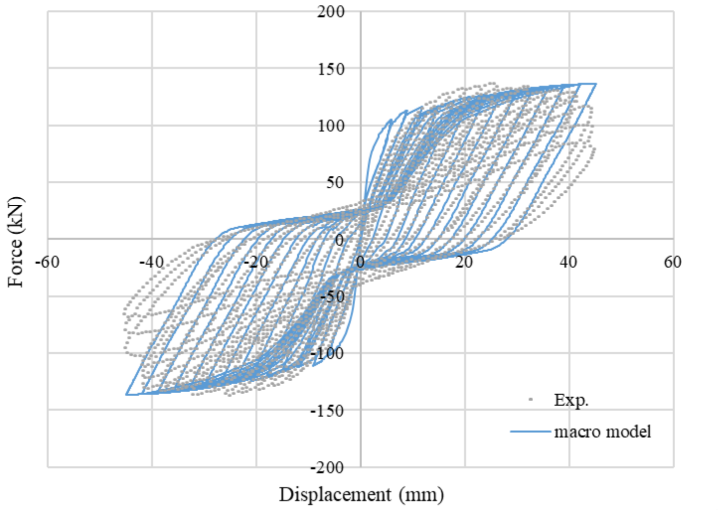

Figure 5-23: Numerical-experimental comparisons on the coupled wall CW2 under cyclic loading with the *macro mo*del

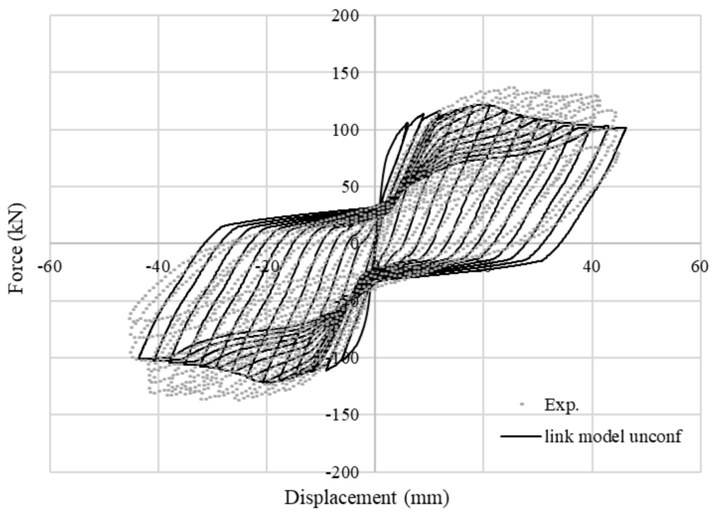

Figure 5-24: Numerical-experimental comparisons on the coupled wall CW2 under cyclic loading using the *link model* without confinement effects

Figure 5-25 shows the numerical-experimental comparison on the cyclic response employing the wide column approach. It can be observed that the wide column model gives less accurate results than the macro-element model predictions shown in Figure 5-22 and Figure 5-23. The peak strength evaluated by the wide column model is 120kN, leading to an underestimation of 12% of the experimental value. Following the attainment of the maximum strength, further discrepancies arise. Unlike the macro-element model prediction, the post-peak softening branch is stabilised and reaches a plateau in the final loop. Moreover, the unloading curves form relatively flat pinched shapes, which may suggest that steel reinforcement contribution dominates the system behaviour in the range of large displacements.

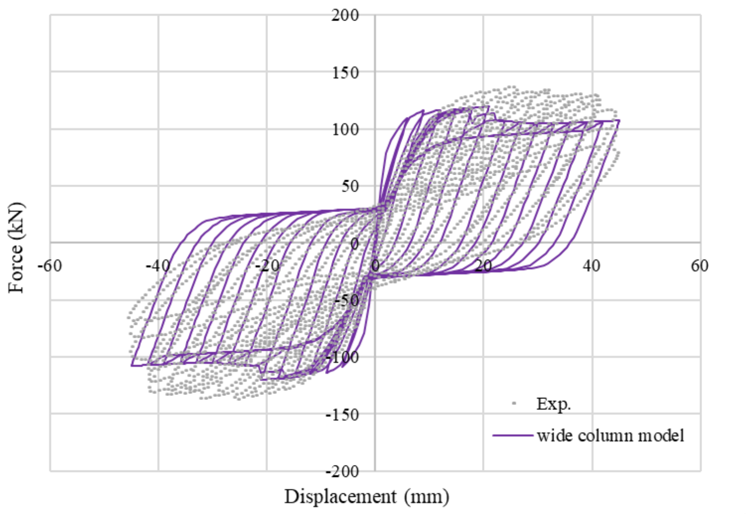

Figure 5-25: Numerical-experimental comparisons of coupled wall CW2 under cyclic loading with the wide column model

5.6 Concluding remarks

In this chapter, the novel macro-element proposed in Chapter 4 has been validated for analysing different RC building components under cyclic loading conditions. The primary consideration is given to attaining accurate results with a minimum computational effort. One of the benefits of the proposed macro-element is that it does not require complex calibration of the input material parameters, as it employs a basic set of concrete and steel reinforcement properties.

Validation studies are conducted considering a range of RC walls with different aspect ratios and loading conditions. Numerical simulations of these wall specimens have generally achieved favourable comparisons between macro-element predictions and experimental results. The main characteristics of the cyclic response are captured with good accuracy by the new macro-element, including stiffness and strength degradations and pinching features of the hysteresis loops. It has been found that the use of at least five macro-elements can lead to accurate response predictions for walls with aspect ratio from 1.0 to 2.0. Besides, concrete material parameters in the confined regions may have major effects on the predicted cyclic response of RC wall specimens. In the absence of experimental data, the recommended value of concrete compressive softening modulus is in the range of -1000MPa to -4000MPa for using the proposed macro-element approach to assess existing structures. Moreover, the macro-element approach demonstrates its ability to represent the actual energy dissipation capacity and the stiffness degradation exhibited in the physical tests.

In addition to solid wall components, a five-storey RC coupled wall has also been analysed, where the global response of the system subjected to equivalent seismic actions is predicted with reasonable accuracy. Compared to the wide column model, the macro-element representation has also shown the ability to consider the shear contribution to the response. Most importantly, the proposed macro-element modelling approach achieves significant computational efficiency compared to existing detailed modelling strategies. This highlights the practical benefits of using the developed modelling strategy with macro-element for an accurate and efficient simulation of a realistic RC building structure with RC walls subjected to seismic actions.

Chapter 6

Application Study – Seismic Analysis of Building with RC Walls

6.1 Introduction

Nonlinear dynamic analysis represents the most accurate analysis technique to investigate the response of RC building structures with shear walls under earthquake loading. Chapter 3 has shown that the use of detailed FE descriptions for shear walls with nonlinear 2D shell or 3D solid elements with sophisticated concrete constitutive models is computationally expensive, thus not suitable for the analysis of large scale structures. To this end, Chapter 4 has proposed an efficient 2D macro-element modelling approach for analysing RC walls under cyclic loading. The proposed shear wall macro-element equipped with a newly developed biaxial concrete model has been implemented in ADAPTIC (Izzuddin, 1991). In Chapter 5, validation studies have shown that the implemented macro-element is capable of providing accurate response predictions of RC wall components, such as individual shear walls and RC coupled walls.

This chapter employs the developed macro-element model to demonstrate its potential when used to represent RC walls as retrofitting components to enhance the seismic performance of a sub-standard RC multi-storey frame building. Firstly, Section 6.2 describes a realistic four-storey RC building which is considered in the application study. Subsequently, Section 6.3 introduces the partitioned modelling approach and the numerical models used in the nonlinear structural analysis. The retrofitting solution using RC walls put forward by Masjuki (2017) is considered in the numerical simulations, where walls are modelled by 2D macro-elements and 1D beam-column elements based on the wide column approach. Subsequently, Section 6.4

performs the seismic analysis of the frame-wall building system. Push-over analysis is carried out to demonstrate that the macro-element accounts for shear deformability and potential shear damage and failure. To investigate the building response to earthquake loading, nonlinear time-history analysis is then performed following an incremental dynamic analysis (IDA) procedure. For comparison purposes, focus is given to the global structural response instead of a detailed seismic assessment concerning individual beam, column, and shear wall components.

6.2 Overview of realistic RC building

The RC building system considered here is a typical four-storey school constructed in Italy in the 1960s. The plan views of the top and bottom two stories and their geometry characteristics are schematically shown in Figure 6-1, where the distribution of 46 columns in total is annotated. The whole building is characterised by irregularities in plan and elevation. The bottom two floors have the same area of 1239m^2, whereas the top two floors feature a reduced area of 660m^2. The inter-storey heights from the first floor to the fourth floor are 3050m, 4250m, 3510m, and 3510m, respectively.

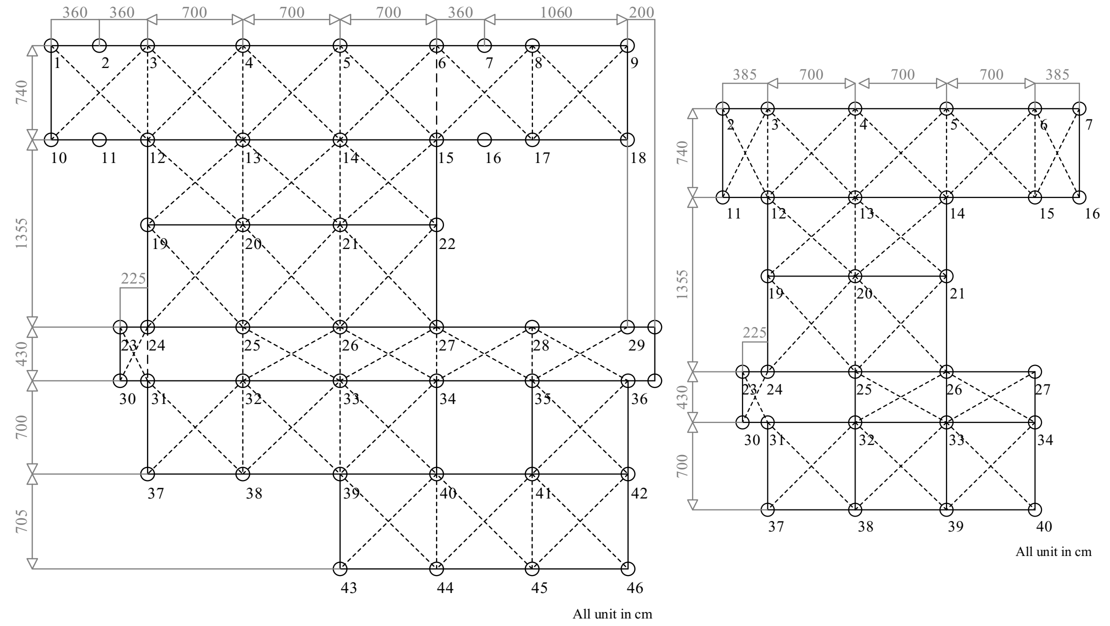

(a) (b)

Figure 6-1: Plan view of the considered four-storey RC building: (1) 1st and 2nd floors; (2) 3rd and 4th floors

The original building was not designed to resist earthquakes but only gravity and wind loading. The gravity load due to the self-weight of each floor is assumed as 4.6kN/m^2. The live load of

3.0kN/m^2 related to the use of the building is applied on each floor, and the live load due to snow of 0.8kN/m^2 is imposed on the top floor.

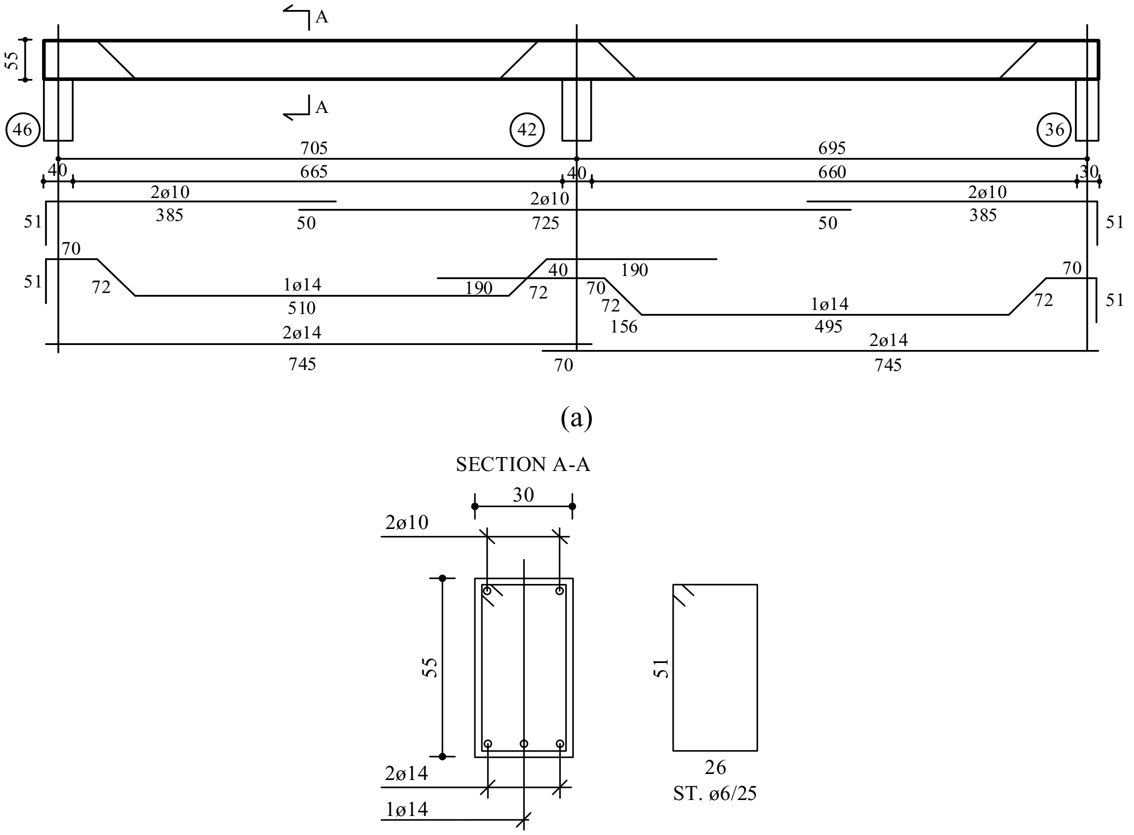

(a)

(b)

Figure 6-2: RC beam 46-42-36: (a) dimensions; (b) section A-A

Detailed geometric details of the cross sections of beams and columns are included in Figures A1 and A2 in Appendix A. A representative drawing of the beam member spanning columns No. 46, 42 and 36 is shown in Figure 6-2, where the reinforcement details of the beam are also given. An example of reinforcement details of columns No. 37 to 40 located at the top and bottom two stories are provided in Figure 6-3.

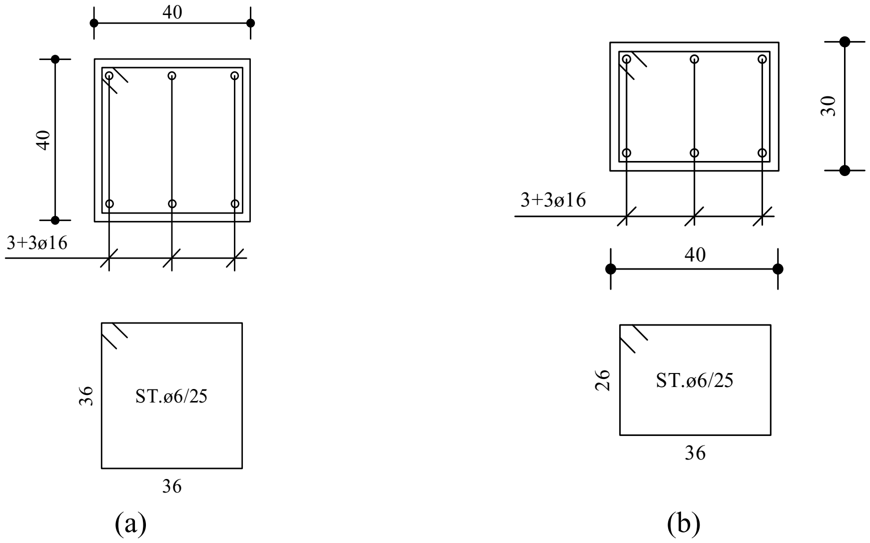

Figure 6-3: Reinforcement details of columns No. 37 to 40 at: (a)1st and 2nd floors; (b) 3rd and 4th floors

6.3 Numerical models of RC buildings

6.3.1 Partitioned modelling approach

Extensive nonlinear dynamic simulations of multi-storey RC building structures under earthquake loading impose considerable computational demand, particularly when using conventional monolithic FE models for representing geometric and material nonlinearity, as highlighted by Izzuddin *et al.* (2013). In view of this intrinsic limitation, a recently developed partitioned modelling method based on the domain partitioning approach (Jokhio & Izzuddin, 2013, 2015) is used for nonlinear analysis of the considered RC buildings to enhance the computational efficiency.

When employing the partitioned modelling strategy, the entire building system is modelled by a parent structure composed of placeholder super-elements representing the partitioned subdomains. A dual super-element that collects the boundary nodes represents every subdomain termed child partition. As illustrated in Figure 6-4, the dual super-elements are modelled under separate processes using parallel computing resources at each iterative step of the solution procedure. The placeholder element passes the nodal displacements at the partitioned boundary to the dual super-elements. Afterwards, the resistance forces and tangent stiffness matrix obtained from dual super-elements wrapping child partitions are returned to the parent structural level. In this respect, two-way communication between the placeholder and dual super-elements guarantees the compatibility and equilibrium to be satisfied synchronously in individual partitions and the partition boundary. The structural response is solved at a smaller subdomain scale and by assembling boundary nodes at the parent level, which allows for effective parallelisation of the structural analysis.

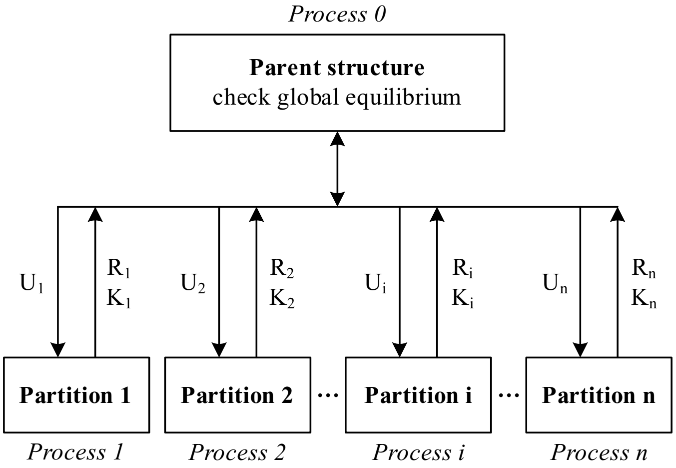

Figure 6-4: Communication between parent structure and child partitions (Izzuddin *et al.*, 2013)

6.3.2 Bare frame and frame-wall building models

The original 4-storey RC building is modelled in ADAPTIC (Izzuddin, 1991). As the most reliable modelling strategy, the distributed plasticity approach is employed to represent the frame components. Beams and columns are modelled by elasto-plastic cubic beam-column elements (Izzuddin & Elnashai, 1993) introduced in Section 3.2.1. The cubic element is formulated based on the fibre approach, allowing for material nonlinearity over the section depth, while geometric nonlinearity is considered by using a co-rotational formulation.

For each RC beam and column, a set of 2-noded cubic elements are used to capture the distributed plasticity resulting from the onset and propagation of cracking in concrete and yielding in steel reinforcement. In particular, each RC column is represented by 6 elements with length ratios {1,2,3,3,2,1}, which capture the possible inelastic deformations concentrated at the column ends. On the other hand, 10 elements with length ratios {1,2,3,2,1,1,2,3,2,1} are used to model each RC beam, where inelastic deformations are expected to develop at the ends and mid-span. The two Gauss sections over each element consist of a number of monitoring points, where the uniaxial cyclic material models 'con1' and 'stl1' are used for concrete and steel reinforcements. The section type 'rcts' (Figure 6-5) allowing for modelling RC beams with an effective slab width in the ADAPTIC library, is adopted for beams and columns.

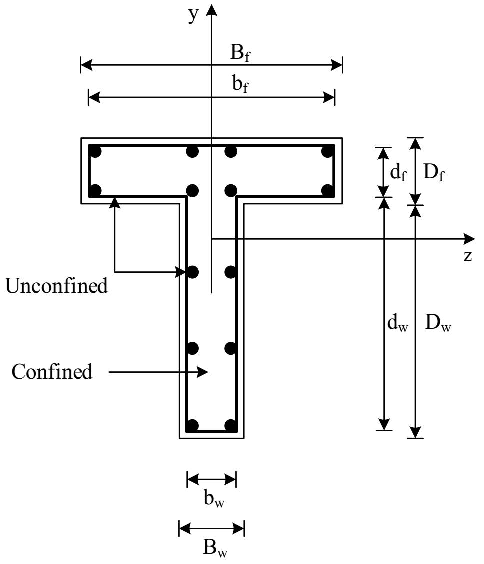

Figure 6-5: Section ‘rcts’ in ADAPTIC

Sophisticated 2D nonlinear finite elements can be employed for an accurate description of the floor slab response. Nevertheless, this detailed modelling strategy may be computationally prohibitive for nonlinear numerical simulations of multi-storey RC buildings under seismic loading. In view of this, a simplified method based on an equivalent planar bracing system suggested by (Fardis, 2009) is adopted to simulate the floors. The equivalent bracing system is essentially a truss model consisting of a peripheral rectangular frame with X-braces. In the numerical models, the 3D link element (‘lnk3’ in ADAPTIC library) with axial and rotational springs is used to simulate the bracing system. Specific stiffness values calculated according to Yettram & Husain (1966) are assigned for the link elements to represent the in-plane stiffness of the floor membrane. In particular, the peripheral links model the axial stiffness by one spring in the middle, and flexural stiffnesses by the two rotational springs at the ends, whereas the diagonal links only possess axial stiffness.

The present work considers the retrofitting solution by Masjuki (2017) using RC shear walls to strengthen the original frame building. Five walls are distributed along the overall storey height at different locations in the building, as indicated in Figure 6-6. The selected wall positions aimed at reducing the eccentricity between the centres of mass and stiffness at each storey level, which is beneficial to avoid possible torsional effects due to structural irregularities under earthquake loading. Moreover, this wall arrangement has been chosen to minimise the intervention along the external perimeter, as the building façades are characterised by large openings. All the walls were designed according to the basic requirements prescribed by EC8 (BSI, 2004b). Figure 6-7 and Figure 6-8 show the reinforcement details and geometry of the five RC wall components. Wall 1 has the same characteristics as Wall 2, while Walls 3, 4 and 5 are identical.

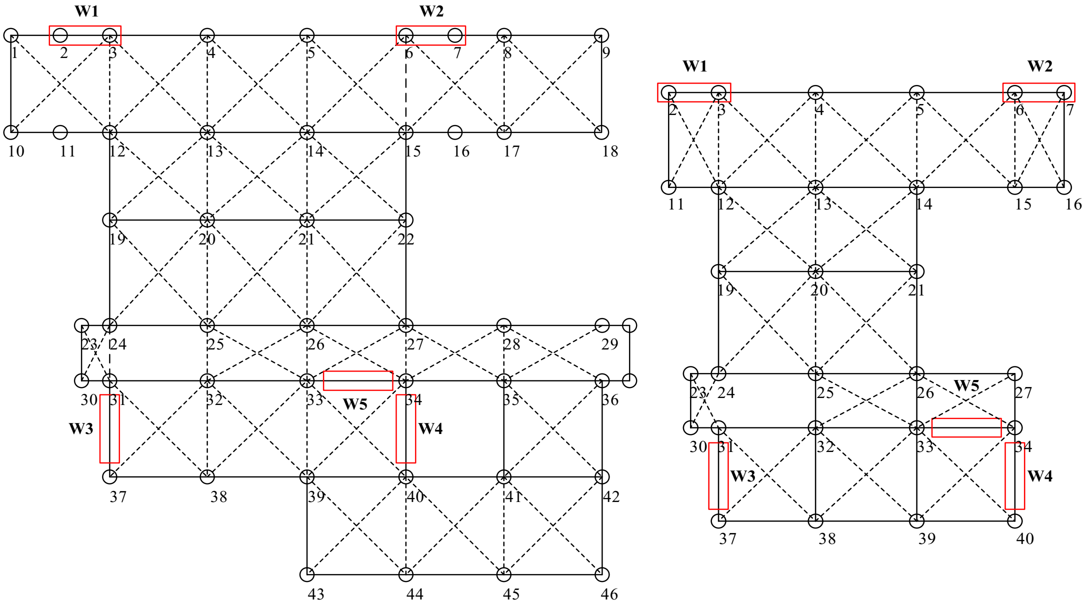

(a) (b)

Figure 6-6: Plan view of the RC wall's locations for: (a) 1st and 2nd; (b)3rd and 4th floors in the building

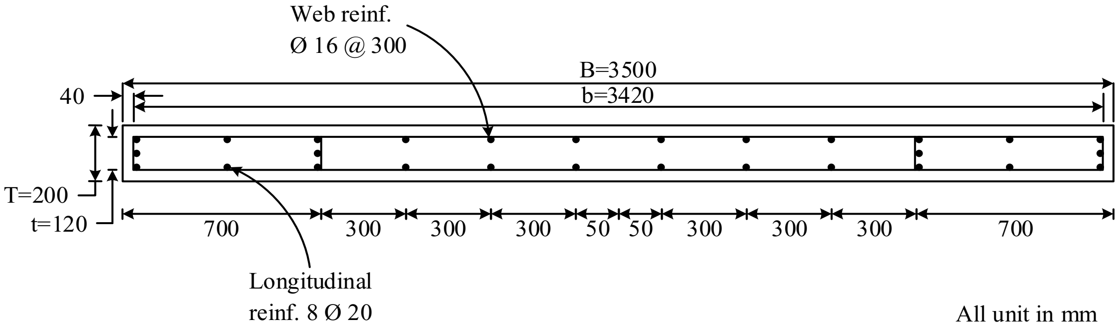

Figure 6-7: Reinforcement details and cross-section for walls 1 and 2 (Masjuki, 2017)

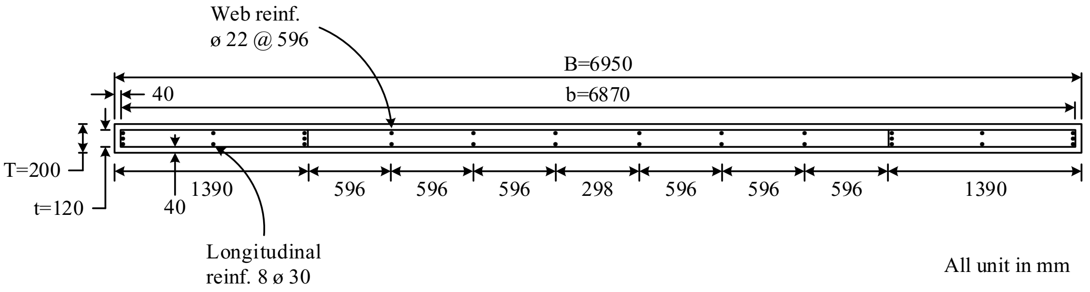

Figure 6-8: Reinforcement details and cross-section for walls 3, 4 and 5 (Masjuki, 2017)

With regard to the RC wall modelling, two alternative approaches (Figure 6-9) employing elasto-plastic cubic elements based on the wide column (WC) analogy or the developed 2D shear wall macro-elements (SWM) have been employed. In the WC models, a RC wall on a specific floor is represented by six 1D cubic elements ('cbp3') with the same length ratios specified for beams. According to the wide column modelling strategy described in Section 2.3.1, two rigid links are used to connect the wall elements at the floor levels to the end nodes of the beams. In the SWM models, four macro-elements ('swm4') are employed to infill the frame at each storey connecting the four corner nodes of each macro-element directly to the nodes of the column elements. The contribution of infill walls within the original building is not considered in the numerical investigation, as it is outside the scope of the current work. The application study does not correspond to the seismic assessment of a realistic building structure, but it is mainly aimed at demonstrating the effectiveness of using of the developed macro-element for modelling RC walls in buildings.

To improve computational efficiency of the nonlinear simulations, the partitioned modelling approach described in the preceding section is employed to model the RC buildings. Figure 6-10 shows the generated bare frame model and illustrates the partitioning strategy for the original 4-storey building. The bare frame structure is divided into four partitions, each of which corresponds to a single storey. The partitioned boundary nodes are the nodes at the different floor levels, as indicated in Figure 6-10, thus the number of nodes at the partitioned boundary is directly associated with the number of columns on each partitioned floor. At the parent structural level, four placeholder super-elements corresponding to the child partitions collect the partitioned boundary nodes. In this respect, the structural response of the main building components is solved in parallel in each partition, which allows a drastic reduction of the computational cost. The material parameters of concrete and steel reinforcement assumed in the numerical simulations of the bare frame and the frame-wall buildings are summarised in Table 6-1.

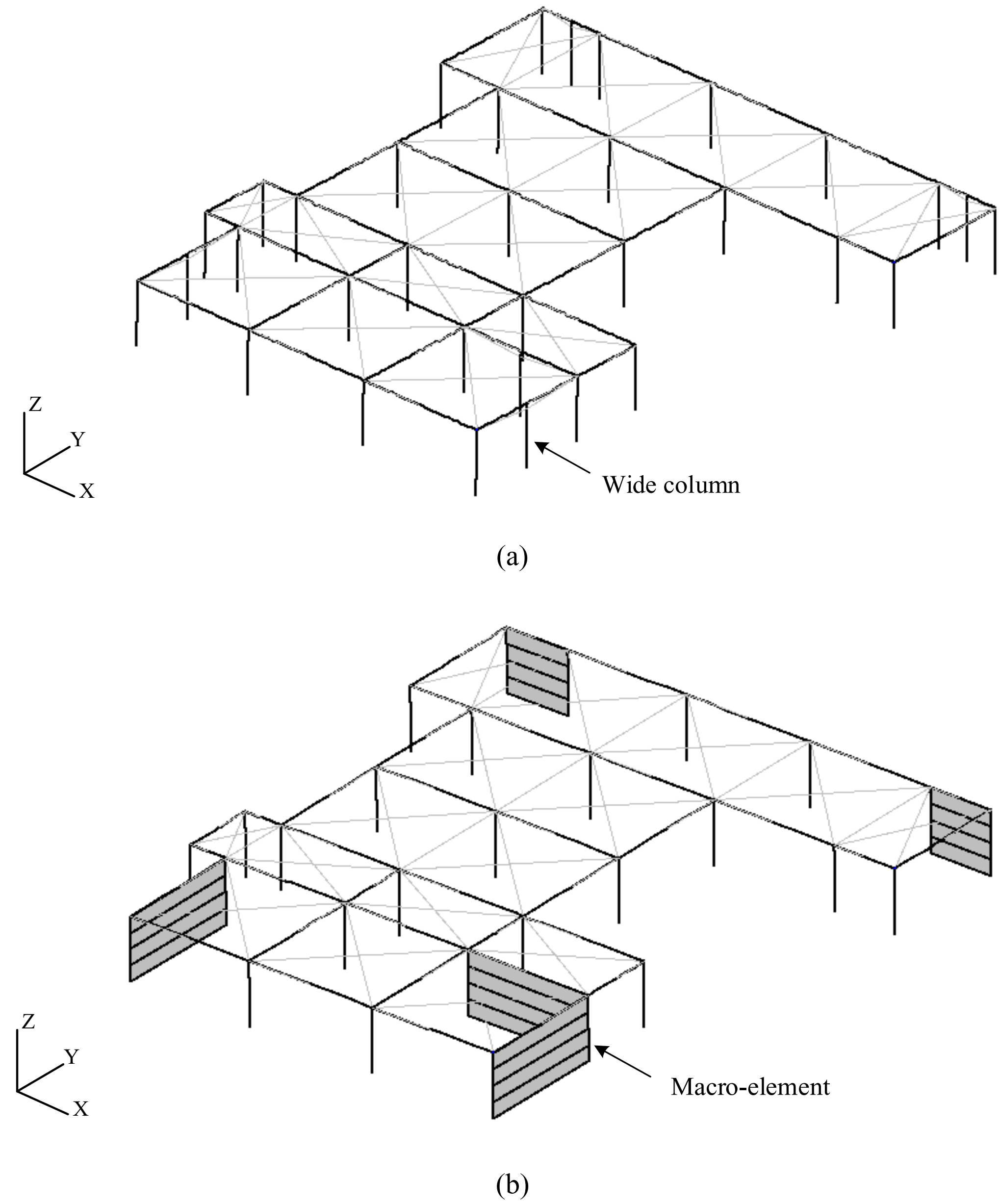

Figure 6-9: Illustration of RC walls modelling - finite element models of the 4th floor: (a) wide column (WC) model; (b) shear wall macro-element (SWM) model

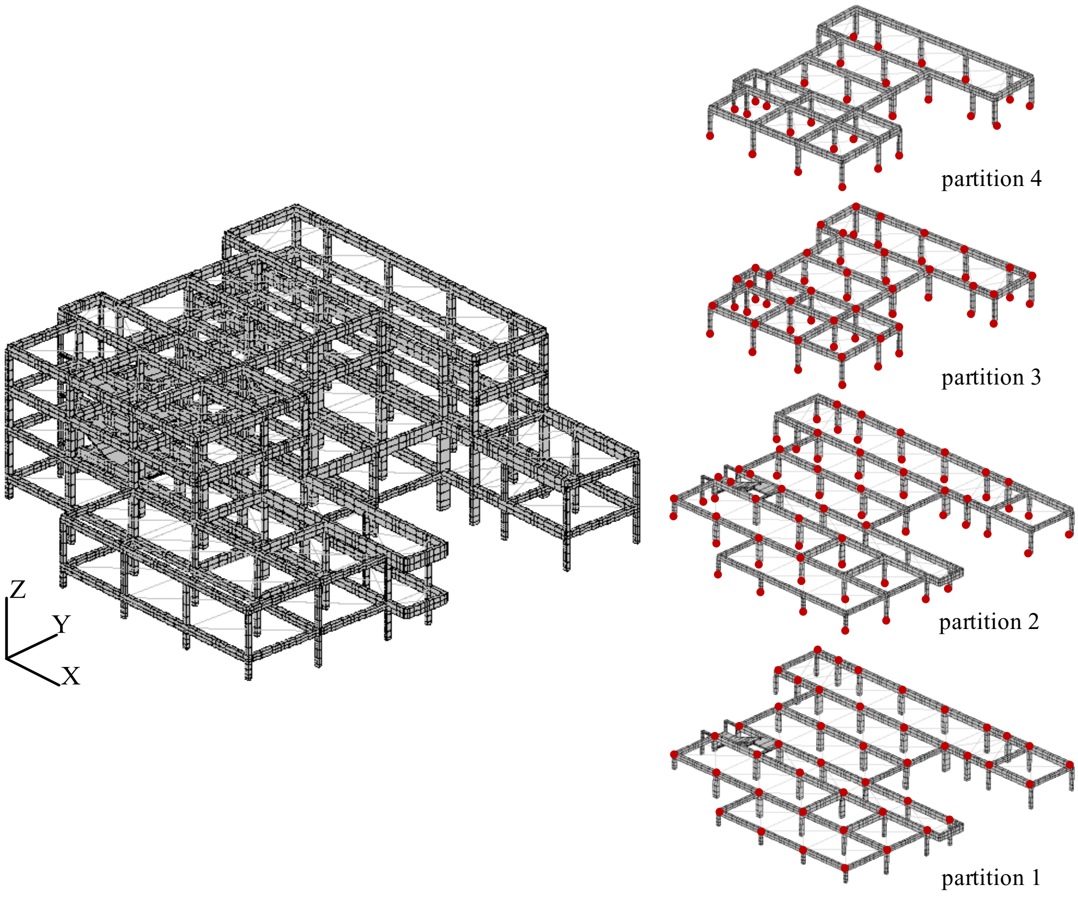

(a) (b)

Figure 6-10: Finite element model of the 3D RC building: (a) bare frame model; (b) illustration of portioned floors

Table 6-1: Material properties for concrete and steel reinforcements

Material	Member	Material property	Value
Concrete	Beam and column	Compressive strength	18.7 MPa
		Modulus of elasticity	26544 MPa
	Shear wall	Compressive strength	17 MPa
		Modulus of elasticity	32836 MPa
Steel reinforcement	Beam	Yield strength	383 MPa
	Column		383 MPa
	Shear wall		391 MPa
	Beam and column	Strain hardening factor	0.01
	Shear wall		0.001

6.4 Nonlinear structural analysis

6.4.1 Push-over analysis

The nonlinear response of RC structures is generally characterised by changing stiffness as a result of crack opening and closure. It is recalled that a dynamic analysis procedure has been employed in Section 3.3 to obtain the monotonic response of RC walls. The same analysis method has been adopted here to overcome possible convergence issues to obtain static push-over curves for the analysed building structures.

Two sets of numerical models have been developed based on the modelling strategy described in Section 6.3. In the frame-wall (*FW*) building, RC walls are modelled by 2D shear wall macro-elements (SWM) and 1D beam elements based on the wide column (WC) approach. Each set of models considers a realistic four-storey building and a two-storey building taking the top two floors from the original four-storey model, with and without RC walls. Hereafter, the model with shear wall macro-elements is called the *SWM model*, while the model using only beam elements is called the *WC model.*

A constant velocity of 0.1 mm/s and a zero acceleration are applied on the slave node, which imposes a linear variation of displacement on all the top nodes of the top storey. The load is applied up to a displacement level of 100mm, covering a range of inelastic deformation in the structure. Structural and non-structural masses are uniformly distributed along the beams in the numerical models employed here and those used for the dynamic time-history analyses in the subsequent section. The bottom nodes are fully restrained simulating fixed ground conditions.

Figure 6-11 and Figure 6-12 depict the push-over responses (i.e. total base shear force v.s. lateral displacement) of the four-storey and two-storey FW building models with reference to the bare frame (*BF*) building response. As evident from the figures, the added RC walls significantly enhance the lateral stiffness and resistance of the original structure. Comparisons are made between the frame-wall models using macro-elements (SWM) and beam elements (WC). In all cases, the SWM models give similar initial stiffness and more flexible response as compared to the WC model predictions. This is attributed to the fact that the SWM allows for shear deformations and shear resistance, which is ignored in the beam element formulation. The discrepancy between the SWM and WC model predictions is more substantial for the two-storey building than the four-storey building since shorter walls are used in the former case with greater contributions of shear deformation. The push-over curves of all the WC models are characterised by hardening response, which is only observed from the four-storey SWM model (Figure 6-11).

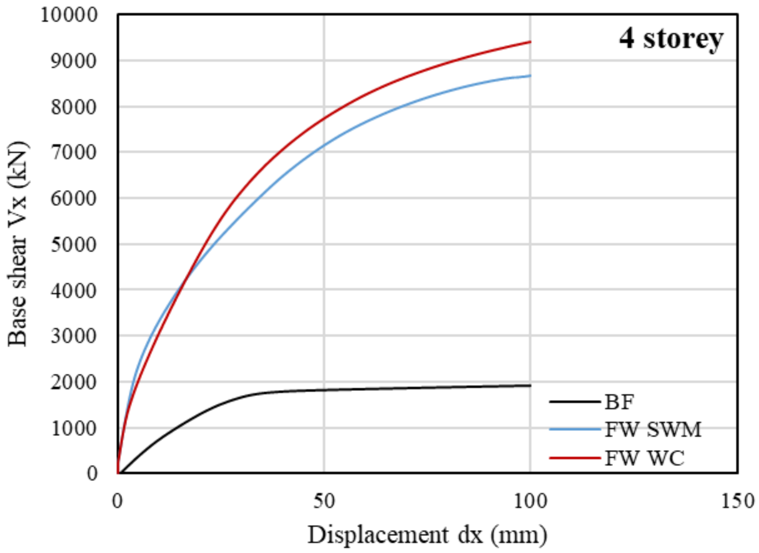

(a)

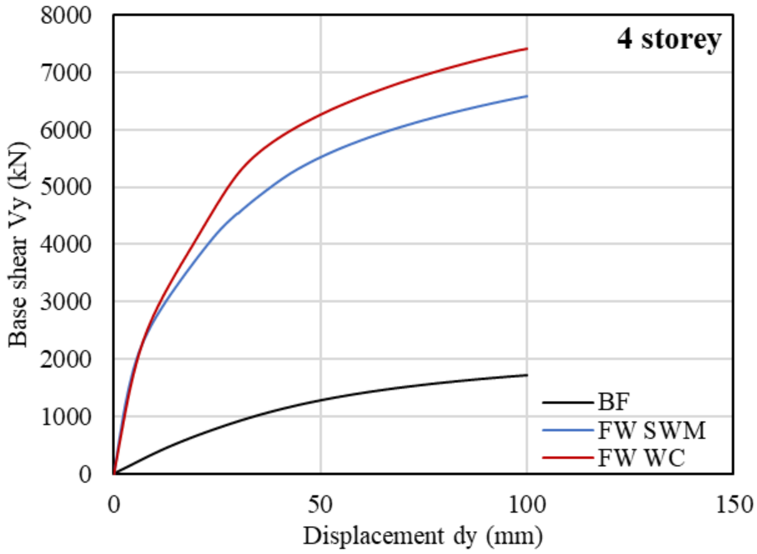

(b)

Figure 6-11: Push-over curve of the 4-storey building with and without shear walls with lateral load applied in the: (a) X-; (b)Y- directions

On the other hand, the two-storey SWM model predictions (Figure 6-12) show that the building model reaches the maximum resistance of around 8000kN, whereafter the responses exhibit relatively flat plateau due to shear failure mode occurring in RC walls at the bottom storey. Figure 6-13 and Figure 6-14 show deflected shapes (displacement scale 1:10) of the 2-storey SWM model subjected to lateral loads in the two global planar directions of the push-over analysis. The deformed RC walls close to the base clearly indicate shear failure.

It is worth noting that the compressive strength of concrete for shear walls is defined as 17 MPa, corresponding to weak concrete material as used in the old existing building. This value was deemed suitable for the 4-storey frame-wall building based on the detailed seismic assessment by Masjuki (2017) but may not be adequate for retrofitting the 2-storey building investigated here. Properly designed walls with a suitable amount of shear reinforcement will prevent shear failure in the critical regions at the wall base.

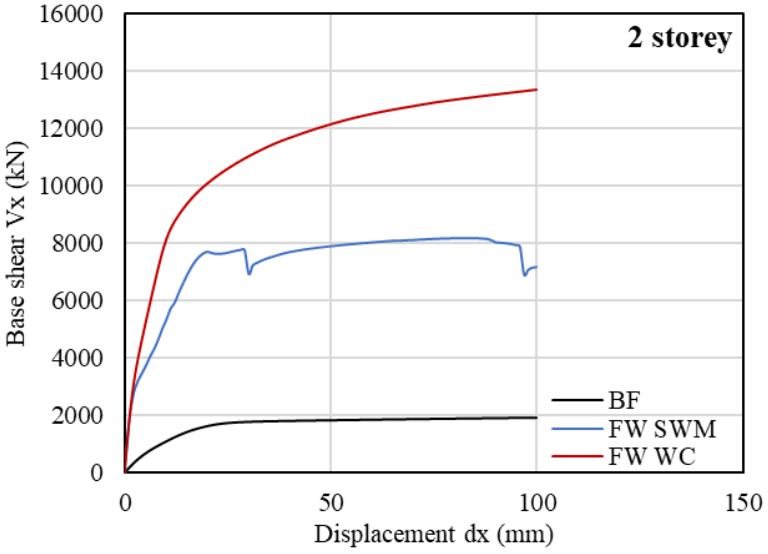

(a)

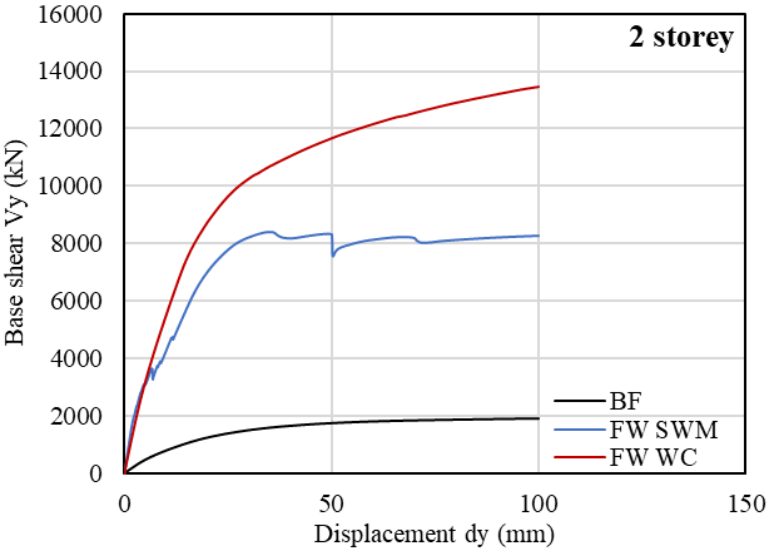

(b)

Figure 6-12: Push-over curve of the 2-storey building with and without shear walls with lateral load applied in the: (a) X-; (b)Y- directions

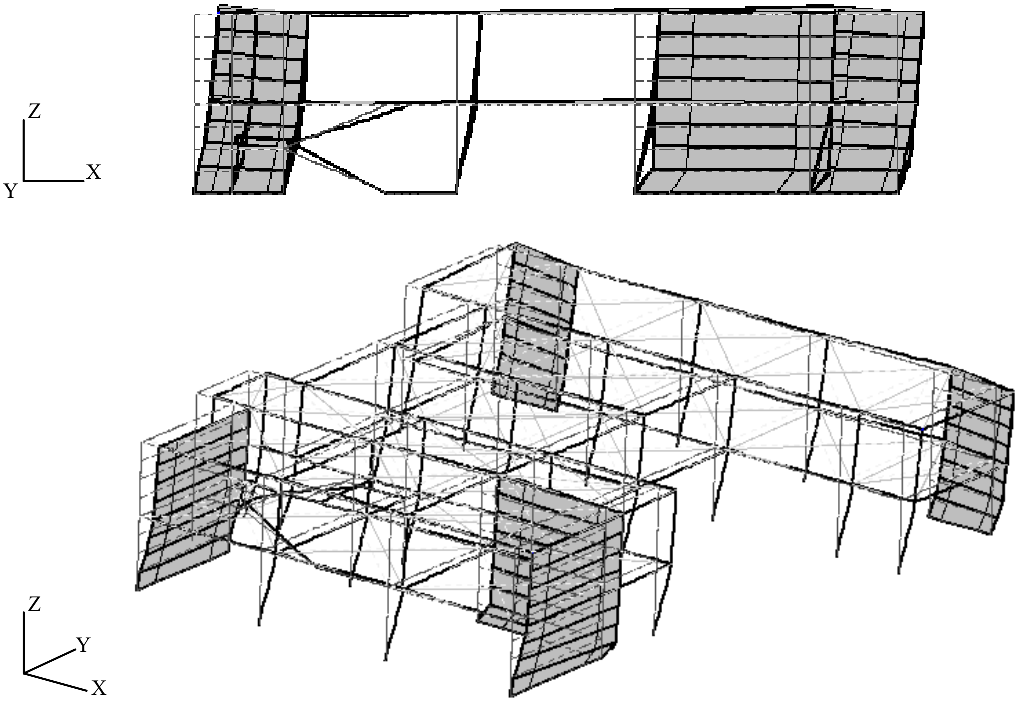

Figure 6-13: Deflection shaps (scale 1:10) of the 2-storey SWM model under push-over in X-direction

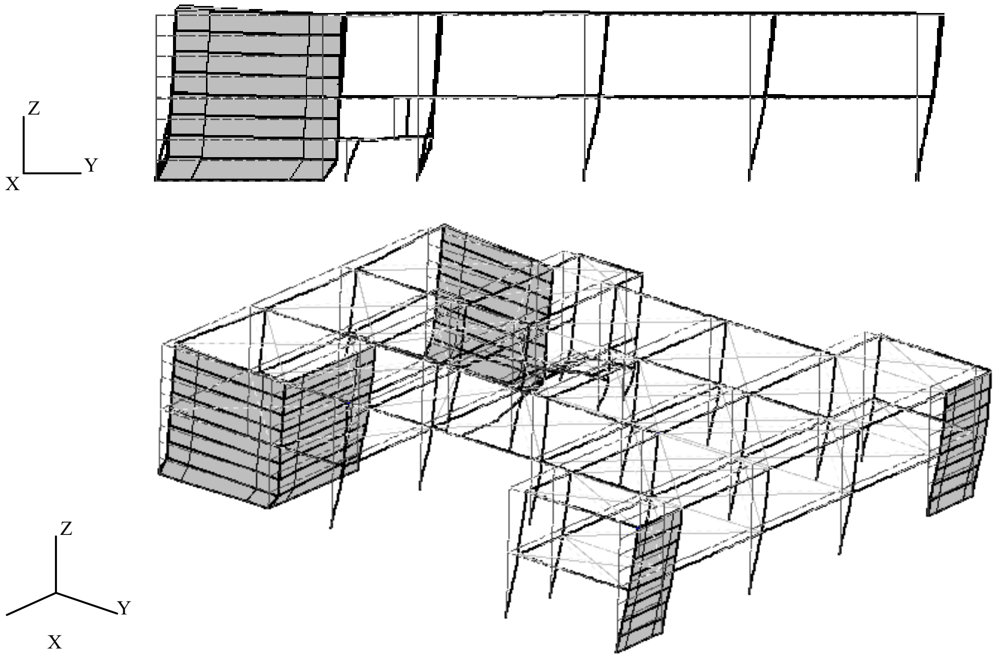

Figure 6-14: Deflection shaps (scale 1:10) of the 2-storey SWM model under push-over in the Y-direction

Parametric analyses have been carried out to assess the influence of the main concrete and steel material parameters on the push-over response in the X-direction of the 2-storey SWM model. The horizontal shear reinforcements are increased to three times the originally assumed value. As shown in Figure 6-15, the increased shear reinforcement barely enhances the overall resistance of the structure, which suggests that the wall shear failure is mainly due to concrete failure. The abrupt drop of the response is associated with a sudden release of energy upon the crack formation and stress redistribution within the building.

The subsequent numerical simulations consider normal strength concrete instead of the weak concrete material adopted by the original retrofitting solution for the 4-storey frame-wall building. Three compressive strengths are selected for the retrofitting walls, namely 25.5 MPa, 29.8 MPa, and 34 MPa, corresponding to 1.5, 1.75 and 2.0 times the value of f_{c1}=17 MPa given in Table 6-1. It can be observed that the abrupt drop in the resistance is shifting towards a larger displacement level, with the increasing concrete compressive strength, indicating that shear failure occurred at increased applied lateral load. The numerical response using f_{c1}= 34 MPa shows that the building tends to fail at a displacement of 100mm. Figure 6-16 compares the numerical response employing f_{c1}= 34 MPa in both the WC and SWM models, which once again confirms the stiffer response of the wide column approach without considering shear deformability.

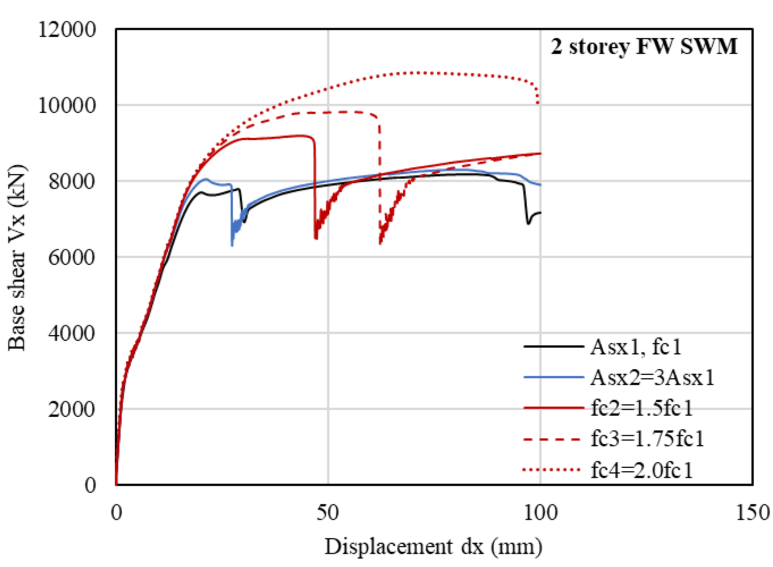

Figure 6-15: Sensitivity of push-over curves to the shear reinforcement amount and concrete compressive strength for the 2-storey frame wall building model

Finally, the yield strength of steel reinforcement is modified to 1.25 and 1.5 times of f_{ys1}=391MPa used in the initial simulations. As shown in Figure 6-17, the model with f_{ys2}=

$1.25f_{ys1}$ gives a stiffer response before the sudden release of energy. The subsequent increase in yield strength only affects the response after the force drop, where major cracks are formed.

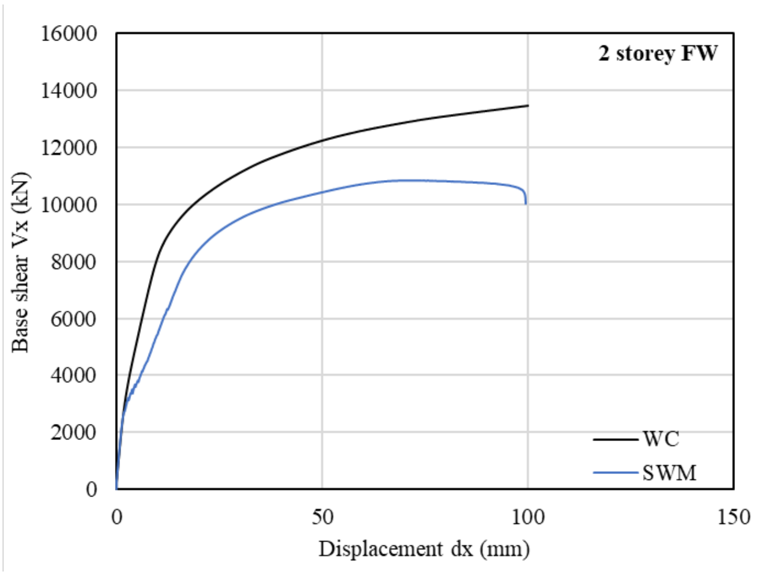

Figure 6-16: Push-over curve of the 4-storey frame-wall building with lateral load applied in X-direction (f_{c1}= 34 MPa)

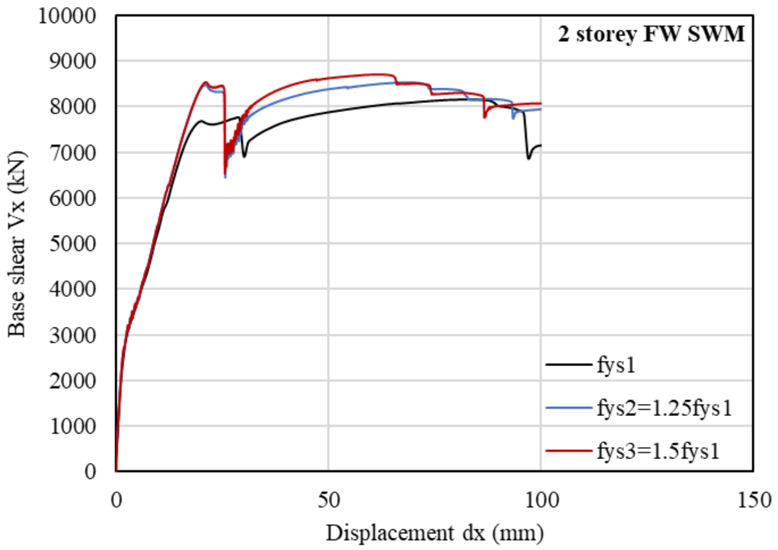

Figure 6-17: Sensitivity of push-over curves to yield strength of steel reinforcement for the 2-storey frame wall building model

6.4.2 Dynamic time-history analysis

6.4.2.1 Accelerograms

The selection of realistic earthquake ground motion records is important in dynamic simulations of RC buildings under seismic loading. EC8 (BSI, 2004b) recommends using a minimum of three accelerograms in the time-history representation of the seismic action. In this respect, three different sets of natural accelerograms recorded in the past seismic events are selected to perform nonlinear time-history analyses.

The main characteristics of the considered earthquake records are summarised in Table 6-2, where the peak ground acceleration (PGA) refers to the maximum absolute value of the ground acceleration.

Table 6-2: Main characteristics of the selected accelerograms

Earthquake ID	Name	Mw	Fault type	Epicentral Distance	PGAx [m/s^2]	PGAy [m/s^2]	EC8 site class
170	Basso Tirreno	6.0	oblique	18	0.72	1.58	C
292	Campano Lucano	6.9	normal	25	0.59	0.59	A
6331	South Iceland (aftershock)	6.4	strike-slip	22	0.51	0.39	A

The selected earthquake records satisfied the spectrum compatibility requirement prescribed by the Italian Seismic Code (NTC, 2008), which were considered in the previous detailed seismic assessment for the same 4-storey building by Masjuki (2017).

The acceleration records are applied at the base of the analysed building models simultaneously in the two orthogonal planar directions, X and Y, whereas the vertical acceleration component is neglected. Figure 6-18 shows the Basso Tirreno earthquake ground motion records used in dynamic simulations, whereas the rest two records are given in Figures A3 and A4 in the appendix.

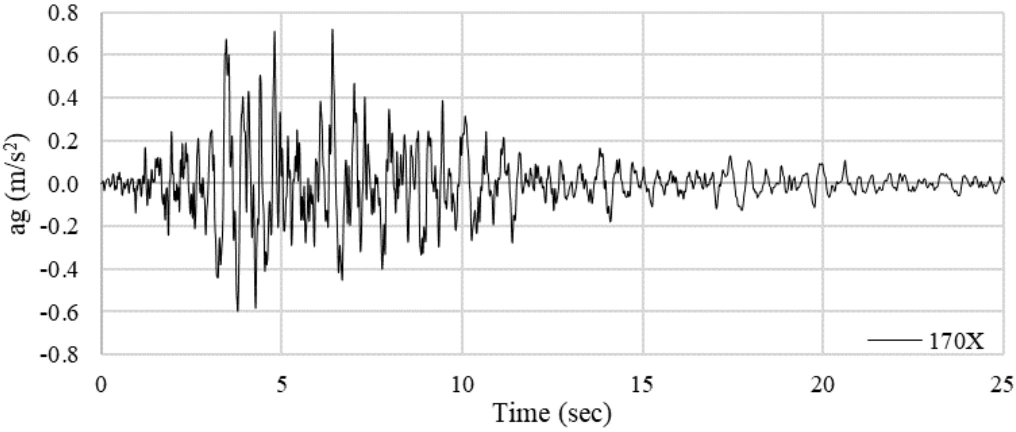

(a)

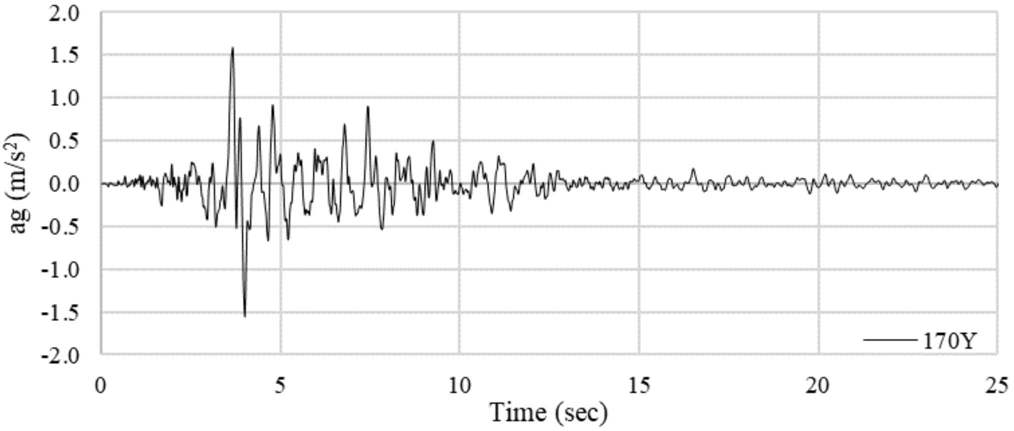

(b)

Figure 6-18: Ground motion acceleration records of Basso Tirreno earthquake (170) in: (a) X- and (b) Y-directions

6.4.2.2 Time history response

The nonlinear dynamic simulations carried out here and in the next section consider the four-storey frame-wall building system, where the RC walls are represented by macro-elements and beam elements. The global structural response is studied by considering the four corner columns at the 4th floor, which are labelled by marker P, Q, M and N in Figure 6-19. As an example, Figure 6-20 shows the lateral displacement relative to the ground of point P in X- and Y directions versus time for both SWM and WC models. The SWM models predict larger displacements before 15sec than the WC models, which can be due to the effects of shear deformation developed in walls.

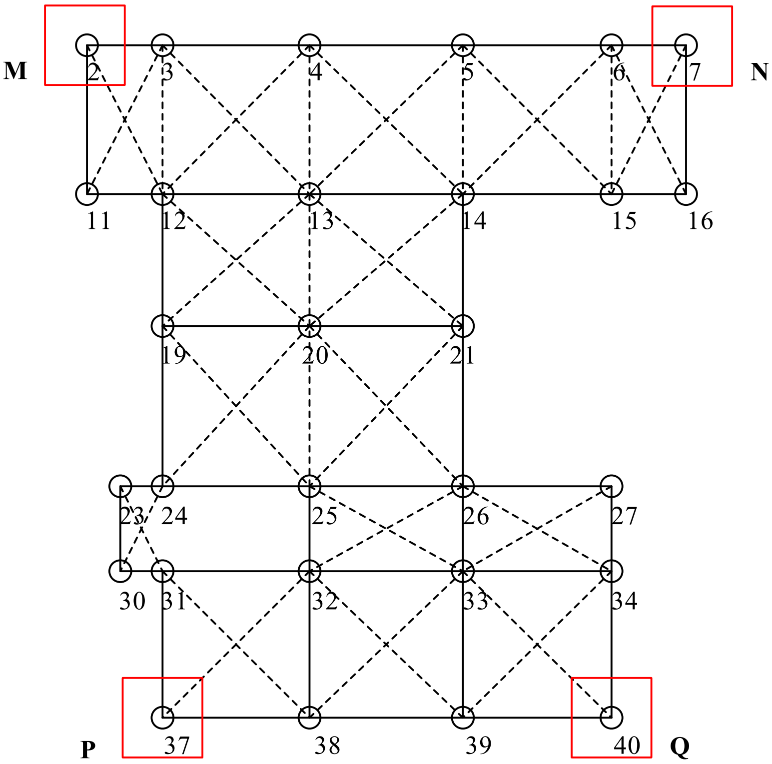

Figure 6-19: Considered four corner columns

The considered building may be subjected to torsional effects due to structural irregularities. The resultant drift taking as the square root of the squared displacements in X- and Y- directions is a more representative measure of the maximum displacement experienced during an earthquake. Figure 6-21 plots the maximum resultant drift relative to the ground against time for column P at the 4th floor. The maximum resultant drifts predicted by WC and SWM models are 19.27mm (at 10.3 sec) and 34.58mm (at 7.6 sec), respectively. It is found that the wall-clock time required by both models is comparable, which once again confirms the computational efficiency of the implemented macro-element model for RC walls.

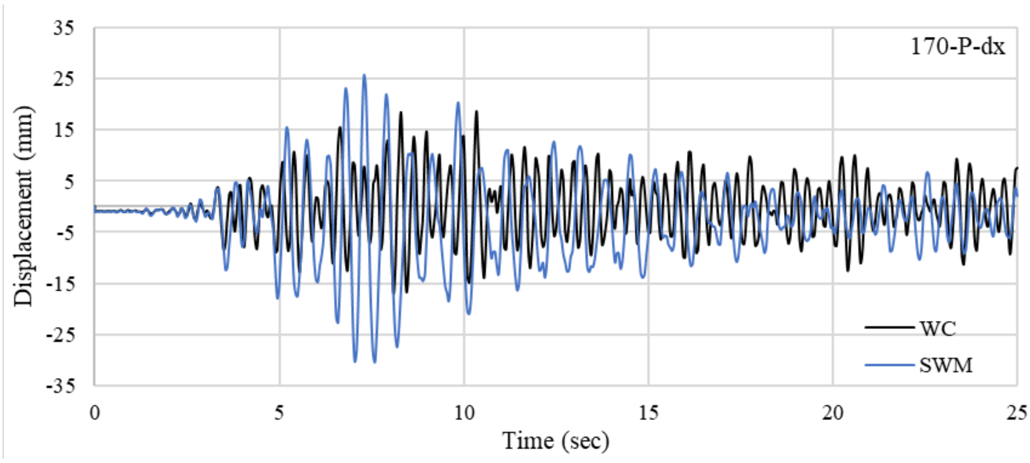

(a)

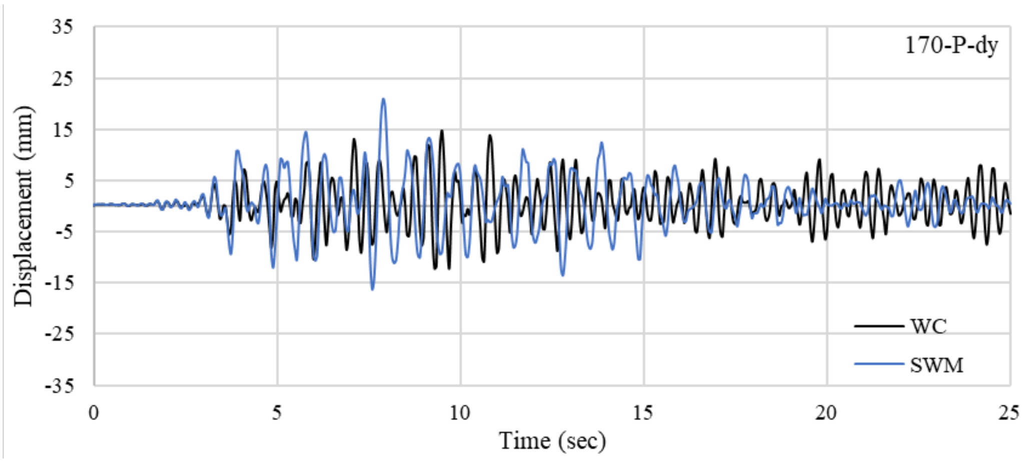

(b)

Figure 6-20: Time history responses of the frame-wall building model: displacements (relative to ground) in (a) X- and (b) Y- directions of column P at the 4th floor under earthquake 170

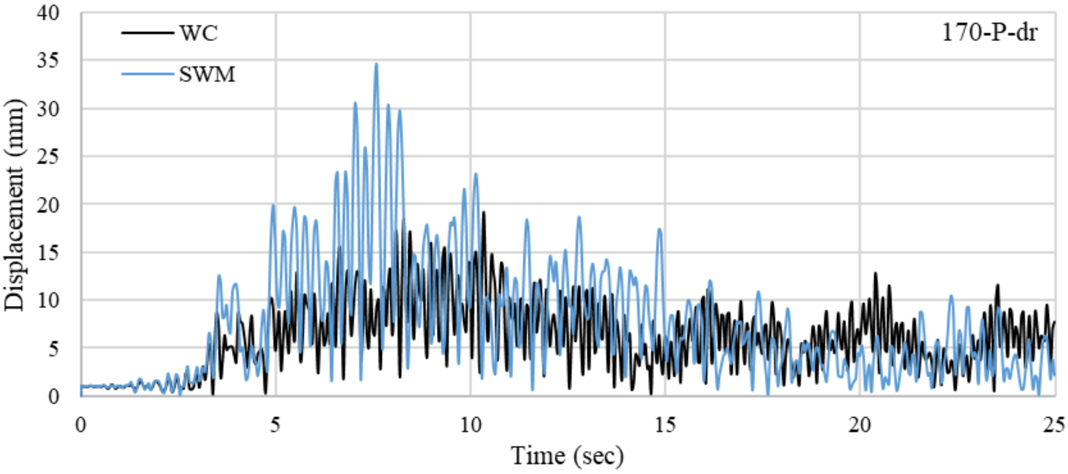

Figure 6-21: Time history responses of the 4-storey frame-wall building model: resultant drifts (relative to ground) of column P at the 4th floor

6.4.3 Incremental dynamic analysis

Further dynamic time-history analyses are carried out in this section following the incremental dynamic analysis (IDA) procedure proposed by Vamvatsikos & Cornell (2002). The IDA method is essentially a parametric assessment to provide a continuous picture of the complete range of the structural performance under seismic loading. It involves performing multiple nonlinear dynamic simulations of the building structure subjected to a set of scaled ground motion records. The resulting IDA curve typically plots one or more ground motion Intensity Measures (IM) of the applied scaled accelerogram against a Damage Measure (DM), representing the structural response of a model under prescribed seismic loading.

The IM should be associated with the structural response of interest to reduce the number of dynamic time-history analyses, as suggested by Kiani & Pezeshk (2017). The IM chosen here is the scale factor (SF) characterising a scaled image of accelerograms. Therefore, a value of SF = 1.0 corresponds to the natural accelerogram. A scaled-down or scaled-up accelerogram is charactered by SF < 1.0 or >1.0 respectively. The level of SF corresponds to the ground motion intensity related to the design earthquake, since the chosen accelerogram represents the design response spectrum.

In the incremental dynamic simulations, the 4-storey frame-wall building is subjected to a series of ground motions represented by the chosen SF ranging from 0.2 to 1.5. Figure 6-22 to Figure 6-25 show the maximum inter-storey drift ratios of the considered four corner columns at the different storey levels. Here, the drift again refers to the resultant drift, as defined in Section 6.4.2.2. With increasing levels of ground motion, the SWM model shows larger deformation at the 1st storey than the stories above, which is not revealed by the WC model predictions. This is because the macro-elements allow for shear deformability and potential shear damage and failure in the RC walls, which is ignored in the WC modelling strategy for RC walls. The inter-storey drift at the 1st storey is more substantial when the natural accelerogram is scaled-up (i.e., SF > 1.0). This indicates that the considered RC walls may not have sufficient resistance against shear failure under more severe seismic events, mainly due to the weak concrete material used for the shear walls.

Under lower levels of ground motions (i.e., SF < 1.0), the SWM and WC models show similar global building responses before significant shear deformation occurs. It can be observed that the maximum inter-storey drift ratios are typically less than 0.2% for the SWM models and 0.1% for the WC model predictions, except for the case of column N (Figure 6-25(a)). It is confirmed again that the macro-element considering shear deformability gives a more flexible response than the beam element model.

The maximum resultant drift ratios of column P at each storey of the 4-storey frame-wall building predicted by the WC and SWM models subjected to scaled earthquake records 292 and 6331 are given in Figures A5 and A6 in the appendix for more information.

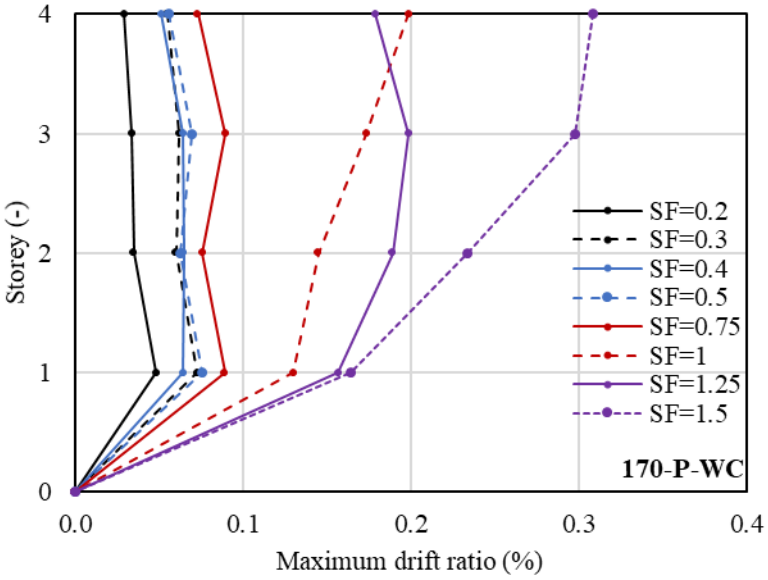

(a)

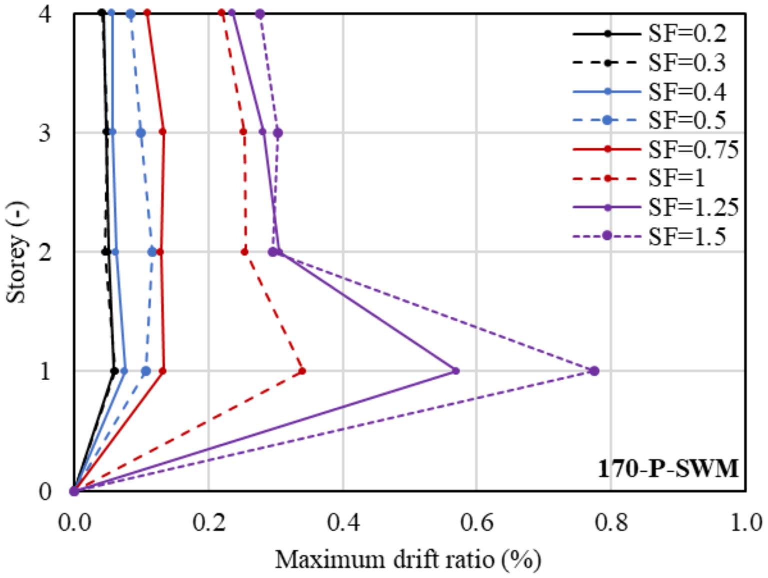

(b)

Figure 6-22: Maximum inter-storey drift ratio of column P at each storey of the 4-storey frame-wall building predicted by: (a) WC and (b) SWM models under scaled ground motions of earthquake 170

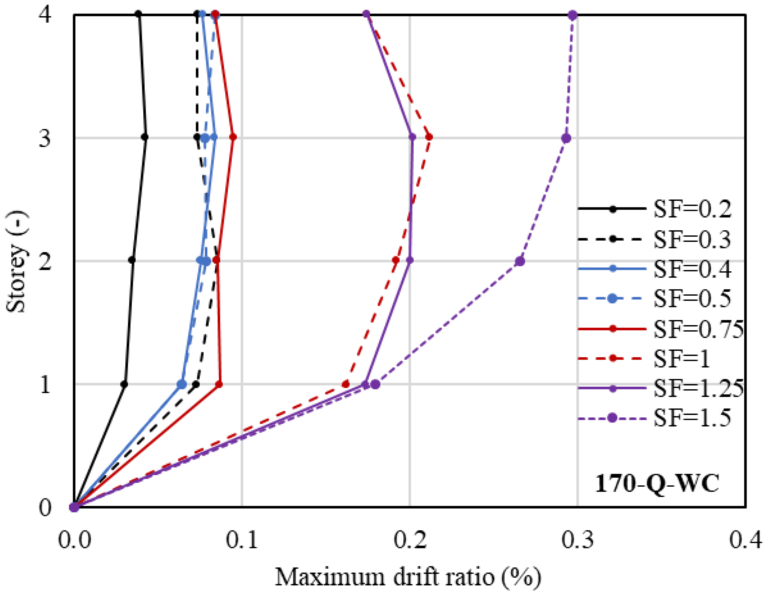

(a)

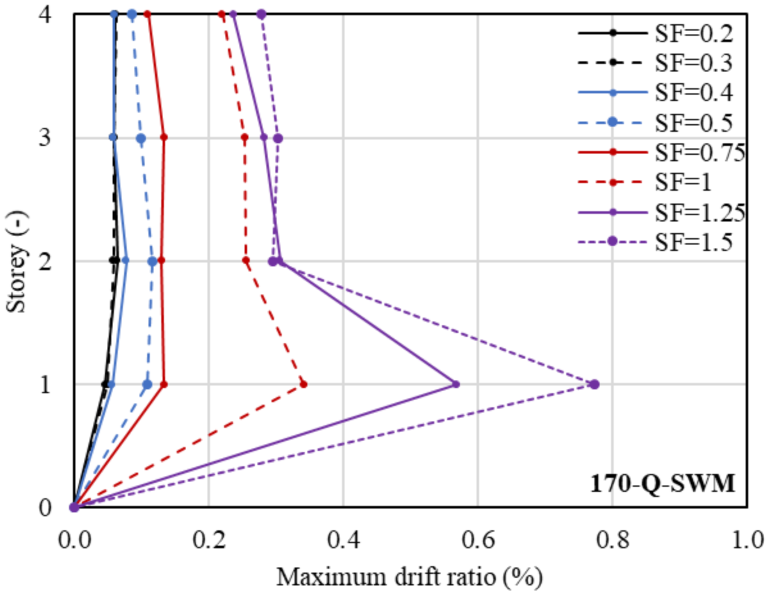

(b)

Figure 6-23: Maximum inter-storey drift ratio of column Q at each storey of the 4-storey frame-wall building predicted by: (a) WC and (b) SWM models under scaled ground motions of earthquake 170

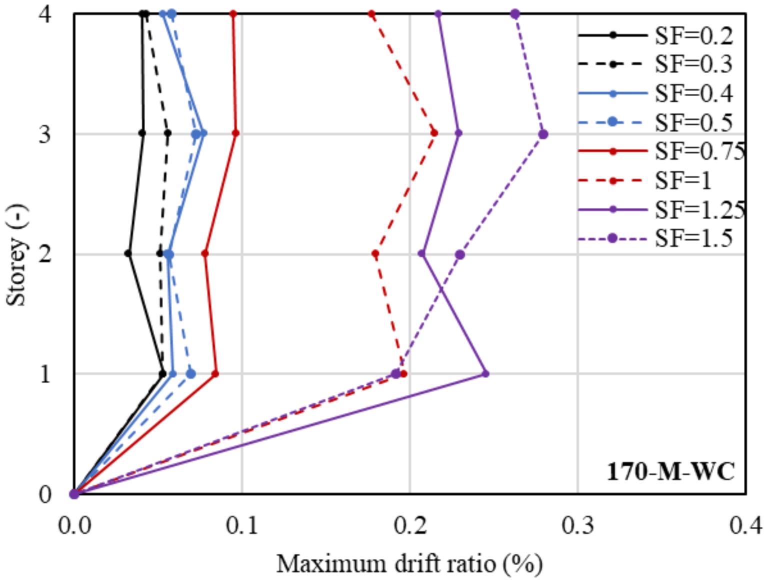

(a)

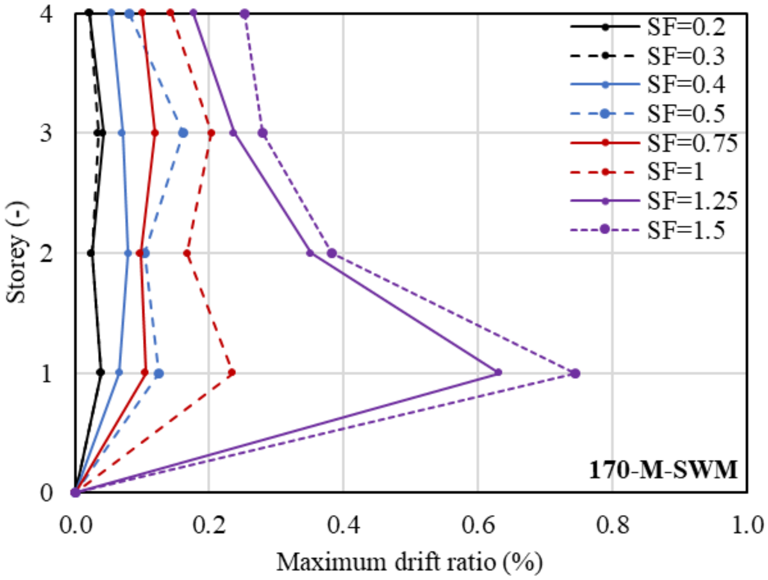

(b)

Figure 6-24: Maximum inter-storey drift ratio of column M at each storey of the 4-storey frame-wall building predicted by: (a) WC and (b) SWM models under scaled ground motions of earthquake 170

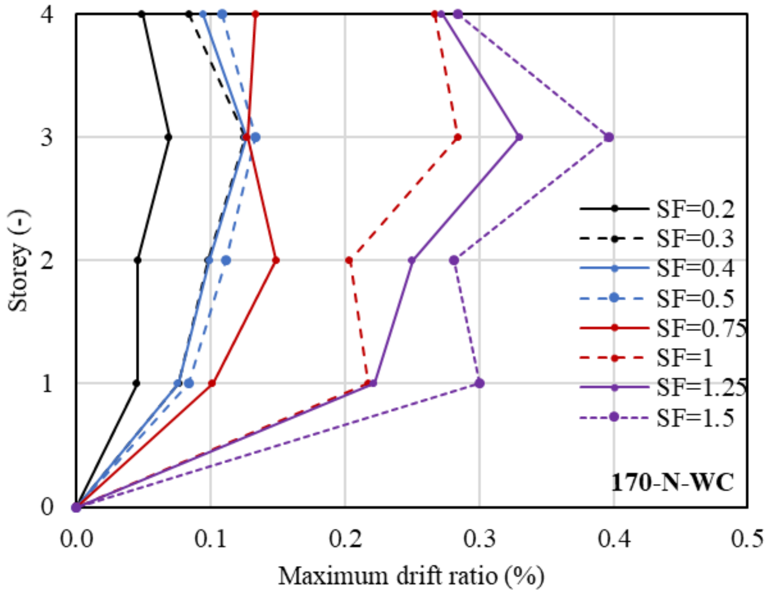

(a)

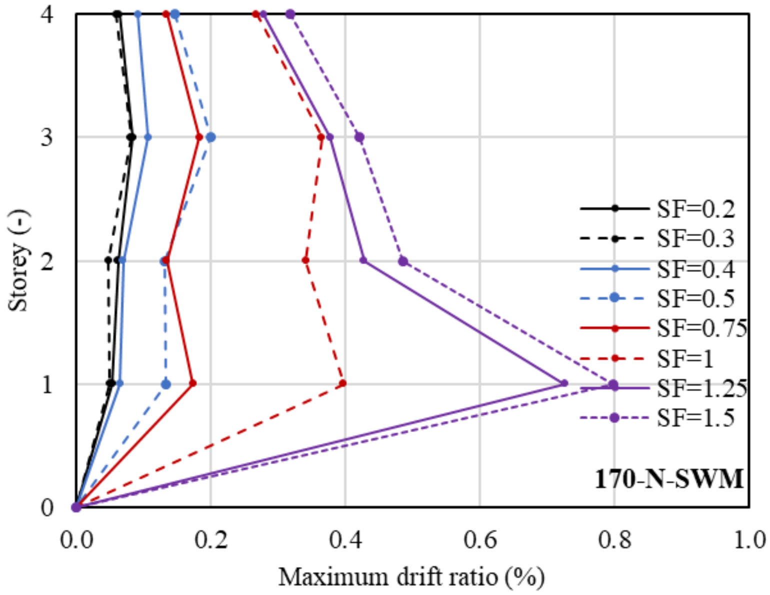

(b)

Figure 6-25: Maximum inter-storey drift ratio of column N at each storey of the 4-storey frame-wall building predicted by: (a) WC and (b) SWM models under scaled ground motions of earthquake 170

The IDA curves are plotted in Figures 6-26 to 6-28 based on the results from Figure 6-22, Figures A5 and A6. They show the SF representing the scaled ground motions with different intensities versus the maximum inter-storey resultant drift ratios of column P at each floor. Comparisons are made between the WC and SWM model predictions. In general, the WC models predict a stiffer response than the SWM models, which is in agreement with the results presented before. The discrepancy of the maximum resultant drift at the 1st floor between the WC and SWM predictions is more pronounced for stronger earthquakes (e.g., SF =1.5), since major shear damage is concentrated at the base of the RC walls at the ground floor, as shown in Figures 6-26 and 6-27. This is not the case for the building under the scaled earthquake 6331 (Figure 6-28), where the RC walls remain adequate to resist potential shear failures. On the other hand, the close agreement between the WC and SWM model predictions implies the flexural dominated behaviour at a specific floor, for example, the 4th floor for earthquake 17 (Figure 6-27) and the 3rd floor for earthquake 292 (Figure 6-26). Furthermore, it can be observed from Figure 6-27 that both models predict a similar initial linear response (SF < 0.5) for floors 2, 3 and 4, where the structural members may be deformed in the elastic range.

It can also be observed that the IDA curves are not smooth and exhibit a back-and-forth weaving behaviour in some cases, for example, the WC response at the 4th floor (Figure 6-26). Vamvatsikos & Cornell (2002) pointed out that this is a typical feature of the IDA curves, which is associated with the rate of DM accumulation. In other words, the accumulation of maximum drifts accelerates at times and decelerates at other times. The deceleration can be significant, thus stopping the accumulation of maximum drifts or even reversing it, therefore pulling the IDA curve to a lower drift level. However, it may be still counter-intuitive that a system shows the same or even reduced drift under higher seismic intensities.

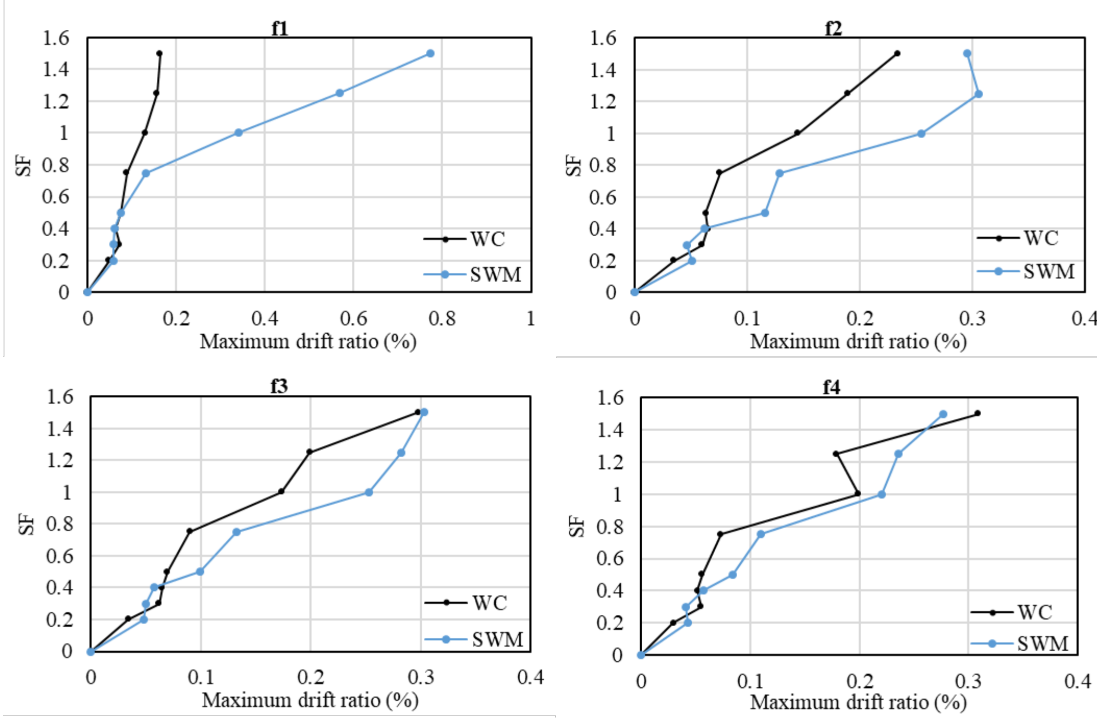

Figure 6-26: IDA curves of maximum inter-storey drift ratio of column P at each floor of the 4-storey frame-wall building under scaled earthquake 170

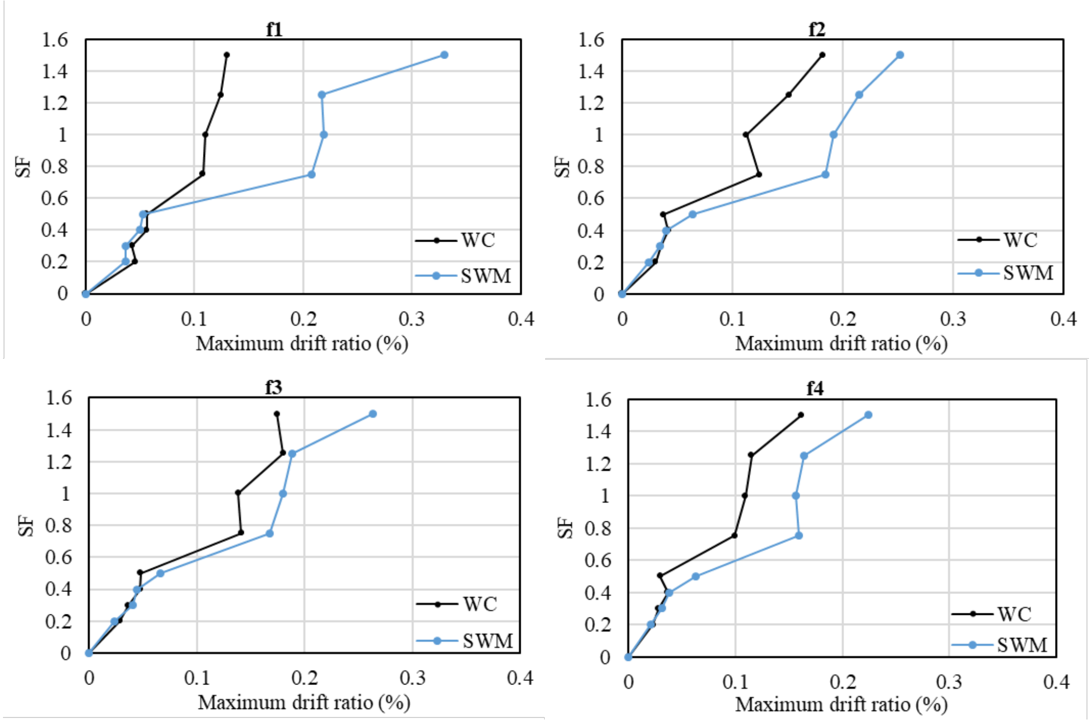

Figure 6-27: IDA curves of maximum inter-storey drift ratio of column P at each floor of the 4-storey frame-wall building under scaled earthquake 292

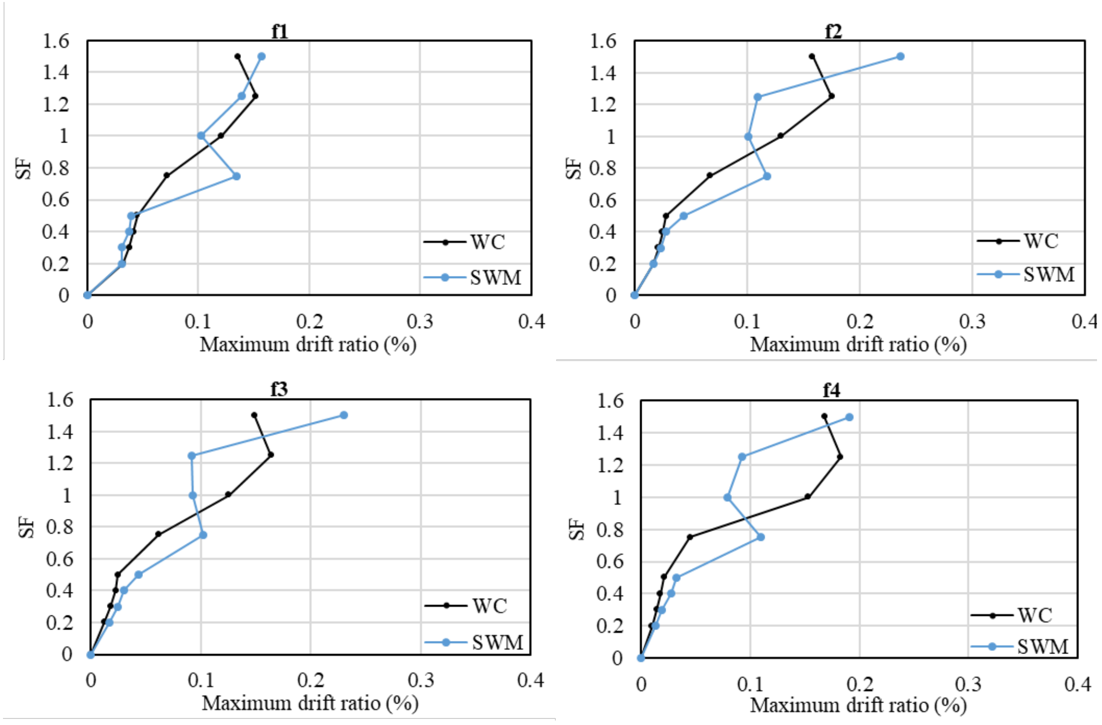

Figure 6-28: IDA curves of maximum inter-storey drift ratio of column P at each floor of the 4-storey frame-wall building under scaled earthquake 6331

6.5 Concluding remarks

This chapter has employed the macro-element approach developed in Chapter 4 for modelling RC walls within a realistic 4-storey frame-wall building system. The numerical results obtained from push-over analyses demonstrate that the developed macro-element model is capable of capturing shear deformations and damage, providing a more flexible response than the wide column model with simple beam elements. An artificial building model was also generated, which takes the top two stories of the original 4-storey building. It has been found that the assumed RC walls are not adequate to resist shear failure in the two-storey frame-wall building. Parametric studies have shown the sensitivity of the macro-element to the main material parameters and the amount of shear reinforcement.

Nonlinear time-history analyses according to an incremental procedure have been conducted to study the global structural response of the 4-storey building. A stiffer response is predicted by the wide column model as compared to the macro-element model. This implies that the wide column approach commonly used in practice may provide unconservative results in the simulations of retrofitted structures using RC walls. It has also been found that the wall-clock time of numerical simulations employing the macro-elements is comparable to that with the wide column approach, which is attributed to the considerable computational benefits achieved by the proposed macro-element representation. This demonstrates that the developed macro-element modelling strategy for RC walls with the aid of partitioned modelling is a computationally efficient and accurate method for nonlinear dynamic analysis of large scale structures, and it can be used for realistic assessment of multi-storey RC buildings with shear walls.

Chapter 7

Conclusions

7.1 Summary

RC walls are commonly used as the primary lateral load resisting components in new buildings and as a global retrofitting solution for old structures. Nonlinear analysis of RC walls under earthquake loading relies on accurate and realistic numerical descriptions. This work is motivated by the need for an efficient numerical modelling approach for RC walls, thus facilitating realistic seismic analysis of RC frame-wall buildings. The primary contribution is the development of an appropriate modelling strategy striking a balance between computational efficiency and numerical accuracy for RC walls under cyclic loading representing seismic actions.

Chapter 2 has summarised the response characteristics of RC walls and the potential failure mechanisms under cyclic loading. Existing modelling approaches and constitutive models for walls subjected to cyclic loading have been reviewed, which provides a consistent basis for this thesis. In the following, the major achievements in this research are highlighted and conclusions are drawn. The main objectives of this research, which have been defined in Chapter 1 and addressed in the subsequent chapters, include (i) a critical evaluation of existing modelling strategies for RC walls; (ii) the development of an accurate and efficient numerical 2D macro-element formulation; (iii) the development of a suitable biaxial concrete constitutive model incorporated into the macro-element; (iv) the validation the developed macro-element formulation against experimental results demonstrating model accuracy and efficiency and (v) the investigation of the seismic response of a realistic RC building with shear walls by employing the developed approach with macro-elements.

7.2 Existing modelling strategies

In the literature limited attempts have been made to simulate RC walls by employing detailed FE models. In the first part of this research, currently available modelling strategies in ADAPTIC (Izzuddin, 1991) are adopted to analyse under cycling loading a slender and a short wall, which were previously investigated in physical tests. The RC wall specimens are represented by models with different levels of sophistication, including (i) 1D models based on the wide column (WC) analogy; (ii) 2D FE models with nonlinear shell elements; and (iii) detailed 3D FE descriptions with solid elements and embedded bar elements. The ability of the employed models to replicate the experimental response of the analysed walls is assessed with focus on accuracy, computational efficiency, and robustness. The numerical results have confirmed that:

- The 1D strategy using beam elements offers simplicity in modelling, but it does not provide information on the stress/strain distributions within RC walls. By contrast, more detailed 2D and 3D FE models provide a more realistic description of the physical behaviour.
- The 1D beam-column model well reproduces the cyclic response of the slender walls dominated by flexural behaviour. On the other hand, it is less accurate in representing short walls with shear dominated behaviour due to the Euler-Bernoulli hypothesis assumed in the element formulation.
- Current 2D and 3D FE models show good potential for accurate simulation of RC walls under monotonic loading. Nevertheless, they provide less accurate predictions in the case of cyclic loading. The advanced concrete damage plasticity model (CDPM) used in 2D and 3D FE models does not enable an accurate description of actual pinching features exhibited by the experimental cyclic response.
- Regarding computational efficiency, the 3D FE models require considerably increased computational efforts (i.e., model generation, wall-clock time of analysis, and calibrations of input material parameters) compared to the 1D and 2D models, which hinder their applications to large scale frame-wall systems.
- All the models showed computational robustness in the simulations of the slender walls, whereas the 2D shell and 3D solid models suffered from convergence issues in the analysis of short walls, especially under cyclic loading conditions.

7.3 Macro-element model

Given the limitations of current modelling strategies for RC walls, the second part of this research proposes a specialised 2D plane stress shear wall macro-element (SWM), which accounts for shear deformation. The proposed 4-noded macro-element is characterised by a grid of monitoring points, where concrete and orthogonal steel reinforcement contributions are considered. Each macro-element can be used to represent a vertical portion of a typical RC wall arrangement.

The proposed macro-element can be linked to a biaxial concrete material model at the monitoring point level. To account for the cyclic loading effects, a biaxial concrete material based on the rotating crack approach is proposed and incorporated into the macro-element formulation. The implemented macro-element is verified at the monitoring point level by numerical tests on single elements and at the element level by analysing RC wall specimens. The results from a mesh sensitivity study recommend using at least four macro-elements to describe an inter-storey height portion of a RC wall to obtain accurate predictions. Material parametric studies suggest that the concrete compressive strength and softening stiffness have the most pronounced influences on the cyclic response. Most importantly, the macro-element relies on a reduced number of material parameters that can be obtained from simple material tests or calibrated based on analytical concrete material models, which is critical for a practical and straightforward application of the developed modelling strategy for RC walls. The computational efficiency is also significantly reduced compared to the detailed 3D solid element or 2D shell element models.

The accuracy of the proposed macro-element model is confirmed by validation studies on RC wall specimens with different aspect ratios and a RC coupled wall system. Experimental results and macro-element predictions have generally shown a very good agreement. The macro-element model enables capturing the main features of cyclic response, including stiffness and strength degradation and the pinching behaviour of the global hysteresis loops. A RC wall with an aspect ratio between 1.0 and 2.0 can be accurately simulated using at least five macro-elements. Additionally, the concrete material parameters in the confined regions may influence the numerical cyclic response of RC walls. It is established that without experimental data for the concrete compressive softening modulus, a value in the range from -1000MPa to -4000MPa can be used for accurate assessment using the proposed macro-element models for RC walls. In addition, it has been found that the developed macro-element approach can realistically represent the actual energy dissipation capacity and the stiffness degradation exhibited by RC walls in physical tests under cyclic loading. The global response of a five-storey RC-coupled wall is also predicted with suitable accuracy. Furthermore, it was also demonstrated that the macro-element model allows for an accurate representation of the shear wall response in comparison to the widely used wide column model.

7.4 Application study

In the final part of the research, the developed macro-element modelling strategy is employed to model RC walls within a realistic four-storey RC frame-wall building subjected to earthquake loading. A recently developed partitioned modelling approach is utilised to enhance computational efficiency.

According to the results of push-over analyses, the inclusion of RC walls substantially improves the lateral resistance of the original bare frame building. The developed macro-element model allowing for shear deformations provides a more flexible response prediction compared to the wide column model with simple beam elements. The top two stories of the original four-storey building were taken into consideration in generating a representative two-storey building model. It has been found that the assumed RC walls are insufficient to resist shear failure in the two-storey frame-wall building. Parametric studies have demonstrated the sensitivity of the macro-element to the main material parameters and the amount of shear reinforcement.

The seismic response of the four-storey frame-wall building has been examined using nonlinear time-history analyses based on an incremental procedure. The wide column model predicts a stiffer response as compared to the macro-element model. Therefore, the wide column approach commonly used in practice may result in unconservative results in the simulation of retrofitted structures using RC walls. Numerical analyses utilising macro-elements require comparable computational efforts to those using the wide column approach.

To this end, the proposed macro-element modelling strategy for RC walls with partitioned modelling represents a computationally efficient and accurate method for nonlinear dynamic analysis of large scale structures. Thus, it can be used for realistic assessment of multi-storey RC buildings with shear walls.

7.5 Future research

Although the developed macro-element model has demonstrated its computational efficiency and accuracy in the conducted research, further improvements could be introduced towards the definition of a more refined modelling strategy for numerical simulations of RC walls under cyclic loading conditions. In this context, the following directions are recommended for future works:

- **Refinement of the macro-element**

The proposed 2D plane stress macro-element is specialised for analysing RC walls with rectangular cross section and uniform thickness under in-plane loads. In this respect, the cross section could be generalised to complex forms, for example, U- or T- shapes in future research. The refined model could also account for different thicknesses in the unconfined web and confinement boundary regions to model walls with thicker boundary elements than the web. Further refinement may involve extending the macro-element from a 2D model into a 3D description, considering biaxial bending and bi-directional shear behaviour, thus allowing for direct modelling of the 3D structural response. On the element formulation front, the macro-element can be refined to include rotational DoFs leading to an improved kinematics representation. Based on the previous research by Siyam *et al*. (2007), geometric nonlinearity could be incorporated into the macro-element adopting a co-rotational approach paving the way for large displacement analysis of 2D planar structural problems.

- **Improvement of the nonlinear material model**

In Chapter 3, the biaxial concrete material model developed by Izzuddin *et al.* (2004) is used for modelling the cyclic response of RC walls with 2D shell elements. The monotonic response is well predicted, while the experimental cyclic response is well represented only for the first few loading cycles. Future enhancements could be introduced into the existing concrete material model specifying suitable unloading/reloading rules for the simulation under cyclic loading conditions. Also, the biaxial material model developed in this research and based on the rotating crack assumption could be improved. Currently, it utilises the uniaxial bi-linear and trilinear stress-strain relationships for concrete and steel materials. More refined nonlinear uniaxial material laws could be linked to the developed biaxial concrete model, and the use of the fixed crack assumption to model the nonlinear behaviour of concrete could be investigated further.

- **Application of macro-element modelling**

The proposed macro-element is particularly beneficial not only for an economic seismic design of new structures, but also for detailed seismic assessment of existing buildings with retrofitted RC walls. Thus, in future application studies, the developed macro-element models for RC walls could be used for accurate seismic assessment of sub-standard buildings, where not only the global displacement response is assessed but also local ductile and brittle failure modes in the structural components of the existing structure are investigated.

Another potential future direction of the research could concern the definition of optimal retrofitting solutions for existing RC buildings equipped with shear walls, where the number, characteristics and position of the wall components within realistic deficient building structures could be established via an automatic procedure using numerical optimisation techniques.

- **Adopted confined concrete model**

In this research, the modified Kent and Park model proposed by Scott *et al*. (1982) is adopted to represent the confinement effects due to the transverse reinforcement in the boundary regions of the considered wall specimens. Alternatively, other confined concrete models such as those suggested by Model Code 2010 (clause 7.2.3.1.6; fib, 2013) and EC2 (clause 3.1.9; BSI, 2004a) can be employed in numerical simulations using the proposed macro-element for the design of new RC wall structures.

References

Abu-Lebdeh, T. M. & Voyiadjis, G. Z. (1993). Plasticity-damage model for concrete under cyclic multiaxial loading. *Journal of Engineering mechanics,* 119(7), 1465-1484.

ACI Committee 318. (2014). ACI Building Code Requirements for Structural Concrete (ACI 318-14) and Commentary (ACI 318R-14). American Concrete Institute, Farmington Hills, MI.

ACI Committee 374. (2013). Guide for Testing Reinforced Concrete Structural Elements Under Slowly Applied Simulated Seismic Loads (ACI 374.2R-13). American Concrete Institute, Farmington Hills, MI.

ASCE/SEI 7-16. (2016). ASCE/SEI 7-16 : Minimum Design Loads for Buildings and Other Structures, American Society of Civil Engineers ASCE/SEI 7-16 edition.

Bangash, M. Y. H. (2001). *Manual of numerical methods in concrete Modelling and applications validated by experimental and site-monitoring data*.

Barrero Bilbao, A. (2016). *Enhanced nonlinear analysis of 3D concrete structures.* PhD Thesis, Imperial College London.

Belarbi, A. & Hsu, T. T. (1995). Constitutive laws of softened concrete in biaxial tension compression. *ACI Structural Journal,* 92(5), 562-573.

Belletti, B., Scolari, M. & Vecchi, F. (2017). PARC_CL 2.0 crack model for NLFEA of reinforced concrete structures under cyclic loadings. *Computers & Structures,* 191, 165-179.

BSI. (2004a) BS EN 1992-1-1:2004: Eurocode 2, Design of concrete structures - part 1-1: general rules and rules for buildings. BSI, London, UK.

BSI. (2004b) BS EN 1998-1:2004 Eurocode 8-1: Design of structures for earthquake resistance - part 1: general rules, seismic actions and rules for building.

BSI. (2005) BS EN 1998-3:2005 Eurocode 8-3:Design of structures for earthquake resistance - Part 3: Assessment and retrofitting of buildings.

Chen, E.-S. & Buyukozturk, O. (1985). Constitutive model for concrete in cyclic compression. *Journal of engineering mechanics,* 111(6), 797-814.

Chisari, C., Macorini, L. & Izzuddin, B. A. (2020). Multiscale model calibration by inverse analysis for nonlinear simulation of masonry structures under earthquake loading. *International Journal for Multiscale Computational Engineering,* 18(2).

Crisfield, M. A. (1991). *Nonlinear finite element analysis of solids and structures.* Volume 1: Essentials.

Dashti, F., Dhakal, R. P. & Pampanin, S. (2017). Numerical modeling of rectangular reinforced concrete structural walls. *Journal of structural engineering,* 143(6), 04017031.

Elghazouli, A. (2016). *Seismic design of buildings to Eurocode 8*, CRC Press.

Elghazouli, A. & Izzuddin, B. (2004). Realistic modeling of composite and reinforced concrete floor slabs under extreme loading. II: Verification and application.

Faraone, G., Hutchinson, T. C., Piccinin, R. & Silva, J. (2019). Cyclic Lateral Load Response of a Full-Scale Flexure-Dominated Shear Wall. *ACI Structural Journal,* 116(6), 281-292.

Fardis, M. N. (2009). *Seismic design, assessment and retrofitting of concrete buildings: based on EN-Eurocode 8*, Springer.

Fardis, M. N. & Chen, E.-S. (1986). A cyclic multiaxial model for concrete. *Computational mechanics,* 1(4), 301-315.

Faria, R., Oliver, J. & Cervera, M. (1998). A strain-based plastic viscous-damage model for massive concrete structures. *International journal of solids and structures,* 35(14), 1533-1558.

Fib. (2013). *Fib Model Code for concrete structures 2010.* Fédération International du Béton, Lausanne, Switzerland.

Gopalaratnam, V. & Shah, S. P. (1985). Softening response of plain concrete in direct tension. *ACI Structural Journal,* 82(3), 310-323.

Grassl, P. & Jirásek, M. (2006). Damage-plastic model for concrete failure. *International journal of solids and structures,* 43(22-23), 7166-7196.

Grassl, P. & Rempling, R. (2008). A damage-plasticity interface approach to the meso-scale modelling of concrete subjected to cyclic compressive loading. *Engineering Fracture Mechanics,* 75(16), 4804-4818.

Grassl, P., Xenos, D., Nyström, U., Rempling, R. & Gylltoft, K. (2013). CDPM2: A damage-plasticity approach to modelling the failure of concrete. *International Journal of Solids and Structures,* 50(24), 3805-3816.

Greifenhagen, C. & Lestuzzi, P. (2005). Static cyclic tests on lightly reinforced concrete shear walls. *Engineering Structures,* 27(11), 1703-1712.

Hatzigeorgiou, G., Beskos, D., Theodorakopoulos, D. & Sfakianakis, M. (2001). A simple concrete damage model for dynamic FEM applications. *International Journal of Computational Engineering Science,* 2(02), 267-286.

He, W., Wu, Y.-F. & Liew, K. (2008). A fracture energy based constitutive model for the analysis of reinforced concrete structures under cyclic loading. *Computer methods in applied mechanics and engineering,* 197(51-52), 4745-4762.

Hidalgo, P., Jordan, R. & Martinez, M. (2002). An analytical model to predict the inelastic seismic behavior of shear-wall, reinforced concrete structures. *Engineering Structures,* 24(1), 85-98.

Hilber, H. M., Hughes, T. J. & Taylor, R. L. (1977). Improved numerical dissipation for time integration algorithms in structural dynamics. *Earthquake Engineering & Structural Dynamics,* 5(3), 283-292.

Hrynyk, T. D. & Vecchio, F. J. (2015). Capturing out-of-plane shear failures in the analysis of reinforced concrete shells. *Journal of Structural Engineering,* 141(12)**,** 04015058.

Hsu, T. T. & Zhu, R. R. (2002). Softened membrane model for reinforced concrete elements in shear. *ACI Structural Journal,* 99, 460-469.

Izzuddin, B. A. (1991). *Nonlinear Dynamic Analysis of Framed Structures.* PhD Thesis, Imperial College, University of London.

Izzuddin, B. A. Advanced large displacement analysis of composite floor slabs. *15th ASCE Engineering Mechanics Division Conference*, 2002 Reston, Virginia. Columbia University in the City of New York.

Izzuddin, B. A. & Elnashai, A. S. (1993). Adaptive space frame analysis. Part II: A distributed plasticity approach. *Proceedings of the Institution of Civil Engineers-Structures and Buildings,* 99(3), 317-326.

Izzuddin, B. A., Macorini, L. & and Rinaldin, G. (2013) Partitioned Modelling for Nonlinear Dynamic Analysis of Reinforced Concrete Buildings for Earthquake Loading. *Proceedings of the Fourteenth International Conference on Civil, Structural and Environmental Engineering Computing*. 1–12.

Izzuddin, B. A., Tao, X. Y. & Elghazouli, A. Y. (2004). Realistic modeling of composite and reinforced concrete floor slabs under extreme loading. I: Analytical method. *Journal of Structural Engineering,* 130(12), 1972-1984.

Jalali, A. & Dashti, F. (2010). Nonlinear behavior of reinforced concrete shear walls using macroscopic and microscopic models. *Engineering Structures,* 32(9), 2959-2968.

Jokhio, G. A. & Izzuddin, B. A. (2013). Parallelisation of nonlinear structural analysis using dual partition super elements. *Advances in Engineering Software,* 60, 81-88.

Jokhio, G. A. & Izzuddin, B. (2015). A dual super-element domain decomposition approach for parallel nonlinear finite element analysis. *International Journal for Computational Methods in Engineering Science and Mechanics,* 16(3), 188-212.

Kabeyaswa, T., Shiohara, H., Otani, S. & Aoyama, H. (1983). Analysis of the full-scale seven-story reinforced concrete test structure. *Journal of the Faculty of Engineering,* 37, 432-478.

Kachanov, L. (1986). *Introduction to continuum damage mechanics*, Springer Science & Business Media.

Kappos, A. (2014). *Earthquake resistant concrete structures*, CRC Press.

Karsan, I. D. & Jirsa, J. O. (1969). Behavior of concrete under compressive loadings. *Journal of the Structural Division,* 95(12), 2543-2564.

Kiani, J. & Pezeshk, S. (2017). Sensitivity analysis of the seismic demands of RC moment resisting frames to different aspects of ground motions. *Earthquake engineering & structural dynamics,* 46(15), 2739-2755.

Kolozvari, K., Arteta, C., Fischinger, M., Gavridou, S., Hube, M., Isakovic, T., Lowes, L., Orakcal, K., Vásquez, J. & Wallace, J. (2018). Comparative study of state-of-the-art macroscopic models for planar reinforced concrete walls. *ACI Structural Journal,* 115(6), 1637-1657.

Kolozvari, K., Biscombe, L., Dashti, F., Dhakal, R. P., Gogus, A., Gullu, M. F., Henry, R. S., Massone, L. M., Orakcal, K. & Rojas, F. (2019). State-of-the-art in nonlinear finite element modeling of isolated planar reinforced concrete walls. *Engineering Structures,* 194, 46-65.

Kolozvari, K., Orakcal, K. & Wallace, J. W. (2015). Modeling of cyclic shear-flexure interaction in reinforced concrete structural walls. I: Theory. *Journal of Structural Engineering,* 141(5), 04014135.

Kotsovos, M. D. & Pavlovic, M. N. (1995). *Structural concrete: finite-element analysis for limit-state design*, Thomas Telford.

Kupfer, H. B. & Gerstle, K. H. (1973). Behavior of concrete under biaxial stresses. *Journal of the engineering mechanics division,* 99(4), 853-866.

Lee, J. & Fenves, G. L. (1998). Plastic-damage model for cyclic loading of concrete structures. *Journal of engineering mechanics,* 124(8), 892-900.

Lemaitre, J. (1985). A continuous damage mechanics model for ductile fracture. Journal of Engineering Materials and Technology, 107(1), 83-89

Lemaitre, J. & Chaboche, J.-L. (1994). *Mechanics of solid materials*, Cambridge university press.

Liu, G.-R. & Quek, S. S. (2013). *The finite element method: a practical course*, Butterworth-Heinemann.

Lu, X. & Chen, Y. (2005). Modeling of coupled shear walls and its experimental verification. *Journal of Structural Engineering,* 131(1), 75-84.

Lu, X., Xie, L., Guan, H., Huang, Y. & Lu, X. (2015). A shear wall element for nonlinear seismic analysis of super-tall buildings using OpenSees. *Finite Elements in Analysis and Design,* 98, 14-25.

Lu, Y., Panagiotou, M. & Koutromanos, I. (2016). Three-dimensional beam-truss model for reinforced concrete walls and slabs – part 1: modeling approach, validation, and parametric study for individual reinforced concrete walls. *Earthquake Engineering & Structural Dynamics,* 45(9), 1495-1513.

Lubliner, J., Oliver, J., Oller, S. & Onate, E. (1989). A plastic-damage model for concrete. *International Journal of solids and structures,* 25(3), 299-326.

Luccioni, B., Oller, S. & Danesi, R. (1996). Coupled plastic-damaged model. *Computer methods in applied mechanics and engineering,* 129(1-2), 81-89.

MacLeod, I. (1973). ANALYSIS OF SHEAR WALL BUILDINGS BY THE FRAME METHOD. *Proceedings of the Institution of Civil Engineers,* 55(3), 593-603.

Macorini, L. & Izzuddin, B. (2011). A non-linear interface element for 3D mesoscale analysis of brick - masonry structures. *International Journal for numerical methods in Engineering,* 85(12), 1584-1608.

Malm, R. (2006). *Shear cracks in concrete structures subjected to in-plane stresses.* PhD Thesis. KTH Royal Institute of Technology

Mansour, M. & Hsu, T. T. (2005a). Behavior of reinforced concrete elements under cyclic shear. I: Experiments. *Journal of Structural Engineering,* 131(1), 44-53.

Mansour, M. & Hsu, T. T. (2005b). Behavior of reinforced concrete elements under cyclic shear. II: Theoretical model. *Journal of Structural Engineering,* 131(1), 54-65.

Mansour, M., Lee, J.-Y. & Hsu, T. T. (2001). Cyclic stress-strain curves of concrete and steel bars in membrane elements. *Journal of Structural Engineering,* 127(12), 1402-1411.

Martinelli, P. & Filippou, F. C. (2009). Simulation of the shaking table test of a seven-story shear wall building. *Earthquake Engineering & Structural Dynamics,* 38(5), 587-607.

Masjuki, S. A. (2017). *Assessment and retrofitting of reinforced concrete buildings with shear walls subject to earthquake loading.* PhD Thesis, Imperial College London.

Massone, L., Orakcal, K. & Wallace, J. (2006). Shear-flexure interaction for structural walls. *Special Publication,* 236, 127-150.

Mazars, J. & Pijaudier-Cabot, G. (1989). Continuum damage theory—application to concrete. *Journal of engineering mechanics,* 115(2), 345-365.

Minga, E., Macorini, L. & Izzuddin, B. A. (2018). A 3D mesoscale damage-plasticity approach for masonry structures under cyclic loading. *Meccanica,* 53(7), 1591-1611.

Ministry of Construction. (1991). “Code for design and construction of reinforced concrete high-rise buildings.” JGJ 3-91, Chinese Building Industry Press, Beijing.

Mitchell, D. & Collins, M. P. (1974) Diagonal compression field theory-a rational model for structural concrete in pure torsion. ACI Journal Proceedings, 71(8), 396-408.

Miyahara, T., Kawakmi, T. & Maekawa, K. (1987). Nonlinear behavior of cracked reinforced concrete plate element under uniaxial compression. *Doboku Gakkai Ronbunshu,* 1987, 249-258.

Mo, Y., Zhong, J. & Hsu, T. T. (2008). Seismic simulation of RC wall-type structures. *Engineering structures,* 30(11), 3167-3175.

Moharram, M., Bompa, D. & Elghazouli, A. (2017). Experimental and numerical assessment of mixed RC beam and steel column systems. *Journal of Constructional Steel Research,* 131, 51-67.

Ngo, D. & Scordelis, A. C. (1967) Finite element analysis of reinforced concrete beams. ACI Journal Proceedings, 64(3), 152-163.

Nilson, A. H. (1968) Nonlinear analysis of reinforced concrete by the finite element method. ACI Journal Proceedings, 65(9), 757-766.

NTC. (2008). "NTC Normativa Tecnica per Le Costruzionii - DM 14 Gennaio 2008."

Oesterle, R., Fiorato, A., Aristizabal-Ochoa, J. & Corley, W. (1980). Hysteretic response of reinforced concrete structural walls. *ACI Special Publication,* 63, 243-273.

Orakcal, K., Ulugtekin, D. & Massone, L. (2012) Constitutive modeling of reinforced concrete panel behavior under cyclic loading. *Proceedings of 15th World Conference on Earthquake Engineering,* 3573

Orakcal, K., Wallace, J. W. & Conte, J. P. (2004). Flexural modeling of reinforced concrete walls-model attributes. *Structural Journal,* 101(5), 688-698.

Ortiz, M. (1985). A constitutive theory for the inelastic behavior of concrete. *Mechanics of materials,* 4, 67-93.

Palermo, D. & Vecchio, F. J. (2003). Compression field modeling of reinforced concrete subjected to reversed loading: formulation. *ACI Structural Journal,* 100(1), 616-625.

Palermo, D. & Vecchio, F. J. (2004). Compression field modeling of reinforced concrete subjected to reversed loading: Verification. *ACI Structural Journal,* 101(5), 155-164.

Panagiotou, M., Restrepo, J. I., Schoettler, M. & Kim, G. (2012). Nonlinear cyclic truss model for reinforced concrete walls. *ACI Structural Journal,* 109(2), 205.

Pang, X.-B. D. & Hsu, T. T. (1995). Behavior of reinforced concrete membrane elements in shear. *Structural Journal,* 92(6), 665-679.

Pang, X.-B. D. & Hsu, T. T. (1996). Fixed angle softened truss model for reinforced concrete. *Structural Journal,* 93(2), 196-208.

Panoskaltsis, V., Lubliner, J. & Monteiro, P. (1994). Rate dependent plasticity and damage for concrete. Cement Manufacture and Use, ASCE, 27-40.

Paulay, T., Priestley, M. & Synge, A. (1982) Ductility in earthquake resisting squat shearwalls. ACI Journal Proceedings, 79(4), 257-269.

Paulay, T. & Priestley, M. N. (1992). *Seismic design of reinforced concrete and masonry buildings*, John Wiley & Sons, Inc.

Penelis, G. G. & Penelis, G. G. (2014). *Concrete buildings in seismic regions*, CRC Press Boca Raton, FL, USA.

Polak, M. A. & Vecchio, F. (1993). Nonlinear analysis of reinforced-concrete shells. *Journal of Structural engineering,* 119(12), 3439-3462.

Pugh, J. S. (2012). *Numerical simulation of walls and seismic design recommendations for walled buildings.* University of Washington.

Pugh, J. S., Lowes, L. N. & Lehman, D. E. (2015). Nonlinear line-element modeling of flexural reinforced concrete walls. *Engineering Structures,* 104, 174-192.

Rashid, Y. R. (1968). Ultimate strength analysis of prestressed concrete pressure vessels. *Nuclear engineering and design,* 7(4), 334-344.

Rots, J. G. & Blaauwendraad, J. (1989). Crack models for concrete, discrete or smeared? Fixed, multi-directional or rotating? *HERON, 34 (1), 1989*.

Salonikios, T. N. (2007). Analytical prediction of the inelastic response of RC walls with low aspect ratio. *Journal of structural engineering,* 133(6), 844-854.

Salonikios, T. N., Kappos, A. J., Tegos, I. A. & Penelis, G. G. (1999). Cyclic load behavior of low-slenderness reinforced concrete walls: Design basis and test results. *Structural Journal,* 96(4), 649-660.

Scott, B. D., Park, R. & Priestley, M. J. N. (1982). Stress-Strain Behavior of Concrete Confined by Overlapping Hoops at Low and High Strain Rates. *ACI Structural Journal,* 79, 13-17.

Simo, J. C. & Ju, J. (1987). Strain-and stress-based continuum damage models—I. Formulation. *International journal of solids and structures,* 23(7), 821-840.

Siyam, A., Izzuddin, B. A. & Smith, D. L. (2007). Large-displacement analysis of planar RC structures. *Journal of structural engineering,* 133**,** 595-605.

Smith, M. (2009) ABAQUS/Standard User's Manual, Version 6.9. Dassault Systèmes Simulia Corp, Providence, RI.

Spacone, E., Filippou, F. C. & Taucer, F. F. (1996). Fibre beam–column model for non-linear analysis of R/C frames: Part I. Formulation. *Earthquake Engineering & Structural Dynamics,* 25(7), 711-725.

Spiliopoulos, K. & Lykidis, G. C. (2006). An efficient three-dimensional solid finite element dynamic analysis of reinforced concrete structures. *Earthquake engineering & structural dynamics,* 35(2), 137-157.

Sümer, Y. & Aktaş, M. (2015). Defining parameters for concrete damage plasticity model. *Challenge Journal of Structural Mechanics,* 1(3), 149-155.

Thermou, G. & Elnashai, A. (2006). Seismic retrofit schemes for RC structures and local-global consequences. *Progress in Structural Engineering and Materials,* 8(1), 1-15.

Tran, T. A. (2012). *Experimental and analytical studies of moderate aspect ratio reinforced concrete structural walls.* PhD Thesis. University of California, Los Angeles.

Tripathi, M., Dhakal, R. P. & Dashti, F. (2020). Nonlinear cyclic behaviour of high-strength ductile RC walls: Experimental and numerical investigations. *Engineering Structures,* 222, 111116.

Ulugtekin, D. (2010). *Analytical Modeling of Reinforced Concrete Panel Elements under Reversed Cyclic Loadings.* MS Thesis. Boğaziçi University.

Vamvatsikos, D. & Cornell, C. A. (2002). Incremental dynamic analysis. *Earthquake engineering & structural dynamics,* 31(3), 491-514.

Vásquez, J. A., de la Llera, J. C. & Hube, M. A. (2016). A regularized fiber element model for reinforced concrete shear walls. *Earthquake Engineering & Structural Dynamics,* 45(13)**,** 2063-2083.

Vecchio, F. J. & Collins, M. P. (1986). The modified compression-field theory for reinforced concrete elements subjected to shear. *ACI Structural Journal,* 83(2), 219-231.

Voyiadjis, G. Z. & Abu-Lebdeh, T. M. (1994). Plasticity model for concrete using the bounding surface concept. *International Journal of Plasticity,* 10(1), 1-21.

Voyiadjis, G. Z., Voyiadjis, G. Z. & Kattan, P. I. (1999). *Advances in damage mechanics: metals and metal matrix composites*, Elsevier.

Vulcano, A., Bertero, V. V. & Colotti, V. (1988) Analytical modeling of RC structural walls. Proceedings, 9th world conference on earthquake engineering, 6, 41-46.

Wu, Y.-T., Lan, T.-Q., Xiao, Y. & Yang, Y.-B. (2017). Macro-modeling of reinforced concrete structural walls: state-of-the-art. *Journal of Earthquake Engineering,* 21(4), 652-678.

Yazdani, S. & Schreyer, H. (1990). Combined plasticity and damage mechanics model for plain concrete. *Journal of engineering mechanics,* 116(7), 1435-1450.

Yettram, A. L. & Husain, H. M. (1966). Plane-framework methods for plates in extension. *Journal of the Engineering Mechanics Division,* 92(1), 157-168.

Zhu, R. R., Hsu, T. T. & Lee, J.-Y. (2001). Rational shear modulus for smeared-crack analysis of reinforced concrete. *Structural Journal,* 98(4), 443-450.

Zienkiewicz, O. C. & Taylor, R. L. (2005). *The finite element method for solid and structural mechanics*, Elsevier.

Zienkiewicz, O. C., Taylor, R. L. & Zhu, J. Z. (2005). *The finite element method: its basis and fundamentals*, Elsevier.

Appendix

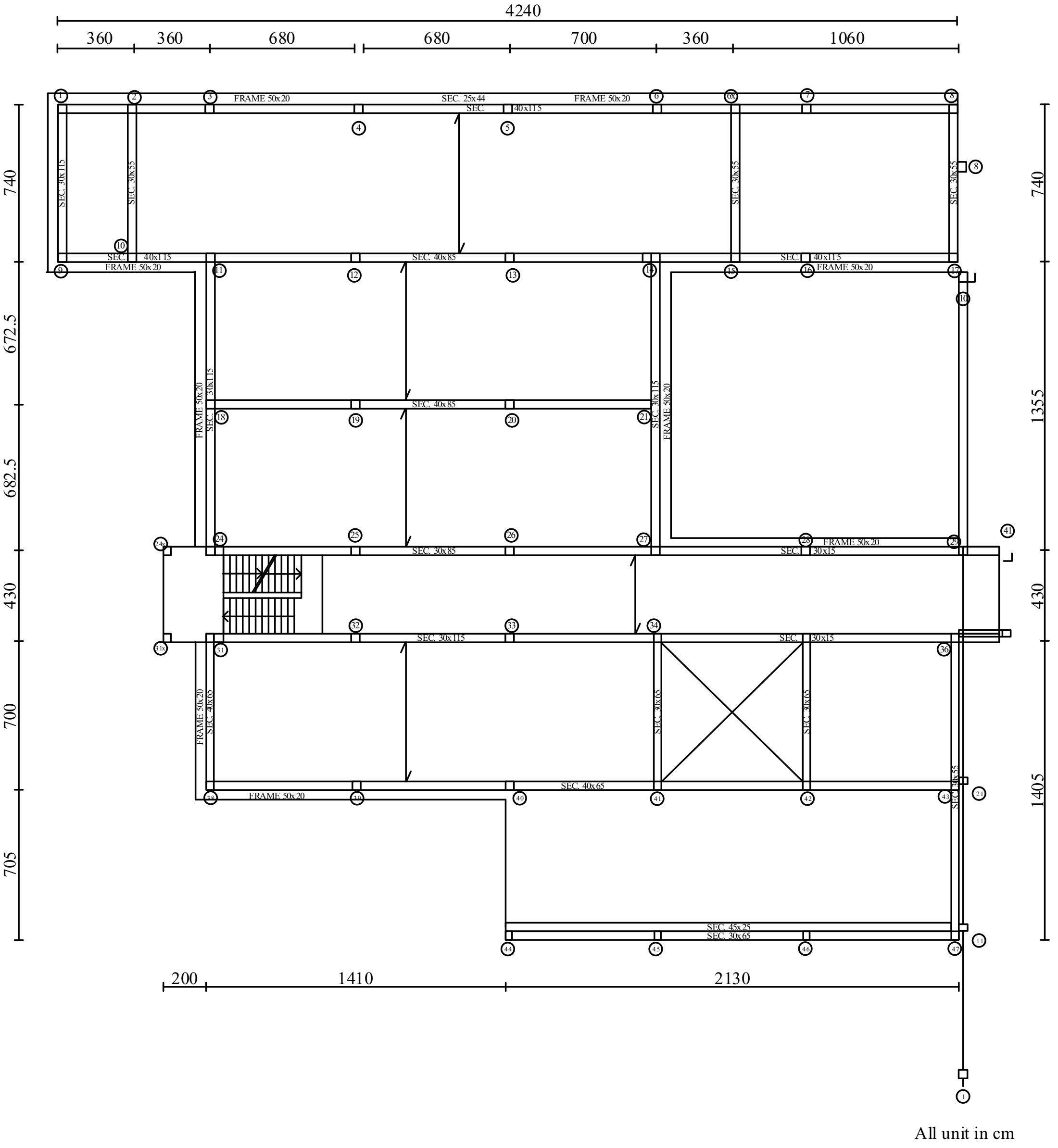

All unit in cm

Figure A1: Plan view of the 1st and 2nd floors of the 4-storey building and geometries of the beam and frame sections

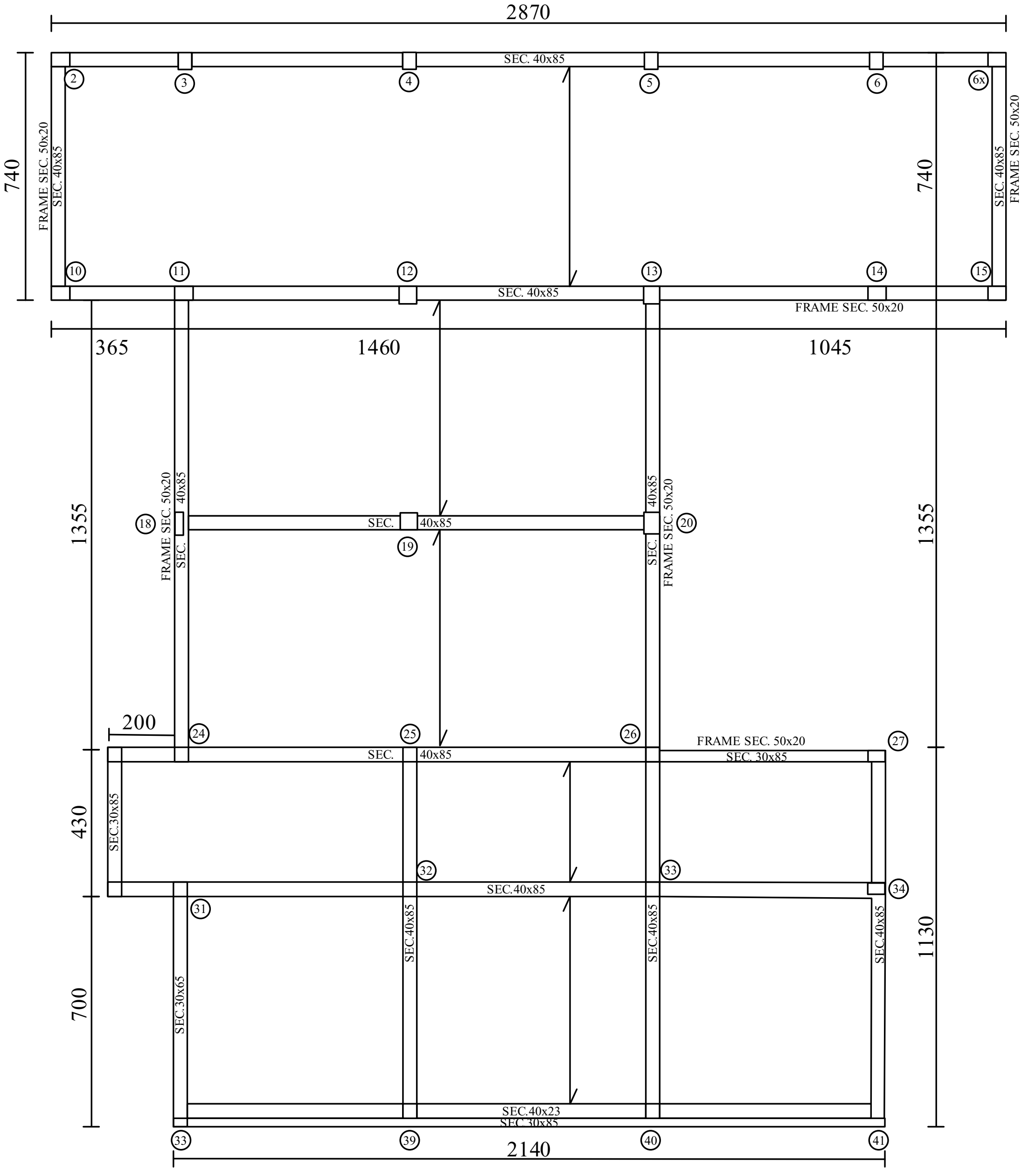

All unit in cm

Figure A2: Plan view of the 3rd and 4th floors of the 4-storey building and geometries of the beam and frame sections

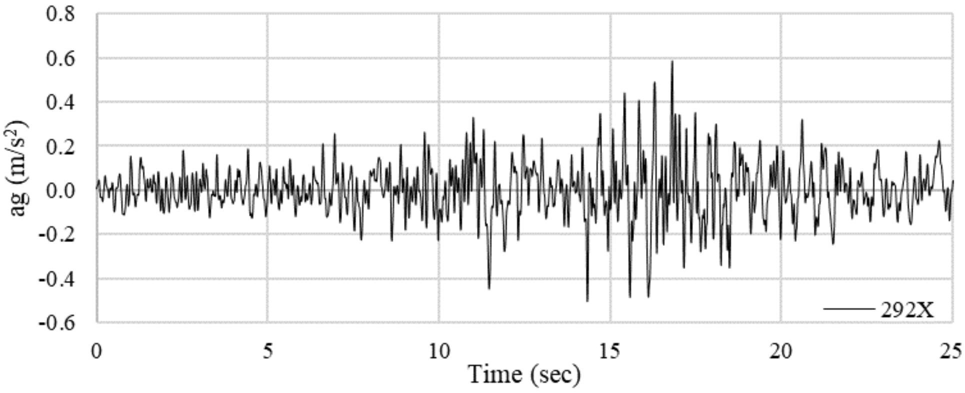

(a)

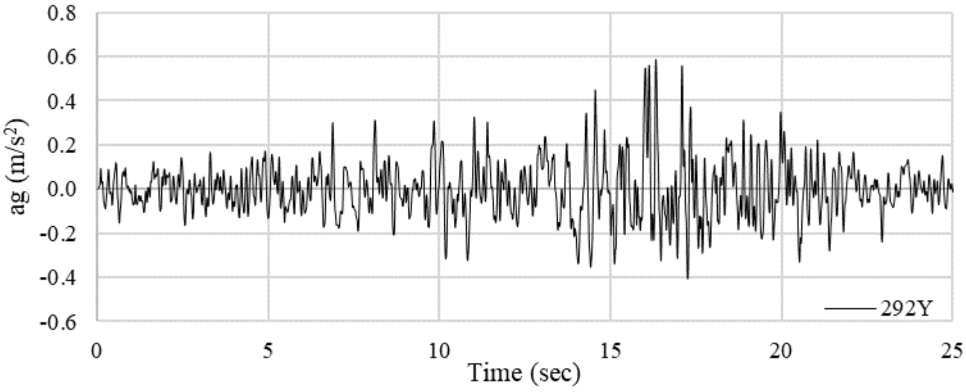

(b)

Figure A3: Ground motion acceleration records of Campano Lucano earthquake (292) in: (a) X- and (b) Y-directions

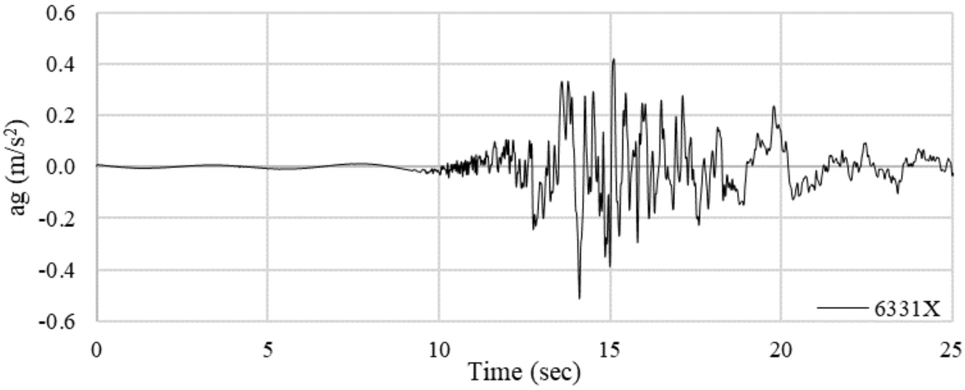

(a)

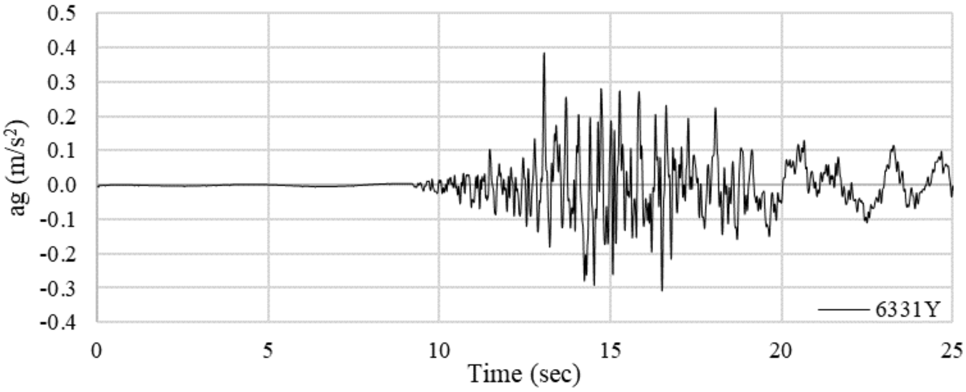

(b)

Figure A4: Ground motion acceleration records of South Iceland earthquake (aftershock) (6331) in: (a) X- and (b) Y-directions

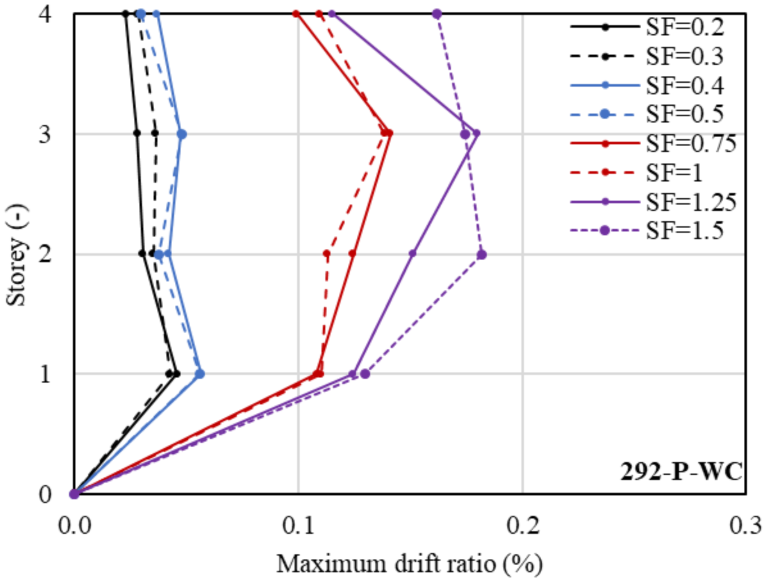

(a)

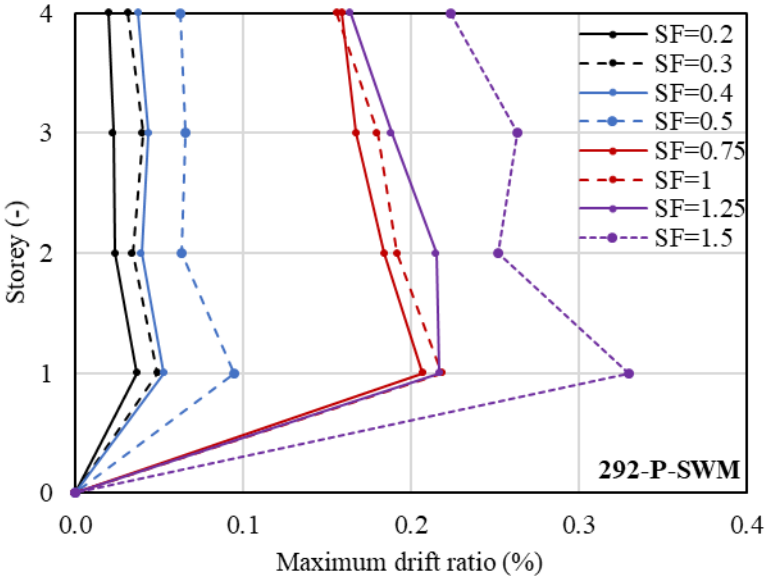

(b)

Figure A5: Maximum inter-storey drift ratio of column P at each storey of the 4-storey frame-wall building predicted by: (a) WC and (b) SWM models under scaled ground motions of earthquake 292

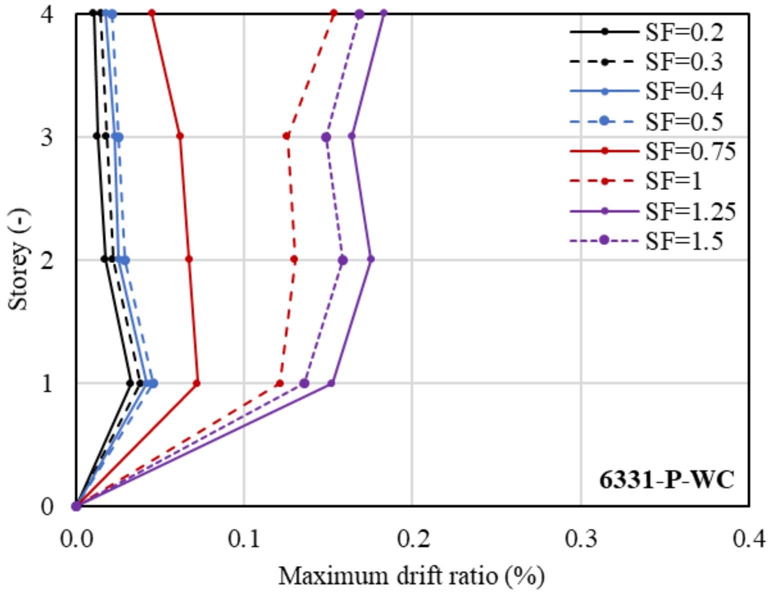

(a)

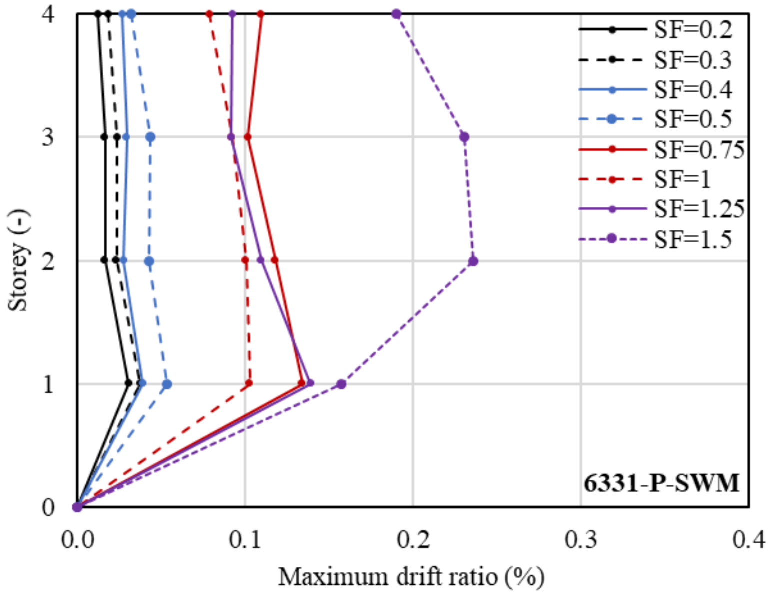

(b)

Figure A6: Maximum inter-storey drift ratio of column P at each storey of the 4-storey frame-wall building predicted by: (a) WC and (b) SWM models under scaled ground motions of earthquake 6331